

**Precise quantification of forces and  
charges at the atomic scale by  
non-contact atomic force and charge  
force microscopy**

**Dissertation**

zur Erlangung des Grades eines  
Doktors der Naturwissenschaften (Dr. rer. nat.)  
am Fachbereich Physik der Universität Osnabrück

vorgelegt von

**Daniel Heile**

– 23. Juni 2023 –



Gutachter der Dissertation:  
Prof. Dr. Michael Reichling  
Dr. Clemens Barth



# Contents

|   |           |
|---|-----------|
| <b>1. Introduction</b>  | <b>1</b>  |
| <b>2. Tip-sample interaction forces</b>   | <b>5</b>  |
| 2.1. Composition of the tip-sample force . . . . .  | 5         |
| 2.2. Atomic forces . . . . .  | 8         |
| 2.2.1. The short-range chemical interaction force . . . . .   | 8         |
| 2.2.2. The interatomic van der Waals force . . . . .  | 11        |
| 2.3. Body forces . . . . .  | 15        |
| 2.3.1. The non-retarded van der Waals force acting between tip and<br>sample body . . . . .         | 15        |
| 2.3.2. Electrostatic force . . . . .  | 18        |
| 2.3.2.1. Model and derivation . . . . .   | 19        |
| 2.3.2.2. Properties and voltage dependency . . . . .  | 24        |
| 2.4. Model for the total tip-sample interaction . . . . .   | 29        |
| <b>3. NC-AFM principle and setup</b>  | <b>35</b> |
| 3.1. Force sensor . . . . .   | 36        |
| 3.2. Frequency modulated non-contact atomic force microscopy (FM NC-<br>AFM) . . . . .              | 39        |
| 3.3. Charge force microscopy (CFM) . . . . .  | 43        |
| 3.4. Amplitude calibration and sensor inclination . . . . .   | 46        |
| <b>4. Quantitative AFM theory</b>   | <b>49</b> |
| 4.1. Coordinates in NC-AFM . . . . .  | 49        |
| 4.2. Harmonic oscillator and transfer function . . . . .  | 52        |
| 4.3. Tip movement in the force field of the sample . . . . .  | 56        |
| 4.3.1. Harmonic approximation . . . . .   | 56        |
| 4.3.2. Harmonic tip oscillation and force field model . . . . .                                     | 58        |
| 4.3.3. Ansatz for solving the equation of motion . . . . .  | 61        |
| 4.4. Derivation of three fundamental AFM equations . . . . .  | 64        |
| 4.5. Averaging functions in AFM and convolution . . . . .   | 65        |
| 4.6. Deconvolution procedure . . . . .  | 68        |
| <b>5. Alignment method for the accurate and precise quantification of tip-<br/>  surface forces</b> | <b>73</b> |

|  |            |
|--|------------|
| <b>6. Quantitative dynamic force microscopy with inclined tip oscillation</b>                                    | <b>87</b>  |
| <b>7. Quantitative CFM theory</b>  | <b>99</b>  |
| 7.1. Modulated electrostatic force contribution to the tip-sample force . . .                                    | 100        |
| 7.2. Harmonic approximation in CFM . . . . .   | 102        |
| 7.3. Fourier series development of the periodically sampled force contributions . . . . .                        | 103        |
| 7.4. Application of the AFM averaging functions . . . . .  | 104        |
| 7.5. Solution of the equation of motion . . . . .  | 106        |
| 7.6. CFM detection . . . . .   | 108        |
| 7.7. Interpretation of CFM signals . . . . .   | 110        |
| <b>8. Modelling nanoscale charge measurements</b>  | <b>113</b> |
| <b>9. Nanoscale charge quantification using CFM</b>  | <b>131</b> |
| <b>10. Summary</b>   | <b>151</b> |
| <b>11. Acknowledgements</b>  | <b>153</b> |
| <b>A. Appendix</b>   | <b>155</b> |
| A.1. Potential energy within the electric field . . . . .  | 155        |
| A.2. Energy due to the external battery . . . . .  | 157        |
| A.3. S model: Metallic sphere at fixed potential against a dielectric or metallic sample . . . . .               | 159        |
| A.3.1. Infinite charge series model . . . . .  | 160        |
| A.3.1.1. Point charge in front of a dielectric (or metallic) half-space . . . . .                                | 161        |
| A.3.1.2. Point charge in front of a conductive sphere at constant potential . . . . .                            | 161        |
| A.3.1.3. Full solution . . . . .   | 162        |
| A.4. Properties of the Fourier transformation . . . . .  | 165        |
| A.5. Decomposition of the tip-sample force in even and odd Fourier coefficients . . . . .                        | 166        |
| A.5.1. $F_{\text{even}}(\tilde{z}_{\text{ts}}(t), \dot{\tilde{z}}_{\text{ts}}(t))$ and cosine function . . . . . | 166        |
| A.5.2. $F_{\text{even}}(\tilde{z}_{\text{ts}}(t), \dot{\tilde{z}}_{\text{ts}}(t))$ and sine function . . . . .   | 167        |
| A.5.3. $F_{\text{odd}}(\tilde{z}_{\text{ts}}(t), \dot{\tilde{z}}_{\text{ts}}(t))$ and cosine function . . . . .  | 168        |
| A.5.4. $F_{\text{odd}}(\tilde{z}_{\text{ts}}(t), \dot{\tilde{z}}_{\text{ts}}(t))$ and sine function . . . . .    | 169        |
| A.6. Derivation of the three AFM equations . . . . .   | 169        |
| A.6.1. Time-averaged form . . . . .  | 169        |
| A.6.1.1. AFM equation 1 . . . . .  | 170        |
| A.6.1.2. AFM equation 2 . . . . .  | 171        |
| A.6.1.3. AFM equation 3 . . . . .  | 172        |
| A.6.2. Spatial form and derivation of the averaging functions . . . . .  | 173        |
| A.6.2.1. AFM equation 1 . . . . .  | 173        |

|  |            |
|--|------------|
| A.6.2.2. AFM equation 2 . . . . .  | 174        |
| A.6.2.3. AFM equation 3 . . . . .  | 176        |
| A.7. AFM equations as solution for the equation of motion . . . . .                      | 177        |
| A.8. Common assumptions for the AFM equations in FM NC-AFM . . . . .                     | 179        |
| <b>Bibliography</b>  | <b>181</b> |
| <b>B. Erklärung über die Eigenständigkeit der erbrachten wissenschaftlichen Leistung</b> | <b>193</b> |





# List of Figures

|      |  |     |
|------|--|-----|
| 2.1. | Composition of tip-sample interaction force . . . . .  | 6   |
| 2.2. | Morse interaction . . . . .  | 9   |
| 2.3. | Lennard-Jones potential . . . . .  | 14  |
| 2.4. | Non-retarded van der Waals body-body interaction force . . . . .   | 17  |
| 2.5. | Electrostatic tip-sample model . . . . .   | 20  |
| 2.6. | Exemplification of the electrostatic force dependencies . . . . .  | 26  |
| 2.7. | Model of the total tip-sample interaction force . . . . .  | 31  |
| 2.8. | Total tip-sample interaction force containing electrostatic interaction . . . . .                        | 32  |
|      |  |     |
| 3.1. | Schematic Cantilever . . . . .   | 36  |
| 3.2. | Setup of a FM NC-AFM with additional FM CL-KPFM . . . . .  | 40  |
| 3.3. | Shift of the resonance peak, due to tip-sample interaction . . . . .                                     | 42  |
| 3.4. | Spectrum of the deflection signal in FM-CL-KPFM . . . . .  | 45  |
| 3.5. | Effect of the cantilever inclination towards the sample . . . . .  | 48  |
|      |  |     |
| 4.1. | Coordinates of NC-AFM . . . . .  | 51  |
| 4.2. | Driven, damped harmonic oscillator . . . . .   | 55  |
| 4.3. | Harmonic oscillation of the tip . . . . .  | 59  |
| 4.4. | Tip oscillation in the sample force field . . . . .  | 62  |
| 4.5. | Cup and cap averaging function . . . . .   | 67  |
| 4.6. | Convolution and deconvolution in AFM . . . . .   | 70  |
|      |  |     |
| A.1. | S model - Metallic sphere against a dielectric or metallic sample . . . . .                              | 160 |
| A.2. | Basic concepts for the infinite charge series method . . . . .   | 160 |
| A.3. | S model with infinite charge series . . . . .  | 162 |
| A.4. | $\hat{\Phi}_{\text{void}}(z_{\text{ts}})$ and $C_{\text{void}}(z_{\text{ts}})$ for the S model . . . . . | 164 |



# List of Tables

|  |    |
|--|----|
| 2.1. Morse potential . . . . .   | 8  |
| 2.2. Lennard-Jones potential . . . . .   | 13 |
| 2.3. Van-der-Waals body-body interaction . . . . .   | 15 |
| 2.4. Sphere-sample capacitor (S model) parameters . . . . .                                      | 25 |
| 2.5. S model configurations . . . . .  | 27 |
| 2.6. Collated list of model parameters for tip-sample force calculation . .                      | 33 |
| 3.1. Properties of cantilevers utilised in this work . . . . .                                   | 38 |
| 4.1. Parameters used for calculation of the harmonic tip oscillation. . .                        | 58 |
| 4.2. Parameters used for calculation of the force field $F_{ts}^z(z_{ts}, \dot{z}_{ts})$ . . . . | 60 |
| 4.3. Assignment of the quantities linked by the three fundamental AFM equations. . . . .         | 65 |

# 1. Introduction

Our ever increasing understanding of interactions in the atomic and sub-atomic regime is a great success of quantum mechanics. During the 20<sup>th</sup> century, elaborate theories describing the interaction between atoms and molecules by electromagnetic forces have been developed [1]. While systems of few atoms can precisely be described by chemical bonding and physical interactions between individual atoms, this approach is not expedient for the description of binding between mesoscopic and macroscopic bodies. For such objects, binding is described phenomenologically as adhesion [2], which is commonly discussed in the framework of integral physical interaction. As the transition between both types of descriptions is fluent, the correct interpretation of force measurements at the nanoscale is a complex matter. To validate interpretations, precise quantitative measurements of nanoscale forces are needed.

The measurement of forces between atoms, molecules and nanoscale objects has been pushed to the physical limits [3, 4, 5] and is of great interest in diverse fields of science and technology including high-resolution analysis of inorganic [6, 7], organic [8, 9, 10], and biological surfaces [11, 12, 13], three-dimensional force mapping [14, 15, 16, 17], Casimir force measurements [18], nanomechanical material characterization [19, 20, 21, 22, 23], capillary force studies [24, 25, 26, 27, 28], hydration layer analysis [29, 30, 31, 32], the study of atom-specific reactivity [33, 34], mechanochemistry [35, 36, 37], quantum dot microscopy [38] and single-spin detection [39, 40].

The technique of frequency modulated non-contact atomic force microscopy (FM NC-AFM) is a powerful tool for measuring forces between an oscillating sharp tip and a surface of any kind with resolution down to the atomic scale [41, 42, 43, 44]. However, the correct interpretation of force measurements at the nanoscale is most difficult as it is the crossover regime where attractive and repulsive forces between individual atoms and forces between mesoscopic bodies act together [2]. In this regime, the force-distance law is not a simple function of the body separation, but is commonly described by the sum of contributions based on different models [45]. Utmost precision in measuring and analysing a force-distance curve is required to test models and to quantify nanoscale interactions. Besides conceptual difficulties in describing tip-surface forces, there are experimental peculiarities severely limiting

## 1. Introduction

accurate force measurements. First, the main measurement signal in NC-AFM is not the force, but the frequency shift of the resonance frequency of the high- $Q$  force probe oscillating in the force field of the sample [44]. The force curve is derived from distant-dependent frequency shift data by numerical deconvolution [46, 47], which is often referred to as force inversion. The result of this inversion can be ill-posed [48], can exhibit large errors in a range of relevant amplitudes [49], or can include severely amplified detection noise [50]. Second, force inversion algorithms yield valid results only if the oscillation amplitude is known precisely [47, 49]. Third, strong gradients in the force field make the measurement susceptible to minute deviations of the probe trajectory from the target curve as they result, for example, from thermal drift even when applying active drift compensation [51, 52].

Within the scope of this thesis, the introduction of the force curve alignment (FCA) method [53] is one major achievement. The FCA method facilitates the accurate and precise measurement of force curves by circumventing the experimental peculiarities and ultimately removing systematic errors in widely accepted practice. The general concept is the repetitive measurement of the tip-surface interaction with different probe oscillation amplitude, delivering a data-set, which is robust against disturbing impacts. While the presence of systematic errors can hardly be identified from a single force curve, a match of individual force curves by an optimisation algorithm enables a self-consistent determination of the error-free tip-surface interaction force. Furthermore, a successful application of the FCA method inherently yields the correct value of the probe oscillation amplitude solving another key challenge of force retrieval from frequency shift data.

The application of the FCA method in the course of this thesis uncovered an often ignored source for systematic error in force retrieval from frequency shift data, namely, a tilt of the probe with respect to the surface normal. A tacit assumption in prevalent AFM theory [44] and inversion algorithms [46, 47] is that the axis of data acquisition (data recording path) is parallel to the axis of probe oscillation (tip sampling path). However, in a typical experimental setup this is not the case, as there are often angles ranging from  $10^\circ$  to  $20^\circ$  present between both axes for technical reasons. Consequences of the inclined AFM probe mount have been identified before [54, 55, 56, 57]. In this work, the established mathematical description for dynamic atomic force microscopy [44] is extended by including free orientations of the tip sampling and data recording path [58] allowing to avoid systematic errors due to probe inclination in the interpretation of force curve and imaging data.

The high sensitivity of FM NC-AFM towards nanoscale forces, allows to observe the influence of charge state changes in nano-objects from the electrostatic part of the tip-sample interaction with high precision [59, 60, 61]. However, the quantification of a static charge contained in a nano-object on the sample surface using a FM NC-AFM is not yet achieved. To solve this challenge, in this work, the

technique of charge force microscopy (CFM) aiming at the precise quantification of static charges located in, on or above the sample substrate is implemented on the fundament of the protocols for accurate force curve measurements developed in the present work. Technically, CFM is based on frequency modulated closed-loop Kelvin probe force microscopy (FM-CL KPFM) [62, 63, 64], a nanoscale imaging technique that is rooted in the measurement of contact potential differences (CPD) [65] and work function differences [66] between tip and sample for metal or semiconductor surfaces. The dynamic technique for measuring electrostatic tip-sample interaction involves the oscillation of the force probe as well as an oscillating bias voltage applied between tip and sample support. In CFM, the signals at the bias oscillation frequency and its first harmonic are measured by side-band detection enabling the quantification of charges by a two-step procedure within the framework of CFM theory [67, 68, 69, 70]. In the first step, distance-dependent data of the tip-surface capacitance is retrieved from evaluating the signal measured at the first harmonic of the bias oscillation frequency yielding parameters for the electrostatic model [71]. In the second step, the electrostatic model is used to analyse the CFM signal measured at the bias oscillation frequency yielding charge quantification of charges in the tip-sample system.

In this work, the theoretical foundation of CFM based on the considerations in [67, 68, 69, 70] has been developed, simulations regarding CFM signal generation have been carried out identifying distant-dependent CFM data as most elucidative for charge quantification, and the two-step routine has been implemented for retrieving the charge from such data. The CFM technique has been applied to experimental data obtained for CeO<sub>2</sub> supported Au nano-clusters, which hold a static charge [72, 73, 74, 75], allowing the quantification of the contained charge.

This thesis is organized as follows: In chapter 2 the forces contributing to the tip-surface interaction are discussed, where special emphasis is given to the description of electrostatic forces due to charges. In chapter 3, the principle of NC-AFM is explained and the experimental setup of FM NC-AFM with CFM is presented. Chapter 4 revisits the fundamentals of quantitative AFM theory before the FCA method is presented in chapter 5. Subsequently, in chapter 6, the established quantitative AFM theory is expanded to allow a description variable tip sampling paths in respect to the data recording path. In chapter 7, the theory behind CFM is presented and formal descriptions of important CFM signals are introduced. Simulations regarding the CFM signal generation, most important parameters for the electrostatic model, and for developing the routine for charge quantification based on distant-dependent CFM data are shown in chapter 8. The experimental application of CFM in the two-step procedure for obtaining the static charge of Au/CeO<sub>2</sub> nano-clusters is presented in chapter 9.



## 2. Tip-sample interaction forces

The idea of any atomic force microscope (AFM) is the measurement of nanoscale interaction forces acting between a sharp tip and a sample surface. Depending on the distance  $z_{ts}$  between tip and sample surface, the tip-sample interaction force  $F_{ts}$  is either repulsive ( $F_{ts} > 0$ ), attractive ( $F_{ts} < 0$ ) or vanishes at an equilibrium point or at sufficiently large distances. In this chapter, the fundamental ideas and mathematical models for describing this force are reported. The chapter is organised as follows: In section 2.1, the composition of the  $F_{ts}$  is generally described naming possible contributions and classifying those into short- and long-range forces. The most important short-range interactions are described in section 2.2. Subsequently the long-range contributions to  $F_{ts}$  are discussed in section 2.3, where special attention is given to the discussion of the electrostatic interaction in a tip-sample capacitor (see section 2.3.2) due to its fundamental importance to the CFM theory. In the concluding section 2.4, models for the separate contributions from the previous sections are merged to describe the overall tip-sample force  $F_{ts}$ .

### 2.1. Composition of the tip-sample force

The tip-sample interaction  $F_{ts}$  is a non-linear function of the distance between tip and sample surface  $z_{ts}$  (see Figure 2.1) and is composed of various forces, which can be roughly distinguished into short- and long-range forces. Short-range forces decline at least with  $\propto z_{ts}^{-6}$  or faster with increasing tip-sample distance  $z_{ts}$  while long-range forces decrease with  $\propto z_{ts}^{-5} \dots z_{ts}^{-1}$ . Consequently short- and long-range forces act differently on a sharp tip in near proximity of a sample surface as exemplified in Figure 2.1. The short-range forces prevalently act between the frontmost tip-apex atoms and the nearest surface atoms. As the short-range tip-sample forces result from the interaction between few or single atoms, these are here classified under the term *atomic forces*  $F_{\text{atomic}}$ . In contrast, the long-range force contributions to  $F_{ts}$  interact not only with the tip apex atoms but also with the complete mesoscopic body of the tip. For that reason, the long-range forces will be referred to as *body forces*  $F_{\text{body}}$  in the following. Considering both contributions, the tip-sample



## 2. Tip-sample interaction forces

interaction force  $F_{ts}$  can formally separated into

$$F_{ts}(z_{ts}) = F_{\text{atomic}}(z_{ts}) + F_{\text{body}}(z_{ts}) \quad (2.1.1)$$

For a further separation one has to consider the different types of nanoscale forces acting between tip and sample. Generally these are van der Waals ( $F_{\text{vdW}}$ ), electrostatic ( $F_{\text{el}}$ ), magnetic ( $F_{\text{mag}}$ ) and chemical forces ( $F_{\text{chem}}$ ) [45]. The magnetic force can be neglected, if a non-magnetic tip-sample system is studied or if magnetic interactions are governed by an external field [76]. As only non-magnetic tip-sample systems are considered in this work, the magnetic forces  $F_{\text{mag}}$  are omitted in the following derivations. The remaining forces are classified according to relation (2.1.1).

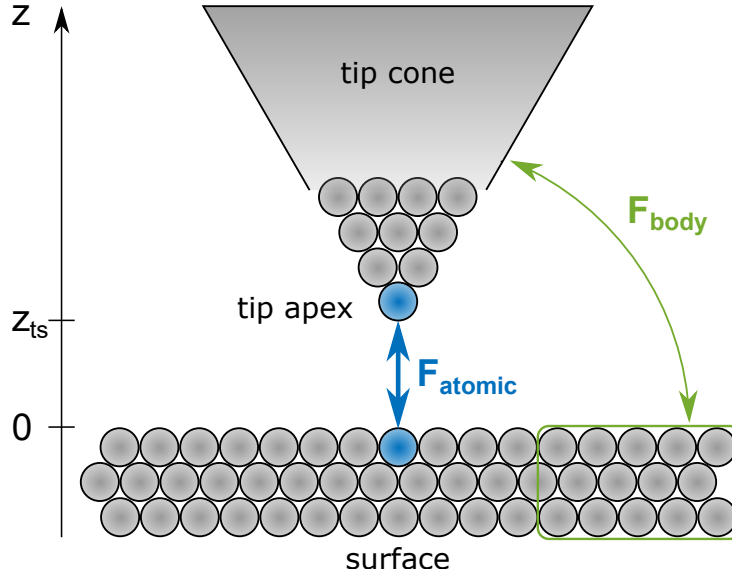


Figure 2.1.: Schematic sketch of the forces acting on a tip in near vicinity of a sample surface. The long-range interactions as van der Waals body forces  $F_{\text{vdW}}^{\text{body}}$  and electrostatic forces  $F_{\text{el}}$  are given between the whole body of the tip, (consisting of the apex, cone and lever) and the sample surface body. Those interactions are represented by  $F_{\text{body}}$  (green). The short-range forces act between the frontmost atoms of the tip apex and the nearest surface atoms. These are indicated by the blue colour and represented by  $F_{\text{atomic}}$ .

The atomic tip-sample force  $F_{\text{atomic}}$  can be expressed as

$$F_{\text{atomic}}(z_{ts}) = F_{\text{chem}}(z_{ts}) + F_{\text{vdW}}^{\text{atomic}}(z_{ts}) \quad (2.1.2)$$

The first contribution are chemical forces  $F_{\text{chem}}$  which have their origin in complex quantum mechanical interactions between atoms giving rise to covalent bonding. They become relevant at tip-sample distances in the range of atomic bonding lengths [41]. The second contribution are short-range interatomic van der Waals forces  $F_{\text{vdW}}^{\text{atomic}}$  acting between the frontmost tip-atoms and nearest surface

atoms. They will become predominant at tip-sample distances above atomic bonding lengths ( $z_{ts} > 1$  nm), where the chemical forces vanish. In the case of ions and dipoles located at the tip and surface also their long-range coulomb interaction has to be considered as additional contribution to  $F_{\text{atomic}}$ . In this overview for the tip-sample forces considering only non-polar atoms, these interactions are omitted.

The long-range body force  $F_{\text{body}}$  is separated into

$$F_{\text{body}}(z_{ts}, V) = F_{\text{vdW}}^{\text{body}}(z_{ts}) + F_{\text{el}}^{\text{body}}(z_{ts}, V) \quad (2.1.3)$$

Where  $F_{\text{vdW}}^{\text{body}}$  represents van-der Waals body interaction between tip body and sample surface, which results from integrating the atomic van-der Waals interactions over the entire tip geometry. While the interatomic van-der Waals forces are short-range, the integrated van-der Waals body interaction  $F_{\text{vdW}}^{\text{body}}$  between entire tip body and sample behaves as  $\propto z_{ts}^{-3} \dots z_{ts}^{-1}$  and thus is a long-range background force contributing to  $F_{\text{body}}$ . The second contribution to the body force  $F_{\text{body}}$  are the long-range electrostatic forces  $F_{\text{el}}^{\text{body}}(z_{ts}, V)$  present between conductive tip and sample at different potentials [62] and for electrostatic charges trapped in the respective tip-sample system [68, 70]. Considering the conductive tip and sample system as a capacitor with a potential difference  $V$ , the electrostatic interaction yields an attractive force  $\propto V^2$  [41]. Accounting relation (2.1.1) considering equations (2.1.2) and (2.1.3), the overall tip-sample interaction force can be written as

$$F_{\text{ts}}(z_{ts}, V) = F_{\text{chem}}(z_{ts}) + F_{\text{vdW}}^{\text{atomic}}(z_{ts}) + F_{\text{vdW}}^{\text{body}}(z_{ts}) + F_{\text{el}}^{\text{body}}(z_{ts}, V) \quad (2.1.4)$$

where all contributions exhibit a specific dependence on the tip-sample distance  $z_{ts}$ . Models for describing the specific distant-dependent behaviour of each contribution will be discussed in the subsequent sections.

## 2.2. Atomic forces

In this section, models for the forces contributing to the atomic interaction  $F_{\text{atomic}}$  between tip and sample are explained in more detail. Model parameters that are used for a fit to experimental data are introduced.

### 2.2.1. The short-range chemical interaction force

The chemical interaction force between tip and sample  $F_{\text{chem}}(z_{\text{ts}})$  arises from the orbital overlap between tip-apex atoms and the nearest surface resulting in the formation of a covalent bond. This interaction becomes prevalent for tip-sample distances in the range of chemical bonds, which is  $z_{\text{ts}} < 1$  nm. The chemical forces yield the atomic and orbital resolution capabilities of NC-AFM [77]. Depending on how the atom orbitals interact, the resulting interaction force can either be attractive or repulsive [41]. The exact interaction of the overlapping atomic electron

| <b>Morse potential</b> |                        |
|------------------------|------------------------|
| $E_b$                  | 4.638 zJ               |
| $\sigma_0$             | 850 pm                 |
| $\kappa$               | $2.50 \text{ nm}^{-1}$ |

Table 2.1.: Morse potential parameters for a Si-Si interaction adapted from [49].

wave functions can be determined by solving the Schrödinger equation. However, for realistic cases, the solution of this partial differential equation becomes rather complex [41]. This is due to the anisotropy of chemical bonding and additional contributions by neighbour and next-neighbour interactions where a correct description of these requires a precise knowledge of the atomic structure of the interacting tip apex, surface site and atomic relaxation [78, 79]. For a qualitative understanding of the chemical interaction between tip and sample, it is sufficient, to use models describing the bonding between only two atoms. One of those is the Morse potential [49, 45, 80, 2]

$$U_{\text{Morse}}(z) = E_b \left[ -2e^{-\kappa(z-\sigma_0)} + e^{-2\kappa(z-\sigma_0)} \right] \quad (2.2.5)$$

Originally this is an approximate description for the potential energy for the nuclei of a diatomic molecule at distance  $z$  [81]. Here,  $E_b$  is the bonding energy (well depth) of the dissociated atoms,  $z$  the distance between the interacting atoms,  $\sigma_0$  the equilibrium bond distance (the position of the potential well minimum at  $-E_b$ ) and  $\kappa$  describes the width of the potential well. By considering the tip-sample

distance  $z_{\text{ts}}$  between the frontmost tip atom and the nearest surface atom as the interaction range  $z$  in the Morse potential (2.2.5), the first derivative provides

$$F_{\text{Morse}}(z_{\text{ts}}) = -\frac{dU_{\text{Morse}}}{dz_{\text{ts}}} = 2\kappa E_b \left[ -e^{-\kappa(z_{\text{ts}} - \sigma_0)} + e^{-2\kappa(z_{\text{ts}} - \sigma_0)} \right] \quad (2.2.6)$$

This force relation qualitatively describes the behaviour of the chemical interaction force  $F_{\text{chem}}(z_{\text{ts}}) \approx F_{\text{Morse}}(z_{\text{ts}})$  between a tip apex atom and a sample atom. The first term of  $F_{\text{Morse}}$  describes the attractive interaction (indicated by the negative sign) and the second term represents the repulsion. The behaviour of  $F_{\text{Morse}}(z_{\text{ts}})$  for two silicon atoms (one at the tip and one at the surface) in interaction as function of their distance  $z_{\text{ts}}$  is exemplified in Figure 2.2. Parameters for calculation of the Si-Si interaction are adapted from [49] and are depicted in Table 2.1. In

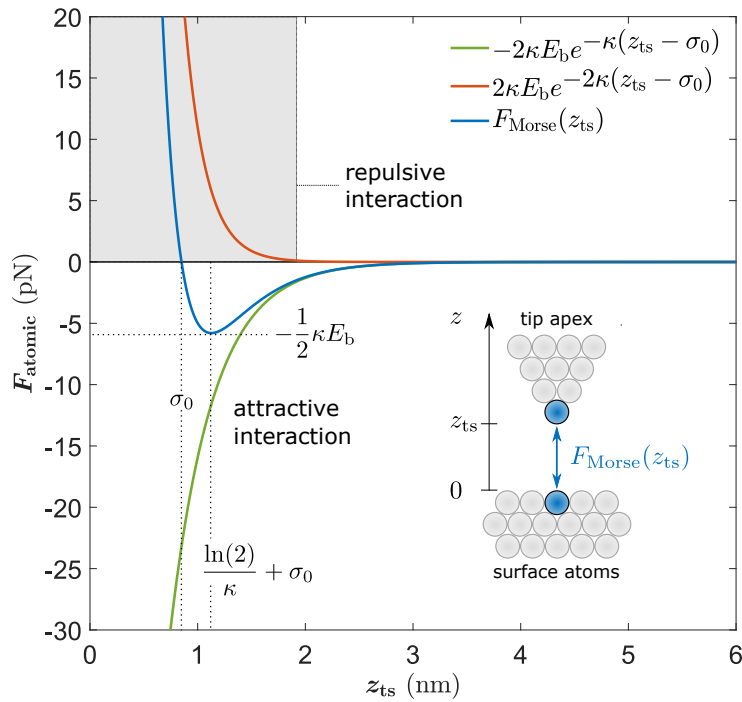


Figure 2.2.: Qualitative model for the chemical interaction force  $F_{\text{chem}}$  as function of the tip-sample distance  $z_{\text{ts}}$ . For modelling, the force  $F_{\text{Morse}}(z_{\text{ts}})$  as function of  $z_{\text{ts}}$  is calculated from the **Morse potential** (2.2.5), which describes the interaction between front-most tip atom and nearest surface atom as depicted in the inset. The Morse force  $F_{\text{Morse}}$  (blue line) is the sum of an attractive contribution (green line) and a repulsive contribution (red line). For the calculations a Si-Si interaction is considered, where the parameters depicted in Table 2.1 are adapted from [49].

Figure 2.2,  $F_{\text{Morse}}(z_{\text{ts}})$  is shown as a blue line while its attractive and repulsive terms are depicted in green and red. For large tip-sample distances, the chemical

## 2. Tip-sample interaction forces

interaction force  $F_{\text{Morse}}$  approaches zero, due to the lack of overlap between the atom orbitals (see the blue line in Figure 2.2). If the tip approaches the sample surface in the range of chemical bonding, the orbitals of the outermost open shells of the tip apex and surface atoms start to overlap. The resulting chemical interaction force is attractive, if that orbital overlap reduces the bonding energy between the interacting atoms. Considering such a case, relation  $F_{\text{Morse}}(z_{\text{ts}})$  reproduces an increasing attraction until the force minimum at  $z_{\text{ts}} = \ln(2)/\kappa + \sigma_0$ , where the strongest attractive force  $-\frac{1}{2}\kappa E_b$  acts between the atoms. Past the minimum, the attractive force decreases again until the equilibrium bonding distance is reached at  $z_{\text{ts}} = \sigma_0$ . Here, the Morse potential (2.2.5) is minimal at  $-E_b$  and, hence, the interaction force between the atoms is zero  $F_{\text{Morse}}(z_{\text{ts}} = \sigma_0) = 0$ . In the case that the tip approaches the surface even further, the resulting interaction force becomes increasingly repulsive (grey box in Figure 2.2). This is due to the strong deformation of all orbitals by the electrostatic repulsion between the electrons and atomic nuclei brought in too close vicinity. An additional and simultaneous effect is, that the overlap of inner closed-shell orbitals is hampered by the Pauli Principle: two electrons can only be in the same volume if they have a different velocity (represented by their quantum state). For the overlap of the closed-shell orbitals the kinetic energy of the internal motion of the excess electrons has to be augmented (brought to a higher state). This energy has to be supplied with the approach of both atoms, which also results in a repulsion [82]. Relation (2.2.6) reproduces that behaviour  $F_{\text{Morse}}(z_{\text{ts}} < \sigma_0) > 0$ , where the tip-sample distance becomes much smaller than the equilibrium bond distance  $z_{\text{ts}} < \sigma_0$ .

### 2.2.2. The interatomic van der Waals force

Van der Waals force is responsible for many macroscopic phenomena like surface tension, wetting behaviour, adhesion and binding in biosystems [2]. While its effect can be observed on the macroscopic scale, the van der Waals force originates from interatomic and intermolecular interactions. Due to their long-range properties, these will strongly contribute to the atomic tip-sample interaction  $F_{\text{atomic}}$ , especially at distances where the short-range chemical forces start to vanish. Three distinct contributions are combined under the term of the van der Waals forces [2]. The induction force (Debye force), the orientation force (Keesom force) and the dispersion force (London force) [82]. Consider two dissimilar atoms 1 and 2 with non-zero permanent dipole moments  $\mu_1$  and  $\mu_2$ , the polarizabilities  $\alpha_{01}$  and  $\alpha_{02}$  and each having only one single absorption frequency  $\nu_1$  and  $\nu_2$ . Both these atoms are assumed to be located in vacuum and at a given temperature  $T \neq 0$  interacting over the distance  $r$  with each other. The van der Waals interaction potential between atoms 1 and 2 can be written as [2]

$$\begin{aligned}
 U_{\text{vdW}}(r) &= -\frac{C_{\text{vdW}}^{1,2}}{r^6} = -\frac{[C_{\text{ind}}^{1,2} + C_{\text{orient}}^{1,2} + C_{\text{disp}}^{1,2}]}{r^6} \\
 &= -\frac{1}{(4\pi\epsilon_0)^2 r^6} \left[ \underbrace{(\mu_1^2 \alpha_{02} + \mu_2^2 \alpha_{01})}_{\text{Debye}} + \underbrace{\frac{\mu_1^2 \mu_2^2}{3k_B T}}_{\text{Keesom}} + \underbrace{\frac{3\alpha_{01} \alpha_{02} h\nu_1 \nu_2}{2(\nu_1 + \nu_2)}}_{\text{London}} \right] \quad (2.2.7)
 \end{aligned}$$

where  $k_B$  is the Boltzmann constant and the notation with 1,2 indicates the specific dependency on the respective material combination between atoms 1 and 2. The first term  $C_{\text{ind}}^{1,2}/r^6$  describes the energy contribution by the induction effect (Debye effect), where the permanent dipole moment  $\mu_1$  of atom 1 induces an additional dipole moment in atom 2 and vice versa. The second term  $C_{\text{orient}}^{1,2}/r^6$  describes the average energy contribution due to the relative orientation between  $\mu_1$  and  $\mu_2$  calculated for all possible orientations according to Boltzmann statistics (Keesom or orientation effect). The third term  $C_{\text{disp}}^{1,2}/r^6$  is the energy contribution due to the dispersion force as described by London [82]. Their origin are quantum mechanical charge fluctuations given in any atom causing instantaneous dipole moments. These fluctuating dipoles generate an electric field interacting with the polarisability of other atoms inducing in-phase dipole moments there, which in return interact with those instantaneous dipole moments [82, 2]. While the first two interactions  $C_{\text{ind}}^{1,2}$  and  $C_{\text{orient}}^{1,2}$  are only present if the interacting atoms 1 and 2 exhibit permanent dipole moments, the dispersion force is omnipresent, since its contribution is independent of permanent dipole moments. This means, that the dispersion forces act between all atoms and molecules, even non-polar and neutral ones, and generally exceed the dipole-dependent induction and orientation force, except for small, highly polar molecules [2]. If tip and sample consist only of non-polar atoms interacting with

## 2. Tip-sample interaction forces

each other via vacuum, the van der Waals interaction potential (2.2.7) can be reduced to the dispersion term

$$U_{\text{vdW}}(r) = -\frac{C_{\text{disp}}^{1,2}}{r^6} = -\frac{3}{2} \frac{\alpha_{01}\alpha_{02}}{(4\pi\epsilon_0)^2 r^6} \frac{h\nu_1\nu_2}{(\nu_1 + \nu_2)} \quad (2.2.8)$$

The equation for the dispersion interaction energy introduced by London [82] provides fairly accurate results for interatomic vacuum interaction, although these are usually lower than values determined with more elaborate models as those take additional absorption frequencies and quadrupole interactions into account as well [83, 2]. In vacuum the dispersion interaction is exclusively attractive, however, for the same reasons already discussed in the previous section, two atoms cannot get unlimited close to each other. The Lennard-Jones potential [84] takes this circumstance into consideration by adding an empirical short-range repulsive term to the dispersion interaction term. It is a frequently used qualitative model (alternatively to the Morse potential) for describing the atomic tip-sample interaction  $F_{\text{atomic}}$  as function of the distance  $r = z_{\text{ts}}$  [80, 41, 2]. The Lennard-Jones potential between one tip apex atom and one surface atom is given by

$$U_{\text{LJ}}(z_{\text{ts}}) = 4E_{\text{b}} \left[ \left( \frac{r_0}{z_{\text{ts}}} \right)^{12} - \left( \frac{r_0}{z_{\text{ts}}} \right)^6 \right] \quad (2.2.9)$$

Here  $r_0$  is the atom-atom distance, where the Lennard-Jones potential becomes zero ( $U_{\text{LJ}}(z_{\text{ts}} = r_0) = 0$ ) and  $E_{\text{b}}$  is the bonding energy between the two atoms. The minimum of the Lennard-Jones potential is given at the atom-atom distance  $z_{\text{ts}} = \sigma_0 = 2^{1/6}r_0$ , where  $\sigma_0$  is the equilibrium bonding distance which is comparable to the one of the Morse potential (2.2.5). The attractive contribution  $\propto z_{\text{ts}}^{-6}$  to the interaction potential is based on the London dispersion term (2.2.8) while the other contribution  $\propto z_{\text{ts}}^{-12}$  is an empirically chosen description of the repulsive interaction between two atoms in close proximity. The atomic interaction force between tip and sample according to the Lennard-Jones potential is given by the negative derivative in respect to  $z_{\text{ts}}$ , which reads as

$$F_{\text{LJ}} = -\frac{\partial U_{\text{LJ}}}{\partial z_{\text{ts}}} = 24 \frac{E_{\text{b}}}{r_0} \left[ 2 \left( \frac{r_0}{z_{\text{ts}}} \right)^{13} - \left( \frac{r_0}{z_{\text{ts}}} \right)^7 \right] \quad (2.2.10)$$

For better comparability to the Morse force  $F_{\text{Morse}}$ , the parameter  $r_0$  from the Lennard-Jones Potential can be expressed by the equilibrium distance  $\sigma_0$  via relation  $r_0 = 2^{-1/6}\sigma_0$ , which yields

$$F_{\text{LJ}} = 12 \frac{E_{\text{b}}}{\sigma_0} \left[ \left( \frac{\sigma_0}{z_{\text{ts}}} \right)^{13} - \left( \frac{\sigma_0}{z_{\text{ts}}} \right)^7 \right] \quad (2.2.11)$$

In Figure 2.3, the behaviour of the Lennard-Jones force  $F_{\text{LJ}}$  as function of the tip-sample distance  $z_{\text{ts}}$  is depicted in comparison with the force  $F_{\text{Morse}}$  resulting from the Morse potential (2.2.6). Both are calculated assuming the same equilibrium

| <b>Lennard-Jones potential</b> |           |
|--------------------------------|-----------|
| $E_b$                          | 4.638 zJ  |
| $\sigma_0$                     | 850 pm    |
| $r_0 = \sigma_0/2^{1/6}$       | 757.26 pm |

Table 2.2.: Lennard-Jones potential parameters for a Si-Si interaction adapted from [49].

bonding distance  $\sigma_0$  (zero point of force) and bonding energy  $E_b$  for a Si-Si interaction [49]. The parameters for calculating  $F_{\text{Morse}}$  and  $F_{\text{LJ}}$  are depicted in Tables 2.1 and 2.2 respectively. For the interatomic Si-Si interaction, the Lennard-Jones force  $F_{\text{LJ}}$  shows a much sharper and deeper minimum at  $z_{\text{ts}} = (13/7)^{1/6}\sigma_0$  than the Morse interaction force  $F_{\text{Morse}}$  at  $\ln(2)/\kappa + \sigma_0$ . This difference can be lead back to the additional parameter  $\kappa$  describing the width of the potential well in  $F_{\text{Morse}}$ , which is missing in  $F_{\text{LJ}}$ . For different atomic interactions with higher values for  $\kappa$  the Morse force  $F_{\text{Morse}}$  can exhibit a much sharper minimum. Furthermore, the attractive contribution of  $F_{\text{LJ}}$  declines much faster than  $F_{\text{Morse}}$  until the force becomes zero at the equilibrium bonding distance at  $z_{\text{ts}} = \sigma_0$ . Past this point,  $F_{\text{Morse}}$  converges to a finite value at  $z_{\text{ts}} = 0$  while  $F_{\text{LJ}}$  diverges to infinity. Consequently, the description of the repulsive interaction is much steeper from  $F_{\text{LJ}}$  in comparison with  $F_{\text{Morse}}$ . Due to its finite value at  $z_{\text{ts}} = 0$ , the Morse force  $F_{\text{Morse}}$  would allow two atoms to get infinitely close to each other, if an external force is sufficiently high enough. As this is not allowed, the Lennard-Jones force  $F_{\text{LJ}}$  is much better suited for describing high repulsions than  $F_{\text{Morse}}$ , which is only a correct description of the interatomic repulsion near its minimum. Both  $F_{\text{Morse}}$  and  $F_{\text{LJ}}$  are commonly used models for the force acting between two interacting atoms [2] and are frequently applied when qualitatively describing the atomic tip-sample interaction  $F_{\text{atomic}}$  [80]. Which potential of both has to be chosen, depends on the exact application. While the Morse potential is better suited for qualitatively describing the chemical interaction due to covalent bonds, the Lennard-Jones potential is more applicable for non-covalent, physical bonds between atoms as those are based on the van der Waals interaction [2].



## 2. Tip-sample interaction forces

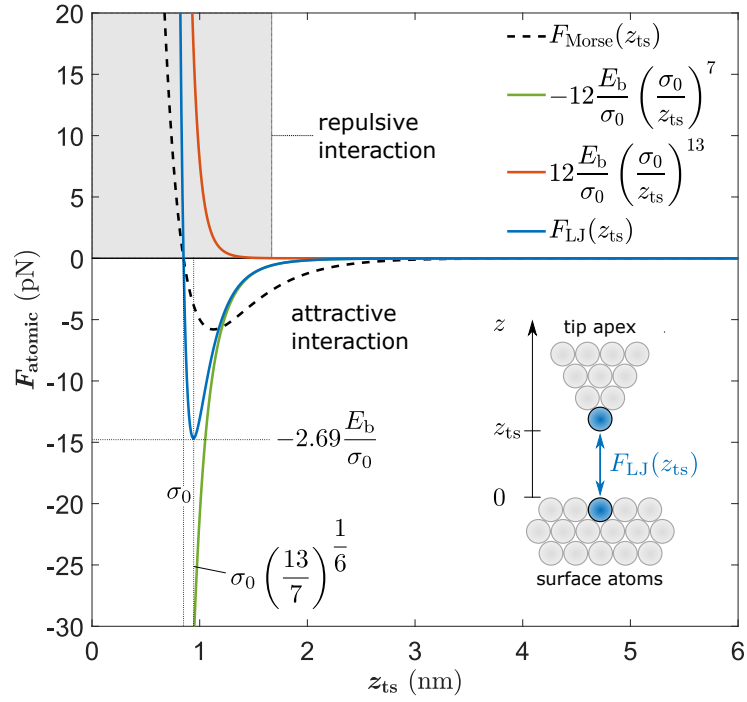


Figure 2.3.: Interaction force  $F_{\text{LJ}}$  between two silicon atoms as function of the tip-sample distance  $z_{\text{ts}}$  derived from the **Lennard-Jones potential** as qualitative model for the atomic tip-sample interaction  $F_{\text{atomic}}$ . The complete force  $F_{\text{LJ}}$  is depicted in blue, while its composing attractive and repulsive contributions are shown in green and red respectively. For comparison the Morse force  $F_{\text{Morse}}$  from the previous Figure 2.2 is indicated by a dashed black line. Parameters for calculation of the Si-Si interaction are shown in Table 2.2.

## 2.3. Body forces

In this section the long-range physical forces acting between the whole body of the tip and the surface are discussed. For several tip geometries, a mathematical model will be introduced.

### 2.3.1. The non-retarded van der Waals force acting between tip and sample body

While the interatomic van der Waals force quickly vanishes with increasing distance, van der Waals interaction between macroscopic bodies is present even at long-range distance regimes. Thereby the van der Waals body-body interaction is prone to retardation effects, which are due to the finite propagation time of the electromagnetic interactions between the fluctuating dipoles in each atom the interacting bodies consist of. If the time required for the signal to travel the distance  $r$  between two atoms becomes comparable or greater than the characteristic evolution time of the interacting atoms, the interaction cannot be considered as instantaneous any more [85]. In this case, retardation effects occur in the van der Waals interaction, which can be described by perturbation theory [86]. One main result of these calculations is, that the retardation-corrected van der Waals interaction varies with  $1/r^7$  at distances above 20 nm [85] instead of  $1/r^6$  as known from the London dispersion force (2.2.8).<sup>1</sup> The Hamaker approach [89] for modelling the van der Waals interaction between macroscopic bodies exclusively considers non-retarded van der Waals interactions. Utilising this approach for modelling  $F_{\text{vdW}}^{\text{body}}$  is justified when exclusively discussing small tip-sample distance regimes  $z_{\text{ts}} < 10$  nm [77]. To

| <b>van-der-Waals body-body interaction</b> |            |
|--|------------|
| $H$  | 357.619 zJ |
| $\Theta$                                   | 29.7°      |
| $R$  | 5 nm       |
| $z_{\text{nt}}$                            | 583.04 pm  |

Table 2.3.: Parameters for calculation of  $F_{\text{vdW}}^{\text{body}}$  based on relation (2.3.13) found by fitting experimental data [53].

calculate the total non-retarded van der Waals interaction between non-polar tip and sample body  $F_{\text{vdW}}^{\text{body}}$ , the London dispersion (2.2.8) between each atom in the

<sup>1</sup>Further reading regarding retardation effects can be found in [87, 88, 2]

## 2. Tip-sample interaction forces

tip body and each atom of the sample has to be taken into consideration. This is possible by following the assumptions made in the Hamaker approach [89]. The first assumption is, that non-retarded van der Waals interactions are additive in such a way that the total interaction can be found by a pairwise summation of the individual interatomic van der Waals interactions between the atoms. By further considering a continuous medium, that summation can be replaced by integration over the volumes  $V$  of the interacting bodies, where each atom occupies the finite volume  $dV$  with a number density  $\rho$ . The last assumption is that the material is homogeneous and isotropic, so that the number density  $\rho$  and the interaction coefficient do not change over the body volumes. Combining these assumptions with relation (2.2.8), the non-retarded total van der Waals interaction force between two arbitrarily shaped bodies can be described via the Hamaker integral [89]

$$F_{\text{vdW}}^{\text{body}} = -\rho_1\rho_2 \int_{V_1} \int_{V_2} \nabla U_{\text{vdW}} dV_1 dV_2 \quad (2.3.12)$$

Here  $\rho_1$  is the density of the tip with the volume  $V_1$  and  $\rho_2$  the density of the sample surface with the volume  $V_2$ . It is immediately apparent, that the non-retarded total van der Waals force (2.3.12) acting between the tip and sample bodies is strongly dependent of the respective body shapes. No matter what exact tip-sample geometries are considered, the execution of this double volume integral is challenging. This challenge has been addressed in literature for several different tip-sample geometries [90, 45, 91]. An extensive comparison and classification of those model calculations can be found in [77]. Argento and French [90] derive a relation for the non-retarded total tip-sample van der Waals interaction force between a radial symmetric parametrised tip model and a flat sample surface. The tip model consist of cone with a half-opening angle  $\Theta$  which is terminated by a half-sphere with the radius  $R$  (see inset of Figure 2.4). The tip model is rotational symmetric along the  $z$ -axis, and hence parametrised along the cone height parallel to  $z$  using the cone radius  $r(z)$ . Furthermore, the maximum cone radius  $r_{\text{max}}$  at the upper end of the tip cone is assumed to be exceedingly bigger than the remaining tip dimensions. The resulting relation describing the van der Waals body-body interaction for the here considered tip-sample system is given by [90]

$$F_{\text{vdW}}^{\text{body}}(\hat{z}) = - \frac{HR^2(\sin \Theta - 1)((R - \hat{z}) \sin \Theta - R - \hat{z})}{6\hat{z}^2(R + \hat{z} - R \sin \Theta)^2} \quad (2.3.13)$$

$$- \frac{H \tan \Theta((\hat{z} + R) \sin \Theta + R \cos(2\Theta))}{6 \cos(\Theta)(\hat{z} + R - R \sin \Theta)^2}$$

where

$$H = H_{1,2} = \pi^2 C_{\text{disp}}^{1,2} \rho_1 \rho_2 \quad (2.3.14)$$

is the Hamaker constant, which magnitude reflects the strength of the van der Waals interactions between the tip and sample bodies with the number densities  $\rho_1$

and  $\rho_2$  in vacuum [89]. Note that  $H = H_{1,2}$  is (as  $C_{\text{disp}}^{1,2}$ ) specific for the respective combination of materials in tip and sample. Further is

$$\hat{z} = z_{\text{ts}} + \Delta z_{\text{nt}} \quad (2.3.15)$$

the distance between tip and sample, where  $\Delta z_{\text{nt}}$  describes the height of a possible nano-tip attached to the mesoscopic tip. The distant-dependent behaviour of the long-range van der Waals body-body interaction  $F_{\text{vdW}}^{\text{body}}$  described by relation (2.3.13) is depicted in Figure 2.4. The parameters utilised for calculation are shown in Table 2.3, resulting from fits to own measurement data [53]. In comparison to

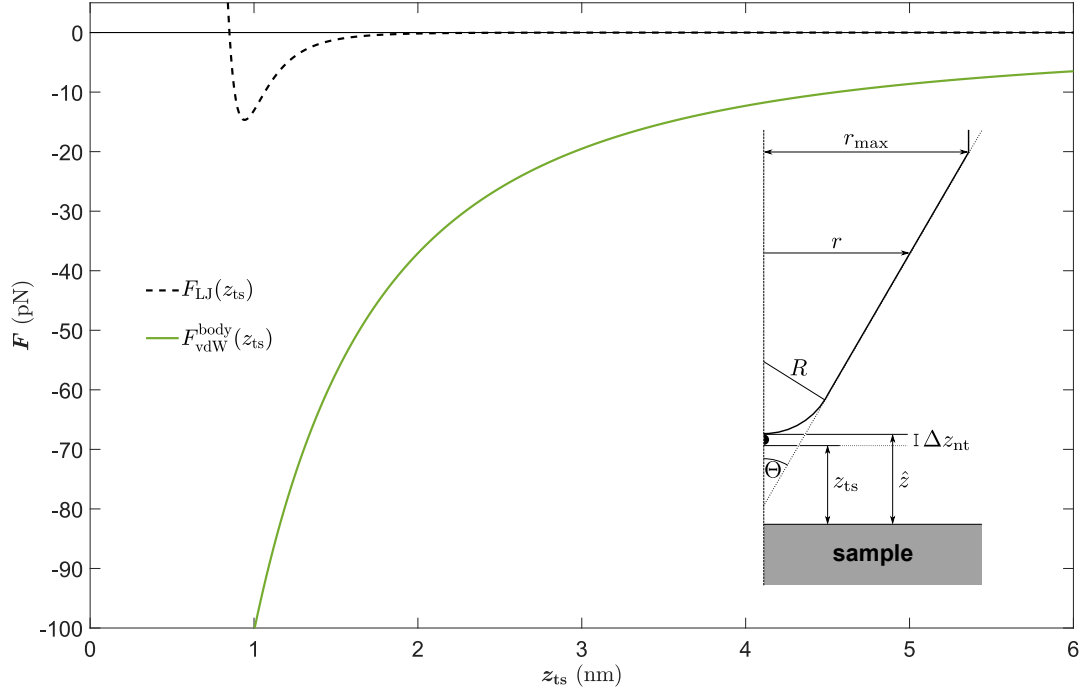


Figure 2.4.: Non-retarded van der Waals body-body interaction force  $F_{\text{vdW}}^{\text{body}}$  between a radial symmetric parametrised tip and a flat sample surface as function of the tip-sample distance  $z_{\text{ts}}$  (green line). For comparison the Lennard-Jones force  $F_{\text{LJ}}$  from the previous Figure 2.3 is shown as a black dashed line. The inset shows the rotational symmetric parametrised tip model considered by Argento and French [90] during the derivation of relation (2.3.13) for describing  $F_{\text{vdW}}^{\text{body}}$ . The tip consists of a sphere with the radius  $R$  which terminates a cone with half-opening angle  $\Theta$ . That model is rotational symmetric along the  $z$ -axis, and hence parametrised using the cone radius  $r(z)$ . The maximum radius of the cone  $r_{\text{max}}$  is assumed to be exceedingly bigger than the remaining tip dimensions. Parameters for calculation of  $F_{\text{vdW}}^{\text{body}}$  are depicted in Table 2.3.

the interatomic van der Waals interactions described by the Lennard-Jones force

## 2. Tip-sample interaction forces

(2.2.10), the non-retarded van der Waals force between the entire tip and sample body (2.3.13) shows exclusively attractive behaviour and decreases to zero much slower with increasing tip-sample distance  $z_{ts}$ . This is due to the  $\propto z_{ts}^{-2}$  dependency of the attractive van der Waals body-body interaction instead of the  $\propto z_{ts}^{-6}$  behaviour of the interatomic van der Waals force presented in section 2.2.2. According to the parametrised tip model, the body-body van der Waals interaction between tip and sample  $F_{\text{vdW}}^{\text{body}}$  acts as a strong, long range attractive background force which is present in every tip-sample system due to the omnipresence of the dispersion force (2.2.8). Within small tip-sample distance regimes  $z_{ts} < 10$  nm, where retardation effects are negligible [85, 88], equation (2.3.13) is a good approximation for the distant-dependent van der Waals tip-sample body-body interaction  $F_{\text{vdW}}^{\text{body}}(z_{ts})$ .

### 2.3.2. Electrostatic force

Conductive tip and metallic sample support electrically connected via an external voltage source  $V_{\text{ext}}$ , together with the sample substrate located in the gap in-between form a tip-sample capacitor. The long-range electrostatic force  $F_{\text{el}}^{\text{body}}$  acting on the tip is determined by the electrostatic characteristics given in the tip-sample capacitor, namely, the capacitance, possible charges located in, on or above the probed substrate and the potential resulting from the capacitor plates and charges. Furthermore,  $F_{\text{el}}^{\text{body}}$  is a function of the tip-sample distance  $z_{ts}$  and the potential difference  $V$  between tip and sample support. In return, the potential difference is determined by a possible contact potential difference between tip and sample support and the externally applied voltage  $V_{\text{ext}}$ . The general principle of CFM is, to adjust the external voltage  $V_{\text{ext}}$  (and thus the potential difference  $V$ ) in such way, that the electrostatic force  $F_{\text{el}}^{\text{body}}(z_{ts}, V)$  acting on the tip is minimized. The adjusted external voltage  $V_{\text{ext}} = V_{\text{bias}}^{\text{min}}$  where  $F_{\text{el}}^{\text{body}}(z_{ts}, V)$  becomes minimal is the CFM signal which contains information on the contact potential difference and charges in the tip-sample capacitor. Based on a quantitative description of the electrostatic force  $F_{\text{el}}^{\text{body}}(z_{ts}, V)$  the information on the charges and contact potential difference can be extracted from  $V_{\text{bias}}^{\text{min}}$ . Hence, the precise description of the electrostatic force  $F_{\text{el}}^{\text{body}}(z_{ts}, V)$  is fundamental to the quantitative CFM evaluation.

A relation for the electrostatic force acting on a finite metallic conductor in a general system of several electrically connected conductors at maintained potentials and fixed point charges in-between their gaps has been derived in the work of Kantorovich *et al.* [67]. By adapting the work of Kantorovich *et al.*, the electrostatic force  $F_{\text{el}}^{\text{body}}$  acting in a tip-sample capacitor with dielectric substrate and charges located in-between its gap has been described [70]. Based on that description of the electrostatic tip-sample  $F_{\text{el}}^{\text{body}}$ , the quantitative CFM theory is developed [68, 69,

70]. For a precise understanding of correct CFM data evaluation, all required derivation steps and assumptions for obtaining the crucial quantitative description of  $F_{\text{el}}^{\text{body}}$  will be presented here extensively, starting with the general considerations of Kantorovich *et al.*

### 2.3.2.1. Model and derivation

Kantorovich *et al.* [67] considers the accumulated potential energy within the electric field of a system, which contains a set of  $m$  finite metallic conductors of arbitrary shape at fixed potentials  $\{\Phi_m\}$  and a distribution of any number  $N$  of point charges  $\{q_i\}$  fixed at positions  $\{\mathbf{r}_i\}$  outside of the conductors. In the case of a spatial movement of any conductor  $m$  in that system, it is assumed that ideal, external batteries maintain the potentials  $\{\Phi_m\}$  of the conductors by redistributing the charges  $\{Q_m\}$  located at their finite surfaces. By incorporating the work carried out by the batteries upon spatial movement of any conductor  $m$  into the resulting change of the systems potential energy, a effective energy relation is derived. The negative spatial derivative of that effective energy is equal to the electrostatic force acting on that conductor  $m$ .

For describing the electrostatic tip-sample force  $F_{\text{el}}^{\text{body}}$  for a system as exemplified in Figure 2.5 the number of conductors considered by Kantorovich *et al.* can be reduced to two [68, 69, 70]. In that case, one arbitrarily shaped conductor represents the tip at a fixed potential  $\Phi_1$  and the other conductor represents the metallic sample support at potential  $\Phi_2$ . The depiction of both conductors in Figure 2.5 is a exemplification for any possible tip-sample geometry, because the theory covers arbitrarily shaped finite conductors without making any assumptions regarding to their dimensions. As both conductors are connected electrically via the external battery  $V_{\text{ext}}$ , their respective fixed electrostatic potentials  $\Phi_1$  and  $\Phi_2$  include the contact potential difference  $V_{\text{CPD}}$  which can build up between both conductors. Consequently the actual potential difference between tip and back-electrode is given by [70]

$$V = \Phi_1 - \Phi_2 = V_{\text{ext}} - V_{\text{CPD}} \quad (2.3.16)$$

Note at this point, that the introduction of a global contact potential difference  $V_{\text{CPD}}$  is equivalent with the assumption that both conductor surfaces (tip and sample support), are homogeneous in respect to their respective work function. Further, for describing a possible dielectric substrate different local permittivity values  $\epsilon_s(\mathbf{r})$  in the space between both conductors are incorporated in addition to the original theoretical work [70]. The point charges  $q_i$  depicted in Figure 2.5 are exemplary and could be placed anywhere in-between the two conductors, where their respective positions  $\mathbf{r}_i$  are relative to the zero position on the dielectric substrate below the tip. The distance in  $z$ -direction between the lowest point of the tip and the

## 2. Tip-sample interaction forces

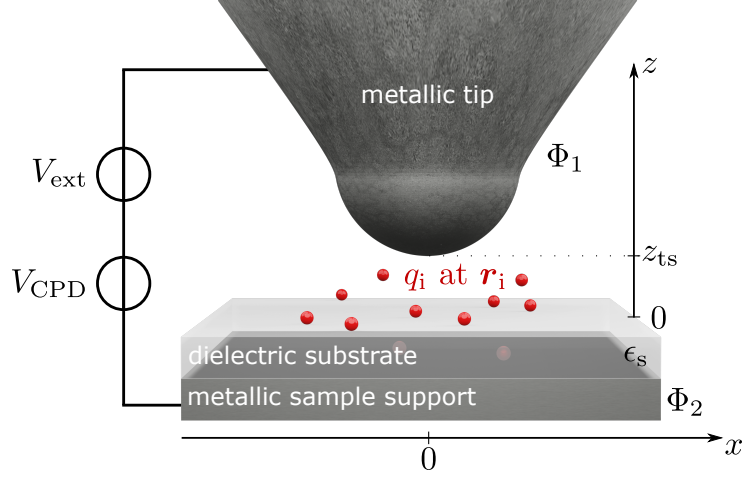


Figure 2.5.: Setup of a tip-sample system consisting of a metallic tip and a metallic sample support between which the external voltage  $V_{\text{ext}}$  is applied to maintain the respective surface potentials  $\Phi_1$  and  $\Phi_2$ . The dielectric medium can be considered by different local dielectric permittivity  $\epsilon_s$  in specific parts of the space between both metals. The placement of the included point charges  $q_i$  at positions  $\mathbf{r}_i$  is exemplary.

dielectric substrate is the tip-sample distance  $z_{\text{ts}}$ . Assuming a linear and isotropic dielectric medium and taking the integral over the volume outside both conductors (as inside the field vanishes) and application of the Poisson equation for the field provides a relation for the total potential energy within the electric field as [67, 70, 92] (full derivation in Appendix A.1)

$$U_{\text{el,f}} = \frac{1}{2} \sum_i q_i \Phi(\mathbf{r}_i) + \frac{1}{2} (\Phi_1 Q_1 + \Phi_2 Q_2) \quad (2.3.17)$$

where the first sum is taken over all point charges and the second sum includes both conductors. The electrostatic potential  $\Phi(\mathbf{r})$  in the system is determined by the external voltage  $V_{\text{ext}}$ , the dielectric medium  $\epsilon_s$ , the point charges  $q_i$  and the conductors. Thereby,  $Q_1$  and  $Q_2$  are the charges generated at the surfaces of the conductors to maintain their potentials  $\Phi_1$  and  $\Phi_2$  imposed by the external voltage  $V_{\text{ext}}$ . The charge  $Q_m$  located on the respective conductor surface  $m = 1, 2$  is given by [67, 70] (see also Appendix A.1)

$$Q_m = -\epsilon_0 \epsilon_s \oint_{S_m} \nabla \Phi(\mathbf{r}) \cdot \mathbf{n} \, ds = -\epsilon_0 \epsilon_s \oint_{S_m} \frac{\partial \Phi(\mathbf{r})}{\partial n} \, ds. \quad (2.3.18)$$

where  $\partial/\partial n$  indicates the derivation in direction of the outward normal vector  $\mathbf{n}$  of the respective conductor surface  $S_m$  [93, 92, 94]. The integration over the field gradient in direction of  $\mathbf{n}$  is taken over the whole conductor surface  $S_m$  where  $\epsilon_s$  is the relative permittivity of the surrounding medium. It has been shown, that the integral over a remote metal surface at infinity (which surrounds the complete

considered system) vanishes, since the potential converges to zero at large distance [92]. Hence, in the scope of this calculation it is not possible to consider infinitely large objects. [67]. Note, that relation (2.3.18) also means, that both conductors in the system are considered in a macroscopic manner.

In order to derive the electrostatic force  $F_{\text{el}}$  acting on the tip in the system described by relation (2.3.17), a movement  $\delta z_{\text{ts}}$  of that tip is introduced [92, 67, 70]. It is assumed here, that the presence and movement of the tip does neither modify the positions of the point charges  $q_i$ , nor the position of the dielectric medium, what implies that possible relaxation effects are neglected in this calculation. Due to the tip movement, the potential  $\Phi(\mathbf{r})$  in the system (2.3.17) changes by  $\delta\Phi(\mathbf{r})$ . Accordingly the potential of each conductor  $m$  deviates from its initial value  $\Phi_m$ , which has to be compensated by a charge flow  $\delta Q_m$  via the external battery. In consequence, the complete work done in the system consists of the change of the potential energy within the field (2.3.17) and the work carried out by the battery for the surface charge redistribution between both conductors ( $\delta Q_1 + \delta Q_2 = 0$ ) in order to maintain their respective potentials  $\Phi_1$  and  $\Phi_2$ . By understanding the battery as a part of the system, the work carried out by it has to reduce the total potential energy of the system and hence is taken with a minus sign in that relation. This leads to an expression for the effective energy of the system [67] (for mathematical depiction see appendix A.2)

$$U_{\text{el}}^{\text{eff}} = \frac{1}{2} \sum_i q_i \Phi(\mathbf{r}_i) - \frac{1}{2} (\Phi_1 Q_1 + \Phi_2 Q_2) \quad (2.3.19)$$

which is the potential energy within the field reduced by the work contribution of the battery as part of the system. In comparison to the potential energy of the field alone (2.3.17), the main difference is the minus sign. Kantorovich *et al.* [67] point to the importance of that difference by showing that relation (2.3.17) does not provide the correct potential energy for a probe point charge far away from the conductors, whereas the relation (2.3.19) for the effective energy does. For deriving a valid relation for the electrostatic force imposed on the tip upon movement in the system, it is crucial to consider the change of the total potential energy including the work carried out by the battery for the charge flow for compensation. The electrostatic force imposed on the tip upon movement is directly related to the change of that effective energy  $U_{\text{el}}^{\text{eff}}$  as a function of the tip position

$$F_{\text{el}} = - \frac{\partial U_{\text{el}}^{\text{eff}}}{\partial z_{\text{ts}}} \quad (2.3.20)$$

where the minus sign follows the general principle that conservative forces act towards reduction of potential energy. The calculation of the electrostatic force by relation (2.3.20) from the systems effective energy (2.3.19) requires the knowledge of the unknown potential distribution  $\Phi(\mathbf{r})$  and the surface charges  $Q_m$ . However, these are implicitly dependent on the charges ( $q_i, \mathbf{r}_i$ ) and the fixed potentials  $\Phi_1$



## 2. Tip-sample interaction forces

and  $\Phi_2$  of the conductors. Addressing this difficulty Kantorovich *et al.* [67] utilizes a Green's function approach to formally separate the potential  $\Phi(\mathbf{r})$  in the system into three terms

$$\Phi(\mathbf{r}) = \Phi_{\text{void}}(\mathbf{r}) + \sum_{i, \mathbf{r} \neq \mathbf{r}_i} \frac{1}{4\pi\epsilon_0} \frac{q_i}{|\mathbf{r} - \mathbf{r}_i|} + \Phi_{\text{img}}(\mathbf{r}) \quad (2.3.21)$$

where the first term is the potential of the charge free ( $N = 0$ , void) system  $\Phi_{\text{void}}$ , created by the conductors and their respective geometries and potentials  $\Phi_m$ . Consequently  $\Phi_{\text{void}}(\mathbf{r})$  is, in contrast to  $\Phi(\mathbf{r})$ , independent of the point charges  $q_i$ . The second term is the summarized potential of the point charges, where the self-action at  $\mathbf{r} = \mathbf{r}_i$  of any point charge  $q_i$  is excluded. The last term is the image potential  $\Phi_{\text{img}}(\mathbf{r})$  due to image charges in the conductors induced by the point charges  $q_i$ . In the scope of the Green's function approach, the induction of additional charges  $Q_m^{\text{ind}}$  on each conductor surface due to the point charges is considered. Consequently the overall surface charge on each respective conductor is given by  $Q_m = Q_m^{\text{ext}} + Q_m^{\text{ind}}$ , where  $Q_m^{\text{ext}}$  are the external charges pumped by the battery and  $Q_m^{\text{ind}}$  the induced charges (which resemble the image charges to  $q_i$ ). Based on that consideration the identity [67, 70]

$$\frac{1}{2} \sum_i q_i \Phi_{\text{void}}(\mathbf{r}_i) = \frac{1}{2} \sum_m Q_m^{\text{ext}} \Phi_m - \frac{1}{2} \sum_m Q_m \Phi_m \quad (2.3.22)$$

can be derived. Therefore, the self-energy change of the conductor due to the induced charges is equal to minus half the energy of the point charges in the field of the bare conductors [67]. Inserting the formal separation (2.3.21) and the identity (2.3.22) resulting from the Green's function approach into relation (2.3.19), one obtains the final separation of the systems effective energy into four energy contributions [67, 70]

$$\begin{aligned} U_{\text{el}}^{\text{eff}} &= -\frac{1}{2} \left( \Phi_1 Q_1^{\text{ext}} + \Phi_2 Q_2^{\text{ext}} \right) + \sum_i q_i \Phi_{\text{void}}(\mathbf{r}_i) \\ &\quad + \frac{1}{8\pi\epsilon_0} \sum_i \sum_{j, j \neq i} \frac{q_i q_j}{|\mathbf{r}_i - \mathbf{r}_j|} + \frac{1}{2} \sum_i q_i \Phi_{\text{img}}(\mathbf{r}_i) \\ &= U_C + U_{q-C} + U_{q-q} + U_{\text{img}} \end{aligned} \quad (2.3.23)$$

The first term  $U_C$  describes energy contribution by the capacitance of the charge free ( $N = 0$ ) system. This becomes more obvious, after short transformations of that term. Starting with the requirement  $Q_1^{\text{ext}} = -Q_2^{\text{ext}} = Q_{\text{ext}}$  of the external battery, which allows to express the remaining potential difference between  $\Phi_1$  and  $\Phi_2$  via  $V$  (2.3.16). Further, introducing the capacitance of the charge free system as  $C_{\text{void}} = Q_{\text{ext}}/V$  yields the well-known negative energy contribution of the capacitor [64, 69, 70]

$$U_C = -\frac{1}{2} C_{\text{void}} V^2 \quad (2.3.24)$$

The second term  $U_{q-C}$  describes the interaction between point charges  $q_i$  and the conductors excluding any image charge interaction. For a tip-sample system delimited by two conductors, the potential  $\Phi_{\text{void}}(\mathbf{r}_i)$  at the charge position  $\mathbf{r}_i$  directly scales with the potential difference  $V$  between both of these conductors. In that case, a normalized electric potential  $\hat{\Phi}_{\text{void}} = \Phi_{\text{void}}/V$  can be utilized providing a relation for the second term as

$$U_{q-C} = \sum_i q_i \hat{\Phi}_{\text{void}}(\mathbf{r}_i) V \quad (2.3.25)$$

All pairwise Coulomb-interactions between the charges  $q_i$  are considered in the third term

$$U_{q-q} = \frac{1}{8\pi\epsilon_0} \sum_i \sum_{j,j \neq i} \frac{q_i q_j}{|\mathbf{r}_i - \mathbf{r}_j|} \quad (2.3.26)$$

of the systems effective energy (2.3.23). As charges  $q_i$  in the tip-sample system are assumed to be fixed at their respective positions  $\mathbf{r}_i$  and independent of the presence and movement of the tip in  $z_{ts}$ , their pairwise Coulomb-interactions  $U_{q-q}$  will not contribute to the electrostatic tip-sample force. The fourth term  $U_{\text{img}}$  of the systems effective energy (2.3.23) describes the contribution due to image interactions, where the image potential  $\Phi_{\text{img}}(\mathbf{r})$  can be further expressed as [67, 70]

$$\Phi_{\text{img}}(\mathbf{r}) = \frac{1}{\epsilon_0} \sum_j q_j \phi_{\text{ind}}(\mathbf{r}, \mathbf{r}_j) \quad (2.3.27)$$

where  $\phi_{\text{ind}}(\mathbf{r}, \mathbf{r}_j)$  is the potential at position  $\mathbf{r}$  caused by the image charge induced by charge  $q_j$  at position  $\mathbf{r}_j$  described by a Green's function. Inserting this relation into the image interaction term yields

$$U_{\text{img}} = \frac{1}{2\epsilon_0} \sum_i \sum_j q_i q_j \phi_{\text{ind}}(\mathbf{r}_i, \mathbf{r}_j) \quad (2.3.28)$$

Inserting the relations (2.3.24) to (2.3.28) into the expression of the effective energy (2.3.23) now allows to calculate the electrostatic force as

$$\begin{aligned} F_{\text{el}}^{\text{body}}(z_{ts}, V) &= \frac{1}{2} \frac{\partial C_{\text{void}}}{\partial z_{ts}} \cdot V^2 \\ &\quad - \sum_{i=1}^N q_i \frac{\partial \hat{\Phi}_{\text{void}}(\mathbf{r}_i)}{\partial z_{ts}} \cdot V \\ &\quad - \frac{1}{2\epsilon_0} \sum_{i=1}^N \sum_{j=1}^N q_i q_j \frac{\partial \phi_{\text{ind}}(\mathbf{r}_i, \mathbf{r}_j)}{\partial z_{ts}} \\ &= F_C(z_{ts}, V) + F_{q-C}(z_{ts}, q_i, V) + F_{\text{img}}(z_{ts}, q_i) \end{aligned} \quad (2.3.29) \quad (2.3.30)$$

which is the final result of this section. In the following, the properties of the electrostatic force and its three contributions are discussed.

## 2. Tip-sample interaction forces

### 2.3.2.2. Properties and voltage dependency

The electrostatic force (2.3.29) in any tip-sample capacitor as exemplified in Figure 2.5 is composed of the capacitance interaction  $F_C(z_{\text{ts}}, V)$  between tip and sample support, the charge-capacitor interaction  $F_{\text{q-C}}(z_{\text{ts}}, q_i, V)$  and the image charge interaction  $F_{\text{img}}(z_{\text{ts}}, q_i)$ . All contributions are dependent on the tip-sample distance  $z_{\text{ts}}$ , the respectively given geometries of tip and sample as well as the dielectric substrate in the gap in-between. Differences occur when comparing the dependencies on the point charge configuration  $q_i$  and the potential difference  $V$  between tip and sample support. While the capacitance interaction  $F_C(z_{\text{ts}}, V)$  is independent of the charges  $q_i$  and  $\propto V^2$ , the charge-capacitor interaction  $F_{\text{q-C}}(z_{\text{ts}}, q_i, V)$  does depend on  $q_i$  and scales linearly with  $V$ , whereas the image charge interaction is dependent on the charges  $q_i$  alone and constant with respect to  $V$ .

The first two contributions  $F_C(z_{\text{ts}}, V)$  and  $F_{\text{q-C}}(z_{\text{ts}}, q_i, V)$  to the electrostatic force (2.3.29) require the characterization of the given void tip-sample capacitor by calculation of the capacitance  $C_{\text{void}}(z_{\text{ts}})$  and the electrostatic potential  $\hat{\Phi}_{\text{void}}(z_{\text{ts}})$ . This can in special cases be performed analytically [67, 95, 96] and in general numerically [71]. However, the calculation for the image charge contribution  $F_{\text{img}}(z_{\text{ts}}, q_i)$  is a challenge, especially for realistic tip-sample geometries and larger number of charges in the gap [70]. Conveniently, the image charge interaction does not contribute to the CFM signal  $V_{\text{bias}}^{\text{min}}$  as it is independent of the given potential difference  $V$  between tip and sample. Hence, in the evaluation of CFM data it is sufficient to evaluate the contributions by  $F_C(z_{\text{ts}}, V)$  and  $F_{\text{q-C}}(z_{\text{ts}}, q_i, V)$  (see chapter 7 for more detail).

To exemplify the voltage and distance dependence of the electrostatic force (2.3.29), a simple sphere-sample model (S model) as depicted in the inset of Figure 2.6(b) can be used. Here, a conductive sphere with radius  $r_{\text{sphere}}$  at a constant potential in vacuum is assumed as the tip, which is at distance  $z_{\text{ts}}$  to the sample given by a dielectric half-space of relative permittivity  $\epsilon_s$ . Consequently, the back-electrode is assumed to be located at  $-\infty$  which is justified as the typical thickness of samples used in AFM is magnitudes larger than the investigated tip-sample distance regimes. Furthermore, a point charge  $q = -1e$  is placed on the sample surface at  $\mathbf{r} = [0, 0, 0]$  centred below the sphere. Calculation of the electrostatic capacitance  $C_{\text{void}}(z_{\text{ts}})$  and normalized potential  $\hat{\Phi}_{\text{void}}(z_{\text{ts}})$  required for  $F_C(z_{\text{ts}}, V)$  and  $F_{\text{q-C}}(z_{\text{ts}}, q_i, V)$  is straightforward for the S model using a infinite image charge series (see Appendix A.3). Due to the simple geometries in this model, the image charge interaction between tip sphere and point charge  $q$  on the sample surface can be calculated analytically and is given by [93, 67]

$$F_{\text{img}}(z_{\text{ts}}, q) = -\frac{1}{4\pi\epsilon_0} \frac{q^2 z_{\text{ts}} r_{\text{sphere}}}{(z_{\text{ts}}^2 - r_{\text{sphere}}^2)^2} \quad (2.3.31)$$

Parameters assumed for the S model are listed in Table 2.4. In Figure 2.6(a), the dependence of the electrostatic force  $F_{\text{el}}^{\text{body}}$  (red) and its components  $F_{\text{C}}$  (blue),  $F_{\text{q-C}}$  (green) and  $F_{\text{img}}$  (horizontal dotted line) on an externally applied bias voltage  $V_{\text{ext}} = V_{\text{bias}}$  at a fixed tip-sample distance  $z_{\text{ts}} = 2 \text{ nm}$  for the S model is depicted. The external voltage  $V_{\text{ext}}$  counteracts with  $V_{\text{CPD}}$  in the total potential difference  $V$  between tip and sample as described in relation (2.3.16).

| <b>sphere-sample model</b> |      |
|----------------------------|------|
| $r_{\text{sphere}}$        | 5 nm |
| $\epsilon_{\text{s}}$      | 24   |
| $V_{\text{CPD}}$           | 1 V  |

Table 2.4.: Assumed parameters for the S model utilised in the exemplification of  $F_{\text{el}}^{\text{body}}$ .

The force contribution by the void tip-sample capacitor  $F_{\text{C}}(z_{\text{ts}}, V)$  is a parabolic function in  $V$  (blue line in Figure 2.6(a)). Independent of the sign of  $V$  and the point charges, the force contribution  $F_{\text{C}}(z_{\text{ts}}, V)$  will be attractive due to  $\partial C_{\text{void}}/\partial z_{\text{ts}} < 0$  for all  $z_{\text{ts}}$  (see Figure A.4(d) in appendix). Consequently, in respect to  $V_{\text{ext}}$  the capacitance interaction force  $F_{\text{C}}(z_{\text{ts}}, V)$  always follows a downward-opened parabola, which has its maximum at  $V_{\text{ext}} = V_{\text{CPD}}$  where the total potential difference  $V$  between tip and sample support and thus  $F_{\text{C}}(z_{\text{ts}}, V)$  become zero.

The interaction between point charges and the tip-sample capacitor  $F_{\text{q-C}}(z_{\text{ts}}, q_i, V)$  is a linear function in respect to  $V_{\text{ext}}$  (green line in Figure 2.6(a)). Depending on the signs of  $q_i$  and the resulting potential difference  $V$ , this force contribution can either be attractive or repulsive. In this example, a negative charge  $q = -1 e$  below the tip is assumed. Due to  $\partial \hat{\Phi}_{\text{void}}/\partial z_{\text{ts}} < 0$  for all  $z_{\text{ts}}$  (see Figure A.4(c) in appendix), the charge-capacitor interaction  $F_{\text{q-C}}(z_{\text{ts}}, q_i, V)$  contributing to the electrostatic force  $F_{\text{el}}^{\text{body}}$  is repulsive for  $V_{\text{ext}} < V_{\text{CPD}}$  ( $V < 0$ ) and attractive for  $V_{\text{ext}} > V_{\text{CPD}}$  ( $V > 0$ ).

The image charge interaction  $F_{\text{img}}(z_{\text{ts}}, q)$  is independent of  $V$  and thus contributes to the electrostatic force  $F_{\text{el}}^{\text{body}}$  in respect of  $V_{\text{ext}}$  as a constant, attractive force offset as indicated by a horizontal dotted line in Figure 2.6 (a).

The electrostatic force  $F_{\text{el}}^{\text{body}}$  is the sum of all contributions  $F_{\text{C}}(z_{\text{ts}}, V)$ ,  $F_{\text{q-C}}(z_{\text{ts}}, q, V)$  and  $F_{\text{img}}(z_{\text{ts}}, q)$  and consequently combines their properties in respect to  $V_{\text{ext}}$ . It follows a downward opened parabola due to the capacitance force  $F_{\text{C}}(z_{\text{ts}}, V)$  which is tilted by the contribution of the charge-capacitor interaction  $F_{\text{q-C}}(z_{\text{ts}}, q, V)$  and offset by the image charge force  $F_{\text{img}}(z_{\text{ts}}, q)$ . The maximum of the parabolic curve representing the minimum attractive electrostatic force (2.3.29) with respect to

## 2. Tip-sample interaction forces

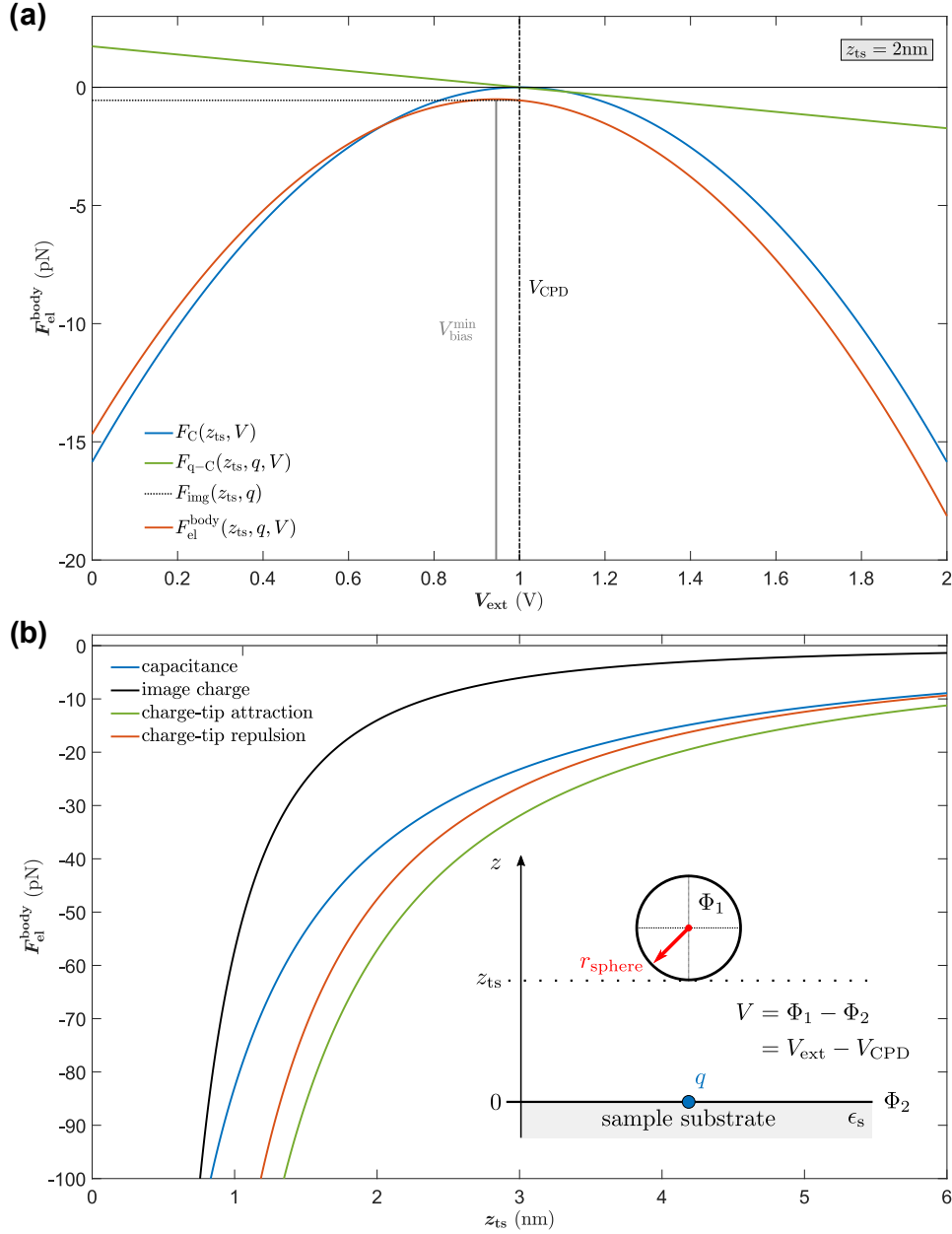


Figure 2.6.: Exemplification of the dependency of the electrostatic force (2.3.29), (a) on a externally applied bias voltage  $V_{\text{ext}} = V_{\text{bias}}$  at a constant distance  $z_{\text{ts}} = 2 \text{ nm}$  for a charge  $q = 1 e$  and (b) on the tip-sample distance  $z_{\text{ts}}$  for different combinations of fixed values for  $q$  and  $V$  as listed in Table 2.5. Both calculations are carried out based on the S model depicted in the inset of (b) (see also appendix A.3). Parameters assumed for the S model are listed in Table 2.4.

$V_{\text{ext}} = V_{\text{bias}}$  is found at

$$V_{\text{bias}}^{\text{min}} = V_{\text{CPD}} + \sum_{i=1}^N q_i \frac{\frac{\partial \hat{\Phi}_{\text{void}}}{\partial z_{\text{ts}}}}{\frac{\partial C_{\text{void}}}{\partial z_{\text{ts}}}} \quad (2.3.32)$$

which is indicated as a vertical grey line in the exemplification shown Figure 2.6 (a). This relation describes the CFM signal for a static tip, which is obtained when minimizing the attractive force on the tip by adjusting the external voltage to  $V_{\text{ext}} = V_{\text{bias}}^{\text{min}}$ . In practice, however, an implementation of CFM in static AFM would not be purposeful for two main reasons. First, the static deflection of the tip as measure for the tip-sample force lies way below the detectability limit. Second, due to the lack of higher harmonic signals, it is impossible to adequately characterize the given tip-sample capacitor for correctly modelling  $C_{\text{void}}(z_{\text{ts}})$  and  $\dot{\Phi}_{\text{void}}(z_{\text{ts}})$  required for the quantitative evaluation of the static CFM signal using relation (2.3.32).

In Figure 2.6(b), the dependency of the electrostatic force  $F_{\text{el}}^{\text{body}}$  (2.3.29) on the tip-sample distance  $z_{\text{ts}}$  is shown for different configurations of  $q$  and  $V$  in the S model as listed in Table 2.5. All other model parameters for calculation remain as listed in Table 2.4. The capacitance configuration is given for a charge-free system  $q = 0$  and any non-zero potential difference  $V$  between tip and back-electrode. Here, the electrostatic force exclusively is given by the attractive capacitance interaction  $F_{\text{el}}^{\text{body}} = F_{\text{C}}(z_{\text{ts}}, V)$  (blue line in Figure 2.6(b)). Further, the distance-dependent curvature of the electrostatic force  $F_{\text{el}}^{\text{body}}$  is determined by  $C_{\text{void}}(z_{\text{ts}})$  alone, which is scaled by the respectively given potential difference  $V$ . For the exemplification a potential difference  $V = 1 \text{ V}$  is assumed.

| configuration         | $q$ in $e$ | $V$ in V |
|-----------------------|------------|----------|
| capacitance           | 0          | 1        |
| image charge          | -1         | 0        |
| charge-tip attraction | -1         | 1        |
| charge-tip repulsion  | -1         | -1       |

Table 2.5.: Parameters for the different configurations of the S model considered in Figure 2.6.

The second configuration is a tip-sample capacitor containing a charge  $q \neq 0$  but the potential difference  $V$  is equalized. Here, exclusively the image charge interaction defines the electrostatic force  $F_{\text{el}}^{\text{body}} = F_{\text{img}}(z_{\text{ts}}, q)$  acting on the tip. For an assumed single point charge  $q = -1 e$  centred below the tip (inset Figure 2.6(b)) the resulting image charge interaction is strong at close distances  $z_{\text{ts}}$  and rapidly vanishes due to its dependency  $\propto z_{\text{ts}}^{-3}$ .

In tip-sample capacitor configurations with non-zero charge  $q$  and potential difference  $V$  between its plates not only the image interaction  $F_{\text{img}}$  but also  $F_{\text{C}}$  and  $F_{\text{q-C}}$  contribute to the electrostatic force  $F_{\text{el}}^{\text{body}}$  acting on the tip. While  $F_{\text{C}}$  and  $F_{\text{img}}$  are exclusively attractive, the charge-capacitor interaction  $F_{\text{q-C}}$  can be either repulsive or attractive depending on the signs of  $q$  and  $V$ . If the charge  $q$  has

## 2. Tip-sample interaction forces

the same sign as the voltage  $V$ , a repulsive interaction between charge and tip in the capacitor occurs, which reduces the overall attractive electrostatic force  $F_{\text{el}}^{\text{body}}$  acting on the tip (red line). In contrast, if the charge  $q$  has the opposite sign as the potential difference  $V$  between tip and sample support, the attractive electrostatic force  $F_{\text{el}}^{\text{body}}$  on the tip is amplified by the presence of that charge  $q$  in the tip-sample capacitor (green line). In all cases, where the charge  $q$  is present also the image interaction has to be accounted for as an additional contribution (black line). The self-interaction of a single charge via its image charge always will be attractive.

## 2.4. Model for the total tip-sample interaction

In the previous sections all force contributions considered in the total tip-sample interaction (2.1.4) are described based on mathematical models and model parameters. In this section, these models and parameters are combined to gain an idea of the overall properties of the total tip-sample interaction force  $F_{\text{ts}}$  acting on the tip. For convenience, all model parameters introduced throughout all previous sections are collated in Table 2.6.

Due to the omnipresent nature of the dispersion forces, the tip-sample force  $F_{\text{ts}}$  will always be a mixture of both, the atomic interaction and  $F_{\text{atomic}}$  and  $F_{\text{vdW}}^{\text{body}}$ . To model this force composition of  $F_{\text{ts}}$ , the Lennard-Jones force (2.2.10) and the van der Waals body-body force (2.3.13) can be used to model the atomic and body forces, which yields

$$\begin{aligned}
 F_{\text{ts}}^{\text{model}_1}(z_{\text{ts}}) &= F_{\text{LJ}}(z_{\text{ts}}) + F_{\text{vdW}}^{\text{body}}(z_{\text{ts}}) & (2.4.33) \\
 &= 12 \frac{E_{\text{b}}}{\sigma_0} \left[ \left( \frac{\sigma_0}{z_{\text{ts}}} \right)^{13} - \left( \frac{\sigma_0}{z_{\text{ts}}} \right)^7 \right] \\
 &\quad - \frac{H R^2 (\sin \Theta - 1) ((R - \hat{z}) \sin \Theta - R - \hat{z})}{6 \hat{z}^2 (R + \hat{z} - R \sin \Theta)^2} \\
 &\quad - \frac{H \tan \Theta ((\hat{z} + R) \sin \Theta + R \cos(2\Theta))}{6 \cos(\Theta) (\hat{z} + R - R \sin \Theta)^2}
 \end{aligned}$$

This or a comparable interaction will be present in every tip-sample system, only the exact composition of the atomic and body forces will change depending on the materials and geometries in the tip-surface system. The distance-dependent behaviour of the tip-sample force model  $F_{\text{ts}}^{\text{model}_1}$  for a Si-Si tip-sample interaction is depicted in Figure 2.7 (red line). For comparison the behaviour of its separate contributions  $F_{\text{LJ}}(z_{\text{ts}})$  (blue line) and  $F_{\text{vdW}}^{\text{body}}(z_{\text{ts}})$  (green line) are depicted as well. All parameters utilised for calculation can be found in Table 2.6.

For  $z_{\text{ts}}$  smaller than the equilibrium bonding length ( $F_{\text{atomic}} = 0$ ), the short-range repulsive atomic interactions are dominant and the tip-sample force  $F_{\text{ts}}$  is repulsive. If  $z_{\text{ts}}$  is in the range around the minimum of  $F_{\text{atomic}}$  the short-range attractive forces are dominant in  $F_{\text{ts}}$ . These become reinforced by the additional long-range attractive body-body van der Waals interactions  $F_{\text{vdW}}^{\text{body}}$ . In this interaction regime the NC-AFM is typically operated, since here the best resolution is possible. At tip-sample distances  $z_{\text{ts}}$  where the atomic interactions  $F_{\text{atomic}}$  start to vanish, the long-range van der Waals force contributions to  $F_{\text{ts}}$  remain.

If tip and sample support are electrically connected and charges are present in, on or above the sample substrate located within their gap, the electrostatic interactions



## 2. Tip-sample interaction forces

may strongly contribute to the total tip-sample force. For correctly modelling the interaction in a tip-sample capacitor the model for the tip-sample force (2.4.33) has to be expanded by the electrostatic force as described by (2.3.29), yielding the relation

$$\begin{aligned}
F_{\text{ts}}^{\text{model}_2}(z_{\text{ts}}, V) &= F_{\text{LJ}}(z_{\text{ts}}) + F_{\text{vdW}}^{\text{body}}(z_{\text{ts}}) + F_{\text{el}}^{\text{body}}(z_{\text{ts}}, q_i, V) \quad (2.4.34) \\
&= 12 \frac{E_{\text{b}}}{\sigma_0} \left[ \left( \frac{\sigma_0}{z_{\text{ts}}} \right)^{13} - \left( \frac{\sigma_0}{z_{\text{ts}}} \right)^7 \right] \\
&\quad - \frac{H R^2 (\sin \Theta - 1) ((R - \hat{z}) \sin \Theta - R - \hat{z})}{6 \hat{z}^2 (R + \hat{z} - R \sin \Theta)^2} \\
&\quad - \frac{H \tan \Theta ((\hat{z} + R) \sin \Theta + R \cos(2\Theta))}{6 \cos(\Theta) (\hat{z} + R - R \sin \Theta)^2} \\
&\quad + \frac{1}{2} \frac{\partial C_{\text{void}}}{\partial z_{\text{ts}}} \cdot V^2 \\
&\quad - \sum_{i=1}^N q_i \frac{\partial \hat{\Phi}_{\text{void}}(\mathbf{r}_i)}{\partial z_{\text{ts}}} \cdot V \\
&\quad - \frac{1}{2\epsilon_0} \sum_{i=1}^N \sum_{j=1}^N q_i q_j \frac{\partial \Phi_{\text{ind}}(\mathbf{r}_i, \mathbf{r}_j)}{\partial z_{\text{ts}}}
\end{aligned}$$

Based on this relation the effect of the electrostatic interaction to the total tip-sample force for different cases can be visualised. For this exemplification the same sphere-sample model as presented in Figure 2.6(b) and Appendix A.3 is used with the parameters shown in Table 2.6. Analogous to the previous section, three different configurations of the S model are assumed, namely, the capacitance, charge-tip repulsion and charge-tip attraction (see Table 2.5). The resulting force curves  $F_{\text{ts}}^{\text{model}_2}$  including the electrostatic interaction (2.4.34) are depicted in Figure 2.8 in comparison with the force curve  $F_{\text{ts}}^{\text{model}_1}$  without the electrostatic interaction (2.4.33) represented as a black dashed line.

The capacitance interaction  $F_{\text{C}}$  increases the range and attraction of the total tip-sample force  $F_{\text{ts}}^{\text{model}_2}$  dependent on the given potential difference  $V$ . Adding a point charge  $q = -1e$  at  $\mathbf{r} = [0 \ 0 \ 0]$  into the tip-sample capacitor also adds contributions by the charge-capacitor force  $F_{\text{q-C}}$  and image charge interaction  $F_{\text{img}}$  into the tip-sample force. While the image charge interaction  $F_{\text{img}}$  further increases the attractive contribution by the electrostatic force to the tip-sample force, the charge-capacitor  $F_{\text{q-C}}$  interaction is either attractive or repulsive depending on the signs of  $q$  and  $V$ . For different signs the contribution by  $F_{\text{q-C}}$  is attractive (charge-tip attraction) and for equal signs  $F_{\text{q-C}}$  becomes repulsive (charge-tip repulsion). All cases shown in Figure 2.8 demonstrate the strong contribution of the electrostatic interaction  $F_{\text{el}}^{\text{body}}$  to the tip-sample force and its sensitivity towards the presence of charges  $q_i$ . Dependent on the applied voltage  $V$  and the charges  $q_i$  present in the tip-sample capacitor, the electrostatic contribution easily can exceed other

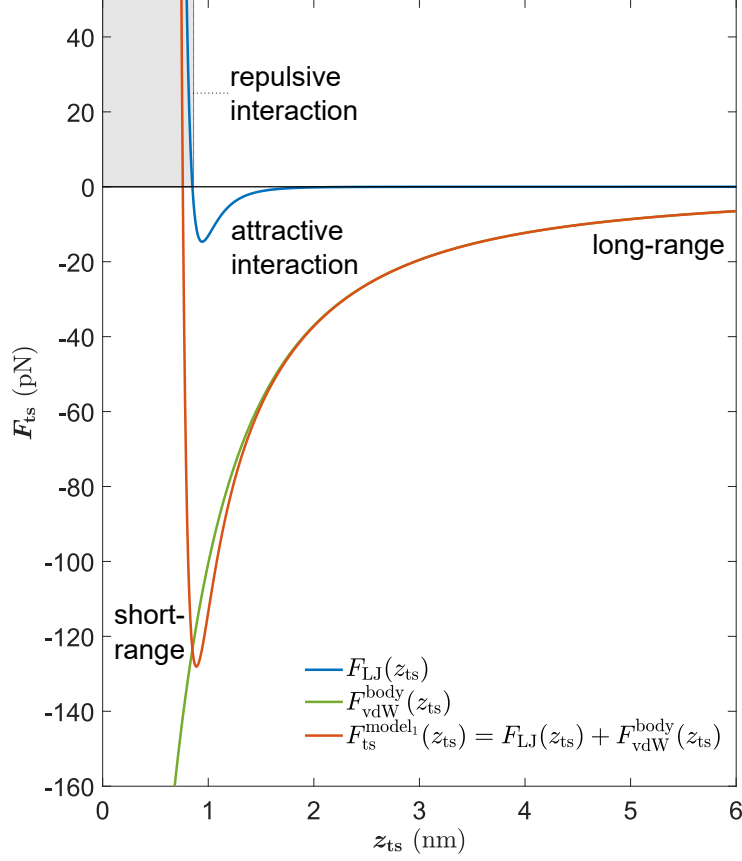


Figure 2.7.: Model for the total tip-sample interaction force. Depicted is the relation (2.4.33) as the sum of the contributing Lennard-Jones force (2.2.10) and van der Waals body-body force (2.3.13) for the parameters listed in Table 2.6. While  $F_{LJ}$  describes the atomic forces acting between the frontmost tip atoms and the nearest surface atoms, the long-range  $F_{vdW}^{body}$  describes the van der Waals interaction between the complete tip body with the sample.

contributing forces. However, as the atomic resolution capabilities in NC-AFM rely on detecting the much smaller atomic forces  $F_{atomic}$ , an exceedingly big electrostatic force  $F_{el}^{body}$  is not desirable. For that reason NC-AFMs typically are operated with electrically connected tip and sample support, allowing for minimization of the electrostatic force by equalizing  $V$  via the external voltage source  $V_{ext}$ . The external voltage where the electrostatic force is minimal  $V_{ext} = V_{bias}^{min}$  is the CFM signal, as it contains the information on  $q_i$  and  $V_{CPD}$  given in the tip-sample capacitor. The theory for quantitatively extracting these information from CFM data obtained in a dynamic NC-AFM measurement is described in chapters 7, 8 and 9.

In conclusion, the force a tip senses near a sample surface consists of a complex entanglement of several nanoscale forces. An exact distinction between the sepa-

## 2. Tip-sample interaction forces

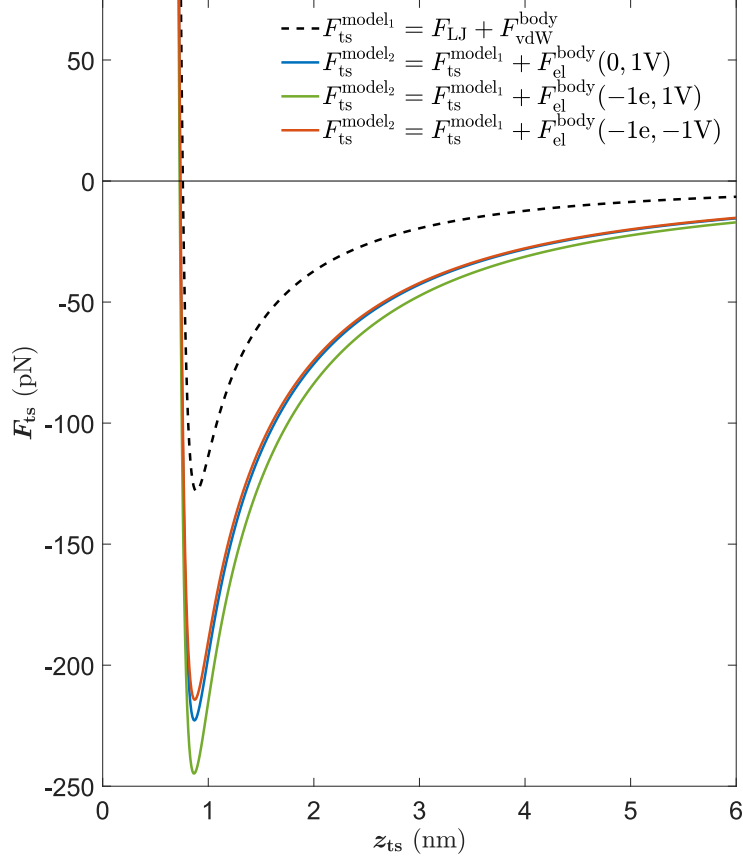


Figure 2.8.: Distance-dependency of the total tip-sample interaction force (2.4.34) including the electrostatic contribution (2.3.29) for different cases. The first case is the void-tip sample capacitor for a voltage  $V = 1 \text{ V}$  (blue line), the second case is the tip-sample capacitor with a single point charge  $q = -1 e$  located  $\mathbf{r} = [0 \ 0 \ 0]$  below the tip for a voltage  $V = 1 \text{ V}$  (green line); and the third case is the tip-sample capacitor with a single point charge  $q = -1 e$  located  $\mathbf{r} = [0 \ 0 \ 0]$  below the tip for a voltage  $V = -1 \text{ V}$  (red line). For reference relation (2.4.33) for the tip-sample force without the electrostatic interaction depicted as a black dashed line. Parameters used for calculation are listed in Tables 2.6 and 2.5.

rate contributions is difficult, as there is no strict border between the descriptions of short-range atomic forces  $F_{\text{atomic}}$  and the long-range body forces  $F_{\text{body}}$ . In literature there are several approaches for extracting the chemical forces from the total tip-sample force in a quantitative manner [97, 98, 45, 77]. A common approach is the subtraction of the long-range force from the total force to yield the force representing the chemical interaction. The long-range interaction as function of tip-sample distance is either measured at a reference position with a well characterised surface exhibiting low chemical activity [97] or calculated based on a model [77, 45]. However, both approaches can be prone to systematic errors. In the first

## 2.4. Model for the total tip-sample interaction

case, force curves from different locations on the surface are subtracted. Since the tip-sample force strongly depends on the surroundings of the tip near the sample surface, this approach is only valid if the surface is completely isotropic. The second approach is limited by the quality of the utilised model for the tip-sample system fitted to the experimental data, to characterise the long-range interaction [98]. In the end, both approaches require a correctly quantified tip-sample force beforehand. The FCA method, a procedure for obtaining accurate and precise tip-sample force data with dynamic NC-AFM will be presented in chapter 5. However, therefore the functionality and theory of dynamic NC-AFM have to be understood first.

|                                |                       |  |            |
|--------------------------------|-----------------------|--|------------|
| <b>Morse potential</b>         |                       | <b>van-der-Waals body-body interaction</b> |            |
| $E_b$                          | 4.638 zJ              | $H$  | 357.619 zJ |
| $\sigma_0$                     | 850 pm                | $\Theta$                                   | 29.7°      |
| $\kappa$                       | 2.50 nm <sup>-1</sup> | $R$  | 5 nm       |
|                                |                       | $z_{nt}$                                   | 583.04 pm  |
| <b>Lennard-Jones potential</b> |                       | <b>electrostatic interaction</b>           |            |
| $E_b$                          | 4.638 zJ              | $r_{\text{sphere}}$                        | 5 nm       |
| $\sigma_0$                     | 850 pm                | $\epsilon_s$                               | 24         |
| $r_0 = \sigma_0/2^{1/6}$       | 757.26 pm             | $V_{\text{CPD}}$                           | 1 V        |

Table 2.6.: Collated list of model parameters for tip-sample force calculation from Tables 2.1, 2.2, 2.3 and 2.4.



### 3. NC-AFM principle and setup

In dynamic NC-AFM, the amplitude and frequency change imposed on the resonant oscillation of a force sensor by the distant-dependent attractive interactions between tip and sample are detected. Thereby the resonance frequency and amplitude of the free oscillation far away from the sample are used as reference. If the oscillating force sensor is brought into close proximity to the sample surface, the tip-movement in the attractive force field of the surface detunes the resonant oscillation. Consequently, the force sensor oscillates at a new amplitude and resonance frequency. If there are no experimental constraints, the information of the tip-sample interaction is distributed over these two observables of the sensor oscillation. To shift the effect of the tip-sample interaction to one observable, a control loop for the force sensor oscillation is used in the NC-AFM which maintains one observable of the oscillation constant while detecting the other. Based on these two configurations, two types of NC-AFM operation can be implemented.

One is amplitude modulated NC-AFM (AM NC-AFM) where the oscillation frequency is maintained while the amplitude change is detected as the main signal. The other configuration exclusively considered in this work, is frequency modulated NC-AFM (FM NC-AFM) [99] where the sensor oscillation amplitude is maintained constant while the frequency shift from its eigenfrequency is detected as the main signal. For any centre position  $z_c$  of tip oscillation  $z_{ts}(t)$ , the frequency shift is related to the cycle-averaged tip-sample force gradient acting on the tip within the turning points  $z_c - A$  and  $z_c + A$ . Within the framework of quantitative AFM theory (see chapter 4), the tip-sample force can be calculated from frequency shift data mapped as function of  $z_c$  [47] (see section 4.6). This requires the knowledge of the exact force sensor properties and the given physical oscillation amplitude.

The relevant force sensor properties, the schematic setup of FM NC-AFM used in this work and amplitude calibration procedures are topic in this chapter. A well working FM NC-AFM and precise interaction force detection are prerequisite for charge force microscopy (CFM). The technical implementation and principles for CFM measurements based on frequency modulated closed-loop kelvin probe force microscopy (FM CL-KPFM) [63, 64] will be discussed in this chapter as well.

### 3.1. Force sensor

The properties of force sensors have a significant influence on the performance of a NC-AFM [80]. Three types of force sensors are commercially available for use in NC-AFM namely silicon cantilevers [100, 101], quartz tuning forks [102, 103] and length-extensional resonators (LER) [104, 105, 106]. While these force sensors are different in application-relevant details [107], their general functionality is based on the same principle. The force sensor is a sensitive, linearly responding spring transforming nanoscale forces acting between tip and sample into a measurable signal. Typically force sensors are built in such a way, that they are rigid in two axes and relatively soft in the third axis used for sensing tip-sample forces [80]. The silicon cantilever with integrated tip as schematically depicted in Figure 3.1 is a good example for this design. It consists of a sharp tip located at the free end of a cantilever beam of length  $l$  attached to a much larger support chip. The sensor is etched as one part from a silicon-wafer [101] in such way, that its tip is oriented in  $[001]$  crystal direction [80]. The anisotropic etching rates of Si allow to etch tips with a very sharp apex along that direction [108]. The cross-section of the cantilever beam is trapezoidal due to the etching planes utilised in the production [101, 80] and characterized by a bottom width  $w_b$ , a top width  $w_t$  and the thickness  $t$ . As depicted in Figure 3.1, the thickness  $t$  of the beam is significantly smaller than its mean width  $\bar{w} = (w_b + w_t)/2$ . Consequently, the beam is rigid against torsion around the  $x$ -axis as well as in the  $y$ -direction while the deflection in  $z$ -direction is favourable. Hence, the beam can easily be driven via the support chip to oscillate exclusively in  $z$ -direction for sensing forces. The properties of interest for any force sensor are its modal stiffness  $k_0$ , its eigenfrequency  $f_0$  and the quality factor  $Q_0$ .

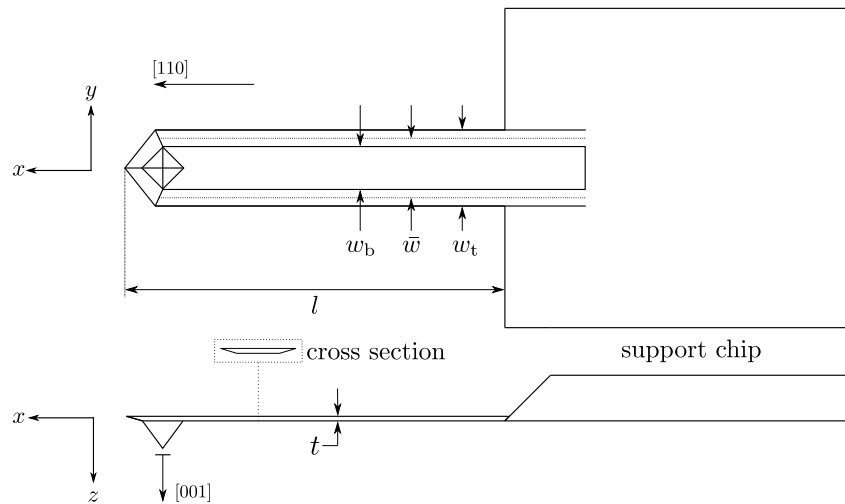


Figure 3.1.: Bottom and side view of a microfabricated silicon cantilever (schematic).

The stiffness  $k$  of the cantilever beam acting against a static deflection in direction of its tip ( $z$ -direction in Figure 3.1) can be derived by solving the static Euler-Bernoulli equation considering deflections much smaller than the beam length (linear response) yielding [109, 110]

$$k = \frac{3YI_y}{l^3} \quad (3.1.1)$$

where  $Y$  is the Young's modulus of the cantilever material and  $I_y$  is the second moment of inertia, a property of the cross-section geometry of the beam, measuring its stiffness against bending. Considering cross-section of the cantilever in the  $y, z$ -plane as shown in Fig. 3.1 its second moment of area acting against bending in  $z$ -direction is given by

$$I_y = \int \int z^2 dz dy \quad (3.1.2)$$

integrated over the respective cross-section area of the beam. The eigenfrequency  $f_0$  and all higher harmonics of the silicon cantilever oscillation can be derived from the dynamic Euler-Bernoulli equation [80]. Assuming the silicon cantilever to be a homogeneous, harmonically oscillating beam with an amplitude much smaller than its length, the eigenfrequency of its  $n$ -th harmonic is given by

$$f_n = \frac{\kappa_n^2}{2\pi l^2} \sqrt{\frac{YI_y}{\rho_m A_{yz}}} \quad \text{with } n = 0, 1, 2, \dots \quad (3.1.3)$$

where  $\kappa_n$  is the  $n$ -th oscillation mode eigenvalue of the differential equation,  $\rho_m$  the mass density of the beam material and  $A_{yz}$  the cross-section area. Note, an characteristic equation for calculation of the eigenvalues  $\kappa_n$  results from the boundary conditions describing the cantilever as an elastic beam fixed at one end and free at the other end. If a tip mass  $m_{\text{tip}}$  at the free end of the cantilever is taken into consideration as well, the characteristic equation describing its eigenvalues  $\kappa_n$  reads as [110]

$$1 + \cos(\kappa_n) \cosh(\kappa_n) + \kappa_n \frac{m_{\text{tip}}}{\rho_m A_{yz} l} [\cos(\kappa_n) \sinh(\kappa_n) - \sin(\kappa_n) \cosh(\kappa_n)] = 0 \quad (3.1.4)$$

The modal stiffness  $k_n$  of the cantilever oscillating in the  $n$ -th mode can be derived by inserting the static stiffness relation (3.1.1) into the eigenfrequency equation (3.1.3), yielding

$$k_n = \frac{12\pi^2 \rho_m A_{yz} l}{\kappa_n^4} f_n^2 \quad \text{with } n = 0, 1, 2, \dots \quad (3.1.5)$$

For the fundamental mode  $n = 0$ , the modal stiffness  $k_0$  is approximately the same as the stiffness  $k$  against static deflection  $k_0 \approx k$  [110].

The quality factor  $Q$  of a damped harmonic oscillation, such as the cantilever is defined as the ratio between the energy  $U$  stored in the oscillation and the energy



### 3. NC-AFM principle and setup

dissipation  $\Delta U$  per oscillation cycle [111]:

$$Q_0 = \frac{2\pi U}{\Delta U} \quad (3.1.6)$$

The effective  $Q$ -factor of the oscillating cantilever  $Q_{\text{eff}}$  is the reciprocal to the total damping of the system and consists of several contributions [112], for instance, the intrinsic damping of the vibrating beam [111, 113, 114, 115, 116], the damping by the cantilever fixation via its support in the microscope [117], or damping by the surrounding medium [111, 118, 119]. The effective quality factor  $Q_{\text{eff}}$  determines the width of the resonance peak of the sensor oscillation, that can be described as a damped, driven harmonic oscillator (see 4.2). A high  $Q_{\text{eff}}$  results in a narrow resonance peak allowing for a signal detection with high signal to noise ratio. Hence force sensors with high  $Q_0$ -factors are preferable in FM NC-AFM [99]. Typical  $Q$ -factors for 300 kHz silicon cantilevers range between 10000 and 40000 [120]. In this

| Property                                  | Nominal Value | Specified Range |
|---|---------------|-----------------|
| Resonance frequency $f_0$ [kHz]           | 330           | 204-497         |
| Force constant $k_0$ [N m <sup>-1</sup> ] | 42            | 10-130          |
| Thickness $t$ [μm]                        | 4             | 3-5             |
| Mean width $\bar{w}$ [μm]                 | 30            | 22.5-37.5       |
| Length $l$ [μm]                           | 125           | 115-135         |

Table 3.1.: Characteristic properties of the *PPP-NCH* silicon cantilevers and platinum-iridium (PtIr<sub>5</sub>) coated silicon cantilevers *PPP-NCHPt* from **Nanosensors**<sup>TM</sup>. The values are from the corresponding data sheet provided by the producer.

work, silicon cantilevers (*PPP-NCH*) and platinum iridium (PtIr<sub>5</sub>) coated silicon cantilevers (*PPP-NCHPt*) from **Nanosensors**<sup>TM</sup> are used. Both sensor types consists of highly doped silicon to dissipate static charge and are chemically inert, where the (*PPP-NCHPt*) sensor exhibits an additional 25 nm double layer chromium Cr and platinum-iridium (PtIr<sub>5</sub>) coating on both sides of the cantilever including the tip. The nominal values for the characteristic parameters of both sensor types provided by the producer are shown in Tab. 3.1. These vary in the specified range due to uncertainties in the microfabrication process by etching. For the same reason also the tip height varies in the range from 10 μm to 15 μm. While the *PPP-NCH* sensors are produced with tip radii < 10 nm the *PPP-NCHPt* sensors exhibit tip radii < 25 nm. Hence the *PPP-NCH* sensors typically provide better resolution capabilities than the *PPP-NCHPt* sensors and are used in applications where high lateral resolution is required. While the *PPP-NCHPt* provide lower resolution in NC-AFM experiments, their great advantage is their higher conductivity due to their coating. For this reason, these sensors are a perfect fit for measuring electrostatic tip-sample forces as this requires high electrical conductivity (see Sec. 2.3.2).

## 3.2. Frequency modulated non-contact atomic force microscopy (FM NC-AFM)

The FM NC-AFM detects a voltage signal related to the frequency shift  $\Delta f$  experienced by a resonantly oscillating force sensor due to the forces acting between its tip and the sample while maintaining a constant oscillation amplitude [99]. Based on the  $\Delta f$  signal the structure of any well prepared sample surface can be explored with atomic resolution [80]. This requires the finely tuned cooperation of several control loops and detection devices. A typical setup of a cantilever-based FM NC-AFM is exemplified Figure 3.2, where the elements for driving and detecting the resonant probe oscillation as well as the devices for positioning and scanning the sample below the tip are depicted. The additional control loop for measuring and minimizing the electrostatic tip-sample forces required for charge force microscopy (CFM) based on a frequency modulated Kelvin probe force microscopy implementation (FM CL-KPFM) is depicted in the red box of Figure 3.2. In this section, first, the fundamental functionality of FM NC-AFM is explained, whereby the external voltage  $V_{\text{ext}}$  is considered as constant. Second, the FM CL-KPFM loop for measuring and minimizing the electrostatic interactions by applying an variable external voltage  $V_{\text{ext}}(t)$  between tip and sample support is discussed.

Sample and cantilever support chip are both fixed to metallic structures with electrical contacts. The sample support is mounted on a piezoceramic tube scanner enabling fine positioning in  $x$ ,  $y$  and  $z$  direction relative to the fixed force sensor. That tube scanner, in return, is mounted on another piezo element utilised for coarse positioning in  $x$  and  $z$  direction. By this the force sensor tip can be brought into interaction range with the surface and all movement required during measurement can be performed. Typically cantilevers are mounted with a small tilt by an angle  $\alpha$  towards the sample to avoid that the cantilever rather than the tip touches the surface. The angle  $\alpha$  therefore also is the angle between sample surface normal and oscillation direction of the cantilever. This circumstance has consequences for the quantitative evaluation of NC-AFM data [58], which will be addressed in chapter 6.

To enable a driven oscillation of the cantilever, its support is mounted on the drive piezo. For FM NC-AFM operation, the cantilever is driven to permanently oscillate at resonance with a constant amplitude controlled by the oscillation feedback loop. Core part of the cantilever excitation is the phase locked loop (PLL) providing the drive signal  $V_{\text{exc}}(t)$  for the cantilever excitation and measuring its response. The PLL consists of a phase-detector, voltage-controlled oscillator (VCO) and a control-loop [41]. For the cantilever excitation, the VCO generates a sinusoidal

### 3. NC-AFM principle and setup

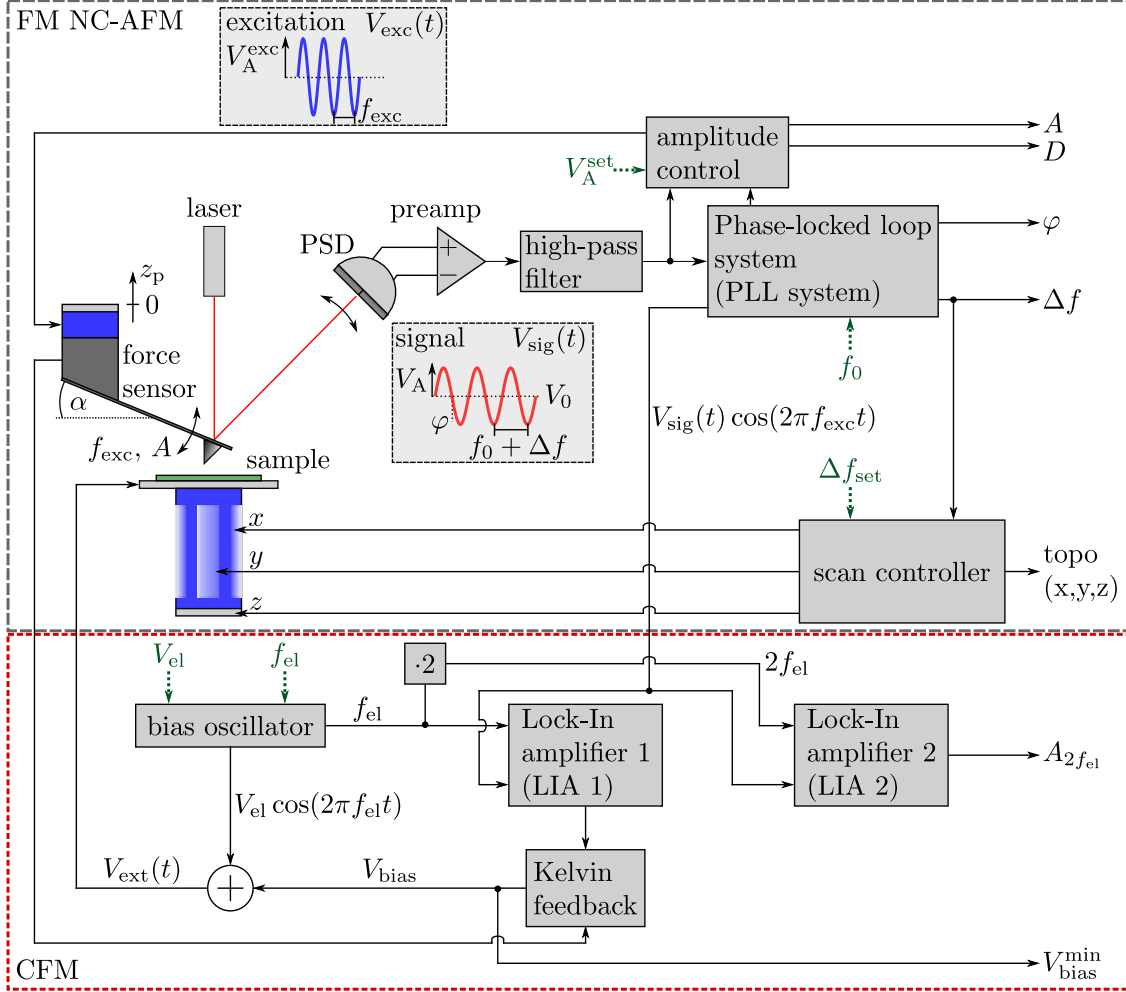


Figure 3.2.: Schematic overview of a cantilever based NC-AFM in the frequency modulation mode. The components required for FM NC-AFM and CFM are framed in grey and red, respectively. Input parameters, which are set previous to the measurement are depicted in green.

signal

$$V_{\text{exc}}(t) = V_A^{\text{exc}} \sin(2\pi f_{\text{exc}} t) \quad (3.2.7)$$

with excitation amplitude  $V_A^{\text{exc}}$  and excitation frequency  $f_{\text{exc}}$ . This is sent as the driving signal to the drive piezo via the amplitude control unit regulating the magnitude of  $V_A^{\text{exc}}$  to obtain the desired value  $V_A^{\text{set}}$  for the oscillation amplitude. The voltage  $D$  proportional to the adjustment of  $V_A^{\text{exc}}$  is a measure for the mean dissipated energy. The cantilever, as a harmonic oscillator, will follow the drive signal  $V_{\text{exc}}(t)$  with the same frequency  $f_{\text{exc}}$  and an a priori unknown physical amplitude  $A$ . The cantilever oscillation is measured as a function of time via the optical beam deflection (OBD) method [121, 41]. Here, the light emitted by a laser is reflected from the back of the cantilever onto a position sensitive detector (PSD). The cur-

### 3.2. Frequency modulated non-contact atomic force microscopy (FM NC-AFM)

rent signals caused by the cantilever oscillation are converted by a transimpedance amplifier into the deflection signal (sensor signal)

$$V_{\text{sig}}(t) = V_0 + V_A \cos(2\pi f_{\text{exc}}t + \varphi) \quad (3.2.8)$$

Where  $V_0$  is an offset voltage resulting from the current centre position of the cantilever oscillation,  $V_A$  is the measured oscillation amplitude voltage related to the physical oscillation amplitude  $A$  (see section 3.4),  $f_{\text{exc}}$  the current frequency of the cantilever due to the excitation and  $\varphi$  is the phase shift relative to the excitation  $V_{\text{exc}}(t)$ . The offset voltage  $V_0$  occurs if the reflected laser point is not perfectly centred on the PSD. This is due to uncertainties in the adjustment of the OBD and the static deflection  $q_s$  of the cantilever centre position caused by the tip-sample interaction. The offset  $V_0$  is eliminated by a high-pass filter before entering the input of the PLL. Note, that thermal noise and detection system noise is always present in the deflection signal  $V_{\text{sig}}(t)$  [122, 123, 50].

The PLL and amplitude control receive the AC part of the sensor signal and the PLL continuously detects the phase shift  $\varphi$  between the deflection signal  $V_{\text{sig}}(t)$  and the excitation signal  $V_{\text{exc}}(t)$  generated by the VCO. To maintain the phase resonance constant at  $\varphi = -\pi/2$ , the VCO-generated excitation frequency  $f_{\text{exc}}$  is adjusted by the PLL to permanently match the current resonance frequency  $f_{\text{res}}$  of the cantilever.

For large distances  $z_{\text{ts}}$  between tip and surface (retracted state), the resonance frequency of the PLL-driven cantilever equals its eigenfrequency  $f_{\text{exc}} = f_{\text{res}} = f_0$  as there is no tip-sample interaction. Prior to any experiment that eigenfrequency  $f_0$  is determined in the retracted state by frequency sweeping and given as reference point to the PLL. If the tip is in interaction range (approached state), the excitation frequency  $f_{\text{exc}}$  of the cantilever shifts from  $f_0$  due to the tip-sample interaction. The resulting frequency shift

$$\Delta f = f_{\text{exc}} - f_0 \quad (3.2.9)$$

is detected by the PLL. This effect can be directly observed, when measuring the frequency spectrum of the deflection signal received at the input of the PLL with another Lock-In device (here Zürich Instruments HF2LI) for the retracted and approached state as shown in Figure 3.3. In the retracted state (blue) the cantilever oscillates at its eigenfrequency  $f_{\text{exc}} = f_0$  set as reference for the PLL. After approach (orange), the resonance frequency of the cantilever  $f_{\text{res}}$  is detuned by  $\Delta f < 0$  due to the tip-sample interaction forces. The PLL follows that detuning by  $\Delta f < 0$  with the excitation frequency  $f_{\text{exc}}$  because it adjusts  $f_{\text{exc}} = f_{\text{res}}$  for maintaining phase resonance. The output voltage of the PLL is proportional to  $\Delta f$  and, therefore, a measure for the tip-sample interaction. It is either recorded as the main measurement signal or forwarded to the  $z_p$ -feedback loop controlling the tip-surface distance.

### 3. NC-AFM principle and setup

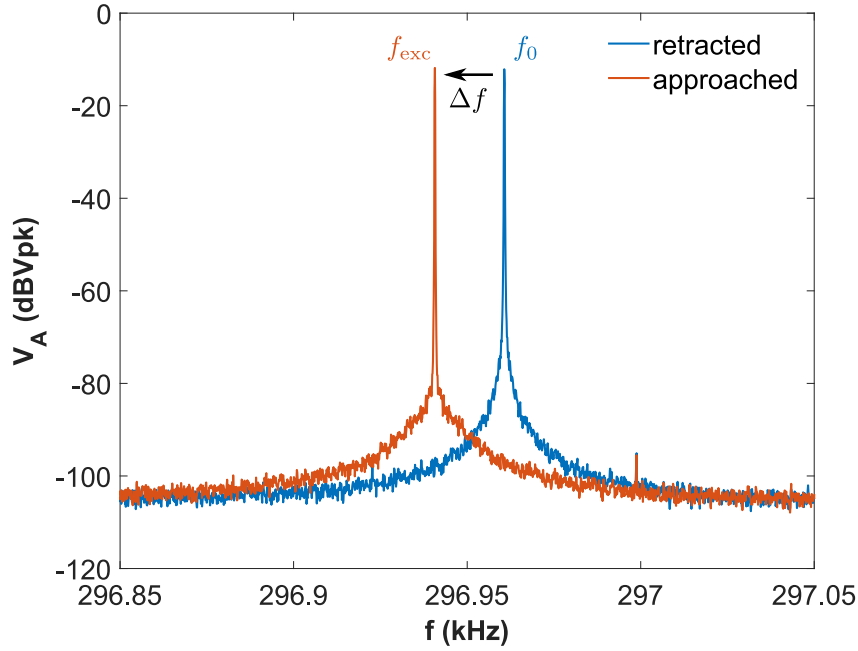


Figure 3.3.: Spectra of the sensor signal (3.2.8) of a *PPP-NCH* silicon cantilever in the Omicron UHV AFM/STM for the retracted (blue) and approached (orange) state in comparison. Both spectra are measured at the input of the PLL of the RHK R9 with a Zürich Instruments HF2LI over 20 averages. In the retracted state (blue) the cantilever is driven to oscillates at its eigenfrequency  $f_{exc} = f_0$  set as reference for the PLL. In the approached state the resonance frequency of the cantilever  $f_{exc}$  is detuned by  $\Delta f < 0$  due to the tip-sample interaction forces.

This choice determines the imaging mode in FM NC-AFM. In the *constant height* mode, the frequency shift  $\Delta f$  from the PLL is measured directly as a function of the lateral position  $(x, y)$  while scanning at a fixed piezo position  $z_p$ . Thus the frequency shift contrast due to the varying tip-sample interaction is the measurement signal [80]. As the  $z_p$ -position is kept constant, this method is only viable for atomically flat surfaces or small sampling areas. For more corrugated surfaces, the *constant frequency-shift (topography)* mode is used instead. Here, the  $z_p$ -feedback loop utilises the  $\Delta f$  signal from the PLL via the scan controller to control the  $z_p$ -position of the sample while scanning along the  $x$ - and  $y$ - directions. The current  $\Delta f$  value is compared to a given set-point  $\Delta f_{set}$  in the scan controller. In the case of a mismatch, the  $z_p$ -position is adjusted accordingly. Measuring the changes  $\Delta z_p$  as a function of the lateral position  $(x, y)$  provides the topography of the sample surface.

### 3.3. Charge force microscopy (CFM)

The contribution of charges located in, on or above the sample substrate to the electrostatic force  $F_{\text{el}}^{\text{body}}$  (2.3.29) is dependent on the potential difference  $V$  between tip and sample support. Charge force microscopy (CFM) aims for quantification of those charges by measuring their voltage-dependent contribution to the electrostatic force  $F_{\text{el}}^{\text{body}}$  imposed on the oscillating tip in FM NC-AFM. The main concept is, to measure and minimize voltage-dependent spectral components of the electrostatic force  $F_{\text{el}}^{\text{body}}$  (2.3.29) which occur when modulating the potential difference  $V$  between tip and sample support. To accomplish this, the external voltage

$$V_{\text{ext}}(t) = V_{\text{bias}} + V_{\text{el}} \cos(2\pi f_{\text{el}} t) \quad (3.3.10)$$

is applied between tip and sample support, which is composed of a loop regulated voltage  $V_{\text{bias}}$  and an oscillating voltage with amplitude  $V_{\text{el}}$  and frequency  $f_{\text{el}}$  generated by an oscillator. The voltage-dependent components of  $F_{\text{el}}^{\text{body}}$  follow the oscillation of  $V_{\text{ext}}(t)$  with frequency  $f_{\text{el}}$ . The approached cantilever senses the oscillation of the electrostatic force while oscillating itself with the frequency  $f_{\text{exc}}$ . This causes several spectral components in the deflection signal received by the PLL, which can be described by (see chapter 7 for mathematical description)

$$\begin{aligned} V_{\text{sig}}^{f_{\text{el}}}(t) = & V_0 + V_A \cos(2\pi f_{\text{exc}} t + \varphi) \\ & + V_A^{f_{\text{el}}} \cos(2\pi f_{\text{el}} t) \\ & + V_A^{2f_{\text{el}}} \cos(2\pi(2f_{\text{el}})t) \\ & + V_A^{f_{\text{exc}}+f_{\text{el}}} \cos(2\pi(f_{\text{exc}} + f_{\text{el}})t + \varphi) \\ & + V_A^{f_{\text{exc}}-f_{\text{el}}} \cos(2\pi(f_{\text{exc}} - f_{\text{el}})t + \varphi) \\ & + V_A^{f_{\text{exc}}+2f_{\text{el}}} \cos(2\pi(f_{\text{exc}} + 2f_{\text{el}})t + \varphi) \\ & + V_A^{f_{\text{exc}}-2f_{\text{el}}} \cos(2\pi(f_{\text{exc}} - 2f_{\text{el}})t + \varphi) \end{aligned} \quad (3.3.11)$$

Where  $V_A^f$  is the measured signal amplitude voltage at the respective frequency  $f$ . For exemplification, the deflection signal spectrum of a cantilever in tip-surface interaction at  $\Delta f = -5$  Hz with active voltage modulation  $V_{\text{ext}}(t)$  is shown in Figure 3.4(a). The shown deflection signal spectrum resulting from  $V_{\text{bias}} = 0$ ,  $V_{\text{el}} = 1$  V and  $f_{\text{el}} = 1567$  Hz in *constant frequency-shift* mode is measured at the PLL input using another spectrum analyser (Zurich Instruments HF2LI). Even though the experimental deflection signal spectrum is subject to noise [123, 50, 124], the spectral components due to the voltage modulation can be easily identified. The signal  $V_A^{f_{\text{exc}} \pm f_{\text{el}}}$  at side-band frequency  $f_{\text{exc}} \pm f_{\text{el}}$  contains the CFM signal, while further information on the capacitance between tip and sample support are contained in the signal  $V_A^{f_{\text{exc}} \pm 2f_{\text{el}}}$  at side-band frequency  $f_{\text{exc}} \pm 2f_{\text{el}}$ .

In this CFM implementation, the signals  $V_A^{f_{\text{exc}} \pm f_{\text{el}}}$  and  $V_A^{f_{\text{exc}} \pm 2f_{\text{el}}}$  at frequencies  $f_{\text{exc}} \pm f_{\text{el}}$  and  $f_{\text{exc}} \pm 2f_{\text{el}}$  are measured with side-band detection using two separate

### 3. NC-AFM principle and setup

Lock-In amplifiers LIA 1 and LIA 2. Because the oscillation frequencies of both signals are related to  $f_{\text{exc}}$ , they constantly change according to the changes of  $f_{\text{exc}}$  due to the current tip-sample interaction. Therefore, the deflection signal  $V_{\text{sig}}^{f_{\text{el}}}(t)$  is demodulated at the current excitation frequency  $f_{\text{exc}}$  by multiplying it with a reference oscillation  $\cos(2\pi f_{\text{exc}}t)$  from the PLL before it is given as input signal to the Lock-In amplifiers. Effectively that demodulation resembles a shift of all spectral components of the deflection signal by  $f_{\text{exc}}$ . Consequently the current excitation frequency  $f_{\text{exc}}$  of the cantilever permanently is the zero-frequency in the demodulated deflection signal  $V_{\text{sig}}^{f_{\text{el}}}(t) \cos(2\pi f_{\text{exc}}t)$ . Hence the signals at  $f_{\text{exc}} \pm f_{\text{el}}$  and  $f_{\text{exc}} \pm 2f_{\text{el}}$  now are fixed at frequencies  $f_{\text{el}}$  and  $2f_{\text{el}}$  of the demodulated signal which is input to the Lock-In amplifiers LIA 1 and LIA 2. These then can detect the signals  $V_{\text{A}}^{f_{\text{exc}} \pm f_{\text{el}}}$  and  $V_{\text{A}}^{f_{\text{exc}} \pm 2f_{\text{el}}}$  at reference frequencies  $f_{\text{el}}$  and  $2f_{\text{el}}$  independent of the excitation frequency  $f_{\text{exc}}$ .

Technically the CFM implementation for measuring the signal  $V_{\text{A}}^{f_{\text{exc}} \pm f_{\text{el}}}$  is equal to a FM CL-KPFM setup. It is a feedback loop based on the signal  $V_{\text{A}}^{f_{\text{exc}} \pm f_{\text{el}}}$  and its dependency on the applied bias voltage  $V_{\text{bias}}$  and the modulation amplitude voltage  $V_{\text{el}}$ . Within in the feedback loop the signal  $V_{\text{A}}^{f_{\text{res}} \pm f_{\text{el}}}$  is minimized by adjusting  $V_{\text{bias}}$ . To accomplish this, LIA 1 is used in the feedback loop to constantly measure  $V_{\text{A}}^{f_{\text{exc}} \pm f_{\text{el}}}$  at reference frequency  $f_{\text{el}}$  in the demodulated deflection of the PLL output. The detected signal amplitude  $V_{\text{A}}^{f_{\text{exc}} \pm f_{\text{el}}}$  is given to the Kelvin feedback, where the voltage  $V_{\text{bias}}$  is adjusted for minimization of  $V_{\text{A}}^{f_{\text{exc}} \pm f_{\text{el}}}$ . Consequently, the component  $V_{\text{A}}^{f_{\text{exc}} \pm f_{\text{el}}}$  constantly vanishes as seen in Figure 3.4(b). The bias voltage  $V_{\text{bias}} = V_{\text{bias}}^{\text{min}}$  where the signal amplitude  $V_{\text{A}}^{f_{\text{exc}} \pm f_{\text{el}}}$  vanishes is the CFM signal, which yields information on the charges  $q_i$  present in the tip-sample capacitor and the contact potential difference  $V_{\text{CPD}}$  between tip and back electrode. The quantitative theory for evaluating the CFM signal  $V_{\text{bias}}^{\text{min}}$  will be discussed in chapter 7.

The signal  $V_{\text{A}}^{f_{\text{res}} \pm 2f_{\text{el}}}$  is detected by LIA 2 synchronized to the reference frequency  $2f_{\text{el}}$ . This signal is related to the capacitance of the tip-sample capacitor and is dependent on  $V_{\text{el}}$  and independent of  $V_{\text{bias}}$  (see chapter 7). Therefore the signal  $V_{\text{A}}^{f_{\text{res}} \pm 2f_{\text{el}}}$  is not affected directly by an active CFM feedback loop. However, when comparing the signal peaks  $V_{\text{A}}^{f_{\text{res}} \pm 2f_{\text{el}}}$  in Figure 3.4 (a) and (b) a noticeable increase of that signal peak can be observed. This is due to the active  $z_{\text{p}}$ -feedback loop in the *constant frequency-shift* mode. The electrostatic force minimization by the CFM feedback loop equals a decrease of the total tip-sample interaction at the current piezo position  $z_{\text{p}}$  of the tip. For maintaining the frequency shift constant at the given set-point  $\Delta f = \Delta f_{\text{set}}$ , the  $z_{\text{p}}$ -feedback loop consequently reduces the distance between tip and sample causing the increase of the capacitance signal  $V_{\text{A}}^{f_{\text{res}} \pm 2f_{\text{el}}}$ . A vivid example for this effect is the capacitance increase of a plate capacitor which plates are brought closer to each other.

Note, to exclude cross-talk in CFM, it is important, that the side-bands  $f_{\text{res}} +$

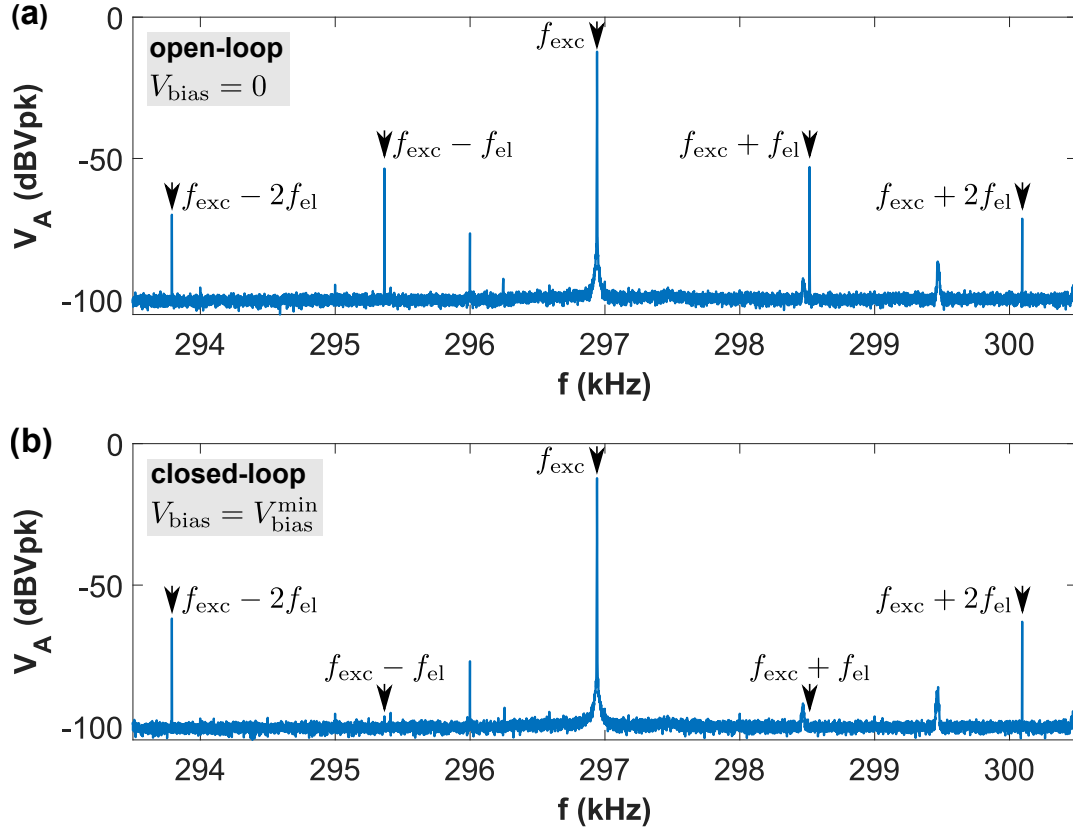


Figure 3.4.: Spectra of the deflection signal (3.3.11) of a *PPP-NCH* silicon cantilever in the Omicron UHV AFM/STM measured in the approached state with active bias modulation (3.3.10) using  $V_{el} = 1$  V and  $f_{el} = 1567$  Hz for two different cases: (a) For an inactive CFM feedback (open-loop) and zero bias voltage  $V_{bias} = 0$ . (b) For an active CFM feedback (closed-loop) adjusting the bias voltage to  $V_{bias} = V_{bias}^{min}$ . Each frequency-spectrum is measured at the PLL input of the RHK R9<sup>TM</sup> with a spectrum analyser (Zurich Instruments HF2LI<sup>TM</sup>) over 20 averages.

$f_{el}$  and  $f_{res} + 2f_{el}$  are outside of the PLL bandwidth detecting the signal at  $f_{res}$ . This is realised by a careful choice of the PLL bandwidth settings and modulation frequency  $f_{el}$ . Typically the bandwidths of the PLL and LIAs are chosen tight, to suppress as much as possible noise and interference (artefact peaks in the spectra of Figure 3.4).



### 3.4. Amplitude calibration and sensor inclination

A key quantity in NC-AFM is the physical oscillation amplitude  $A$  of the sensor, as it is required for the force deconvolution from  $\Delta f(z_p)$  data [47]. Thereby  $A$  is not directly accessible in experiment, but assumed to be proportional to the measured voltage amplitude  $V_A$  with  $S$  being the factor of proportionality. The amplitude then is given by relation

$$A = S \cdot V_A \quad (3.4.12)$$

Experimentally determining a value for  $S$  is referred to as amplitude calibration. Various methods for amplitude calibration have been used in the field of NC-AFM. While some methods rely on a systematic variation of the amplitude voltage set-point  $V_A^{\text{set}}$  in the presence of tip-sample interaction with active  $z_p$ -feedback [125, 126, 127], other methods are based on interferometry [128, 129]. The latter in principle yield very precise distance measurements as they use the wavelength and speed of light as reference, but are prone to systematic error introduced by a misalignment of the laser spot on the cantilever. Furthermore, interferometric methods are not possible for a OBD based NC-AFM as presented here.

From the methods involving the tip-sample interaction the constant  $\gamma$ -method [125] based on an approximation by the normalized frequency shift  $\gamma = k_0 A^{3/2} \Delta f / f_0$  [130] appears conceptually advantageous. In the calibration experiment, the amplitude voltage set-point  $V_A^{\text{set}}$  is stepwise increased, while the given normalized frequency shift set-point  $\gamma_{\text{set}}$  is maintained constant by adjusting the frequency shift set-point  $\Delta f_{\text{set}}$ . In the topography mode, the  $z_p$ -feedback loop adjusts the piezo position  $z_p$  accordingly. The amplitude calibration factor  $S = \Delta z_p / \Delta V_A^{\text{set}}$  is the slope of the graph of piezo positions  $z_p$  as function of the voltage amplitude set-points  $V_A^{\text{set}}$ . Although, it is possible to obtain a fairly precise amplitude calibration with the constant  $\gamma$ -method at excessively high set-points for the normalized frequency shift  $\gamma_{\text{set}}$ , it is not reliable when reasonable set-points  $\gamma_{\text{set}}$  are chosen for preventing a tip-crash into the sample [53] (see chapter 5).

The serious limitations of popular amplitude calibration procedures have led to the development of the force curve alignment (FCA) method [53] in the scope of this work (see chapter 5). The FCA method is based on successive measurements of  $\Delta f(z_p)$  curves for systematically chosen amplitude voltage set-points  $V_A^{\text{set}}$ . The iterative alignment optimisation of the force curves deconvoluted from the measured  $\Delta f(z_p, V_A^{\text{set}})$  by adjusting the value for  $S$  and correcting drift yields inherently the accurate results for the amplitude calibration and drift correction parameters. Beyond that, the FCA method provides the true tip-surface interaction force curve which is the foundation for successful evaluation of distant-dependent CFM-data. Based on a correct amplitude calibration also the physical oscillation amplitudes of the other spectral components caused by the modulated electrostatic force can

### 3.4. Amplitude calibration and sensor inclination

be described. The calibration factor provides the physical capacitance signal  $A_{2fel}$  from the voltage  $V_A^{f_{exc} \pm 2f_{el}}$  as

$$A_{2fel} = S \cdot V_A^{f_{exc} \pm 2f_{el}} \quad (3.4.13)$$

In principle, all amplitude calibration methods are straightforward. However, the typical tilt of the cantilever towards the sample by angle  $\alpha$  as previously indicated in Figure 3.2 has to be addressed, when aiming for the determination of the true physical oscillation amplitude  $A$  of the sensor. Calibration methods which utilise an active  $z_p$ -feedback loop will first hand retrieve the cantilever amplitude  $A_z$  in respect to the  $z$ -axis. However, the physical oscillation direction is parallel to cantilever beam normal which does not align with the  $z$ -axis if the cantilever is tilted towards the sample as sketched in Figure 3.5. From that sketch directly the relation between both amplitudes can be obtained as

$$A_z = A \cos(\alpha) \quad (3.4.14)$$

Considering relations (3.4.12) and (3.4.14) provides the sensitivity factor with respect to the  $z$ -axis

$$S_z = S \cos(\alpha) \quad (3.4.15)$$

Which is the amplitude calibration factor which is actually retrieved by the  $\gamma$ - and FCA-method in case of a cantilever inclination  $\alpha \neq 0$ . Hence, for obtaining the calibration factor  $S$  providing the physical oscillation amplitude  $A$  when multiplied with the current amplitude voltage  $V_A$  the factor  $\cos(\alpha)$  has to be considered. Another effect occurring due to the cantilever inclination is a lateral movement of the tip by

$$\Delta x = A_z \tan(\alpha) \quad (3.4.16)$$

In one oscillation cycle the tip moves laterally by a range of  $2\Delta x$  along the sample surface. While this will have no serious effect for an isotropic surface, above a nano-feature as an adsorbed atom, molecule or atomic cluster, the tip will be affected by lateral force gradients during its oscillation. In this case, the measured  $\Delta f$ -data will not provide the correct tip-sample force when evaluated in respect to the  $z$ -axis as it is done in the fundamental quantitative AFM theory [44] where a non-tilted sensor is considered. Consequently, a neglected cantilever inclination can be an source for systematic error when measuring force curves, especially when the sample surface is not isotropic. However, a post-process amplitude calibration via the FCA method uncovers systematic errors in obtained experimental data (see chapter 5). Furthermore, for considering the effects of an inclined tip oscillation on force measurements the fundamental quantitative AFM theory [44] is enhanced in [58] allowing an arbitrary oscillation direction of the tip. The publication [58] has been produced in the context of this work and can be found in chapter 6.

### 3. NC-AFM principle and setup

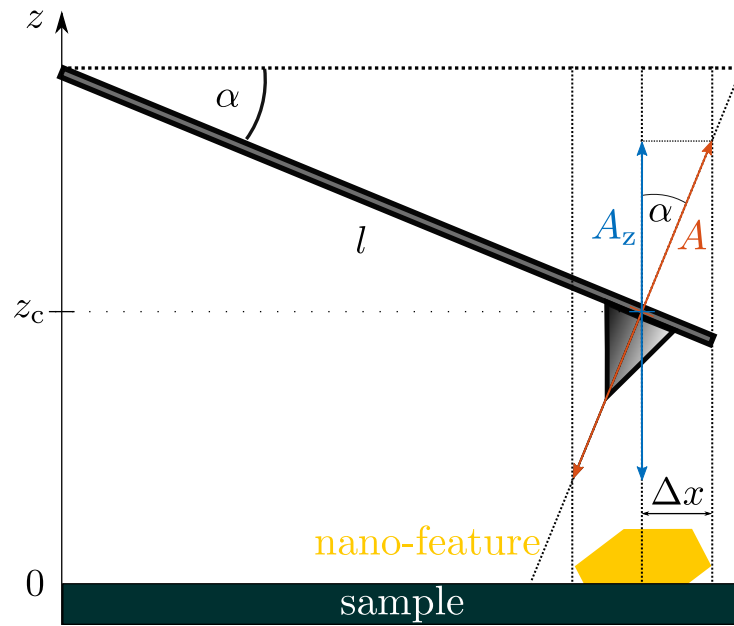


Figure 3.5.: Effect of the cantilever inclination towards the sample. The amplitude  $A_z$  is the projection of the physical oscillation amplitude  $A$  on the  $z$ -axis perpendicular to the sample surface. The lateral movement of the tip from the measurement position above the nano-feature is a function of the physical amplitude  $A$ .

## 4. Quantitative AFM theory

In this chapter, the quantitative AFM theory based on the general approach introduced in [44] is presented demonstrating the derivation of three fundamental AFM equations. These link the measured observables of an AFM experiment and the sensor properties with the physical properties of the tip-sample force. Due to the general formalism, it is possible to quantitatively evaluate measurements taken in any AFM mode based on the three AFM equations [44]. For the derivation of these equations the harmonic approximation is used and it is further assumed that the tip oscillation is exclusively perpendicular to the sample surface ( $A = A_z$ ). Therefore, the tip-sampling path and the data recording path along the piezo axis  $z_p$  are parallel and all described tip-sample forces are normal forces  $F_{ts}^z$ . This chapter is organised as follows: First the general coordinates of NC-AFM will be formally introduced in analogy to [58] where the force sensor is approximated by a harmonic oscillator oscillating along the  $z$ -axis oriented normal to the sample surface. Second, the transfer function for the driven, damped harmonic oscillation of the force sensor in the case of negligible tip-surface interaction is derived. Third, the tip movement in the force field of the sample is described within the harmonic approximation yielding the three AFM equations. The here discussed fundamental AFM theory is expanded in chapter 6 for describing non-parallel tip-sampling and data recording paths.

### 4.1. Coordinates in NC-AFM

A precise definition of the involved probe and sample coordinates as well as the probe dynamical parameters is prerequisite for the quantitative physical understanding of the data acquired with FM NC-AFM. In dynamic AFM, the tip-sample force  $\vec{F}_{ts}$  is measured as a function of the tip-sample position  $\vec{r}_{ts}$  which is usually described in Cartesian coordinates, where the origin is placed on the sample surface in such way that the  $z$ -axis with unit vector  $\vec{e}_z$  is oriented perpendicular to the surface as depicted in Fig. 4.1. The tip-sample distance  $z_{ts}$  is measured along the  $z$ -axis, while lateral movements are described by the  $x$ - and  $y$ -axes. In typical AFM implementations, the force measurement is restricted to nominally measuring

#### 4. Quantitative AFM theory

the normal component of the tip-sample force  $F_{\text{ts}}^z = \vec{F}_{\text{ts}} \cdot \vec{e}_z$  often denoted by  $F_N$ . The ideal force curve is a measurement of  $F_{\text{ts}}^z(z_{\text{ts}})$  at a fixed position  $(x_{\text{ts}}, y_{\text{ts}})$  on the sample surface while the measurement of  $F_{\text{ts}}^z(x_{\text{ts}}, y_{\text{ts}}, z_{\text{ts}})$  is referred to as force mapping and measuring  $F_{\text{ts}}(x_{\text{ts}}, y_{\text{ts}})$  describes imaging in the original sense of force microscopy as a raster scanning microscopy.

In a dynamic measurement of the tip-surface force, the force sensor acts as a high- $Q$  oscillator which elastically responds to  $\vec{F}_{\text{ts}}$  by static and dynamic deflection described by  $\vec{q} = q \cdot \vec{e}_q$  where  $\vec{e}_q$  describes the unit vector along the tip sampling path during oscillation. The tip sampling path describes the path along which the tip periodically moves during oscillation. Typically, this path is assumed to be straight and parallel to  $\vec{e}_z$ . Due to the properties of typical force sensors (see Sec. 3.1) it can be assumed, that the sensor is infinitely stiff in directions perpendicular to  $\vec{e}_q$  and its response is linear along  $\vec{e}_q$ . In that case, the static probe response in interaction follows Hooke's law  $F_{\text{ts}}^z(x_{\text{ts}}, y_{\text{ts}}, z_{\text{ts}}) = kq$ , where  $k$  is the static sensor force constant (3.1.1). In the dynamic mode, the force sensor is excited to oscillate periodically along the  $q$ -axis  $q(t) = q(t + 1/f_{\text{exc}})$  following the excitation frequency  $f_{\text{exc}}$ . Dependent on the given  $f_{\text{exc}}$ , the force sensor has the modal stiffness  $k_n$  with  $(n = 0, 1, 2 \dots)$  (see relation 3.1.5). As the excitation frequency  $f_{\text{exc}}$  in typical operation of dynamic AFM is chosen to be near the eigenfrequency of the fundamental mode  $f_0$ , the modal stiffness of the force sensor is given by  $k_0$  during oscillation.

To bring the tip in the desired interaction range with the surface and to perform the movements required for imaging, force mapping and taking force curves either sample or sensor are attached to coarse and fine positioning elements allowing wide range and precise movement in all directions. The implementation of the positioning system based on piezoelectric elements depends on the respective NC-AFM construction. However, as only the relative positions between sensor and sample surface are of interest in the quantitative AFM theory, generic coordinates can be defined. In Figure 4.1, the respective positioning movements of a sensor in respect to the sample, the sensor oscillation and its response to the tip-surface force are illustrated for the case of parallel tip sampling and data recording paths. Thereby the data recording path is the path along which the oscillating force sensor is moved when taking a force curve. Here the data recording path is assumed to be parallel to the movement direction of the piezo  $z_p$ .

Before any measurement, the sensor assembly is at far away from the sample surface and has to be moved towards the surface by the coarse positioning system. At the end of this coarse approach (Figure 4.1(a)), the piezo rests in a relaxed state at position  $z_{\text{crs}}$  and the tip at its starting position  $z_0$ . In their relaxed state, the  $z$ -piezo and sensor have the length  $l_p^0$  and  $l_s^0$  respectively. For the fine approach (Figure 4.1(b)), a voltage is applied to the  $z$ -piezo causing its extension to the length  $l_p > l_p^0$  that is described by a piezo position  $z_p$  on the separate axis  $z_p$ .

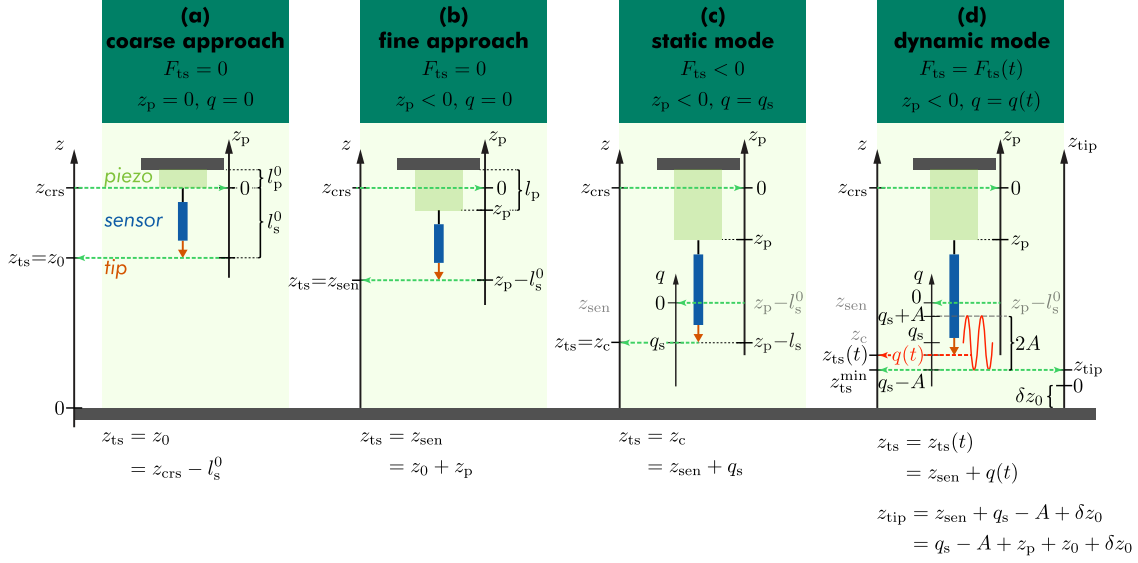


Figure 4.1.: NC-AFM coordinates [58], explanation in text.

with unit vector  $\vec{e}_p$  and with the origin chosen to coincide with  $z_{crs}$  position. Unit vectors  $\vec{e}_z$  and  $\vec{e}_p$  are chosen to point in the same direction so that a piezo extension  $z_p < 0$  results in an approach of the tip towards the sample surface while  $z_p > 0$  indicates a tip retraction. The coarse and fine approach define the sensor position  $z_{sen} = z_0 + z_p$  which is equal to the tip-sample distance  $z_{ts}$  if the force  $F_{ts}$  acting on the tip is unmeasurable small as it is the case for sufficiently large  $z_{ts}$ . Upon further approach, the tip experiences a measurable force resulting in a static sensor displacement  $q_s$  described on the  $q$ -axis with its origin chosen at  $z_{sen}$  (Figure 4.1(c)). Due to the static sensor displacement  $q_s$  the tip moves from  $z_{sen}$  to the tip centre position  $z_c = z_{sen} + q_s$ , which is equal to the new tip-sample distance  $z_{ts}$ . The direction of  $\vec{e}_q$  is chosen parallel to  $\vec{e}_z$ , hence a sensor displacement  $q < 0$  corresponds to a tip movement towards the surface. Note, that the tip centre position  $z_c$  cannot easily be set or determined in experiment for two reasons: The static sensor displacement  $q_s$  is governed by the a priori unknown force curve and smaller than the detection limits of most NC-AFM implementations. In dynamic NC-AFM operation at interaction range, the sensor oscillates with an amplitude  $A$  symmetrically around  $q_s$  with the turning points  $q_s + A$  and  $q_s - A$  (Figure 4.1(d)). The momentary tip position at any time  $t$  is described by the displacement  $q(t)$  and the position  $z_{ts}(t)$ , where  $z_{ts}^{min}$  denotes the position of the lower turning point of the oscillation.

In principal, tip-positions and sensor dynamics can well be described with positions in respect to the  $z$ -axis. Practically, however, this axis is of limited use, because its zero point cannot be defined in a reasonable way. This is due to the fact that neither  $z_{crs}$  and  $l_s^0$  can be determined with atomic scale precision, which would be needed

#### 4. Quantitative AFM theory

for properly taking into account the force curve  $F_{\text{ts}}^z(z_{\text{ts}})$ . Additionally a conceptual difficulty is given in defining the position of the surface at the atomic scale. As every force curve acquired on a surface diverges for  $z_{\text{ts}} \rightarrow 0$  (see section 2.4), one natural choice of the  $z$ -axis origin would be the  $z$ -value approached by the diverging force. This point, however, is not accessible in experiment. Instead, precise values for the piezo position  $z_{\text{p}}$  and the sensor displacement  $q(t)$  are experimentally available. To derive a force-distance curve in a dynamic AFM experiment, the usual procedure is therefore the measurement of the distant-dependent frequency shift  $\Delta f(z_{\text{p}})$  of the sensor excitation frequency  $f_{\text{exc}}$  that results when phase resonance for the sensor oscillation is maintained (see section 3.2) while measuring along the data recording path [99]. The resulting  $\Delta f(z_{\text{p}})$  curve is a convolution of the covered part of the force curve  $F_{\text{ts}}^z(z_{\text{ts}})$  and a kernel depending on the stabilised sensor oscillation amplitude  $A$  [46, 47]. A sophisticated analysis of the  $\Delta f(z_{\text{p}})$  curves measured at different oscillation amplitudes  $A$  yields a precise result for the force curve [53], yet with an arbitrary origin along the  $z$ -axis. In theoretical modelling and analysis of tip-sample interactions, it has been established as a standard to represent force curves as  $F_{\text{ts}}^z = F_{\text{ts}}^z(z_{\text{ts}}^{\text{min}})$  [47]. Due to the practical inaccessibility of  $z_{\text{ts}}^{\text{min}}$  for the representation of experimental force curves, an axis  $z_{\text{tip}}$  that is identical to the  $z$ -axis except for an unknown offset  $\delta z_0$  for the tip starting position is used (see Figure 4.1(d)). A force curve resulting from analysis of measured data can thus be described as  $F_{\text{ts}}^z(z_{\text{tip}})$  where  $z_{\text{tip}} = z_{\text{ts}}^{\text{min}} - \delta z_0$ .

## 4.2. Harmonic oscillator and transfer function

In the previous chapter (section 3.1) various force sensors utilised in NC-AFM have been introduced. However, the utilised force sensor type is a detail of the setup and should not transport enter the general AFM theory. As the oscillation amplitudes used in NC-AFM are so small that a linear response of the displacement to an external force can be expected, each force sensor is effectively a oscillating spring, with the tip mass at its end. Consequently, the oscillation of any force sensor with respect to the  $q$ -axis is mathematically described as a damped, driven harmonic oscillator. For the interaction-free oscillation, the equation of motion is given by

$$m\ddot{q}(t) + kq(t) + \gamma\dot{q}(t) = F_{\text{exc}}(t) \quad (4.2.1)$$

Where  $k$  is the stiffness of the sensor against static deflection in direction of  $q$ ,  $m$  the effective mass of the force sensor and  $\gamma$  the internal damping constant. The externally applied excitation force  $F_{\text{exc}}(t)$  drives the sensor periodically with a frequency  $f_{\text{exc}}$  causing its periodic displacement  $q(t)$  with the same frequency and the phase  $\varphi$  as response. The eigenfrequency of the harmonic oscillator is given by

$$f_0 = \frac{1}{2\pi} \sqrt{\frac{k}{m}} \quad (4.2.2)$$

and its quality factor is described by relation

$$Q_0 = \frac{\sqrt{km}}{\gamma} \quad (4.2.3)$$

Inserting (4.2.2) and (4.2.3) into (4.2.1) and further considering  $k \approx k_0$  yields the relation

$$\frac{k_0}{(2\pi f_0)^2} \ddot{q}(t) + k_0 q(t) + \frac{k_0}{2\pi f_0 Q_0} \dot{q}(t) = F_{\text{exc}}(t) \quad (4.2.4)$$

for the damped, driven and freely oscillating harmonic oscillator containing solely properties which characterise the force sensor as introduced in Sec. 3.1. The stationary solution of equation (4.2.4) can be obtained by a Fourier transformation ansatz [131]

$$\mathcal{F}[g(t)](f) = \frac{1}{\sqrt{2\pi}} \int_{-\infty}^{\infty} g(t) e^{-2\pi i f t} dt \quad (4.2.5)$$

where  $\mathcal{F}[g(t)](f)$  is a functional of the frequency  $f$  describing the Fourier transformation (frequency spectrum) of the time-dependent function  $g(t)$ . Applying the Fourier transformation (4.2.5) allows the consideration of (4.2.4) in the frequency domain as

$$\frac{k_0}{(2\pi f_0)^2} \mathcal{F}[\ddot{q}(t)](f_{\text{exc}}) + k_0 \mathcal{F}[q(t)](f_{\text{exc}}) + \frac{k_0}{2\pi f_0 Q_0} \mathcal{F}[\dot{q}(t)](f_{\text{exc}}) = \mathcal{F}[F_{\text{exc}}(t)](f_{\text{exc}}) \quad (4.2.6)$$

where the following identities regarding Fourier transformations of time derivatives (derivation shown in Appendix A.4) have been used.

$$\mathcal{F}[\dot{g}(t)](f) = 2\pi i f \mathcal{F}[g(t)](f) \quad (4.2.7)$$

$$\mathcal{F}[\ddot{g}(t)](f) = (2\pi i f)^2 \mathcal{F}[g(t)](f) \quad (4.2.8)$$

Equation (4.2.6) can be simplified to

$$\mathcal{F}[q(t)](f_{\text{exc}}) = G_{\text{ho}}(f_{\text{exc}}) \cdot \mathcal{F}[F_{\text{exc}}(t)](f_{\text{exc}}) \quad (4.2.9)$$

where

$$G_{\text{ho}}(f_{\text{exc}}) = \frac{1}{k_0 \left[ \left( 1 - \frac{f_{\text{exc}}^2}{f_0^2} \right) + i \frac{f_{\text{exc}}}{f_0 Q_0} \right]} \quad (4.2.10)$$

is the complex amplitude transfer function of the harmonic oscillator describing the amplitude and phase transfer from the excitation to the oscillator response at the current excitation frequency  $f_{\text{exc}}$ . The transfer function  $G_{\text{ho}}$  depends on the known properties of the oscillator. Equation (4.2.9) shows, that the force sensor oscillation spectrum  $\mathcal{F}[q(t)](f_{\text{exc}})$  depends on both, the externally applied excitation spectrum  $\mathcal{F}[F_{\text{exc}}(t)](f_{\text{exc}})$  and the transfer function  $G_{\text{ho}}(f_{\text{exc}})$ . For harmonic excitation as used in FM NC-AFM, the probe response is a single line spectrum



#### 4. Quantitative AFM theory

representing a harmonic oscillation with amplitude and phase that are the experimental observables. The probe oscillation amplitude is proportional to the absolute value of the complex amplitude transfer function  $G_{\text{ho}}(f_{\text{exc}})$

$$|G_{\text{ho}}(f_{\text{exc}})| = \frac{1}{k_0 \sqrt{\left(1 - \frac{f_{\text{exc}}^2}{f_0^2}\right)^2 + \left(\frac{f_{\text{exc}}}{f_0 Q_0}\right)^2}} \quad (4.2.11)$$

The phase of the harmonic oscillation results from the fraction between the imaginary and real part of  $G_{\text{ho}}(f_{\text{exc}})$  and can be described as

$$\varphi_{\text{ho}} = \arctan2 \left[ -\frac{f_{\text{exc}}}{f_0 Q_0}, 1 - \left(\frac{f_{\text{exc}}}{f_0}\right)^2 \right] = \begin{cases} \arctan \left( \frac{-\frac{f_{\text{exc}}}{f_0 Q_0}}{1 - \left(\frac{f_{\text{exc}}}{f_0}\right)^2} \right) & : f_{\text{exc}} < f_0 \\ -\frac{\pi}{2} & : f_{\text{exc}} = f_0 \\ \arctan \left( \frac{-\frac{f_{\text{exc}}}{f_0 Q_0}}{1 - \left(\frac{f_{\text{exc}}}{f_0}\right)^2} \right) - \pi & : f_{\text{exc}} > f_0 \end{cases} \quad (4.2.12)$$

The definition via the arctan2 function is advantageous, as thus the phase  $\varphi_{\text{ho}}$  is a continuous function of the excitation frequency  $f_{\text{exc}}$ . The amplitude (4.2.11) and phase (4.2.12) as function of the normalised excitation frequency  $f_{\text{exc}}/f_0$  for different quality factors  $Q_0$  are depicted in Figure 4.2 (a) and (b) respectively. The force sensor oscillation amplitude  $|G_{\text{ho}}|(f_{\text{exc}})$  has a maximum if the excitation frequency  $f_{\text{exc}}$  matches the resonance frequency  $f_{\text{res},0}$  which is described by

$$f_{\text{res},0} = f_0 \sqrt{1 - \frac{1}{2Q_0^2}} \quad (4.2.13)$$

As typical quality factors  $Q_0$  of force sensors utilised in NC-AFM are in the magnitude of several thousands (see Sec. 3.1), the resonance frequency  $f_{\text{res},0}$  of the freely oscillating cantilever can be considered as equal to its eigenfrequency  $f_0$ . The height and width of the resonance peak at  $f_{\text{exc}} = f_{\text{res},0}$  is determined by the respective quality factor  $Q_0$  which is related to the full width half maximum  $\Delta f_{\text{FWHM}}$  of the peak via relation

$$Q_0 = \sqrt{3} \frac{f_0}{\Delta f_{\text{FWHM}}} \quad (4.2.14)$$

Hence, small values for  $Q_0$  result in lower, broader resonance peaks while larger values yield higher, sharper peaks. The quality factor of any force sensor can be

determined from the width of its resonance peak and relation (4.2.14). For large values of  $Q_0$ , the phase  $\varphi_{\text{ho}}$  as function of  $f_{\text{exc}}/f_0$  approaches at resonance a sharp step from 0 to  $-\pi$ . For respective smaller values of  $Q_0$ , that step of  $\varphi_{\text{ho}}$  turns into a smooth transition from 0 to  $-\pi$  approached asymptotically.

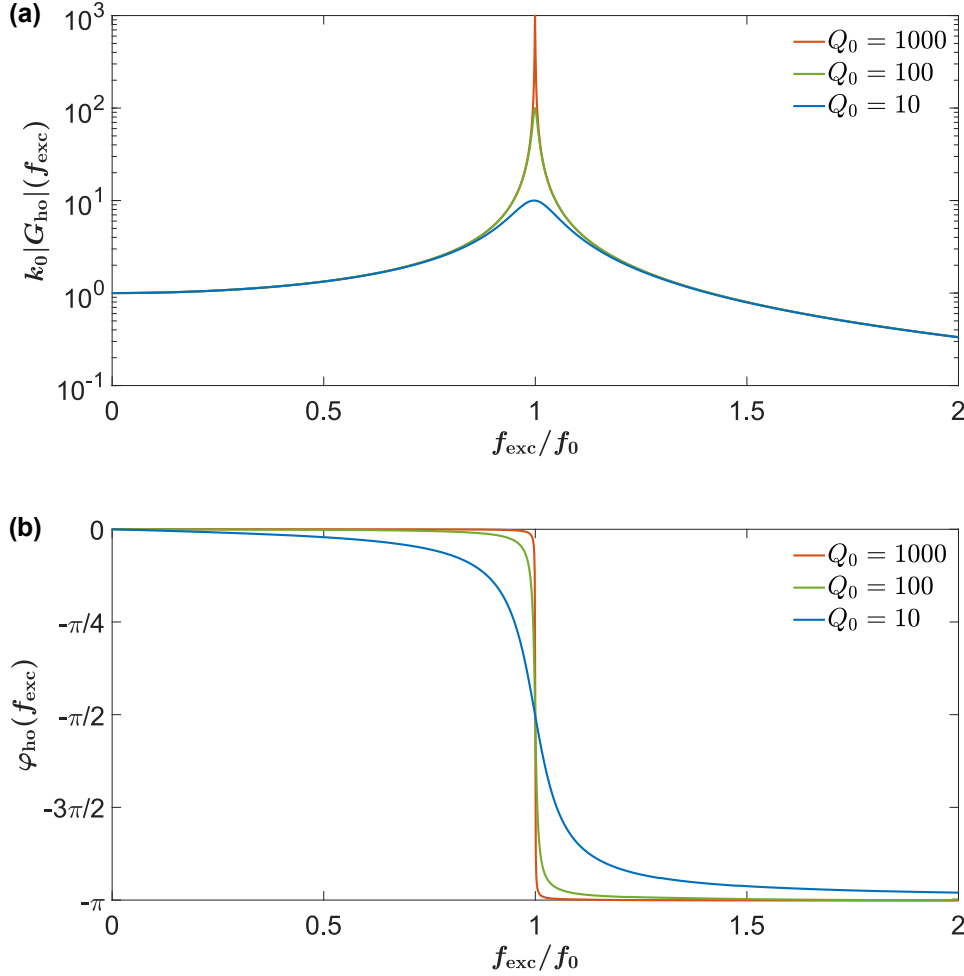


Figure 4.2.: a) Amplitude  $k_0|G_{\text{ho}}|$  and b) phase  $\varphi_{\text{ho}}$  of the driven, damped harmonic oscillator as function of the normalised excitation frequency  $f_{\text{exc}}/f_0$  calculated for three different quality factors  $Q_0$ .

If the excitation parameters are known, the relation (4.2.9) directly yields the sensor displacement  $q(t)$  as solution. For an excitation as

$$F_{\text{exc}}(t) = F_s + F_0 \cos(2\pi f_{\text{exc}}t) \quad (4.2.15)$$

containing a static force component  $F_s$  and an amplitude  $F_0$ , the exact solution for the displacement is given by

$$q(t) = q_s + A \cos(2\pi f_{\text{exc}}t + \varphi) \quad (4.2.16)$$

with the static displacement  $q_s = F_s/k_0$ , the amplitude  $A = |G_{\text{ho}}(f_{\text{exc}})|F_0$  and the phase  $\varphi = \varphi_{\text{ho}}(f_{\text{exc}})$ .

### 4.3. Tip movement in the force field of the sample

In a dynamic experiment, the tip is periodically brought to close proximity to a sample surface and senses the normal tip-sample force  $F_{\text{ts}}^z(z_{\text{ts}}(t), \dot{z}_{\text{ts}}(t))$  during its oscillation [44]. Formally, the interaction is composed of conservative forces parametrised by the tip-sample distance  $z_{\text{ts}}(t)$  (forces as presented in chapter 2) and dissipative effects due to the tip movement described by the tip velocity  $\dot{z}_{\text{ts}}(t)$ . Taking conservative and dissipative tip-sample forces  $F_{\text{ts}}^z(z_{\text{ts}}(t), \dot{z}_{\text{ts}}(t))$  into account, the equation of motion of the force sensor with tip-surface interaction is

$$\frac{k_0}{(2\pi f_0)^2} \ddot{q}(t) + k_0 q(t) + \frac{k_0}{2\pi f_0 Q_0} \dot{q}(t) = F_{\text{exc}}(t) + F_{\text{ts}}^z(z_{\text{ts}}(t), \dot{z}_{\text{ts}}(t)) \quad (4.3.17)$$

Here, the solution as presented in the previous section is no longer expedient, because  $F_{\text{ts}}^z(z_{\text{ts}}(t), \dot{z}_{\text{ts}}(t))$  is dependent on  $q(t)$  via the relation  $z_{\text{ts}}(t) = z_0 + z_p + q(t)$  (see Section 4.1 and Fig. 4.1(d)). Furthermore, due to the non-linear nature of the tip-sample interaction force  $F_{\text{ts}}^z(z_{\text{ts}}(t), \dot{z}_{\text{ts}}(t))$  in respect to the tip-sample distance  $z_{\text{ts}}$ , the oscillation of the tip becomes anharmonic. In consequence, the differential equation (4.3.17) cannot be analytically solved without the knowledge of the tip-sample interaction  $F_{\text{ts}}^z(z_{\text{ts}}(t), \dot{z}_{\text{ts}}(t))$  or using an adequate approximation.

#### 4.3.1. Harmonic approximation

The harmonic approximation is the commonly used approach for solving the equation of motion (4.3.17) and describing the tip movement in the force field of the sample. Historically the harmonic approximation found application under several different names in literature [80, 132, 133, 134, 135, 136]. The first assumption within the harmonic approximation is, that the force sensor is driven exclusively harmonically by the excitation force

$$\boxed{\tilde{F}_{\text{exc}}(t) = F_0 \cos(2\pi f_{\text{exc}} t)} \quad (4.3.18)$$

where  $F_0$  is the excitation force amplitude and the tilde  $\sim$  indicates that the marked variable originates from the harmonic approximation. The second assumption is, that the force sensor oscillation  $q(t)$  in the force field of the sample is has a harmonic time dependence described by

$$\boxed{\tilde{q}(t) = q_s + A \cos(2\pi f_{\text{exc}} t + \varphi)} \quad (4.3.19)$$

Hence, within the harmonic approximation, the tip deflection  $\tilde{q}(t)$  in interaction with the surface is well defined and can fully be described by a limited set of observable parameters, namely, the static deflection  $q_s$ , the oscillation amplitude  $A$ ,

### 4.3. Tip movement in the force field of the sample

current excitation frequency  $f_{\text{exc}}$  and phase  $\varphi$ . Consequently the harmonic approximation effectively acts as a frequency space filter for the force sensor oscillation  $q(t)$  as it provides the probe transfer function at the fundamental mode oscillation at  $f_{\text{exc}}$  while higher harmonic components created by the tip-surface interaction are suppressed. The harmonic approximation is valid if the tip-sample interaction is merely a small disturbance of the harmonic deflection  $\tilde{q}(t)$  (the amplitudes of higher harmonics in  $q(t)$  due to tip-surface interaction are negligibly small). As tip-sample forces measured in NC-AFM are typically small, it is generally accepted that the harmonic approximation well describes the probe dynamics for a non-zero tip-sample interaction.

Considering the deflection  $\tilde{q}(t)$  within the coordinates of NC-AFM (see section 4.1) the tip-sample distance then is given by

$$\begin{aligned} \tilde{z}_{\text{ts}}(t) &= z_0 + z_p + \tilde{q}(t) \\ &= z_0 + z_p + q_s + A \cos(2\pi f_{\text{exc}}t + \varphi) \\ &= z_c + A \cos(2\pi f_{\text{exc}}t + \varphi) \end{aligned} \quad (4.3.20)$$

and the tip-velocity as

$$\dot{\tilde{z}}_{\text{ts}}(t) = \dot{\tilde{q}}(t) = -2\pi f_{\text{exc}}A \sin(2\pi f_{\text{exc}}t + \varphi) \quad (4.3.21)$$

By applying the harmonic approximation, the equation of motion (4.3.17) can be simplified to

$$\frac{k_0}{(2\pi f_0)^2} \ddot{\tilde{q}}(t) + k_0 \tilde{q}(t) + \frac{k_0}{2\pi f_0 Q_0} \dot{\tilde{q}}(t) = \tilde{F}_{\text{exc}}(t) + F_{\text{ts}}^z(\tilde{z}_{\text{ts}}(t), \dot{\tilde{z}}_{\text{ts}}(t)) \quad (4.3.22)$$

Here the tip movement is predefined by  $\tilde{q}(t)$ , but the measurable parameters  $q_s$ ,  $A$ ,  $f_{\text{exc}}$  and  $\varphi$  contained within depend on the a priori unknown tip-sample force  $F_{\text{ts}}^z(\tilde{z}_{\text{ts}}(t), \dot{\tilde{z}}_{\text{ts}}(t))$ . Linking a general description of the a priori unknown tip-sample force  $F_{\text{ts}}^z(\tilde{z}_{\text{ts}}(t), \dot{\tilde{z}}_{\text{ts}}(t))$  via the equation of motion (4.3.22) with the measurable parameters  $q_s$ ,  $A$ ,  $f_{\text{exc}}$  and  $\varphi$  yields three fundamental equations of the quantitative AFM theory [44]. These derivations will be shown in the following, starting with the general description of the tip-sample force  $F_{\text{ts}}^z(\tilde{z}_{\text{ts}}(t), \dot{\tilde{z}}_{\text{ts}}(t))$  probed by the harmonically oscillating tip.

### 4.3.2. Harmonic tip oscillation and force field model

In this section the tip oscillation in a model force field within the harmonic approximation is exemplified for discussing the general properties of the a priori unknown tip-sample force  $F_{\text{ts}}^z(\tilde{z}_{\text{ts}}(t), \dot{\tilde{z}}_{\text{ts}}(t))$  which the tip senses on its path  $(\tilde{z}_{\text{ts}}(t), \dot{\tilde{z}}_{\text{ts}}(t))$ . Normally, the tip-sample force  $F_{\text{ts}}^z(\tilde{z}_{\text{ts}}(t), \dot{\tilde{z}}_{\text{ts}}(t))$  defines the parameters  $q_s$ ,  $A$ ,  $f_{\text{exc}}$  and  $\varphi$  of the tip oscillation described by  $\tilde{z}_{\text{ts}}(t)$  and  $\dot{\tilde{z}}_{\text{ts}}(t)$ . However, at this point, the three AFM equations which solve the equation of motion (4.3.22) and link the tip-sample force  $F_{\text{ts}}^z(\tilde{z}_{\text{ts}}(t), \dot{\tilde{z}}_{\text{ts}}(t))$  with the oscillation parameters are not derived yet. Therefore, in this example, the tip oscillation parameters required by  $\tilde{z}_{\text{ts}}(t)$  and  $\dot{\tilde{z}}_{\text{ts}}(t)$  are not calculated from the model force, but instead are set to predefined values assuming an equilibrium state with the model force. The assumed parameters for the tip movement in the force field are listed in Table 4.1. First, the tip movement described by the tip-sample distance  $\tilde{z}_{\text{ts}}(t)$  and  $\dot{\tilde{z}}_{\text{ts}}(t)$  is discussed alone, and subsequently the model force field is introduced for discussing the sampled force  $F_{\text{ts}}^z(\tilde{z}_{\text{ts}}(t), \dot{\tilde{z}}_{\text{ts}}(t))$ . In Figure 4.3(a) the tip position  $\tilde{z}_{\text{ts}}(t)$  and (b) the tip velocity  $\dot{\tilde{z}}_{\text{ts}}(t)$  as function of time as well as (c) the tip path in the  $\dot{\tilde{z}}_{\text{ts}}(t)$ - $\tilde{z}_{\text{ts}}(t)$  plane for one cycle  $1/f_{\text{exc}}$  of the harmonic tip oscillation are depicted. The assumed parameters for calculation can be found in Table 4.1.

| <b>tip oscillation <math>\tilde{z}_{\text{ts}}(t)</math></b> |         |
|--|---------|
| $z_c$  | 4 nm    |
| $A$  | 2 nm    |
| $f_{\text{exc}}$   | 300 kHz |

Table 4.1.: Parameters used for calculation of the harmonic tip oscillation.

The tip-sample distance  $\tilde{z}_{\text{ts}}(t)$  as function of time (Figure 4.3(a)) can be separated via the tip velocity  $\dot{\tilde{z}}_{\text{ts}}(t)$  into two phases, namely the approach phase (blue) and retract phase (green). In the approach phase the tip velocity is negative  $\dot{\tilde{z}}_{\text{ts}} \leq 0$  (see Figure 4.3(b)), here the tip moves towards the lower turning point  $z_c - A$  of its oscillation reducing its distance  $z_{\text{ts}}(t)$  to the sample (see Figure 4.3(a)). In return, a positive tip velocity  $\dot{\tilde{z}}_{\text{ts}} \geq 0$  resembles the retract phase from the sample surface, as here the tip moves away from the sample increasing the tip-sample distance  $z_{\text{ts}}(t)$ . In the  $\dot{\tilde{z}}_{\text{ts}}$ - $\tilde{z}_{\text{ts}}$  plane, the tip movement over one oscillation cycle  $1/f_{\text{exc}}$  is an ellipsoid with its centre at  $[\tilde{z}_{\text{ts}}, \dot{\tilde{z}}_{\text{ts}}] = [z_c, 0]$  that is drawn as a circle by the choice of scaling in Figure 4.3(c). On this ellipsoidal path the tip-sample force  $F_{\text{ts}}^z(\tilde{z}_{\text{ts}}(t), \dot{\tilde{z}}_{\text{ts}}(t))$  is probed by the tip.

For exemplification of a equilibrium state oscillation of the tip in interaction, it can be assumed that the force field of the sample  $F_{\text{ts}}^z(z_{\text{ts}}, \dot{z}_{\text{ts}})$  is a mathematically smooth function in respect to  $z_{\text{ts}}$  and  $\dot{z}_{\text{ts}}$  [44]. Following Borel's lemma [131] the

### 4.3. Tip movement in the force field of the sample

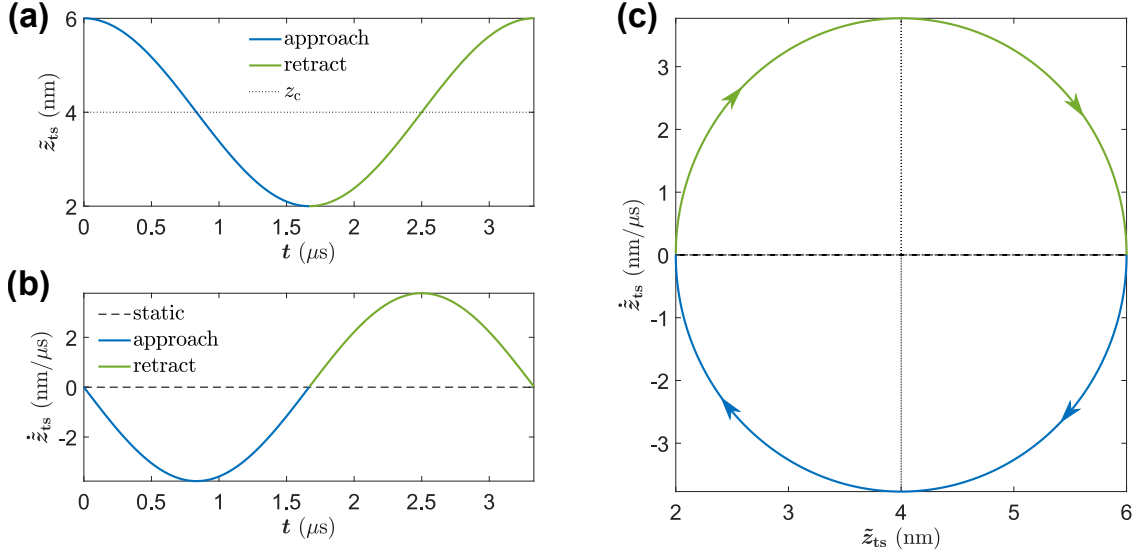


Figure 4.3.: Movement of the tip during harmonic oscillation. (a) Tip-sample distance  $\tilde{z}_{ts}(t)$  and (b) tip velocity  $\dot{\tilde{z}}_{ts}(t)$  as function of time  $t$  as well as the (c) tip path in the  $\dot{\tilde{z}}_{ts}(t)$ - $\tilde{z}_{ts}(t)$  plane for one cycle  $1/f_{\text{exc}}$  of the harmonic tip oscillation. The movement consist of two phases, the approach phase (blue) and the retract phase (green) differentiated by the different sign of the tip velocity  $\dot{\tilde{z}}_{ts}(t)$ . The static case for  $\dot{\tilde{z}}_{ts} = 0$  is indicated by a black dashed line. Parameters for calculation are shown in Table 4.1.

tip-sample force, as every other smooth function, can be developed in a Taylor series as

$$F_{ts}^z(z_{ts}, \dot{z}_{ts}) = F_{ts}^z(z_{ts}) + \sum_{n=1}^{\infty} c_n \dot{z}_{ts}^n \quad (4.3.23)$$

Here the  $n = 0$  term is the conservative distant-dependent static tip-sample force  $F_{ts}^z(z_{ts})$  which is independent of  $\dot{z}_{ts}$ . The rest of the polynomial describes the force contributions dependent on the tip velocity  $\dot{z}_{ts}$ . Considering the power of  $\dot{z}_{ts}$ , the terms of that polynomial can be separated into even and odd contributions with respect to  $\dot{z}_{ts}$ . The even contributions will be indifferent during approach and retract phase of the tip, while the odd contributions will change their sign dependent on the direction of the tip velocity  $\dot{z}_{ts}$ .

To exemplify the effect of both contributions, an arbitrary force field  $F_{ts}^z(z_{ts}, \dot{z}_{ts})$  is calculated based on the Taylor series (4.3.23). The static force  $F_{ts}^z(z_{ts})$  is modelled by  $F_{ts}^{\text{model1}}(z_{ts})$  (see equation 2.4.33) using the parameters listed in Table 2.6. The remaining polynomial is terminated after  $n = 3$  for convenience and the coefficients  $c_1$ ,  $c_2$  and  $c_3$  are arbitrarily chosen to the values as listed in Table 4.2. The resulting force field  $F_{ts}^z(z_{ts}, \dot{z}_{ts})$  contains an equal number of even and odd terms with respect to  $\dot{z}_{ts}$ .

| <b>tip velocity coefficients</b> |                                    |
|----------------------------------|------------------------------------|
| $c_1$                            | $1 \text{ nN s m}^{-1}$            |
| $c_2$                            | $30 \text{ nN s}^2 \text{ m}^{-2}$ |
| $c_3$                            | $5 \text{ }\mu\text{N s m}^{-3}$   |

Table 4.2.: Parameters used for calculation of the force field  $F_{\text{ts}}^z(z_{\text{ts}}, \dot{z}_{\text{ts}})$ .

In Figure 4.4(a) the force field  $F_{\text{ts}}^z(z_{\text{ts}}, \dot{z}_{\text{ts}})$  is shown as function of tip-sample distance  $z_{\text{ts}}$  and the tip-velocity  $\dot{z}_{\text{ts}}$  (grey surface plot). The path of the conservative static force  $F_{\text{ts}}^z(z_{\text{ts}})$  (as known from Fig. 2.7) is indicated by an orange line. The tip oscillates harmonically (as described before in Fig. 4.3(c)) in the force field of the sample  $F_{\text{ts}}^z(z_{\text{ts}}, \dot{z}_{\text{ts}})$  sensing the interaction force  $F_{\text{ts}}^z(\tilde{z}_{\text{ts}}(t), \dot{\tilde{z}}_{\text{ts}}(t))$  on its ellipsoid path described by  $\tilde{z}_{\text{ts}}(t)$  and  $\dot{\tilde{z}}_{\text{ts}}(t)$ . As the probed tip-sample force on the tip path  $F_{\text{ts}}^z(\tilde{z}_{\text{ts}}(t), \dot{\tilde{z}}_{\text{ts}}(t))$  is a function of  $\tilde{z}_{\text{ts}}(t)$  and  $\dot{\tilde{z}}_{\text{ts}}(t)$  which are given within the harmonic approximation by (4.3.20) and (4.3.21) two general properties can be noted here. One, the sampled tip-sample force  $F_{\text{ts}}^z(\tilde{z}_{\text{ts}}(t), \dot{\tilde{z}}_{\text{ts}}(t))$  is a periodic function of time  $t$  with the period  $T = 1/f_{\text{exc}}$ . The second property of the probed tip-sample force  $F_{\text{ts}}^z(\tilde{z}_{\text{ts}}(t), \dot{\tilde{z}}_{\text{ts}}(t))$  results, when considering the equation of motion (4.3.22). As the harmonic oscillation of the tip in the sample force field follows the excitation force  $\tilde{F}_{\text{exc}}(t)$  with the phase shift  $\varphi$ , the probed tip-sample force  $F_{\text{ts}}^z(\tilde{z}_{\text{ts}}(t), \dot{\tilde{z}}_{\text{ts}}(t))$  has to have the same phase shift  $\varphi$  in respect to the excitation.

Dependent on the respective symmetry of the sample force field  $F_{\text{ts}}^z(z_{\text{ts}}, \dot{z}_{\text{ts}})$  with respect to the tip velocity  $\dot{z}_{\text{ts}}$ , the sampled interaction force  $F_{\text{ts}}^z(\tilde{z}_{\text{ts}}(t), \dot{\tilde{z}}_{\text{ts}}(t))$  during approach phase  $\dot{\tilde{z}}_{\text{ts}}(t) < 0$  and retract phase  $\dot{\tilde{z}}_{\text{ts}}(t) > 0$  can differ from each other. To clarify this, the sampled force  $F_{\text{ts}}^z(\tilde{z}_{\text{ts}}(t), \dot{\tilde{z}}_{\text{ts}}(t))$  in the  $[z_{\text{ts}}, \dot{z}_{\text{ts}} = 0, F_{\text{ts}}^z(z_{\text{ts}})]$ -plane of the conservative force has to be considered as shown in Figure 4.4(b). Here, the interaction force sampled on the approach path  $F_{\text{ts}}^z(\tilde{z}_{\text{ts}}(t), \dot{\tilde{z}}_{\text{ts}}(t) < 0)$  strongly differs from the interaction force sampled on the retract path  $F_{\text{ts}}^z(\tilde{z}_{\text{ts}}(t), \dot{\tilde{z}}_{\text{ts}}(t) > 0)$ . The consequence is a hysteresis of the sampled force  $F_{\text{ts}}^z(\tilde{z}_{\text{ts}}(t), \dot{\tilde{z}}_{\text{ts}}(t))$  between the turning points  $z_c - A$  and  $z_c + A$  of the tip oscillation. This yields dissipative effects, as the enclosed area  $\oint F_{\text{ts}}^z(\tilde{z}_{\text{ts}}(t), \dot{\tilde{z}}_{\text{ts}}(t)) dz_{\text{ts}}$  in between approach and retract path of the sampled force  $F_{\text{ts}}^z(\tilde{z}_{\text{ts}}(t), \dot{\tilde{z}}_{\text{ts}}(t))$  is the dissipated energy during each oscillation cycle.

The strength of those dissipative effects depends on the symmetry of the force field  $F_{\text{ts}}^z(z_{\text{ts}}, \dot{z}_{\text{ts}})$  as a function of  $\dot{z}_{\text{ts}}$ . If there are no odd components with respect to  $\dot{z}_{\text{ts}}$  in the force field  $F_{\text{ts}}^z(z_{\text{ts}}, \dot{z}_{\text{ts}})$ , the sampled interactions on approach and retract path are equal. This is exemplified in Figure 4.4(c), where the sampled force  $F_{\text{ts}}^z(\tilde{z}_{\text{ts}}(t), \dot{\tilde{z}}_{\text{ts}}(t))$  in the  $[z_{\text{ts}}, \dot{z}_{\text{ts}} = 0, F_{\text{ts}}^z(z_{\text{ts}})]$ -plane for a tip oscillation in a force field  $F_{\text{ts}}^z(z_{\text{ts}}, \dot{z}_{\text{ts}})$  without any odd contributions ( $c_1 = 0$  and  $c_2 = 0$ ) is depicted. Here, approach and retract path are identical which means that the enclosed area and dissipated

### 4.3. Tip movement in the force field of the sample

energy are zero. Note, however, that the sampled force  $F_{\text{ts}}^z(\tilde{z}_{\text{ts}}(t), \dot{\tilde{z}}_{\text{ts}}(t))$  slightly differs from the static force  $F_{\text{ts}}^z(z_{\text{ts}}, 0)$  due to the even force contribution by the tip velocity  $\dot{\tilde{z}}_{\text{ts}}(t)$ . The result of Figure 4.4(c) indicates, that the odd contributions with respect to  $\dot{\tilde{z}}_{\text{ts}}$  in the force field  $F_{\text{ts}}^z(z_{\text{ts}}, \dot{z}_{\text{ts}})$  of the previous example shown in Figure 4.4(b) are responsible for the dissipative effects.

In general, the force field and thus the probed tip-sample force  $F_{\text{ts}}^z(\tilde{z}_{\text{ts}}(t), \dot{\tilde{z}}_{\text{ts}}(t))$  is a sum of both, even and odd contributions [137, 138, 139, 44]

$$F_{\text{ts}}^z(\tilde{z}_{\text{ts}}(t), \dot{\tilde{z}}_{\text{ts}}(t)) = F_{\text{even}}(\tilde{z}_{\text{ts}}(t), \dot{\tilde{z}}_{\text{ts}}(t)) + F_{\text{odd}}(\tilde{z}_{\text{ts}}(t), \dot{\tilde{z}}_{\text{ts}}(t)) \quad (4.3.24)$$

Where  $F_{\text{even}}$  contains all force contributions to the tip-sample force which are even in respect to  $\dot{\tilde{z}}_{\text{ts}}$  yielding

$$F_{\text{even}}(\tilde{z}_{\text{ts}}, \dot{\tilde{z}}_{\text{ts}}) = F_{\text{ts}}^z(\tilde{z}_{\text{ts}}, -\dot{\tilde{z}}_{\text{ts}}) \quad (4.3.25)$$

and  $F_{\text{odd}}$  contains all force contributions which are odd in respect to  $\dot{\tilde{z}}_{\text{ts}}$  providing

$$F_{\text{odd}}(\tilde{z}_{\text{ts}}(t), \dot{\tilde{z}}_{\text{ts}}(t)) = -F_{\text{odd}}(\tilde{z}_{\text{ts}}, -\dot{\tilde{z}}_{\text{ts}}) \quad (4.3.26)$$

The even and odd decomposition of the probed tip-sample force  $F_{\text{ts}}^z(\tilde{z}_{\text{ts}}(t), \dot{\tilde{z}}_{\text{ts}}(t))$  as shown in relation (4.3.24) is in line with the general mathematical theorem, that every function can be expressed uniquely as sum of an even and odd functions [131]. Thereby, however, the terms  $F_{\text{even}}$  and  $F_{\text{odd}}$  are a mathematical description and do not strictly resemble the separation in conservative and dissipative forces [137, 138, 139, 44]. Based on the periodicity of  $F_{\text{ts}}^z(\tilde{z}_{\text{ts}}(t), \dot{\tilde{z}}_{\text{ts}}(t))$  and its parity decomposition (4.3.24) into  $F_{\text{even}}$  and  $F_{\text{odd}}$  the solution ansatz for the equation of motion (4.3.22) is developed in the next section.

#### 4.3.3. Ansatz for solving the equation of motion

The probed tip-sample force  $F_{\text{ts}}^z(\tilde{z}_{\text{ts}}(t), \dot{\tilde{z}}_{\text{ts}}(t))$  on the tip path is a priori unknown. However, due to its sampling,  $F_{\text{ts}}^z(\tilde{z}_{\text{ts}}(t), \dot{\tilde{z}}_{\text{ts}}(t))$  is a periodic function with frequency  $f_{\text{exc}}$  and as such can be generally expressed as a Fourier series [44]

$$F_{\text{ts}}^z(\tilde{z}_{\text{ts}}(t), \dot{\tilde{z}}_{\text{ts}}(t)) = F_{\text{even}}^{(0)} + \sum_{n=1}^{\infty} F_{\text{even}}^{(n)} \cos(2\pi n f_{\text{exc}} t + \varphi) + \sum_{n=1}^{\infty} F_{\text{odd}}^{(n)} \sin(2\pi n f_{\text{exc}} t + \varphi) \quad (4.3.27)$$

The phase  $\varphi$  accounts for the phase the tip oscillation and tip-sample force (4.3.24) sampled by it have in relation to the driving force  $\tilde{F}_{\text{exc}}(t)$ . The zeroth order  $n = 0$  of the Fourier series considers a time-independent constant force offset of the sampled



#### 4. Quantitative AFM theory

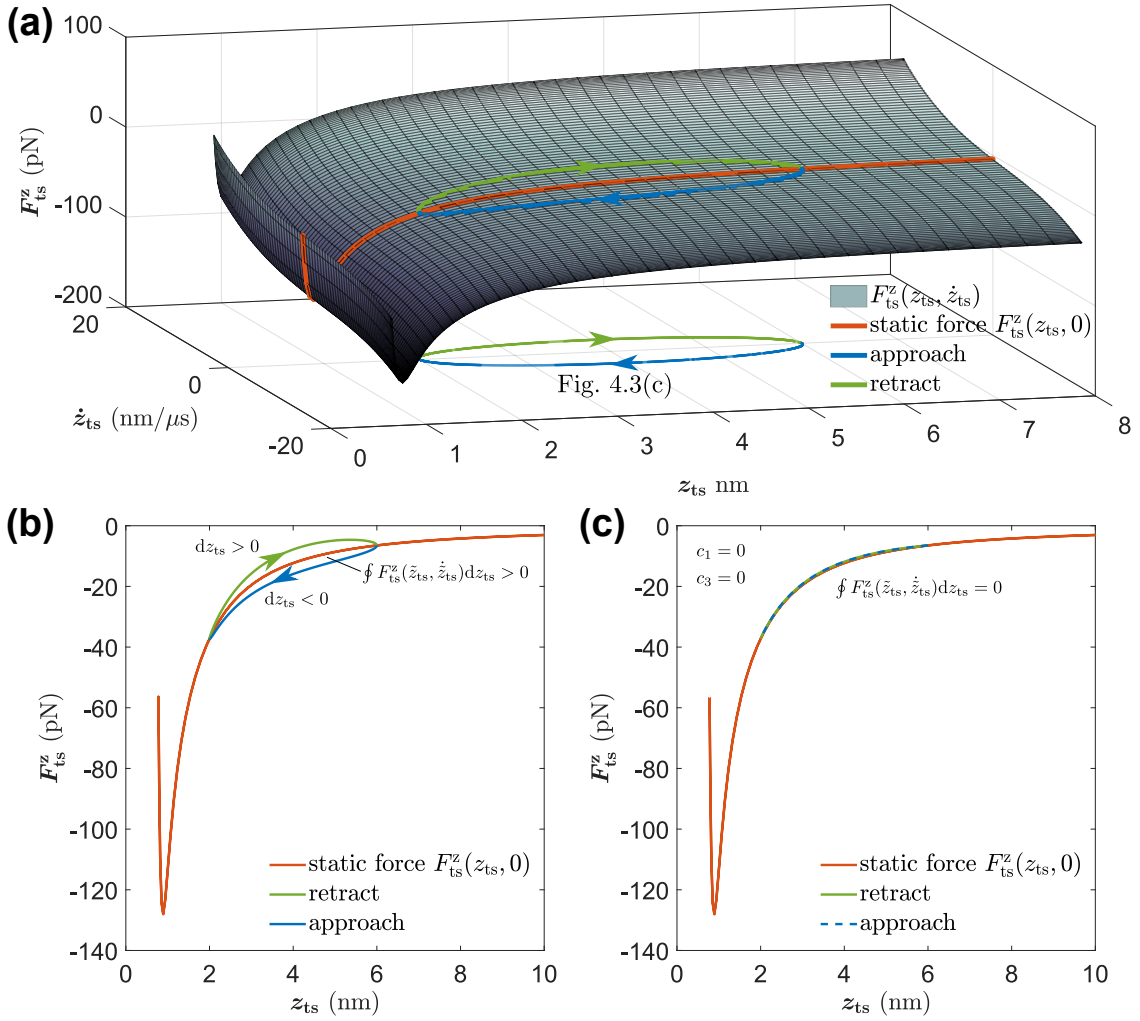


Figure 4.4.: Exemplification of the harmonic tip oscillation in the normal force field  $F_{\text{ts}}^z(\tilde{z}_{\text{ts}}(t), \dot{\tilde{z}}_{\text{ts}}(t))$  of the sample (a) as function of the tip-sample distance  $z_{\text{ts}}$  and the tip velocity  $\dot{z}_{\text{ts}}$  and (b) its projection to the  $[z_{\text{ts}}, \dot{z}_{\text{ts}} = 0, F_{\text{ts}}^z]$ -plane. For comparison, in (c) the  $[z_{\text{ts}}, \dot{z}_{\text{ts}} = 0, F_{\text{ts}}^z]$ -projection of the tip oscillation for a force field  $F_{\text{ts}}^z(\tilde{z}_{\text{ts}}(t), \dot{\tilde{z}}_{\text{ts}}(t))$  without the odd contributions  $c_1$  and  $c_3$ . The paths of the approach phase  $\dot{z}_{\text{ts}} \leq 0$  and retract phase  $\dot{z}_{\text{ts}} \geq 0$  of the tip oscillation in the force field  $F_{\text{ts}}^z(\tilde{z}_{\text{ts}}(t), \dot{\tilde{z}}_{\text{ts}}(t))$  is indicated by a blue or a green line respectively where an arrow indicates the movement direction (see also Figure 4.3(c)). The conservative static force  $F_{\text{ts}}^z(z_{\text{ts}}) = F_{\text{ts}}^{\text{model}1}(z_{\text{ts}})$  is indicated by an orange line. Parameters used for calculation of the tip movement and force field  $F_{\text{ts}}^z(\tilde{z}_{\text{ts}}(t), \dot{\tilde{z}}_{\text{ts}}(t))$  are listed in Table 4.1 and in Table 2.6 respectively.

tip-sample force  $F_{\text{ts}}$  which per definition is even. The coefficients for  $n \geq 1$  are given by the Fourier series definition [131] and are expressed via the sampled tip-sample

### 4.3. Tip movement in the force field of the sample

force on the tip path  $F_{\text{ts}}(\tilde{z}_{\text{ts}}(t), \dot{\tilde{z}}_{\text{ts}}(t))$  as

$$F_{\text{even}}^{(n)} = \lim_{T \rightarrow \infty} \frac{2}{T} \int_0^T F_{\text{ts}}^z(\tilde{z}_{\text{ts}}(t), \dot{\tilde{z}}_{\text{ts}}(t)) \cos(2\pi n f_{\text{exc}} t + \varphi) dt \quad (4.3.28)$$

and

$$F_{\text{odd}}^{(n)} = \lim_{T \rightarrow \infty} \frac{2}{T} \int_0^T F_{\text{ts}}^z(\tilde{z}_{\text{ts}}(t), \dot{\tilde{z}}_{\text{ts}}(t)) \sin(2\pi n f_{\text{exc}} t + \varphi) dt \quad (4.3.29)$$

Assuming the tip-sample interaction  $F_{\text{ts}}^z(\tilde{z}_{\text{ts}}(t), \dot{\tilde{z}}_{\text{ts}}(t))$  as perfectly periodic in  $1/f_{\text{exc}}$  both relations can be simplified to one cycle, yielding

$$F_{\text{even}}^{(n)} = 2f_{\text{exc}} \int_0^{1/f_{\text{exc}}} F_{\text{ts}}^z(\tilde{z}_{\text{ts}}(t), \dot{\tilde{z}}_{\text{ts}}(t)) \cos(2\pi n f_{\text{exc}} t + \varphi) dt \quad (4.3.30)$$

$$F_{\text{odd}}^{(n)} = 2f_{\text{exc}} \int_0^{1/f_{\text{exc}}} F_{\text{ts}}^z(\tilde{z}_{\text{ts}}(t), \dot{\tilde{z}}_{\text{ts}}(t)) \sin(2\pi n f_{\text{exc}} t + \varphi) dt \quad (4.3.31)$$

Defining the time average for a periodic function  $f(t)$  with period  $T = 1/f_{\text{exc}}$  as

$$\langle f(t) \rangle_t = f_{\text{exc}} \int_0^{1/f_{\text{exc}}} f(t) dt \quad (4.3.32)$$

allows the description of both Fourier coefficients (4.3.30) and (4.3.31) in a shorter form:

$$F_{\text{even}}^{(n)} = 2 \left\langle F_{\text{ts}}^z(\tilde{z}_{\text{ts}}(t), \dot{\tilde{z}}_{\text{ts}}(t)) \cos(2\pi n f_{\text{exc}} t + \varphi) \right\rangle_t \quad (4.3.33)$$

and

$$F_{\text{odd}}^{(n)} = 2 \left\langle F_{\text{ts}}^z(\tilde{z}_{\text{ts}}(t), \dot{\tilde{z}}_{\text{ts}}(t)) \sin(2\pi n f_{\text{exc}} t + \varphi) \right\rangle_t \quad (4.3.34)$$

Inserting relation (4.3.24) for the sampled tip-sample force into these relations shows the validity of these definitions, as in (4.3.33) the product between tip-sample force and the cosine function extracts exclusively the even force contributions over the time-average as non-zero. This is also the case for relation (4.3.34) where the product between all odd force contributions and the odd sine function is the only non-zero term within the time-average. The corresponding calculations fully shown in the Appendix A.5.

Note, the simplification of the Fourier coefficients (4.3.28) and (4.3.29) to one oscillation cycle  $1/f_{\text{exc}}$  implies that the here derived solution ansatz (4.3.27) describes the tip-sample force  $F_{\text{ts}}^z(\tilde{z}_{\text{ts}}(t), \dot{\tilde{z}}_{\text{ts}}(t))$  exclusively in equilibrium states, where the tip oscillates harmonically in interaction with fixed parameters  $q_s$ ,  $A$ ,  $f_{\text{exc}}$  and  $\varphi$  (as assumed in the exemplification before). Hence, changes of the tip-sample interaction during measurement are only described within the resulting theory by the difference between equilibrium states before and after the change. Consequently, when measuring the tip sample force, the time at any mapped data point has to be sufficiently large enough so that the force sensor oscillation can adjust to equilibrium state in the currently given interaction.

## 4.4. Derivation of three fundamental AFM equations

The developed formalism is used to derive three fundamental AFM equations linking physical properties of the sampled tip-sample force with measurable observables  $q_s$ ,  $A$ ,  $f_{\text{exc}}$  and  $\varphi$  of the tip oscillation and the sensor properties  $k_0$ ,  $Q_0$ ,  $f_0$  [44]. The first step is to calculate the time-averaged form of these equations by evaluating the Fourier series (4.3.27). Assuming within the harmonic approximation that the amplitudes of all higher harmonics are negligible small, all terms higher than the fundamental mode  $n = 1$  are omitted thereby <sup>1</sup>. Evaluating the remaining Fourier coefficients  $F_{\text{even}}^{(0)}$ ,  $F_{\text{even}}^{(1)}$  and  $F_{\text{odd}}^{(1)}$  using of the equation of motion (4.3.17), the deflection (4.2.16) and excitation (4.3.18) given by the harmonic approximation yields the time-averaged form of the three AFM equations (see in Appendix A.5 and A.6.1 for all derivation steps)

$$\langle F_{\text{even}}(\tilde{z}_{\text{ts}}, \dot{\tilde{z}}_{\text{ts}}) \rangle_t = k_0 q_s \quad (4.4.35)$$

$$\langle F_{\text{even}}(\tilde{z}_{\text{ts}}, \dot{\tilde{z}}_{\text{ts}}) \cdot (\tilde{q} - q_s) \rangle_t = \frac{k_0 A^2}{2} \left[ 1 - \frac{f_{\text{exc}}^2}{f_0^2} \right] - \frac{F_0 A}{2} \cos(\varphi) \quad (4.4.36)$$

$$\langle F_{\text{odd}}(\tilde{z}_{\text{ts}}, \dot{\tilde{z}}_{\text{ts}}) \cdot \dot{\tilde{q}} \rangle_t = \frac{\pi k_0 A^2 f_{\text{exc}}^2}{Q_0 f_0} + \pi f_{\text{exc}} A F_0 \sin(\varphi) \quad (4.4.37)$$

Where (4.4.35) is the static part of the tip-sample interaction, (4.4.36) describes influence of the tip-sample force on the sensor oscillation and (4.4.37) describes the dissipation. All physical properties of the tip-sample interaction in their time-averaged form are expressed via experimental accessible quantities (see Tab. 4.3). While the sensor properties (as introduced in Sec. 3.1) are determined independently before the experiment [110, 120, 112], the measurable observables of the sensor oscillation controlled by the PLL and amplitude control are recorded during experiment. However, due to the time-averages the tip-sample force in relations (4.4.35)-(4.4.37) is a function of time. For determining the tip-sample force these relations thus are of limited use in practice, as in experiment all parameters are measured along the data recording path which is a function of the piezo position  $z_p$ . This can be addressed by transforming each time-average over the oscillation cycle into an spatial-average along the tip sampling path between the turning points  $z_c - A$  and  $z_c + A$  of the tip oscillation. The resulting spatial-average of the tip-sample force is then a function of the oscillation centre position  $z_c$  which is identical to the experimentally accessible piezo position  $z_p$  except for the coordinate zero point. The transformation of all time-averages yields the averaging functions commonly used in AFM, which will be presented in the next section.

---

<sup>1</sup>If higher harmonics of the tip oscillation in the sample force field are of interest, the Fourier series has to be evaluated respectively further.

| time-averaged physical parameters   | measurable observables                  | sensor properties            |
|---|---|------------------------------|
| $\langle F_{\text{even}}(\tilde{z}_{\text{ts}}, \dot{\tilde{z}}_{\text{ts}}) \rangle_t$                         | $q_s$                                   | $k_0$                        |
| $\langle F_{\text{even}}(\tilde{z}_{\text{ts}}, \dot{\tilde{z}}_{\text{ts}}) \cdot (\tilde{q} - q_s) \rangle_t$ | $A, f_{\text{exc}}, \varphi, F_0$       | $k_0, f_0$                   |
| $\langle F_{\text{odd}}(\tilde{z}_{\text{ts}}, \dot{\tilde{z}}_{\text{ts}}) \cdot \dot{\tilde{q}} \rangle_t$    | $A, f_{\text{exc}}, \varphi, F_0$       | $k_0, f_0, Q_0$              |
| of interest in spatial form   | controlled by PLL and amplitude control | determined before experiment |

Table 4.3.: Assignment of the quantities linked by the three fundamental AFM equations.

## 4.5. Averaging functions in AFM and convolution

For transforming the time-averages of all AFM equations (4.4.35)-(4.4.37) into distant-dependent spatial-averages along the tip-sampling path parallel to  $z_{\text{ts}}$  a projection of their time-dependency to  $z_{\text{ts}}$  has to be realised within the integration. Due to the harmonic approximation, the time-dependent tip-movement  $\tilde{z}_{\text{ts}}(t)$  and velocity  $\dot{\tilde{z}}_{\text{ts}}(t)$  are well known as (4.3.20) and (4.3.21). Thus, at any point of time  $t$  within one oscillation cycle  $T = 1/f_{\text{exc}}$  the position  $[\tilde{z}_{\text{ts}}(t), \dot{\tilde{z}}_{\text{ts}}(t), F_{\text{ts}}^z(\tilde{z}_{\text{ts}}(t), \dot{\tilde{z}}_{\text{ts}}(t))]$  on the circular path of the tip in the force field of the sample is well known (see Figure 4.4). The general approach for the projection is, to parametrise this movement directly by the tip-sample distance  $\tilde{z}_{\text{ts}}$  instead of the time  $t$ . However, for any given tip-sample distance  $\tilde{z}_{\text{ts}}$  of the harmonic tip-movement in the sample force field there are two possible tip-velocities  $\dot{\tilde{z}}_{\text{ts}}(\tilde{z}_{\text{ts}})$  and  $-\dot{\tilde{z}}_{\text{ts}}(\tilde{z}_{\text{ts}})$  (see Figure 4.4) which in respect to the tip-sample force generally are not equal  $F_{\text{ts}}^z(\tilde{z}_{\text{ts}}, \dot{\tilde{z}}_{\text{ts}}(\tilde{z}_{\text{ts}})) \neq F_{\text{ts}}^z(\tilde{z}_{\text{ts}}, -\dot{\tilde{z}}_{\text{ts}}(\tilde{z}_{\text{ts}}))$ . This is due to the fact that the tip-sample force  $F_{\text{ts}}^z$  in general contains even and odd contributions in respect to the tip-velocity as shown in relation (4.3.24). Gladly, the first two AFM equations (4.4.35) and (4.4.36) exclusively consider  $F_{\text{even}}$ . In respect to  $F_{\text{even}}$  alone, the tip approach and retract path are equal meaning that both tip-velocities  $\dot{\tilde{z}}_{\text{ts}}(\tilde{z}_{\text{ts}})$  and  $-\dot{\tilde{z}}_{\text{ts}}(\tilde{z}_{\text{ts}})$  provide the same force  $F_{\text{even}}(\tilde{z}_{\text{ts}}, \dot{\tilde{z}}_{\text{ts}}(\tilde{z}_{\text{ts}})) = F_{\text{even}}(\tilde{z}_{\text{ts}}, -\dot{\tilde{z}}_{\text{ts}}(\tilde{z}_{\text{ts}}))$ . Hence for an even force in respect to  $\dot{\tilde{z}}_{\text{ts}}$  can be defined

$$F_{\text{even}}^{\circ}(\tilde{z}_{\text{ts}}(t)) = F_{\text{even}}(\tilde{z}_{\text{ts}}(t), \dot{\tilde{z}}_{\text{ts}}(\tilde{z}_{\text{ts}}(t))) = F_{\text{even}}(\tilde{z}_{\text{ts}}(t), \dot{\tilde{z}}_{\text{ts}}(t)) \quad (4.5.38)$$

Where  $F_{\text{even}}^{\circ}(\tilde{z}_{\text{ts}}(t))$  is the force along the ellipsoidal tip sampling path parametrised exclusively by  $z_{\text{ts}}$ . Based on this definition, the time-averages of the first two AFM equations (4.4.35) and (4.4.36) can be projected to the tip-sampling path parallel to  $z_{\text{ts}}$  (see Appendix A.6.2).

Because the third AFM equation (4.4.37) considers the dissipation due to  $F_{\text{odd}}$ , the direct parametrisation as for the even force (4.5.38) is not possible due to the odd

#### 4. Quantitative AFM theory

parity in  $\dot{\tilde{z}}_{\text{ts}}$ . However, the odd force can be expressed as

$$F_{\text{odd}}(\tilde{z}_{\text{ts}}(t), \dot{\tilde{z}}_{\text{ts}}(t)) = -\gamma_{\text{ts}}(\tilde{z}_{\text{ts}}(t), \dot{\tilde{z}}_{\text{ts}}(t)) \cdot \dot{q}(t) \quad (4.5.39)$$

where the function  $\gamma_{\text{ts}}(\tilde{z}_{\text{ts}}(t), \dot{\tilde{z}}_{\text{ts}}(t))$  is a damping coefficient defined along the tip sampling path, which is an even function in respect to  $\dot{\tilde{z}}_{\text{ts}}$ . In analogy to (4.5.38), the even function  $\gamma_{\text{ts}}(\tilde{z}_{\text{ts}}(t), \dot{\tilde{z}}_{\text{ts}}(t))$  on the tip sampling path can be exclusively parametrised by the tip-sampling path  $\tilde{z}_{\text{ts}}(t)$  yielding

$$\gamma_{\text{ts}}^{\circ}(\tilde{z}_{\text{ts}}(t)) = \gamma(\tilde{z}_{\text{ts}}(t), \dot{\tilde{z}}_{\text{ts}}(\tilde{z}_{\text{ts}}(t))) = \gamma(\tilde{z}_{\text{ts}}(t), \dot{\tilde{z}}_{\text{ts}}(t)) \quad (4.5.40)$$

Inserting the relations (4.5.38) and (4.5.39) with (4.5.40) into the time-average integrals of the AFM equations (4.4.35)-(4.4.37) and transforming those into spatial ones yields two weighted average functions [44] (see full derivations in Appendix A.6.2). These are the cup-average

$$\langle f^{\circ} \rangle_{\cup}(z_c) = \int_{-A}^{+A} f^{\circ}(z_c + z) w_{\cup}(z) dz \quad (4.5.41)$$

with the cup-averaging function

$$w_{\cup}(z) = \frac{1}{\pi \sqrt{A^2 - z^2}} \quad (4.5.42)$$

and the cap-average

$$\langle f^{\circ} \rangle_{\cap}(z_c) = \int_{-A}^{+A} f^{\circ}(z_c + z) w_{\cap}(z) dz \quad (4.5.43)$$

with the cap-averaging function

$$w_{\cap}(z) = \frac{2}{\pi A^2} \sqrt{(A^2 - z^2)} \quad (4.5.44)$$

The spatial weighted averages (4.5.41) and (4.5.43) are line integrals along the tip sampling path projected to  $z_{\text{ts}}$  which is parametrised by  $z$  between the turning points  $-A$  and  $+A$  of the tip oscillation with respect to  $z_c$ . Thereby  $f^{\circ}$  describes the projection of an arbitrary even function  $f$  along the tip sampling path to  $z_{\text{ts}}$ . The coordinate  $z$  is the current position of the tip oscillation within the range  $[z_c - A, z_c + A]$  considered in the integration. While here  $z$  is assumed parallel to  $z_{\text{ts}}$ , in chapter 6 the case of a tip oscillation direction not parallel to  $z_{\text{ts}}$  is discussed. The corresponding averaging functions  $w_{\cup}$  and  $w_{\cap}$  as function of the integration parameter  $z$  are depicted in Fig. 4.5(a) and (b) respectively. The cup-averaging function  $w_{\cup}(z)$  as depicted in Figure 4.5(a) has the shape of a cup in the interval  $z \in [-A, A]$ . The averaging function  $w_{\cup}(z)$  is big at the turning points of the tip at  $z = -A$  and  $z = A$  where the tip velocity is the lowest and becomes small

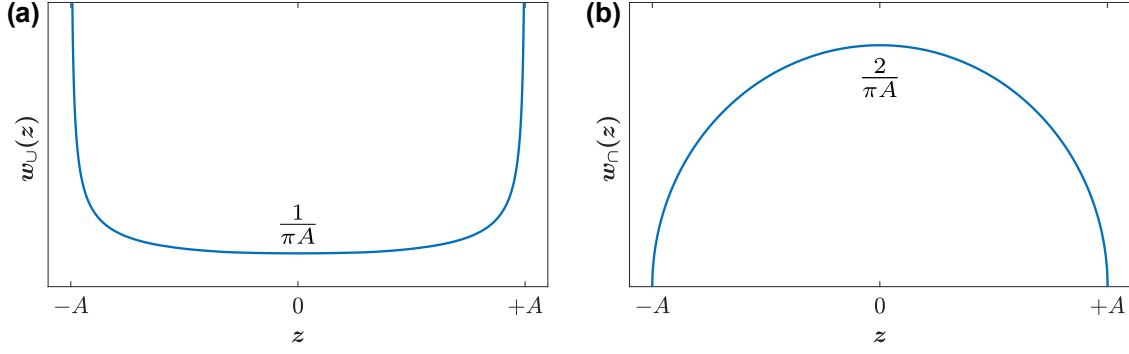


Figure 4.5.: Averaging functions in NC-AFM as function of the integration parameter  $z$ . (a) The cup-averaging function  $w_U(z)$  and (b) the cap-averaging function  $w_O(z)$ . Both functions are only defined in the range  $[-A, A]$  and become complex for  $|z| > A$ .

for high tip-velocities around the oscillation centre  $z = 0$ . In contrast, the cap-averaging function  $w_O(z)$  as depicted in Figure 4.5(b) has the shape of a cap. It is zero at the turning points  $z = -A$  and  $z = A$  and becomes maximal at the centre of oscillation  $z = 0$ . Both averaging functions  $w_U(z)$  and  $w_O(z)$  are only defined within the interval  $z \in [-A, A]$  and become complex for  $|z| > A$ . The cup- and cap averages in the definitions (4.5.41) and (4.5.43) describe a convolution of the function  $f^\circ$  with either  $w_U$  or  $w_O$  as kernel.

The transformation of the time-averages in the equations (4.4.35)-(4.4.37) to the spatial cup- and cap-average yields the final expression of the three AFM equations (Appendix A.6.2)

$$\langle F_{\text{even}}^\circ \rangle_U(z_c) = k_0 q_s \quad (4.5.45)$$

$$\langle k_{\text{ts}}^\circ \rangle_O(z_c) = k_0 \left[ 1 - \frac{f_{\text{exc}}^2}{f_0^2} \right] - \frac{F_0}{A} \cos(\varphi) \quad (4.5.46)$$

$$\langle \gamma_{\text{ts}}^\circ \rangle_O(z_c) = -\frac{k_0}{2\pi f_0 Q_0} - \frac{F_0}{2\pi f_{\text{exc}} A} \sin(\varphi) \quad (4.5.47)$$

where

$$k_{\text{ts}}^\circ(z_c + z) = \frac{dF_{\text{even}}^\circ(z_c + z)}{dz} = \frac{dF_{\text{even}}^\circ(z_{\text{ts}})}{dz_{\text{ts}}} \quad (4.5.48)$$

is the tip-sample force gradient along the tip-sampling path parametrised by  $z$  parallel to  $z_{\text{ts}}$ . Inserting the AFM equations into the equation of motion (4.3.22) enables a similar solution as presented for the free harmonic oscillator as shown in section (4.2) providing an effective amplitude transfer function  $G'_{\text{ho}}(f_{\text{exc}})$  and phase  $\varphi'_{\text{ho}}(f_{\text{exc}})$  (see Appendix A.7). The solution leads the tip oscillation in the sample force field back to a free oscillation of the tip with an effective stiffness  $k'$ , damping  $\gamma'$  and force constant  $F'_s$ .

#### 4. Quantitative AFM theory

In the AFM equations, the physical quantities  $F_{\text{even}}^\circ$ ,  $k_{\text{ts}}^\circ$  and  $\gamma_{\text{ts}}^\circ$  are contained in their convoluted forms  $\langle F_{\text{even}}^\circ \rangle_{\cup}$ ,  $\langle k_{\text{ts}}^\circ \rangle_{\cap}$ ,  $\langle \gamma_{\text{ts}}^\circ \rangle_{\cap}$ . For extracting the physical quantities from the cup- and cap average, the inverse operation called deconvolution is required.

### 4.6. Deconvolution procedure

Several different numerical recipes for deconvolving the cup- and cap-average are proposed in literature [140, 141, 47, 142]. The basis for the deconvolution is to obtain averages for several partly overlapping tip sampling paths in the force  $F_{\text{ts}}^z$  measured along the data recording path. Thereby it is assumed that the overlapping tip-sampling paths are parallel to the data recording path.

Far away from the sample at  $z_\infty$ , the force on the entire path of the tip is zero. Hence, all averages in the AFM equations are also zero. By gradually approaching the sample with overlapping tip sampling paths, at some point the tip will sample on a path where  $F_{\text{ts}}^z$  is not entirely zero. That sampled non-zero  $F_{\text{ts}}^z$  gives rise to a change of the three averages in the AFM equations due to the part of the path in  $F_{\text{ts}}^z$  that has not been sampled before. The difference to the previously sampled path yields the tip-sample force at the lower turning point  $z_c - A$ . Based on this consideration, Sader and Jarvis introduced a formalism [47] from which the following general deconvolution relations [69]

$$f^\circ(z_c - A) = \langle f^\circ \rangle_{\cup}(z_c) - \int_{z_c - A}^{z_\infty} \left[ \sqrt{\frac{2A}{z - (z_c - A)}} \left( \frac{d\langle f^\circ \rangle_{\cup}(z)}{dz} - \sqrt{\frac{2}{\pi}} \frac{d\langle f^\circ \rangle_{\cup}(z + A)}{dz} \right) \right] dz \quad (4.6.49)$$

for the cup-average and

$$f^\circ(z_c - A) = -\frac{\partial}{\partial z_c} \int_{z_c - A}^{z_\infty} \left[ \left( 1 + \sqrt{\frac{A}{64\pi(z - (z_c - A))}} \right) \langle f^\circ \rangle_{\cap}(z) - \sqrt{\frac{A^3}{2(z - (z_c - A))}} \frac{\partial \langle f^\circ \rangle_{\cap}(z)}{\partial z} \right] dz \quad (4.6.50)$$

for the cap-average are derived. Here  $f^\circ$  is the representative function which is retrieved from distant-dependent cup-average data in equation (4.6.49) and from a distant-dependent cap-average data in relation (4.6.50). For a deconvolution it is

required from  $f^\circ$  to be a unique function of the tip-sample distance  $z_{\text{ts}}$  over the entire interval probed by the tip. A criterion which is only fulfilled when  $f^\circ$  is exclusively even in respect to the tip velocity  $\dot{z}_{\text{ts}}$  [44]. The physical quantities  $F_{\text{even}}^\circ$ ,  $k_{\text{ts}}^\circ$  and  $\gamma_{\text{ts}}^\circ$  meet this requirement and therefore can be retrieved from distant-dependent  $\langle F_{\text{even}}^\circ \rangle_{\cup}(z_c)$ ,  $\langle k_{\text{ts}}^\circ \rangle_{\cap}(z_c)$  and  $\langle \gamma_{\text{ts}}^\circ \rangle_{\cap}(z_c)$  data obtained via the AFM equations.

Experimentally, this can be realized by variation of the  $z$ -piezo displacement  $z_p$  for changing the tip-sample distance while the excitation parameters ( $F_0$ ,  $f_{\text{exc}}$ ) and observables ( $q_s$ ,  $A$ ,  $\varphi$ ) are measured. Typically therefore  $z_p$  is reduced from a given interaction point  $\Delta f(z_p) < 0$  to the point of small or vanishing interaction  $\Delta f(z_p) \approx 0$ . Based on the resulting data, the AFM equations (4.5.45)-(4.5.47) are used for calculating  $\langle F_{\text{even}}^\circ \rangle_{\cup}$ ,  $\langle k_{\text{ts}}^\circ \rangle_{\cap}$  and  $\langle \gamma_{\text{ts}}^\circ \rangle_{\cap}$  as function of  $z_p$ . Using the deconvolution relations (4.6.49) and (4.6.50) the physical quantities  $F_{\text{even}}^\circ$ ,  $k_{\text{ts}}^\circ$  and  $\gamma_{\text{ts}}^\circ$  as function of  $z_{\text{tip}}$  can be obtained.

Note, formally the cup- and cap-averages in the AFM equations are denoted by the dependence of  $z_c = z_0 + q_s + z_p$ . In experiment, however, the centre position  $z_c$  typically is not known, because of the inaccessibility of  $q_s$ . Therefore here typically the adjusted piezo position  $z_p$  is directly used as coordinate having an unknown offset. For indicating that unknown offset in deconvoluted experimental data, the coordinate  $z_{\text{tip}}$  is used.

Considering the AFM equations, in theory, it is possible to obtain the even contribution to the tip-sample force  $F_{\text{even}}^\circ$  in two different ways. Either by deconvolving distant-dependent  $\langle F_{\text{even}}^\circ \rangle_{\cup}(z_c)$  data obtained from the first AFM equation (4.5.45) via relation (4.6.49) or by deconvolving  $\langle k_{\text{ts}}^\circ \rangle_{\cap}(z_c)$  from the second AFM equation (4.5.46) via relation (4.6.50) with subsequent integration along  $z_{\text{ts}}$ . As  $q_s$  typically lies below the detectability limits, the latter is the common approach in FM NC-AFM for obtaining the tip-sample force curve  $F_{\text{even}}^\circ(z_{\text{ts}}^{\text{min}})$  and therefore is exemplified in the following.

Figure 4.6 shows the convolution of the tip-sample force gradient  $k_{\text{ts}}^\circ(z_{\text{ts}})$  and its deconvolution into the force curve  $F_{\text{even}}^\circ(z_{\text{ts}}^{\text{min}})$ . The tip-sample force gradient  $k_{\text{ts}}^\circ(z_{\text{ts}})$  as depicted in Figure 4.6(a) is calculated based on the model force  $F_{\text{ts}}^{\text{model1}}(z_{\text{ts}})$  (see equation 2.4.33) and the parameters listed in Table 2.6. For calculating the convoluted cap-average  $\langle k_{\text{ts}}^\circ \rangle_{\cap}(z_c)$  based on relation (4.5.43) as depicted in Figure 4.6(b), an oscillating tip with amplitude  $A = 5$  nm is assumed.

An example for the convolution between  $k_{\text{ts}}^\circ(z_c + z)$  and  $w_{\cap}(z)$  for  $z_c = 6.5$  nm is shown in the insets of Figure 4.6(a). The tip oscillation position  $z$  ranges between  $-A$  and  $A$ , wherewith the tip-sample force gradient data ranges from  $k_{\text{ts}}^\circ(z_c - A)$  to  $k_{\text{ts}}^\circ(z_c + A)$  (black dashed line) around the current centre position  $z_c$  and is multiplied



#### 4. Quantitative AFM theory

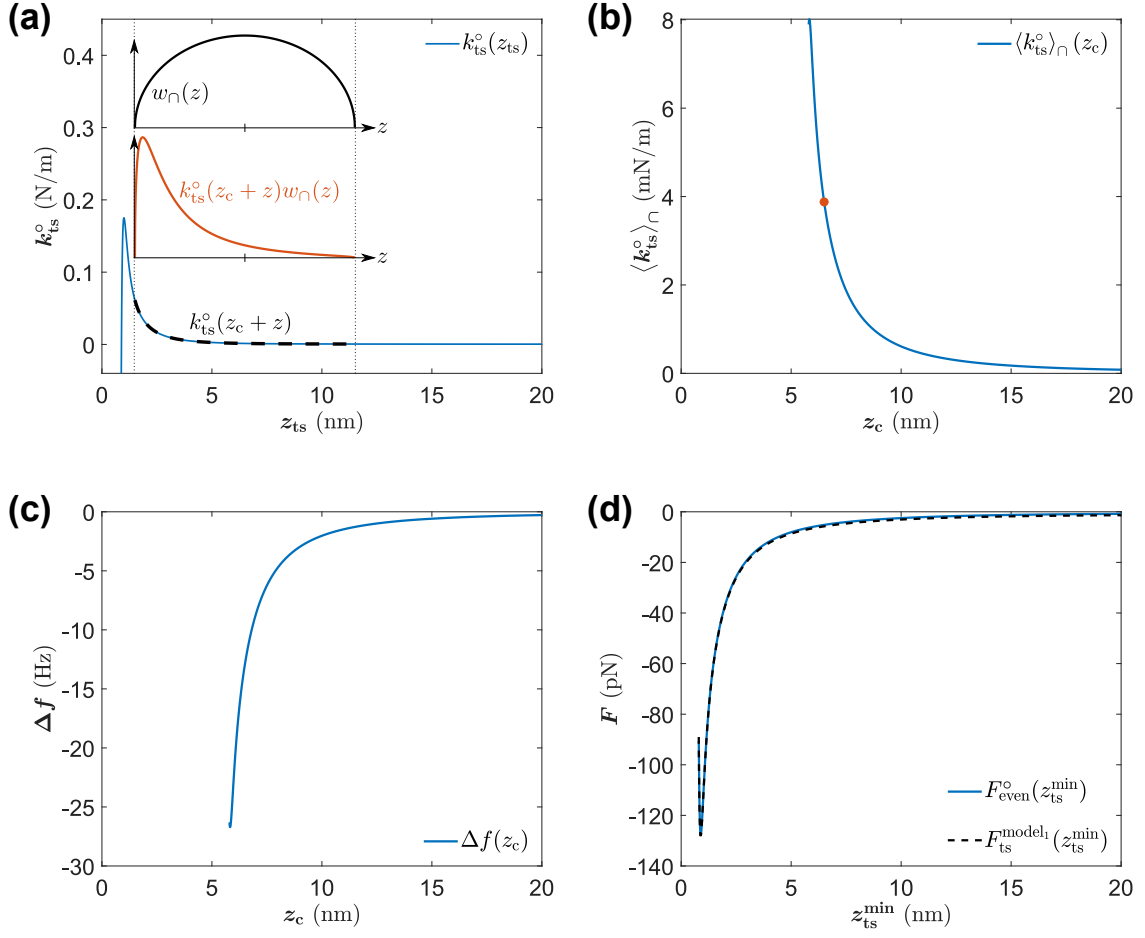


Figure 4.6.: Example for the convolution and deconvolution in AFM. (a) Tip-sample force gradient  $k_{ts}^o$  as function of  $z_{ts}$  calculated from model force  $F_{ts}^{\text{model}_1}(z_{ts})$  and parameters shown in Table 2.6. The inset shows an example for the product of  $k_{ts}^o(z_c + z)$  with  $w_\cap(z)$  for assumed oscillation amplitude  $A = 5$  nm and centre position  $z_c = 6.5$  nm. (b) Convolution  $\langle k_{ts}^o \rangle_\cap$  as function of  $z_c$ , the orange dot indicates the point resulting from the convolution shown in the inset of (a). (c) Frequency shift  $\Delta f$  as function of  $z_c$  calculated from (b). (d) Tip-sample force  $F_{\text{even}}^o$  as function of  $z_{ts}^{\min}$  resulting from the deconvolution procedure based on the  $\Delta f(z_c)$  data shown in (c). For comparison the model force  $F_{ts}^{\text{model}_1}(z_{ts}^{\min})$  is shown as a black dashed line.

with  $w_\cap(z)$  (black line) resulting in the function  $k_{ts}^o(z_c + z)w_\cap(z)$  (orange line). The integration according to relation (4.5.43) then yields the value of convolution at the current centre position  $z_c$  as indicated by the orange point in Figure 4.6(b). Repeating this procedure along  $k_{ts}^o(z_{ts})$  for any possible centre position of oscillation  $z_c$  yields the convoluted cap-average  $\langle k_{ts}^o \rangle_\cap(z_c)$  as shown in Figure 4.6(b). Based on the second AFM equation (4.5.46) the frequency shift  $\Delta f(z_c) = f_{\text{exc}}(z_c) - f_0$  is

calculated from the  $\langle k_{\text{ts}}^{\circ} \rangle_{\cap}(z_c)$  data, assuming a FM NC-AFM measurement with an eigenfrequency  $f_0 = 300$  kHz, a modal stiffness  $k_0 = 45$  N m<sup>-1</sup> and the phase  $\varphi = -\pi/2$ . The calculated  $\Delta f(z_c)$  curve is shown Figure 4.6(c), which would be the result of a FM NC-AFM measurement for determining a tip-sample force curve.

This is the starting point of the deconvolution procedure for obtaining the tip-sample force curve  $F_{\text{even}}^{\circ}(z_{\text{ts}}^{\text{min}})$  with  $z_{\text{ts}}^{\text{min}} = z_c - A$ . Previous to the deconvolution, the cap-averaged tip-sample force gradient  $\langle k_{\text{ts}}^{\circ} \rangle_{\cap}(z_c)$  has to be calculated from the measured  $\Delta f(z_c)$  data using the second AFM equation (4.5.46) with the parameters from experiment. Subsequently, the resulting  $\langle k_{\text{ts}}^{\circ} \rangle_{\cap}(z_c)$  data is deconvolved using relation (4.6.50) yielding the tip-sample force gradient  $k_{\text{ts}}^{\circ}(z_{\text{ts}}^{\text{min}})$ , which has to be integrated along  $z_{\text{ts}}^{\text{min}}$  for obtaining the tip-sample force  $F_{\text{even}}^{\circ}(z_{\text{ts}}^{\text{min}})$  as final result. In Figure 4.6(d) the retrieved tip-sample force curve  $F_{\text{even}}^{\circ}(z_{\text{ts}}^{\text{min}})$  (blue line) is shown in comparison with the true force curve represented by  $F_{\text{ts}}^{\text{model}1}(z_{\text{ts}}^{\text{min}})$  (black dashed line). The tip-sample force curve  $F_{\text{even}}^{\circ}(z_{\text{ts}}^{\text{min}})$  deconvolved from the measured  $\Delta f(z_c)$ -data reproduces the true tip-sample force with high precision.






While the retrieval of the tip-sample force curve based on theoretical  $\Delta f(z_c)$  data is straight forward, the accurate quantification of the tip-sample force based on experimental  $\Delta f(z_p)$  data provides more of a challenge. This is due to noise, thermal drift and piezo creep imposed on any  $\Delta f(z_p)$  curve measured in an FM NC-AFM experiment. Hence, the force retrieval from a single taken experimental  $\Delta f(z_p)$  curve will not necessarily provide the true tip-sample force curve, as systematic error remain unnoticed. However, several  $\Delta f(z_p)$  curves measured at the same lateral position on the sample surface have to follow the same tip-sample force law and thus have to align after their deconvolution if measured correctly. A perfect alignment inherently indicates that the correct tip-sample force curve is determined. Based on this idea, the force curve alignment method (FCA) [53] was developed in the scope of this work which will be presented in the following chapter.



## **5. Alignment method for the accurate and precise quantification of tip-surface forces**

The quantitative interpretation of nanoscale forces requires utmost precision in measuring and analysing force-distance curves. However, the conceptual difficulties in describing tip-surface forces have to be seen alongside experimental challenges that severely limit accurate force measurements with dynamic force microscopy. Here, a procedure to determine accurate and precise force-distance curves in force measurements with NC-AFM is introduced [53]. While a single force curve can be prone to systematic, often unnoticed errors, here the self-consistent retrieval of interaction forces by an alignment procedure using repetitive measurements with the force probe oscillating at varied amplitudes is demonstrated. First, evidence for the correctness of this procedure from model data is given. The force curve, the actual oscillation amplitude, and thermal drift are correctly determined. Second, the precision in force measurements by the force curve alignment (FCA) method is demonstrated by processing experimental data. While the acquisition of single curves reveals inconsistent results precise force data are delivered with FCA.

The following work initially was published in [53].

**Alignment method for the accurate and precise quantification of tip-surface forces**Daniel Heile <sup>\*</sup>, Reinhard Olbrich <sup>\*</sup>, Michael Reichling , and Philipp Rahe <sup>†</sup>  
*Fachbereich Physik, Universität Osnabrück, Barbarastrasse 7, 49076 Osnabrück, Germany* (Received 30 June 2020; revised 14 December 2020; accepted 15 December 2020; published 5 February 2021)

We introduce a procedure to determine accurate and precise force-distance curves in dynamic force measurements utilizing a sharp tip. While single force curves are prone to systematic, often unnoticed errors, we present their self-consistent retrieval by an alignment procedure using repetitive measurements with the force probe oscillating at varied amplitude. By processing model data, we show that the procedure provides the valid force curve, the actual oscillation amplitude, and fully compensates thermal drift. The benefit of the method is demonstrated by application to experimental data.

DOI: [10.1103/PhysRevB.103.075409](https://doi.org/10.1103/PhysRevB.103.075409)**I. INTRODUCTION**

The understanding of binding in matter is a great success of quantum mechanics and over a century, elaborate theories describing the interaction between atoms and molecules by electromagnetic forces have been developed [1]. While, for systems up to a certain size, chemical bonds and physical interactions can precisely be described by the interaction between individual atoms, this is not practical and elucidating for the description of binding between mesoscopic and macroscopic bodies. For such objects, binding is commonly discussed in the framework of integral physical interactions phenomenologically described as adhesion [2]. Most relevant in nanoscale force measurements, there is no strict border between these two types of descriptions.

The measurement of forces between atoms, molecules, and nanoscale objects has been pushed to the physical limits [3–5] and is of great interest in diverse fields of science and technology including high-resolution analysis of inorganic [6–8], organic [9–11], and biological surfaces [12–14], three-dimensional (3D) force mapping [15–18], Casimir force measurements [19], nanomechanical material characterization [20–24], capillary force studies [25–29], hydration layer analysis [30–33], the study of atom-specific reactivity [34,35], mechanochemistry [36–38], quantum dot microscopy [39], and single-spin detection [40,41]. The technique of noncontact atomic force microscopy (NC-AFM) allows dynamic force measurements between an oscillating sharp tip and a surface of any kind, with a resolution down to the atomic scale [42–45]. Still, the interpretation of force measurements at the nanoscale is most difficult as this is the crossover regime where forces between individual atoms and molecules as well as forces between mesoscopic bodies act together. In this regime, the force-distance law is not a simple function of the

body separation, but is often described as a sum of contributions based on different models [46]. Utmost precision in measuring and analyzing a force-distance curve is required to test models and to quantify the nanoscale interactions.

The conceptual difficulties in describing tip-surface forces have to be seen alongside experimental peculiarities severely limiting accurate dynamic force measurements. First, the primary measurement signal in NC-AFM is not the force, but the shift in the resonance frequency of a high- $Q$  force probe oscillating in the force field above the surface [44]. The force curve is derived from frequency shift data by numerical deconvolution, commonly referred to as force inversion [47,48]. The result of this inversion can be ill-posed [49], can exhibit large errors in a range of relevant amplitudes [50], or can include severely amplified detection system noise [51]. Second, the force inversion algorithms yield valid results only if the oscillation amplitude is known accurately [48,50]. Third, strong gradients in the force field make the measurement susceptible to minute deviations of the probe trajectory from the target curve as they result, for example, from thermal drift even when applying active drift compensation [52,53].

In the present paper, we introduce the force curve alignment (FCA) method facilitating the accurate and precise measurement of force curves by circumventing experimental peculiarities and ultimately removing systematic errors in widely accepted present practice. The central concept is the repetitive measurement of the tip-surface interaction with different probe oscillation amplitudes, delivering a data set, which is robust against disturbing impacts. While the presence of systematic errors can hardly be identified from a single interaction curve, a match of the individual force curves by an optimisation algorithm enables a self-consistent determination of the error-free tip-surface interaction force curve. A key challenge for retrieving the force from frequency shift data is accurately determining the probe oscillation amplitude  $A$ . The physical oscillation amplitude  $A$  is derived from the measured voltage amplitude  $V_A$  via the calibration factor  $S$  defined as  $A = S \cdot V_A$ . The calibration is principally straightforward, however, obtaining an accurate result is practically most difficult. Among various methods suggested [54–61], those involving the tip-surface interaction [55,56,58] ensure that the

<sup>\*</sup>These authors contributed equally to this work.

<sup>†</sup>prahe@uni-osnabrueck.de

*Published by the American Physical Society under the terms of the Creative Commons Attribution 4.0 International license. Further distribution of this work must maintain attribution to the author(s) and the published article's title, journal citation, and DOI.*

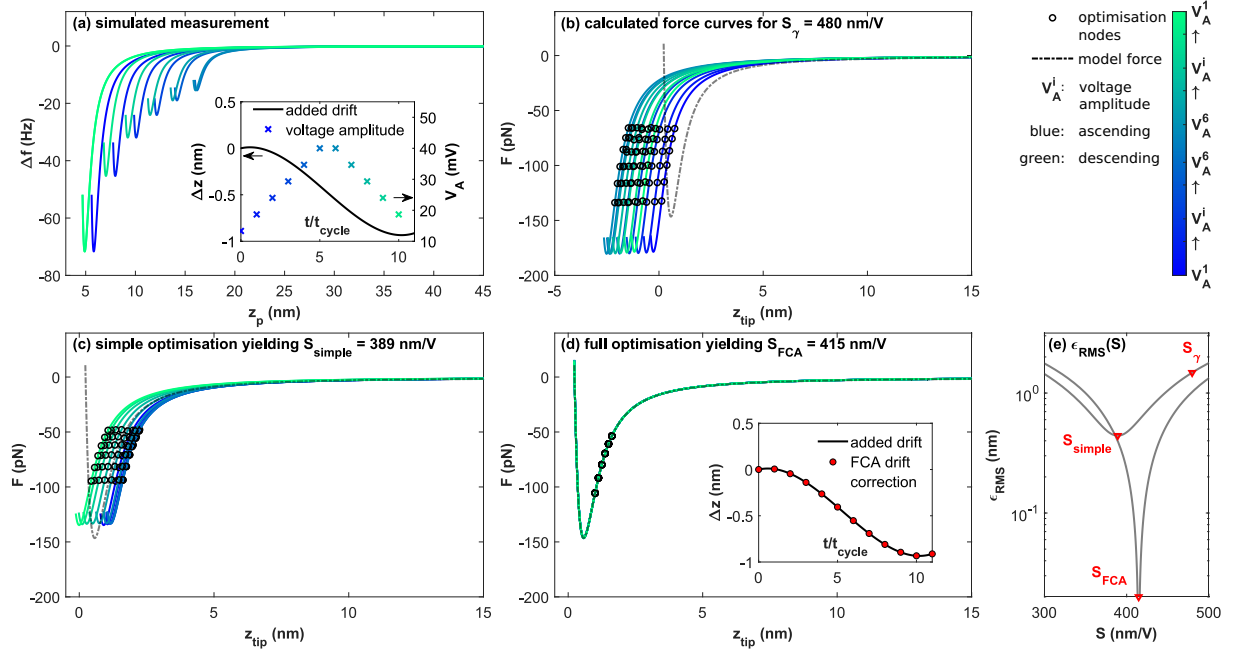


FIG. 1. Stages of model data processing with the FCA method. (a) Simulated frequency shift  $\Delta f^i[z_p + \Delta z(t^i)]$  data for six ascending and six descending voltage amplitudes  $V_A^i$  (see inset) including thermal drift  $\Delta z(t)$  (see inset).  $z_p$  denotes the piezo position. (b) Curves  $F^i(z_{tip})$  of the normal force as a function of the tip position  $z_{tip}$  derived from the  $\Delta f^i[z_p + \Delta z(t^i)]$  data using the starting value  $S_\gamma = 480$  nm/V, zero drift, and the Sader-Jarvis force inversion algorithm [48].  $z_{tip}$  is defined as the minimum tip-surface distance attained in the lower turning point of the oscillatory tip motion (see Fig. 4 in Appendix A). The dash-dotted line is the model force curve used for generating the artificial frequency shift data. Black circles are optimization nodes used for the FCA correction. (c) Simplified FCA alignment (without considering thermal drift) yielding  $S_{simple} = 389$  nm/V. (d) Accurate force curves resulting from applying the full FCA procedure yielding  $S_{FCA} = 415$  nm/V. The inset demonstrates the excellent match between the  $\Delta z(t^i)$  corrections resulting from FCA and the artificial  $\Delta z(t)$  input. (e) Residual error  $\epsilon_{RMS}$  as a function of  $S$  together with the positions of the approximations  $S_\gamma$  and  $S_{simple}$  as well as the accurate value  $S_{FCA}$ .

calibrated amplitude corresponds to the position of the tip. This is a most important aspect which challenges calibration methods based on interferometry: Although the latter methods yield in principle very precise distance measurements as they use the wavelength or speed of light as a reference of unprecedented accuracy [54,59], a slight misalignment of the laser spot on the cantilever will introduce a systematic error with respect to the tip amplitude relevant for the force measurement. Conceptually advantageous is the  $\gamma$ -method [55], which is based on an approximation by the normalized frequency shift [62]. As demonstrated in Appendix B, this method may yield reasonably good results under certain conditions, but may also fail and is, therefore, not suitable when seeking for a highly accurate calibration. The limitations of the presently available amplitude calibration procedures have been a major driving force for developing the FCA method that inherently yields an accurate value for  $S$ . In the following, first the validity of the FCA method is demonstrated by applying FCA to model data that are based on measured force curves. Second, the practicability of FCA is shown by application to experimental data acquired on a  $\text{CeO}_2(111)$  surface decorated with gold nanoparticles.

## II. FORCE CURVE ALIGNMENT METHOD

Intermediate and final results of a model force measurement run are compiled in Fig. 1 for demonstration and

verification of the FCA method. FCA relies on the measurement of a set of  $2N$  (here:  $N = 6$ ) tip retraction and approach cycles, with ascending (blue shadings) and descending (green shadings) amplitude voltage values  $V_A^i$ . A set of the corresponding artificial frequency shift  $\Delta f^i(z_p)$  curves [Fig. 1(a)] is calculated from a model force curve  $F_{mod}(z_{tip})$  resembling an experimental measurement (see Appendix A) by applying the appropriate transformation [44] for the set of voltage amplitudes  $V_A^i$  [see inset in Fig. 1(a)] with  $S = 415$  nm/V. Furthermore, artificial nonlinear thermal drift  $\Delta z(t)$  [see inset in Fig. 1(a)] is added to the tip positions  $z_{tip}$  with magnitudes and velocities of the drift chosen to match values typically found in experiments. As a result, the drift-influenced data of a typical experiment is generated. While the resulting  $\Delta f^i(z_p)$  curves representing different  $V_A^i$  as shown in Fig. 1(a) naturally differ from each other due to the amplitude-dependency of the absolute frequency-shift value [62], curves having the same  $V_A^i$  value differ due to the introduced thermal drift  $\Delta z(t^i)$ .

An estimate for the amplitude calibration factor and thermal drift parameters is used to calculate the corresponding set of force curves as the starting point for the FCA optimization. We choose  $S_\gamma = 480$  nm/V as the estimate from the  $\gamma$ -method [55] (see Appendix B) and start with zero drift. The set of resulting force curves  $F^i(z_{tip})$  calculated with the Sader-Jarvis algorithm [48] is shown in Fig. 1(b). It is immediately apparent that all  $F^i(z_{tip})$  curves are shifted along the  $z_{tip}$

axis relative to each other, differ in their slope and curvature, and none of them coincides with the true force curve that is known for this simulation and displayed as a dash-dotted line in Figs. 1(b)–1(d). Similar results are obtained with the matrix algorithm [47] (see Appendix H).

In a simple version of the FCA optimisation, force curves  $F^i(z_{\text{tip}})$  are corrected for the error in  $S$  but not for thermal drift. To this end, six optimization nodes are defined on each curve [black circles in Figs. 1(b)–1(d)], each belonging to a set of six given force values along the curve. With one free parameter, namely  $S$ , the optimization procedure recalculates the curves with iteratively optimized  $S$  so that the value for  $\epsilon_{\text{RMS}}$  representing the RMS value of the deviation between the optimization nodes of each curve from a chosen reference curve (the first curve in the data set) is minimized. The improvement by the optimization is evident from Fig. 1(c) showing force curves with a reduced spread close to the true curve. This optimization yields a better estimate for the amplitude calibration factor of  $S_{\text{simple}} = 389 \text{ nm/V}$ , however, the residual spread of the force curves is evidence for their distortion by thermal drift.

To retrieve the true force curve, we apply the full FCA optimization procedure including the adjustment of a third-order drift polynomial for approximating the thermal drift  $\Delta z(t)$  to the  $F^i(z_{\text{tip}})$  curves from Fig. 1(b) with results shown in Fig. 1(d) (see Appendixes E and F for the measurement and analysis protocol, respectively, and the Supplemental Material [63] for the program code). The full optimization yields 12  $F_{\text{FCA}}^i(z_{\text{tip}})$  force curves not discernible from each other and perfectly matching the true force curve. In addition to fully recovering the artificially obscured force data, the FCA method yields the correct amplitude calibration factor  $S_{\text{FCA}} = 415 \text{ nm/V}$ . The inset in Fig. 1(d) presents an excellent match between the discrete drift corrections determined by the FCA optimization and the artificially introduced drift polynomial. The graph shown in Fig. 1(e) demonstrates the reliability of the FCA method when applied to a perfect set of data: for the full FCA optimisation, the function  $\epsilon_{\text{RMS}}(S)$  describing the residual error exhibits one sharp minimum allowing for a precise determination of  $S$  and the true force curve. Note that the value of  $\epsilon_{\text{RMS}}$  corresponding to  $S_{\text{FCA}}$  is nearly ten orders of magnitudes smaller than it is drawn in Fig. 1(e) and solely represents the numerical error.

### III. RESULTS AND DISCUSSION

The practicability of the method is demonstrated for the real experimental data shown in Fig. 2. We performed measurements on a well-prepared  $\text{CeO}_2(111)$  surface exhibiting large flat terraces separated by steps with the height of a O-Ce-O triple layer [64–66]. Regularly shaped gold clusters with lateral dimensions of typically 10 nm and measured heights of typically 1 to 3 nm were introduced as nanoscale irregularities. Two strongly different tips were used to acquire interaction curves representative for two typical experimental conditions in dynamic force measurements at room temperature under ultra-high vacuum conditions (see Appendix D for details). The first tip was a silicon tip subjected to sputtering and potential contamination after exposure to the residual gas and sample contact. This bare silicon tip acts as a representative for “sharp” tips typically used for NC-AFM imaging.

The second tip was a Pt/Ir-coated silicon tip as typically used for Kelvin probe force microscopy with a usually larger tip radius due to the coating. An NC-AFM image of the surface taken with a silicon tip is shown in the inset of Fig. 2(a). The two red dots mark typical positions where force curves were acquired: Central on a single gold cluster (“on-cluster”) and in a region representing the flat surface (“off-cluster”). Care has been taken in the latter case to measure forces far away from clusters, step edges, or other disturbances.

In full analogy to the analysis steps applied to the simulated data, the graphs in Fig. 2(a) show the original measurements  $\Delta f^i(z_p)$  taken with the bare silicon tip. At both positions, the  $\Delta f^i(z_p)$  curves were sampled in 12 approach/retract cycles with ascending and descending voltage amplitudes  $V_A^i$  ranging from 13.3 to 40 mV. Note that data were deliberately not acquired close to or beyond the minima of the force curves to avoid any tip change that would severely compromise the force measurement. The graphs in Fig. 2(b) show the  $F^i(z_{\text{tip}})$  data after force inversion but before the optimization. We used a starting value of  $S = S_y = 480 \text{ nm/V}$  and assumed zero drift for the start of on-cluster and off-cluster experiments.

Figure 2(c) represents the result using the full FCA procedure for this series of measurements. Individual data points from the aligned force curves are shown as gray dots while average curves determined for off-cluster and on-cluster measurements are shown as green and orange lines, respectively. It is immediately apparent that the off-cluster measurement yields an excellent match of the aligned forces and unambiguously provides the tip-sample force curve. The optimization yields  $S = S_{\text{FCA}}^{\text{off}} = (414.6 \pm 1.9) \text{ nm/V}$  as the accurate result for this measurement. The specified error reflects the accuracy of determining the minimum in  $\epsilon_{\text{RMS}}$  as estimated from the width of the  $\epsilon_{\text{RMS}}(S)$  curve (see Appendix G for details).

The spread across the individual force curves is larger in the on-cluster data shown in Fig. 2(c), in agreement with observing a larger spread in the  $\Delta z(t^i)$  values (orange line in the left inset) and an  $\epsilon_{\text{RMS}}(S_{\text{FCA}}^{\text{on}})$  value larger by a factor of 4.4 than  $\epsilon_{\text{RMS}}(S_{\text{FCA}}^{\text{off}})$  (right inset). The amplitude calibration factor of  $S_{\text{FCA}}^{\text{on}} = (383 \pm 8) \text{ nm/V}$  is furthermore smaller than  $S_{\text{FCA}}^{\text{off}}$ . We attribute these differences to a systematic error introduced by the inclination of the direction of probe oscillation from the surface normal ( $\alpha = 12.5^\circ$  for our instrument). The inclination is not compatible with the force inversion algorithm integrating the weighted frequency shift along the surface normal (see Appendix C for a discussion). On a homogeneous and isotropic surface, where the force is a function of  $z_{\text{tip}}$  only, the inclination can be compensated by a projection of the oscillation coordinate to the surface normal. However, when measuring above a cluster with dimensions comparable to the tip radius, the tip experiences lateral force gradients and measurements with different oscillation amplitude will be differently influenced by them, ultimately resulting in incorrect force measurements. This is convincing evidence that the FCA method is able to unravel so far unnoticed sources for inaccurate force measurements.

Measurements with the Pt/Ir-coated tip were performed and analyzed in exactly the same manner with final results for one representative measurement compiled in Fig. 2(d). For this probe we find values of  $S_{\text{FCA}}^{\text{on}} = (165.5 \pm 0.9) \text{ nm/V}$  and  $S_{\text{FCA}}^{\text{off}} = (169.3 \pm 0.5) \text{ nm/V}$ , both significantly smaller than the value for the silicon tip due to the high optical reflectivity

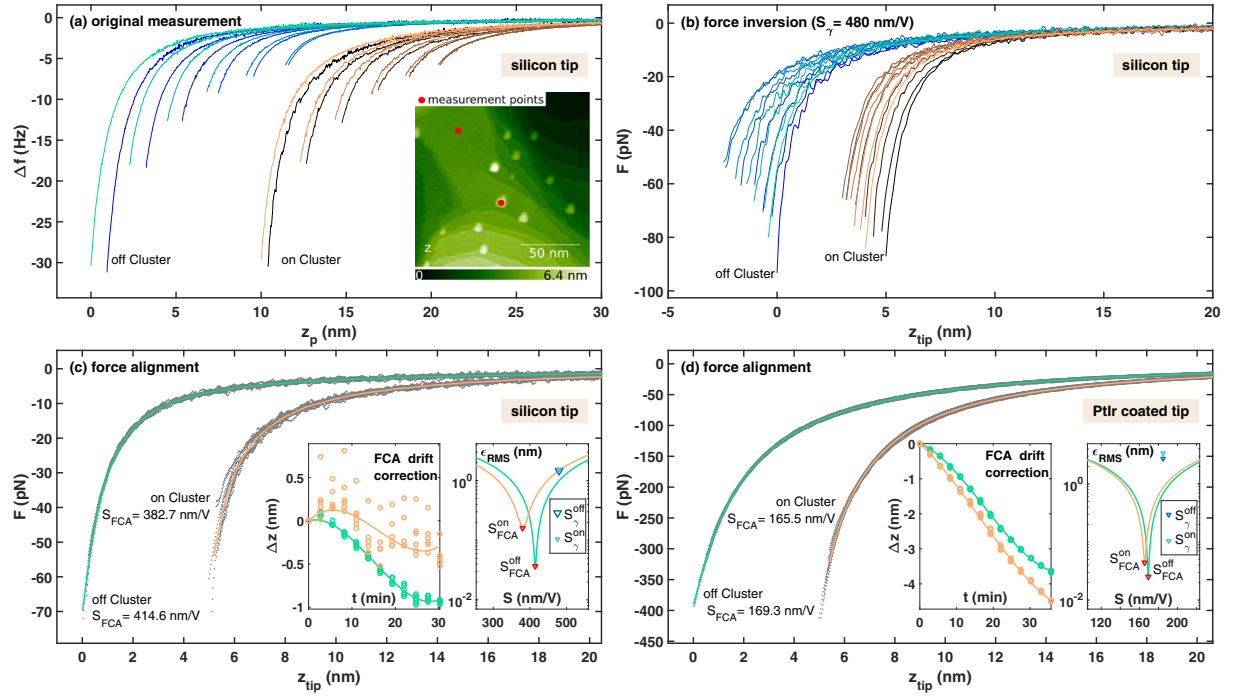


FIG. 2. Experimental force measurements on a  $\text{CeO}_2(111)$  surface decorated with gold clusters. Results compiled in (a)–(c) represent measurements taken with the bare silicon tip while panel (d) displays the final results of measurements performed with a Pt/Ir coated silicon tip. The steps of force inversion and full FCA optimisation were carried out in exactly the same manner as for the model data analysis shown in Fig. 1. Measurements were performed for positions at the center of gold clusters (on-cluster) as well as on atomically flat terraces far from step edges and other disturbances (off-cluster) and are coded with blue/green and black/orange colors, respectively. On-cluster and off-cluster positions are exemplary shown as red dots in the inset of (a), which is a NC-AFM topography image of the gold decorated  $\text{CeO}_2(111)$  surface taken with the bare silicon tip. The green and orange curves shown in (c) and (d) are averaged curves of the force curve data plotted as gray points. The left insets in (c) and (d) display the drift polynomial  $\Delta z(t)$  yielded by the FCA optimisation (solid line) and the deviations from the mean curve found for the six optimisation nodes (circles). The right insets in (c) and (d) display  $\epsilon_{\text{RMS}}(S)$ , similar to Fig. 1(e), for on- and off-cluster measurements.

of the metal coated cantilever. Other basic observations are the very same as for the silicon tip, yet, the more slowly decaying forces highlight the larger tip radius resulting from the Pt/Ir coating. The difference between  $S_{\text{FCA}}^{\text{on}}$  and  $S_{\text{FCA}}^{\text{off}}$  is tiny compared to the bare silicon tip measurement. This is intelligible considering that a tip with a larger tip radius experiences smaller lateral force gradients as the force is averaged over a larger area.

#### IV. CONCLUSIONS

The measurements and their analysis in the framework of FCA deliver a very consistent picture. For a set of high quality data, the FCA method yields the true tip-surface interaction force curve free from critical systematic errors as well as an accurate and highly precise value for the amplitude calibration factor. It is noteworthy that an accurate value for  $S$  is most important for an accurate determination of the modal sensor stiffness  $k_0$  [67], another key parameter for force measurements. The FCA method can easily be adapted to the needs of the experiment, specifically, the user can tailor the FCA optimization function. If a measurement is compromised by any kind of disturbance that cannot be compensated for by

the user implemented optimization function, force curves will not coincide what clearly indicates a problem with the dataset or the chosen correction function. FCA offers great flexibility in its application as it is compatible with a direct force measurement as well as with any force inversion algorithm. This especially concerns force mapping experiments, where thermal drift that is usually the major problem for long-lasting measurements, is fully compensated by FCA. Hence, FCA can equally well be used for static AFM, intermitted contact AFM, and NC-AFM. It facilitates the quantitative analysis of force measurements with unprecedented accuracy and precision in any environment and at any temperature provided the force curve is deterministic what implies sufficient stability of tip and surface. It can be anticipated that FCA will have a significant impact in a large number of fields in physics, chemistry, and biology as well as in cross-disciplinary sciences and nanotechnology.

#### ACKNOWLEDGMENTS

This work was supported by the Deutsche Forschungsgemeinschaft via Grants No. RA2832/1-1, No. RE1186/21-1, and No. RE1186/23-1. We thank Jonas Heggemann for most helpful discussions on the method.



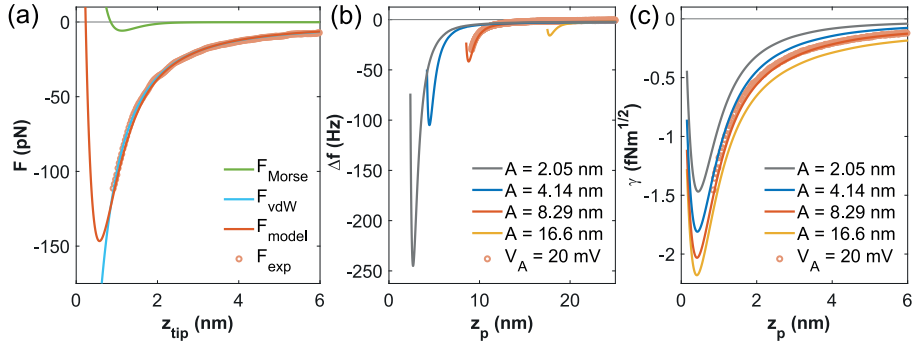


FIG. 3. (a) Interaction force  $F$  used for the simulations. A combined Morse (green line) and van der Waals (blue line) interaction [69] is adjusted to fit an experimentally measured force-distance curve (circles). (b) Frequency shift  $\Delta f$  and (c) normalized frequency shift  $\gamma$  calculated for different amplitudes from the force in (a). Experimental data included as circles.

#### APPENDIX A: MODEL FORCE CURVES

To create a model force curve for testing the FCA method, we use a combination of Morse and van der Waals interaction forces for all simulations

$$F_{\text{model}}(z_{\text{ts}}) = F_{\text{Morse}}(z_{\text{ts}}) + F_{\text{vdW}}(z_{\text{ts}}), \quad (\text{A1})$$

similar to the separation of interactions in Refs. [46,68]. One contribution is the force corresponding to the Morse potential

$$V_{\text{Morse}}(z_{\text{ts}}) = E_b [2e^{-\kappa(z_{\text{ts}} - \sigma_0)} - e^{-2\kappa(z_{\text{ts}} - \sigma_0)}], \quad (\text{A2})$$

describing the short-range interaction by

$$F_{\text{Morse}}(z_{\text{ts}}) = 2E_b\kappa [ -e^{-\kappa(z_{\text{ts}} - \sigma_0)} + e^{-2\kappa(z_{\text{ts}} - \sigma_0)} ]. \quad (\text{A3})$$

The van der Waals force derived by Argento and French [69] as the force between a cone with half opening angle  $\Theta$ , terminated with a half sphere of radius  $R$ , and Hamaker constant  $H$

$$F_{\text{vdW}}(z_{\text{ts}}) = - \frac{HR^2(\sin \Theta - 1)[(R - \hat{z}) \sin \Theta - R - \hat{z}]}{6\hat{z}^2(R + \hat{z} - R \sin \Theta)^2} - \frac{H \tan \Theta [(\hat{z} + R) \sin \Theta + R \cos(2\Theta)]}{6 \cos(\Theta)(\hat{z} + R - R \sin \Theta)^2} \quad (\text{A4})$$

is used to describe the interaction of the mesoscopic tip with the surface. Here,  $\hat{z} = z_{\text{ts}} + z_{\text{offset}}$ , where  $z_{\text{offset}}$  describes the height of the nanotip attached to the mesoscopic tip. Accordingly, we find for the force gradients

$$k_{\text{Morse}}(z_{\text{ts}}) = 2E_b\kappa^2 [e^{-\kappa(z_{\text{ts}} - \sigma_0)} - 2e^{-2\kappa(z_{\text{ts}} - \sigma_0)}] \quad (\text{A5})$$

$$k_{\text{vdW}}(z_{\text{ts}}) = \frac{H}{6\hat{z}^3(R + \hat{z} - R \sin \Theta)^2} \times [R(2R^2 + 3R\hat{z} + (2R - \hat{z}) \times (-2(R + \hat{z}) + R \sin(\Theta)) \sin \Theta) + \hat{z}^3 \tan^2 \Theta]. \quad (\text{A6})$$

These terms are used within the quantitative AFM framework [44] to calculate the frequency shift curve  $\Delta f(z_p)$ . The starting point is an experimentally obtained force curve shown as orange circles in Fig. 3(a). The parameters  $H$ ,  $\Theta$ , and  $z_{\text{offset}}$  of the van der Waals interaction were fitted (with  $R = 5$  nm kept fixed) to these experimental data acquired on a CeO<sub>2</sub>(111)

surface with a bare silicon tip. For the Morse potential we adapted a model for the interaction between Si atoms [50] with the herein used parameters specified in Table I.

Figure 3(a) presents the experimental force data ( $F_{\text{exp}}$ , circles) as well as the calculated Morse ( $F_{\text{Morse}}$ , green), van der Waals ( $F_{\text{vdW}}$ , blue), and total ( $F_{\text{model}}$ , red) force curves. The latter curves are calculated using the parameters listed in Table I.

The model force data  $F_{\text{model}}(z_{\text{tip}})$  is used to calculate frequency shift  $\Delta f(z_p)$  curves for representative oscillation amplitude ranging from about 2 to 20 nm [Fig. 3(b)] with the quantitative AFM framework [44]. Experimental  $\Delta f$  data are included in Fig. 3(b) and match the simulation result for  $A = 8.5$  nm as expected from the sensitivity factor and the chosen voltage amplitude. In a further step,  $\Delta f(z_p)$  curves are converted into  $\gamma(z_p)$  curves using the definition of the normalised frequency shift [62] [Fig. 3(c)]. This figure highlights the limitations of the concept of the normalized frequency shift: even for the two largest amplitudes of 8.29 and 16.6 nm, the  $\gamma(z_p)$  curves do not match.

In Fig. 4 we explain the use of the symbols to describe the probe position along  $z$ . Once the coarse approach is completed, the tip is positioned by adjusting the piezoposition  $z_p$  to yield a certain tip-sample distance  $z_{\text{ts}}$ . While the relative movement in  $z_p$  is well known from a respective calibration, the absolute position  $z_{\text{ts}}$  is *a priori* not known. As the force curve  $F(z_{\text{ts}})$  does not have a well-defined endpoint, the origin  $z = 0$  cannot easily be defined and is practically chosen with an arbitrary offset. In a dynamic measurement,  $z_{\text{ts}}$  is a function

TABLE I. Parameters for the Morse and van der Waals interactions used within the simulations.

| Morse interaction         |                        |
|---------------------------|------------------------|
| $E_b$                     | 4.638 zJ               |
| $\sigma_0$                | 850 pm                 |
| $\kappa$                  | $2.50 \text{ nm}^{-1}$ |
| van der Waals interaction |                        |
| $H$                       | 357.619 zJ             |
| $\Theta$                  | $29.7^\circ$           |
| $R$                       | 5 nm                   |
| $z_{\text{offset}}$       | 583.04 pm              |

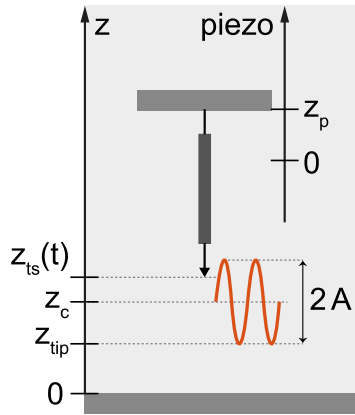


FIG. 4. Axis system describing the vertical  $z$  positions. The notation follows Ref. [44].

of time and  $z_{ts}(t)$  is often assumed as a quasiharmonic oscillation around the center position  $z_c$  with amplitude  $A$  [44]. The Sader-Jarvis force inversion algorithm is implemented to yield the force as a function of the tip-surface distance specified by the lower turning point  $z_{tip}$  of the oscillation. Therefore, we plot measured frequency shift curves  $\Delta f(z_p)$  as a function of the known coordinate  $z_p$  with an arbitrarily chosen origin. Likewise, the force curve  $F(z_{tip})$  determined by the force inversion is plotted as a function of the coordinate  $z_{tip}$  with an arbitrarily chosen origin.

#### APPENDIX B: $\gamma$ -METHOD

The  $\gamma$ -method is a well-established standard procedure to determine the sensitivity factor  $S$  based on a sequence of approach and retract cycles performed with a set of voltage amplitudes  $V_A^i$ . These voltage amplitudes represent *a priori* unknown physical oscillation amplitudes  $A^i$  [55]. For each set point representing a certain  $V_A^i$ , the mean tip-sample distance  $z_c = \bar{z}_{ts}$  is adjusted by changing the piezo position  $z_p^i$  to a value representing the same predefined tip-sample interaction. Crucially, the tip-sample interaction cannot be measured but is commonly estimated by the normalised frequency shift  $\gamma = k_0 A^{3/2} \Delta f / f_0$  where  $k_0$  is the modal probe stiffness,  $\Delta f$  the observed frequency shift, and  $f_0$  the probe eigenfrequency [62].

In the calibration experiment,  $V_A$  is stepwise increased and decreased (up and down), while the given normalized frequency shift  $\gamma_{set}$  is kept constant by the choice of an appropriate frequency-shift setpoint  $\Delta f_{set}^i$ . As a consequence, the topography feedback loop adjusts  $z_p^i$  accordingly. The amplitude calibration factor  $S_{\gamma,z} = \Delta z_p / \Delta V_A$  is the slope of the graph in a plot of the piezopositions  $z_p^i$  as a function of the voltage amplitudes  $V_A^i$ . An exemplary result of this procedure for a silicon tip over the ceria surface is shown in Fig. 5. Note that in this and all other measurements, the  $\gamma$ -method does not directly yield  $S_\gamma$ , but  $S_{\gamma,z} = S_\gamma \cos(\alpha)$  as the direction of the oscillation is usually inclined by an angle of  $\alpha$  (in the present setup  $\alpha \approx 12.5^\circ$ ) with respect to the surface normal (see Appendix C for further details). The  $S_\gamma = S_{\gamma,z} / \cos \alpha$  value derived from this calibration curve was used as the

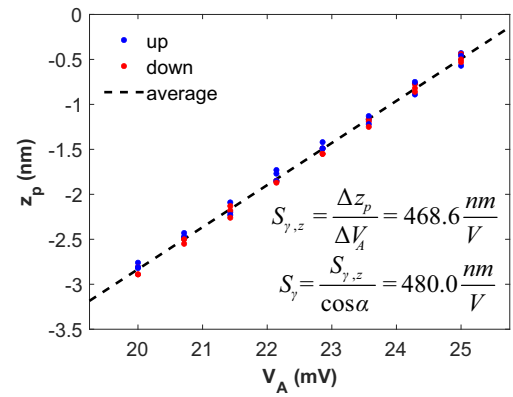


FIG. 5. Determination of the sensitivity factor  $S$  utilizing the  $\gamma$ -method for a silicon probe over a ceria surface.  $S_{\gamma,z}$  follows from the slope of a linear regression and  $S_\gamma$  from a correction for the inclination  $\alpha$  between the cantilever oscillation and the surface normal ( $\alpha \approx 12.5^\circ$  for the herein used system).

starting value for the force curve alignment in Fig. 1(b) of the main paper.

The accuracy of the  $\gamma$ -method is analyzed by simulations, yielding results shown in Fig. 6 together with corresponding experimental measurements. The realistic model force curve as described in Appendix A is used for calculating  $\gamma(z)$  curves for different  $V_A^1$ ; exemplary  $\gamma(z)$  curves are shown in Fig. 3(c). Several  $S_\gamma$  measurements were performed experimentally with the same tip for a series of  $\gamma_{set}$  values and three different starting voltage oscillation amplitudes  $V_A^1$  (start values are increased by 25% for the  $\gamma$ -method). Experimental (circles) and simulated (lines) data for  $S_\gamma$  of these calibration cycles in Fig. 6 display the determined values for  $S_\gamma$  as a function of  $\gamma_{set}$  and various starting voltage amplitudes  $V_A^1$ . The horizontal line marks the true value of  $S = S_{FCA}$  as obtained by the FCA method. As evident from these data, the  $\gamma$ -method is prone to errors as the result for  $S_\gamma$  clearly depends on the chosen parameters. Valid results can only be

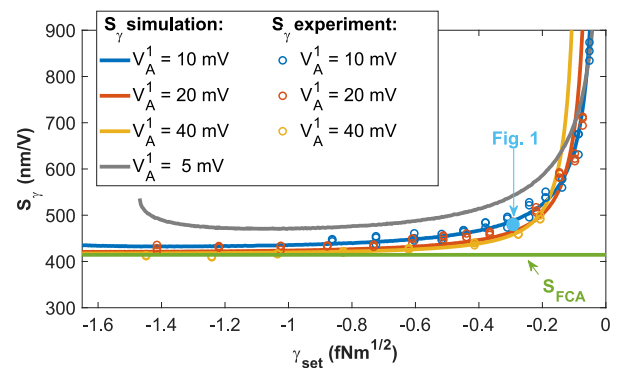


FIG. 6. Simulation and experimental results for determining  $S$  using the  $\gamma$ -method. Experimental data are represented by circles while solid lines are the result of simulations. The value  $S_\gamma = 480 \text{ nm/V}$  marked by “Fig. 1” is used as the starting value  $S_\gamma$  for the FCA method in Fig. 1.

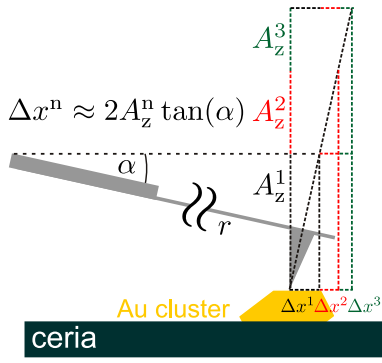


FIG. 7. Effect of the cantilever inclination towards the sample surface. The lateral movement of the tip  $\Delta x^n$  from the measurement position above an Au cluster is a function of the oscillation amplitude  $A_z^n$ .

expected for very large start amplitudes  $A$  and in the limit of strong tip-surface interaction  $\gamma_{\text{set}}$ . For start amplitudes  $A^1$  below 5 nm, as are commonly used in NC-AFM imaging, we note that the  $S_\gamma$  curves do not approach  $S_{\text{FCA}}$  but are always offset. In this case, the set point  $\gamma_{\text{set}}$  cannot be further reduced beyond about  $\gamma_{\text{set}} \sim -1.5 \text{ fN m}^{1/2}$  as the minimum of the  $\gamma(z)$  curve is already located close to this value. Experimental data in Fig. 6 were taken with a fairly sharp silicon tip interacting with the  $\text{CeO}_2(111)$  surface. We find that the  $S_\gamma$  offsets and deviations from  $S_{\text{FCA}}$  are even larger when using a tip with a larger tip radius such as a Pt/Ir-coated coated tip (data not shown). In summary, the  $\gamma$ -method yields an estimate of  $S$  that may be close to the true value, however, it is not a reliable procedure to determine an accurate value for  $S$ .

#### APPENDIX C: EFFECTS OF CANTILEVER INCLINATION

In many experimental setups, the direction of the probe oscillation is inclined by a small angle  $\alpha$  with respect to the the surface normal (see Fig. 7). Hence the distinction between two different amplitudes  $A$  and  $A_z$  is important. The first one,  $A$ , is the physical oscillation amplitude of the cantilever beam end, while  $A_z$  is the projection on the surface normal vector with  $A_z = A \cos \alpha$ . The oscillation voltage amplitude  $V_A$  is measured in the experiment. This voltage amplitude is linked to the physical oscillation amplitude by the sensitivity factor  $S = A/V_A$ . Hence a sensitivity factor representing the vertical component only can be defined as  $S_z = S \cdot \cos \alpha = A_z/V_A$ . Consequently, the cantilever inclination not only requires the distinction between two physical amplitudes  $A$  and  $A_z$  but also the distinction between two sensitivity factors  $S$  and  $S_z$ .

An inclination of the cantilever oscillation to the surface normal is further relevant when measuring in the vicinity of a small surface feature (see Fig. 7), as it results in a lateral displacement  $\Delta x$  between the lower and the upper turning point during every oscillation cycle. Increasing the amplitude  $A_z$  results in a larger lateral movement  $\Delta x$  of the tip, which can be described by the relation  $\Delta x \approx 2A_z \tan(\alpha)$  (for oscillation amplitudes that are small compared to the cantilever beam length, the circular trajectory can be well approximated by a

straight segment). While this lateral movement has no effect on measurements on large, homogeneous, and isotropic areas of the sample surface, it introduces a systematic error when measurements of a small object such as a metal cluster are performed. As Fig. 7 exemplifies, an increase of the amplitude results in a lateral movement of the tip possibly beyond the cluster surface area. Thus, the force gradient in the vicinity of the cluster affect the force measurement, specifically for large oscillation amplitudes. As the force inversion algorithm does not take this into account, but rather considers an oscillation along the surface normal, this results in an erroneous force curve. As seen in Figs. 2(c) and 2(d) of the main paper, this is a notable effect.

#### APPENDIX D: EXPERIMENTAL METHODS

Sample preparation and NC-AFM measurements were performed in an ultra-high vacuum (UHV) system at a base pressure in the  $10^{-11}$  mbar regime.  $\text{CeO}_2(111)$  surfaces were prepared on a single crystal (SurfaceNet GmbH, Rheine, Germany) by cycles of argon ion sputtering ( $p_{\text{Ar}} = 10^{-5}$  mbar,  $U = 1.5 \text{ kV}$ ,  $I = 15 \text{ mA}$ , 5 min) followed by annealing at high temperature ( $1150 \pm 25 \text{ K}$ ) for 15 minutes, see Refs. [64,65] for further details. Gold was subsequently deposited onto the  $\text{CeO}_2(111)$  sample held at room temperature by using small gold pieces (Purity: 99.99 + %, Goodfellow) in a crucible of an electron beam evaporator (type EFM 3i from Focus GmbH, Huenstetten, Germany). Regularly shaped gold nanoparticles (typical widths of 10 nm and heights of 1 to 3 nm) were formed in a postdeposition annealing step at a temperature of about  $(520 \pm 25) \text{ K}$ .

NC-AFM measurements were conducted using a modified [70] commercial ultra-high vacuum AFM/STM instrument (ScientaOmicron, Taunusstein, Germany) connected to an R9 (RHK Technology, Troy (MI), USA) SPM controller. Additionally, an atom tracking system [53] enabled the measurement and compensation of drift during the experiment. Drift effects were further reduced by a dedicated temperature control of the laboratory. Kelvin probe force microscopy [71] with sideband detection was activated to minimize electrostatic background forces. A bias modulation at a frequency of  $f_{\text{el}} = 1567 \text{ Hz}$  and with an amplitude of  $1 \text{ V}_p$  was used. On the gold clusters, a local Kelvin signal up to  $V_{\text{KPFM}} = 1.7 \text{ V}$  larger compared to the terraces was observed during the measurements presented here.

Experiments were performed with standard silicon (type PPP-NCH, Nanosensors, Switzerland, specified tip radius  $< 10 \text{ nm}$ ) and platinum iridium (Pt/Ir) coated silicon cantilevers (type NCHPt, Nanosensors, Switzerland, specified tip radius  $< 25 \text{ nm}$ ). To remove the oxide layer and contaminants, cantilevers were subjected to argon ion sputtering with the following parameters: Si cantilever:  $p_{\text{Ar}} = 10^{-5}$  mbar,  $U = 0.5 \text{ kV}$ ,  $I = 15 \text{ mA}$ , 5 min; Pt/Ir-coated cantilever:  $p_{\text{Ar}} = 10^{-6}$  mbar,  $U = 0.5 \text{ kV}$ ,  $I = 15 \text{ mA}$ , 2 min.

A bare silicon and a Pt/Ir-coated silicon cantilever with parameters  $f_0 = 277523 \text{ Hz}$ ,  $k_0 = 57.43 \text{ N/m}$ , and  $Q = 22000$  (bare silicon) as well as  $f_0 = 277203 \text{ Hz}$ ,  $k_0 = 18.58 \text{ N/m}$ , and  $Q = 18900$  (Pt/Ir-coated silicon) were used during the experiments. The cantilever-specific force constants were measured using the thermal method [67] and the eigenfre-

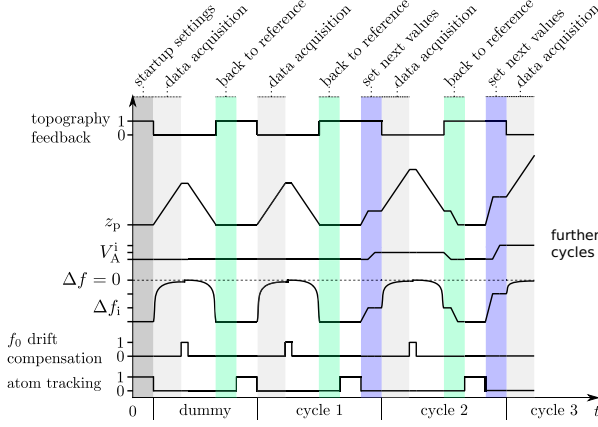


FIG. 8. Data acquisition protocol for FCA.

quencies determined with the tip retracted by about 60 nm from the surface. Due to the system geometry, the direction of the cantilever oscillation is tilted with respect to the surface normal by  $\alpha \approx 12.5^\circ$ .

#### APPENDIX E: FCA MEASUREMENT PROTOCOL

A set of  $2N$  distance-dependent  $\Delta f(z_p)$  curves is acquired with ascending and descending voltage amplitude values  $V_A^i$  ( $V_A^1, V_A^2, \dots, V_A^N, V_A^N, V_A^{N-1}, \dots, V_A^1$ ).

Data acquisition is started when sufficient time has passed after the initial approach to reduce piezo creep artefacts. At this point, atom tracking is activated to measure the residual drift and to compensate for the linear component by the feed-forward technique [53]. It is helpful to acquire a “dummy” curve before the first measurement curve to ensure that the piezo scanner yields a similar response during the whole measurement set.

An initial estimate for the sensitivity factor  $S$  is made using the  $\gamma$ -method. Using this estimate, a series  $V_A^1, \dots, V_A^N$  of  $N$  voltage amplitudes is chosen in the physical amplitude range of interest. For the first voltage amplitude  $V_A^1$  and a suitable frequency shift setpoint  $\Delta f_1$ , the unscaled normalised frequency shift  $\gamma^* = \gamma_1 \cdot f_0 / (k_0 S^{3/2}) = (V_A^1)^{3/2} \Delta f_1$  is calculated. The data acquisition procedure for each amplitude value proceeds along the steps schematically depicted in Fig. 8. These steps are repeated  $2N$  times for  $N$  different amplitudes using ascending and descending voltage amplitude values.

(1) Atom tracking is used to measure lateral and vertical drift. Based on this measurement, the linear drift vector for the feed-forward compensation is updated, feed-forward activated, and atom-tracking stopped.

(2) The voltage amplitude is set to the next value and the frequency-shift set point is adjusted according to  $\gamma^*$ . To reduce the risk of tip instabilities, the frequency shift setpoint is increased after increasing the amplitude value and decreased before decreasing the amplitudes value.

(3) The topography feedback is switched off.

(4) The NC-AFM signals are sampled while ramping  $z_p$  through the given range. The  $z_p$  ramp range has to be chosen to be at least  $2A_{\max}$  for the largest amplitude  $A_{\max}$  for a reliable

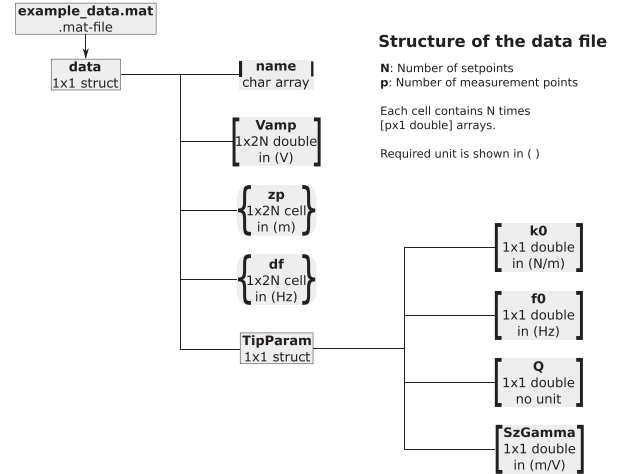


FIG. 9. Schematic construction of the struct EXAMPLE\_DATA.MAT in MATLAB.

force calculation. In the present case, we choose amplitudes up to about 20 nm with a  $z_p$  range of 60 nm in 25 pm steps.

(5) With the tip held at the largest separation to the surface, the center frequency  $f_0$  is readjusted in the phase-locked loop to compensate for thermal drift of the center frequency.

(6) The tip is then moved back to the surface and the topography feedback is reactivated.

(7) The procedure is repeated by starting with step 1 until all voltage amplitude values are processed.

We typically measure a total of 12 or 14  $\Delta f(z)$  curves per position, thus using six or seven different amplitudes. To determine nonlinear drift and creep artifacts in the dataset, it is most helpful to acquire the curves in equidistant time steps. Hence, the complete FCA measurement protocol is implemented in a script form to ensure that the curves are measured in equidistant time steps  $t_{\text{cycle}}$ .

#### APPENDIX F: FCA DATA ANALYSIS PROCEDURE

The true force-distance curve is derived from the measured set of  $\Delta f(z_p)$  curves by a multiparameter optimization algorithm. This algorithm is implemented in the MATLAB method `applyFCA` explained here in detail. The `applyFCA` function requires as input several arguments for the optimisation process. These are `SGFILTPARAM`, `NODEPARAM`, `OPTIONS`, `DATA_PATH`, and `SAVE_PATH`. `SGFILTPARAM` is a MATLAB struct containing information about the frame size and order of the Savitzky-Golay filter [72] applied during the force inversion for calculating the derivative [73]. All information about the node placement on the reference force curve is saved in the struct `NODEPARAM`. The `OPTIONS` struct contains the options for the built-in MATLAB function `FMINSEARCH` utilized by this implementation. Default values suitable for FCA are included. The results of `APPLYFCA` are saved in the directory set in `SAVE_PATH` and the data file is loaded from the location given in `DATA_PATH`. By running the script `RUN_FCA.M`, all parameters are set and inserted into the function `APPLYFCA`. The complete optimization can directly

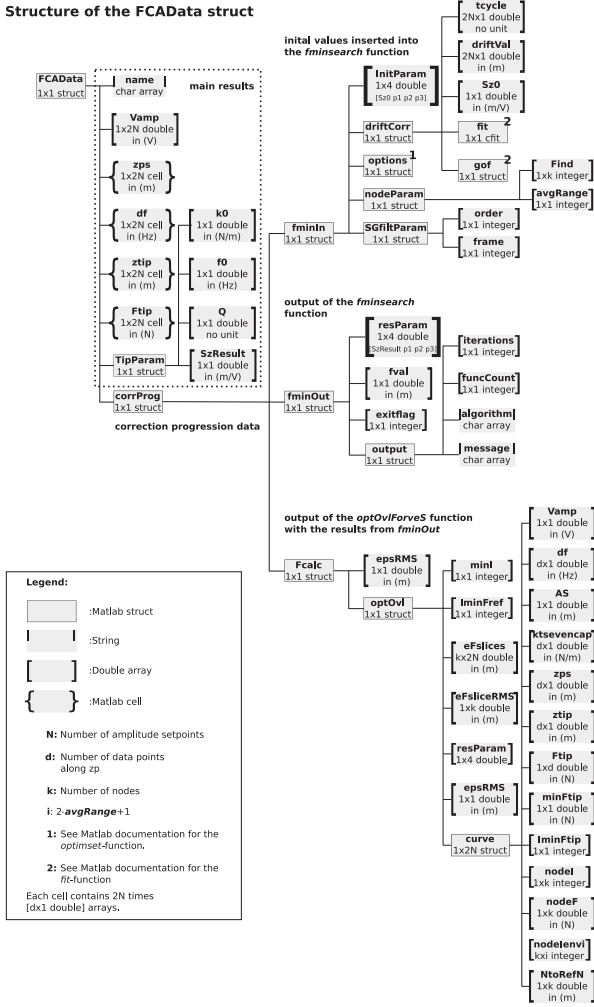


FIG. 10. Schematic overview of the output data of FCA.

be run by using the example data provided in the file EXAMPLE\_DATA.MAT (see Fig. 9). The corresponding results (structure of the result struct shown in Fig. 10) are stored in the file EXAMPLE\_DATA\_FCARESULT.MAT. This file resides in the SAVE\_PATH folder as the input data after running RUN\_FCA.M. The input data file (here EXAMPLE\_DATA.MAT) is copied to the output folder and thus stored with all generated output data. The example data fulfill the minimum requirements of one measured data set as outlined in Fig. 9. The minimum requirements are matrices with the frequency shift data (field  $df$ ), the voltage amplitudes (field  $Vamp$ ), the piezopositions (field  $zps$ ), the basic cantilevers properties determined in the experiment (force constant  $k\theta$ , cantilever eigenfrequency  $f\theta$ , and quality factor  $Q$ ), and an estimation of the sensitivity factor  $S_z$  which is here stored in the field  $S_zGuess$ .

The flowchart in Fig. 11 depicts the work flow of the FCA method as implemented in the script RUN\_FCA.M. This script executes the optimization process in APPLYFCA as the central routine. In a first step, initial parameters for  $S_z$  and for the drift compensation are calculated. With an initial estimation

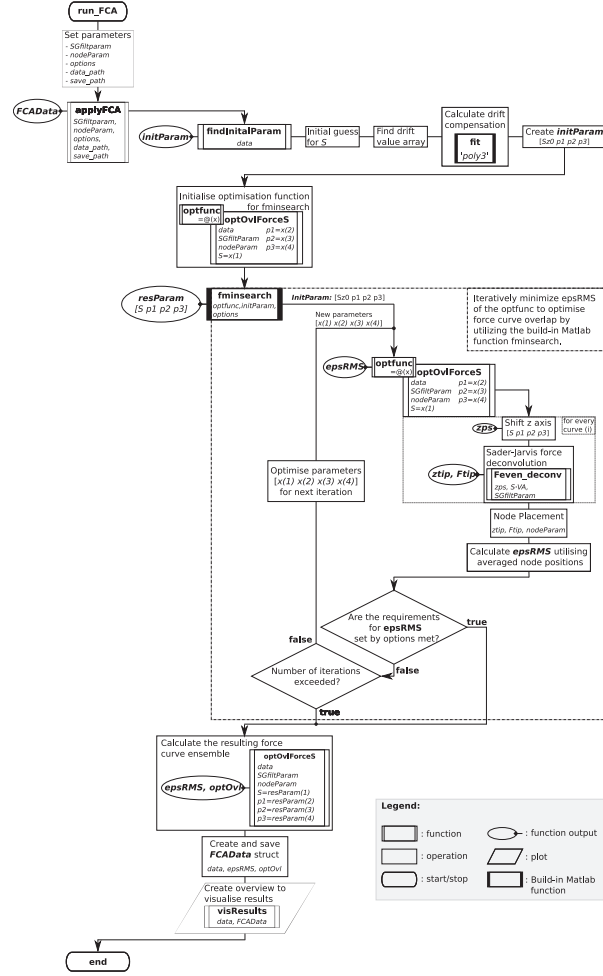


FIG. 11. Flowchart for FCA analysis procedure.

for  $S_z$  (e.g., by using  $S_{y,z}$ ), the voltage amplitudes  $V_A^i$  are converted to the physical oscillation amplitudes  $A^i$ . The drift is approximated by a third-order polynomial. The initial  $S_z$  value and the polynomial coefficients  $p_1, p_2, p_3$  are saved in INITPARAM. This four parameter tuple ( $S_z, p_1, p_2, p_3$ ) is optimized to find a minimum deviation between nodes placed on the set of force curves utilising the build-in MATLAB function FMINSEARCH. The force conversion is executed by the script FEVEN\_DECONV.M using the inversion algorithm by Sader and Jarvis [48]. In the set of force curves, six nodes with equivalent forces are placed within the region of steep slope of every force curve. To prohibit that the nodes are affected by data outliers, every node is averaged over five samples. As a measure of the curve's deviation, the RMS deviation ( $epsRMS$ ) of all nodes with respect to those of a reference curve is calculated. Hence, the final EPSRMS value is a measure for the quality of the optimisation. The reference curve is the first curve of the measurement set, it is drift free and thus is not affected by the drift correction but rather only shifted by  $S_z$ . The nodes are placed with respect to the smallest shared absolute force value of the complete force curve ensemble. This optimization

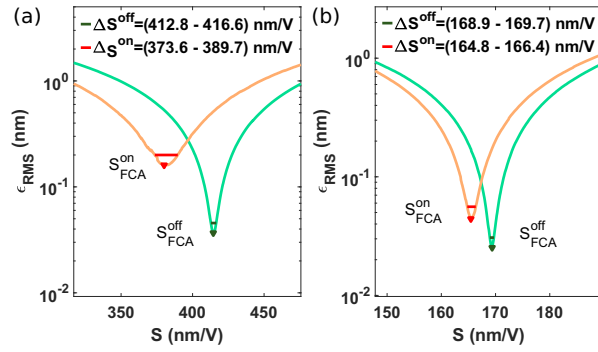


FIG. 12. Error analysis for the FCA method. The width of the  $\epsilon_{\text{RMS}}(S)$  curves 25% above the minimum  $\epsilon_{\text{RMS}}$  value is marked by horizontal lines. Analysis for (a) silicon and (b) Pt/Ir-coated tip.

routine terminates when a specific threshold value for the optimization or an iteration limit is reached. This termination criteria can be set in the OPTIONS struct for FMINSEARCH. Note that the code strictly uses  $S_z$ , the conversion to  $S$  has to be performed with the resulting value.

#### APPENDIX G: ERROR ANALYSIS

To quantify the quality of the FCA optimization, we introduce an analysis based on the  $\epsilon_{\text{RMS}}(S)$  curves as shown in Fig. 12. The curves are the result of keeping the optimized drift polynomial constant and calculating  $\epsilon_{\text{RMS}}$  for  $S$  values around the minimal value  $S_{\text{FCA}}$ . The width of the curves around the minimum can be interpreted as the uncertainty of the optimized result due to experimental errors where a narrow dip in  $\epsilon_{\text{RMS}}(S)$  reflects a small uncertainty in the optimized force curves. As a conservative estimate for the accuracy of  $S_{\text{FCA}}$ , we determine the full width of the  $\epsilon_{\text{RMS}}(S)$  curve at an  $\epsilon_{\text{RMS}}$  value 25% above the minimum value. This is shown for the measurements with the

silicon [Fig. 12(a)] and Pt/Ir coated cantilever [Fig. 12(b)] and yields  $S_{\text{FCA}}^{\text{off}} = (414.6 \pm 1.9) \text{ nm/V}$  and  $S_{\text{FCA}}^{\text{on}} = (383 \pm 8) \text{ nm/V}$  for the bare silicon tip and  $S_{\text{FCA}}^{\text{off}} = (169.3 \pm 0.5) \text{ nm/V}$  and  $S_{\text{FCA}}^{\text{on}} = (165.5 \pm 0.9) \text{ nm/V}$  for the Pt/Ir-coated tip. For both off cluster measurements,  $S$  varies by less than 0.5%, highlighting the robustness of the FCA method.

#### APPENDIX H: FCA WITH MATRIX FORCE INVERSION ALGORITHM

All results in the main paper are based on the FCA method utilizing the force inversion algorithm introduced by Sader and Jarvis [48]. In this Appendix we demonstrate that FCA can be performed equally well with the MATRIX algorithm [47] for force inversion with the comparison reproducing known differences between the two algorithms [50].

Figure 13 presents results of FCA with the MATRIX algorithm applied to the datasets from the simulation [Fig. 13(a)] as well as from the experimental off-cluster measurements with the silicon [Fig. 13(b)] and Pt/Ir-coated [Fig. 13(c)] tips. The input data for FCA with the MATRIX algorithm used in Fig. 13 are identical to the data used in the main paper for FCA with the Sader-Jarvis algorithm (see Figs. 1 and 2 of the main paper) besides applying a Savitzky-Golay smoothing filter [72] with frame size 22 and of order 2 to the frequency shift  $\Delta f$  data. We chose to apply this prefilter as a strategy to yield similar noise levels in the resulting force data as achieved with FCA+Sader/Jarvis. In the latter case, a Savitzky-Golay filter is used at the derivation step (see also Appendix F), however, a similar strategy for calculating the derivative in the MATRIX algorithm is not provided. Thus, we revert to filtering the input  $\Delta f$  data.

The results for the sensitivity factor  $S$  are virtually identical to the ones yielded with the Sader-Jarvis algorithm. The force curves resulting from the simulated data [Fig. 13(a)] show a perfect overlap and the residual error  $\epsilon_{\text{RMS}}$  represents again solely the numerical error. An excellent overlap of the force

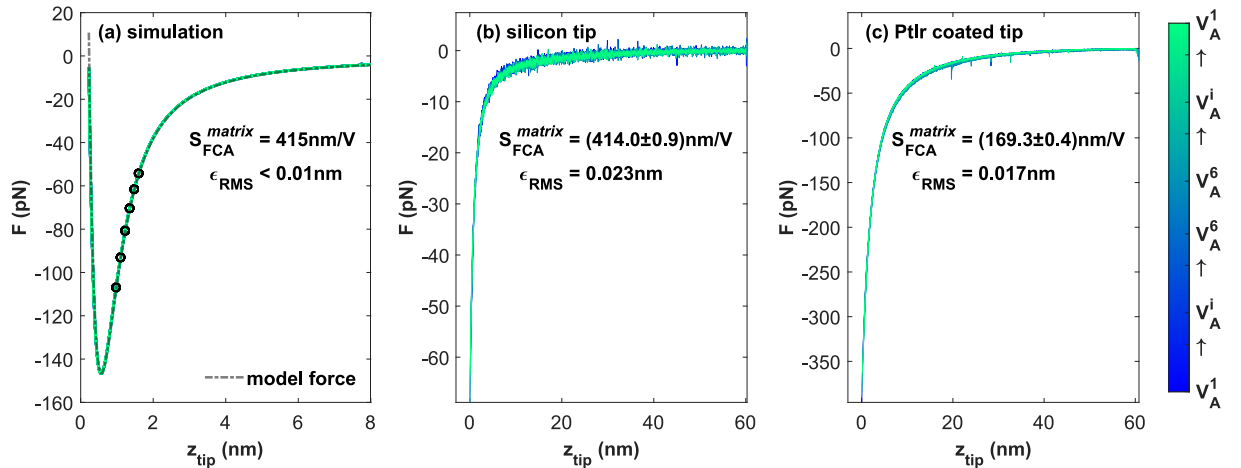


FIG. 13. Results of the FCA method utilizing the MATRIX force inversion algorithm [47] for (a) a simulated data set (identical model force as in the main paper, see also Fig. 1) and experimental measurements performed with (b) a silicon tip [off-cluster, see also Fig. 2(c)], and (c) a Pt/Ir-coated tip [off-cluster, see also Fig. 2(d)].

curves with slightly smaller  $\epsilon_{\text{RMS}}$  values are also found for the experimental data acquired with the silicon and Pt/Ir-coated tips. The slight differences in the resulting values, in the noise levels, and the number of single outliers apparent in Figs. 13(b) and 13(c) are explained by the different filtering strategies as outlined before. We found that the sensitivity

values  $S$  calculated with FCA+MATRIX slightly differ at decimal places when modifying the filter parameters, yet, these fluctuations are well within the accuracy of the FCA method. A detailed discussion on the differences between the two force inversion algorithms has been presented before by Welker *et al.* [50].

- [1] L. Kantorovich, *Quantum Theory of the Solid State: An Introduction*, Fundamental Theories of Physics, Vol. 136 (Springer Science, Dordrecht, The Netherlands, 2004), p. 626.
- [2] J. N. Israelachvili, *Intermolecular and Surface Forces (Third Edition)* (Academic, San Diego, CA, 2011), p. iii.
- [3] H. J. Mamin and D. Rugar, *Appl. Phys. Lett.* **79**, 3358 (2001).
- [4] L. L. Liu, S. Kheifets, V. Ginis, and F. Capasso, *Phys. Rev. Lett.* **116**, 228001 (2016).
- [5] V. Blums, M. Piotrowski, M. I. Hussain, B. G. Norton, S. C. Connell, S. Gensemer, M. Lobino, and E. W. Streed, *Sci. Adv.* **4**, eaao4453 (2018).
- [6] M. A. Lantz, H. J. Hug, R. Hoffmann, P. J. A. van Schendel, P. Kappenberger, S. Martin, A. Baratoff, and H. J. Güntherodt, *Science* **291**, 2580 (2001).
- [7] Y. Sugimoto, P. Pou, M. Abe, P. Jelinek, R. Pérez, S. Morita, and O. Custance, *Nature* **446**, 64 (2007).
- [8] H. F. Wen, Q. Z. Zhang, Y. Adachi, M. Miyazaki, Y. Sugawara, and Y. J. Li, *Appl. Surf. Sci.* **505**, 144623 (2020).
- [9] A. M. Sweetman, S. P. Jarvis, H. Q. Sang, I. Lekkas, P. Rahe, Y. Wang, J. B. Wang, N. R. Champness, L. Kantorovich, and P. Moriarty, *Nat. Commun.* **5**, 3931 (2014).
- [10] P. Jelínek, *J. Phys.: Condens. Matter* **29**, 343002 (2017).
- [11] H. Mönig, S. Amirjalayer, A. Timmer, Z. Hu, L. Liu, O. Díaz Arado, M. Cnudde, C. A. Strassert, W. Ji, M. Rohlfling, and H. Fuchs, *Nat. Nanotechnol.* **13**, 371 (2018).
- [12] L. Costa, M. S. Rodrigues, E. Newman, C. Zubieta, J. Chevrier, and F. Comin, *J. Mol. Recognit.* **26**, 689 (2013).
- [13] S. Senapati, A. B. Poma, M. Cieplak, S. Filipek, and P. S. H. Park, *Anal. Chem.* **91**, 7226 (2019).
- [14] F. S. Ruggeri, T. Sneideris, M. Vendruscolo, and T. P. J. Knowles, *Arch. Biochem. Biophys.* **664**, 134 (2019).
- [15] E. T. Herruzo, H. Asakawa, T. Fukuma, and R. Garcia, *Nanoscale* **5**, 2678 (2013).
- [16] E. I. Altman, M. Z. Baykara, and U. D. Schwarz, *Acc. Chem. Res.* **48**, 2640 (2015).
- [17] A. Sweetman, M. Rashid, S. Jarvis, J. Dunn, P. Rahe, and P. Moriarty, *Nat. Commun.* **7**, 10621 (2016).
- [18] D. Martin-Jimenez and R. Garcia, *J. Phys. Chem. Lett.* **8**, 5707 (2017).
- [19] J. Laurent, H. Sellier, A. Mosset, S. Huant, and J. Chevrier, *Phys. Rev. B* **85**, 035426 (2012).
- [20] E. Voloshina and Y. Dedkov, *Phys. Rev. B* **93**, 235418 (2016).
- [21] L. A. Jurado, H. Kim, A. Rossi, A. Arcifa, J. K. Schuh, N. D. Spencer, C. Leal, R. H. Ewaldt, and R. M. Espinosa-Marzal, *Phys. Chem. Chem. Phys.* **18**, 22719 (2016).
- [22] L. R. Dickinson, B. M. J. M. Suijkerbuijk, S. Berg, F. H. M. Marcelis, and H. C. Schniepp, *Energy & Fuels* **30**, 9193 (2016).
- [23] P. M. Claesson, I. Dobryden, G. Li, Y. J. He, H. Huang, P. A. Thoren, and D. B. Haviland, *Phys. Chem. Chem. Phys.* **19**, 23642 (2017).
- [24] R. Pawlak, C. Drechsel, P. D'Astolfo, M. Kisiel, E. Meyer, and J. I. Cerda, *Proc. Nat. Acad. Sci. USA* **117**, 228 (2020).
- [25] C. Chiutu, A. M. Sweetman, A. J. Lakin, A. Stannard, S. Jarvis, L. Kantorovich, J. L. Dunn, and P. Moriarty, *Phys. Rev. Lett.* **108**, 268302 (2012).
- [26] M. S. Rodrigues, L. Costa, J. Chevrier, and F. Comin, *Appl. Phys. Lett.* **101**, 203105 (2012).
- [27] A. Caló, O. V. Robles, S. Santos, and A. Verdaguier, *Beilstein J. Nanotechnol.* **6**, 809 (2015).
- [28] S. Kawai, A. S. Foster, T. Björkman, S. Nowakowska, J. Björk, F. F. Canova, L. H. Gade, T. A. Jung, and E. Meyer, *Nat. Commun.* **7**, 11559 (2016).
- [29] M. J. Shon, S. H. Rah, and T. Y. Yoon, *Sci. Adv.* **5**, 12 (2019).
- [30] T. Fukuma, B. Reischl, N. Kobayashi, P. Spijker, F. F. Canova, K. Miyazawa, and A. S. Foster, *Phys. Rev. B* **92**, 155412 (2015).
- [31] H. Söngen, B. Reischl, K. Miyata, R. Bechstein, P. Raiteri, A. L. Rohl, J. D. Gale, T. Fukuma, and A. Kühnle, *Phys. Rev. Lett.* **120**, 116101 (2018).
- [32] H. Söngen, Y. M. Morais Jaques, L. Zivanovic, S. Seibert, R. Bechstein, P. Spijker, H. Onishi, A. S. Foster, and A. Kühnle, *Phys. Rev. B* **100**, 205410 (2019).
- [33] B. Reischl, P. Raiteri, J. D. Gale, and A. L. Rohl, *J. Phys. Chem. C* **123**, 14985 (2019).
- [34] A. Sweetman, J. Stirling, S. P. Jarvis, P. Rahe, and P. Moriarty, *Phys. Rev. B* **94**, 115440 (2016).
- [35] J. Onoda, M. Ondráček, P. Jelínek, and Y. Sugimoto, *Nat. Commun.* **8**, 15155 (2017).
- [36] J. N. Ladenthin, T. Frederiksen, M. Persson, J. C. Sharp, S. Gawinkowski, J. Waluk, and T. Kumagai, *Nat. Chem.* **8**, 935 (2016).
- [37] S. Garcia-Manyes and A. E. M. Beedle, *Nat. Rev. Chem.* **1**, 0083 (2017).
- [38] A. Sweetman, I. Lekkas, and P. Moriarty, *J. Phys.: Condens. Matter* **29**, 074003 (2017).
- [39] C. Wagner, M. F. B. Green, P. Leinen, T. Deilmann, P. Krüger, M. Rohlfling, R. Temirov, and F. S. Tautz, *Phys. Rev. Lett.* **115**, 026101 (2015).
- [40] D. Rugar, R. Budakian, H. J. Mamin, and B. W. Chui, *Nature* **430**, 329 (2004).
- [41] L. Thiel, Z. Wang, M. A. Tschudin, D. Rohner, I. Gutiérrez-Lezama, N. Ubrig, M. Gibertini, E. Giannini, A. F. Morpurgo, and P. Maletinsky, *Science* **364**, 973 (2019).
- [42] Z. Sun, M. P. Boneschanscher, I. Swart, D. Vanmaekelbergh, and P. Liljeroth, *Phys. Rev. Lett.* **106**, 046104 (2011).
- [43] C. Barth, A. S. Foster, C. R. Henry, and A. L. Shluger, *Adv. Mater.* **23**, 477 (2011).
- [44] H. Söngen, R. Bechstein, and A. Kühnle, *J. Phys.: Condens. Matter* **29**, 274001 (2017).
- [45] B. Voigtländer, *Atomic Force Microscopy*, 2nd ed., NanoScience and Technology (Springer Nature, Cham, Switzerland, 2019).

- [46] M. Guggisberg, M. Bammerlin, C. Loppacher, O. Pfeiffer, A. Abdurixit, V. Barwich, R. Bennewitz, A. Baratoff, E. Meyer, and H. J. Güntherodt, *Phys. Rev. B* **61**, 11151 (2000).
- [47] F. J. Giessibl, *Appl. Phys. Lett.* **78**, 123 (2001).
- [48] J. E. Sader and S. P. Jarvis, *Appl. Phys. Lett.* **84**, 1801 (2004).
- [49] J. E. Sader, B. D. Hughes, F. Huber, and F. J. Giessibl, *Nat. Nanotechnol.* **13**, 1088 (2018).
- [50] J. Welker, E. Illek, and F. J. Giessibl, *Beilstein J. Nanotechnol.* **3**, 238 (2012).
- [51] J. Lübke, M. Temmen, P. Rahe, and M. Reichling, *Beilstein J. Nanotechnol.* **7**, 1885 (2016).
- [52] M. Abe, Y. Sugimoto, T. Namikawa, K. Morita, N. Oyabu, and S. Morita, *Appl. Phys. Lett.* **90**, 203103 (2007).
- [53] P. Rahe, J. Schütte, W. Schniederberend, M. Reichling, M. Abe, Y. Sugimoto, and A. Kühnle, *Rev. Sci. Instrum.* **82**, 063704 (2011).
- [54] J. F. Portolés, P. J. Cumpson, J. Hedley, S. Allen, P. M. Williams, and S. J. B. Tendler, *J. Exp. Nanosci.* **1**, 51 (2006).
- [55] G. H. Simon, M. Heyde, and H.-P. Rust, *Nanotechnology* **18**, 255503 (2007).
- [56] Y. Sugimoto, Y. Nakajima, D. Sawada, K. I. Morita, M. Abe, and S. Morita, *Phys. Rev. B* **81**, 245322 (2010).
- [57] J. F. Gonzales Martinez, I. Nieto-Carvajal, and J. Colchero, *Nanotechnology* **24**, 185701 (2013).
- [58] S. S. Borysov, D. Forchheimer, and D. B. Haviland, *Beilstein J. Nanotechnol.* **5**, 1899 (2014).
- [59] F. J. Azcona, A. Jha, C. Yáñez, R. Atashkhoei, and S. Royo, *Sensors* **16**, 997 (2016).
- [60] L. Hao, Q. Wang, P. Peng, Z. Cao, W. Jiao, F. Yang, W. Liu, R. Wang, and X. He, *Ultramicroscopy* **174**, 106 (2017).
- [61] O. E. Dagdeviren, Y. Miyahara, A. Mascaro, and P. Grütter, *Rev. Sci. Instrum.* **90**, 013703 (2019).
- [62] F. J. Giessibl, *Phys. Rev. B* **56**, 16010 (1997).
- [63] See Supplemental Material at <http://link.aps.org/supplemental/10.1103/PhysRevB.103.075409> for the program code.
- [64] H. H. Pieper, C. Lammers, L. Tröger, S. Bahr, and M. Reichling, *Rev. Sci. Instrum.* **83**, 055110 (2012).
- [65] H. H. Pieper, C. Derks, M. H. Zoellner, R. Olbrich, L. Tröger, T. Schroeder, M. Neumann, and M. Reichling, *Phys. Chem. Chem. Phys.* **14**, 15361 (2012).
- [66] R. Olbrich, G. E. Murgida, V. Ferrari, C. Barth, A. M. Llois, M. Reichling, and M. V. Ganduglia-Pirovano, *J. Phys. Chem. C* **121**, 6844 (2017).
- [67] J. Lübke, M. Temmen, P. Rahe, A. Kühnle, and M. Reichling, *Beilstein J. Nanotechnol.* **4**, 227 (2013).
- [68] S. Kuhn and P. Rahe, *Phys. Rev. B* **89**, 235417 (2014).
- [69] C. Argento and R. H. French, *J. Appl. Phys.* **80**, 6081 (1996).
- [70] S. Torbrügge, J. Lübke, L. Tröger, M. Cranney, T. Eguchi, Y. Hasegawa, and M. Reichling, *Rev. Sci. Instrum.* **79**, 083701 (2008).
- [71] M. Nonnenmacher, M. P. O'Boyle, and H. K. Wickramasinghe, *Appl. Phys. Lett.* **58**, 2921 (1991).
- [72] A. Savitzky and M. J. E. Golay, *Anal. Chem.* **36**, 1627 (1964).
- [73] S. Kuhn, M. Kittelmann, Y. Sugimoto, M. Abe, A. Kühnle, and P. Rahe, *Phys. Rev. B* **90**, 195405 (2014).





## 6. Quantitative dynamic force microscopy with inclined tip oscillation

With the possibility to precisely measure forces with dynamic AFM using FCA [53], it is revealed that the inclination of the cantilever, leading to an inclination of the tip oscillation path of usually  $10^\circ$  to  $20^\circ$  with respect to the surface normal, is not considered in the prevalent description for dynamic AFM. Yet, this inclination can have a notable effect on force measurements by causing systematic errors in experimental force data.

In the following manuscript, therefore the mathematical description of dynamic AFM is extended by a free orientation of the oscillation path and the measurement of nanoscale forces with an inclined sensor not along the vertical direction  $z$  as is common practice, but rather along an inclined axis  $w$  is proposed. This axis is defined to be parallel to the inclined oscillation path in order to generate the necessary overlap for the force deconvolution procedures. Using numerical calculations, first the effects of an inclined tip oscillation for prevalent data acquisition and analysis protocols are simulated and the resulting systematic deviation are revealed. Second, data acquisition and force recovery along the inclined axis  $w$  is simulated yielding excellent agreement between the raw and recovered data. For a conservative force field, the resulting force principally contains the same physical information as a vertical measurement, yet it represents the projection along the axis  $w$ .

Summarising, the following manuscript extends the theory of dynamic AFM by including the angle of an inclined tip oscillation, discusses the physical consequences from simulated data on force measurements, and introduces a modified protocol for AFM-based force measurements with an inclined sensor.

The following work initially was published in [58].



## Quantitative dynamic force microscopy with inclined tip oscillation

Philipp Rahe<sup>\*</sup>, Daniel Heile, Reinhard Olbrich and Michael Reichling

### Full Research Paper

Open Access

Address:  
Fachbereich Physik, Universität Osnabrück, Barbarastrasse 7, 49076  
Osnabrück, Germany

Email:  
Philipp Rahe<sup>\*</sup> - prahe@uni-osnabrueck.de

\* Corresponding author

Keywords:  
atomic force microscopy; cantilever; quantitative force measurement;  
sampling path

*Beilstein J. Nanotechnol.* **2022**, *13*, 610–619.  
<https://doi.org/10.3762/bjnano.13.53>

Received: 10 February 2022  
Accepted: 25 May 2022  
Published: 06 July 2022

Associate Editor: T. Glatzel

© 2022 Rahe et al.; licensee Beilstein-Institut.  
License and terms: see end of document.

### Abstract

In the mathematical description of dynamic atomic force microscopy (AFM), the relation between the tip–surface normal interaction force, the measurement observables, and the probe excitation parameters is defined by an average of the normal force along the sampling path over the oscillation cycle. Usually, it is tacitly assumed that tip oscillation and force data recording follows the same path perpendicular to the surface. Experimentally, however, the sampling path representing the tip oscillating trajectory is often inclined with respect to the surface normal and the data recording path. Here, we extend the mathematical description of dynamic AFM to include the case of an inclined sampling path. We find that the inclination of the tip movement can have critical consequences for data interpretation, especially for measurements on nanostructured surfaces exhibiting significant lateral force components. Inclination effects are illustrated by simulation results that resemble the representative experimental conditions of measuring a heterogeneous atomic surface. We propose to measure the AFM observables along a path parallel to the oscillation direction in order to reliably recover the force along this direction.

### Introduction

Atomic force microscopy (AFM) is a quantitative technique that allows for probing the force field above a surface in one, two, or three dimensions. While imaging in a plane parallel to the surface provides nanoscale and atomic structural information [1], force curves, usually acquired along a recording path perpendicular to the surface, provide quantitative information about the details of the tip–surface interaction when properly analysed [2]. Recently, a universal description of quantitative

dynamic force microscopy based on the harmonic approximation has been developed [3], yielding three central equations that link the physical interaction parameters force  $\vec{F}_{ts}$  and damping  $\vec{\gamma}_{ts}$  with the measurement observables static deflection  $q_s$ , oscillation amplitude  $A$ , and phase  $\varphi$  as well as the excitation parameters frequency  $f_{exc}$  and force  $F_{exc}$ . This theory specifically predicts the distant-dependent frequency shift of a tip moved perpendicular to a surface for a given force curve.

Inversion formulae are available that allow for the extraction of the interaction force from measured frequency-shift data [4,5].

A tacit assumption of all prevalent algorithms for force inversion is that the axis of data acquisition (herein denoted as the recording path, usually the axis of the piezo scanner,  $z_p$ ) is parallel to the axis of the oscillation (herein denoted as the sampling path). However, in a typical experimental setup this is not the case. Instead, angles of  $10^\circ$  to  $20^\circ$  between these two directions are often present for technical reasons. Consequences of this inclined AFM cantilever mount have been identified before, in particular for atomic force microscopy performed in static (“contact”) mode where an effective spring constant [6-8] has been introduced and a torque [9,10] as well as load [11] correction has been applied. Additionally, a tilted cantilever has been found to lead to a modification of the tip-sample convolution [12], to enhance the sensitivity of the measurement to the probe side [13], and to influence results of multifrequency AFM and Kelvin probe force microscopy [14]. In the presence of a viscous damping layer, in-plane dissipation mechanisms have been found to cause systematic changes of the phase shift in amplitude-modulation AFM depending on the cantilever inclination [15]. Furthermore, it has been proposed to use the presence of a lateral component in the tip oscillation path for the investigation of in-plane material properties, such as the in-plane shear modulus [16]. Last, the influence of the inclination between oscillation direction and surface plane has been used in lateral force microscopy to determine the probe oscillation amplitude [17].

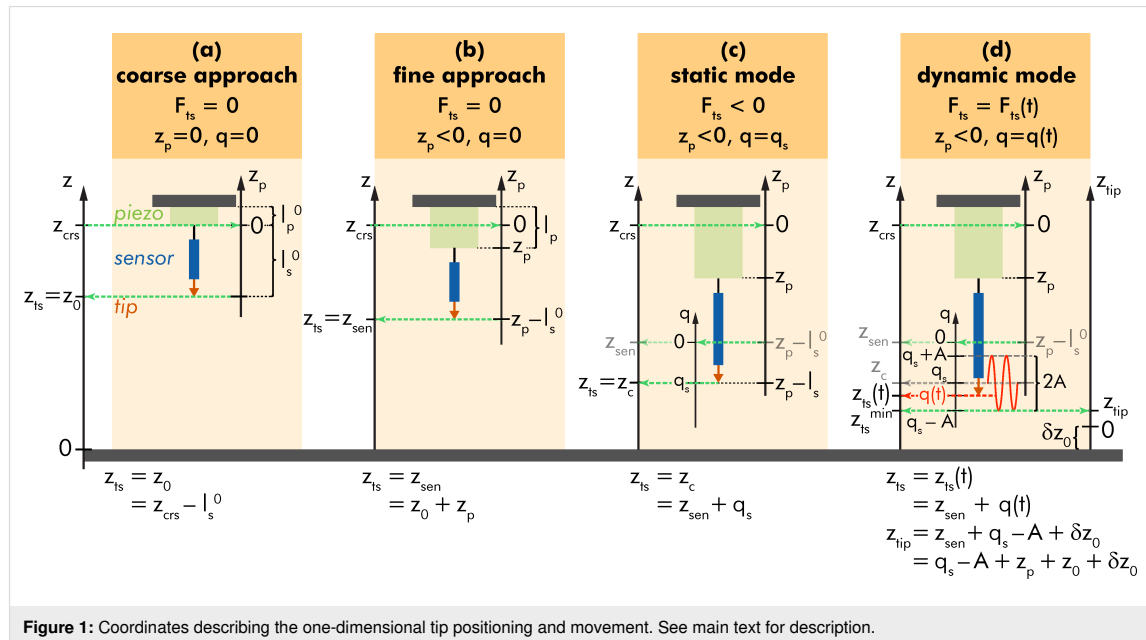
Here, we extend the established mathematical description for dynamic atomic force microscopy [3] by including free orientations of the tip sampling and data recording paths. The resulting formulae are discussed and implications for precise force measurements [2] are identified and quantified. Most importantly, the data acquisition with an inclined tip sampling path requires modifications of the experimental procedures and data analysis protocols for force measurements to avoid systematic errors in the interpretation of force curve and imaging data.

## Results and Discussion

### Sensor positioning, sensor displacement, and tip position

Prerequisite to quantitative force microscopy is a precise definition of the involved probe and sample coordinates as well as probe dynamical parameters that are outlined in the following.

In dynamic AFM, the force  $\vec{F}_{ts}$  acting between a sharp tip and the surface under investigation is measured as a function of the tip position  $\vec{r}_{ts}$  that is usually described in Cartesian coordinates with the origin placed in the sample surface and the  $z$ -axis with unit vector  $\vec{e}_z$  oriented perpendicular to the surface as shown in Figure 1. Lateral movements of the tip as applied for imaging are associated with the  $x$  and  $y$  axes, while the tip-sample distance  $z_{ts}$  is measured along the  $z$ -axis. In most AFM implementations, the force measurement is restricted to nominally measuring the normal component of the tip-sample force  $F_{ts}^z = \vec{F}_{ts} \cdot \vec{e}_z$ , often denoted by  $F_N$ . The ideal force curve



is a measurement of  $F_{\text{ts}}^z(z_{\text{ts}})$  while the measurement of  $F_{\text{ts}}^z(x_{\text{ts}}, y_{\text{ts}}, z_{\text{ts}})$  is referred to as force mapping.

To measure the tip–surface force in a dynamic measurement, the force probe acts as a high-Q oscillator and elastically responds to  $\bar{F}_{\text{ts}}$  by static and dynamic displacement described by  $q = \bar{q} \cdot \bar{e}_q$  with  $\bar{e}_q$  being the unit vector along the tip sampling path. This path is usually straight and assumed to be strictly parallel to  $\bar{e}_z$ . Furthermore, we assume an infinitely stiff sensor in directions perpendicular to  $\bar{e}_q$  as well as a linear sensor response along  $\bar{e}_q$ . Then, the static probe response follows Hooke’s law  $F_{\text{ts}}^z(x_{\text{ts}}, y_{\text{ts}}, z_{\text{ts}}) = kq$ , with  $k$  being the static sensor force constant [18]. In dynamic mode operation, the sensor is excited to periodic displacement  $q(t) = q(t + 1/f_{\text{exc}})$  along the  $q$ -axis at an excitation frequency  $f_{\text{exc}}$ .

To bring the tip in the desired range of interaction with the surface and to perform the movements required for imaging, force mapping, and taking force curves, the sensor is moved by coarse and fine positioning elements acting at least along the  $z$ -axis. To accomplish this, the sensor is attached to a piezo element allowing for fine positioning that, in turn, is attached to a coarse positioning system. The respective sensor positioning movements, the sensor oscillation, and its response to the mean tip–surface force are illustrated in the sketches of Figure 1 for the case of parallel tip sampling and data recording paths.

Initially, the sensor assembly is moved towards the surface by the coarse positioning system so that the relaxed piezo rests at position  $z_{\text{crs}}$  and the tip at its starting position  $z_0$  (Figure 1a). In its relaxed state, the  $z$  piezo and the force sensor have a length of  $l_p^0$  and  $l_s^0$ , respectively. Applying a voltage to the  $z$ -piezo results in an extension of the piezo length  $l_p$  that is described as a piezo position  $z_p$  on the separate axis  $z_p$  with unit vector  $\bar{e}_p$  and with the origin chosen to coincide with the  $z_{\text{crs}}$  position (Figure 1b). As the unit vectors  $\bar{e}_z$  and  $\bar{e}_p$  are chosen to point into the same direction, a piezo extension  $z_p < 0$  results in an approach of the tip towards the surface while  $z_p > 0$  indicates a tip retraction. Coarse and fine approach define the sensor position  $z_{\text{sen}} = z_0 + z_p$ , which is at this point identical to the tip position (tip–sample distance)  $z_{\text{ts}}$  as the force  $F_{\text{ts}}$  acting on the tip is unmeasurably small for sufficiently large  $z_{\text{ts}}$ . Upon further approach of the sensor, however, the tip experiences a measurable force, yielding a static sensor displacement  $q_s$  described on the  $q$ -axis with the origin chosen at  $z_{\text{sen}}$ , corresponding to the tip centre position  $z_c = z_{\text{sen}} + q_s$  (Figure 1c). As  $\bar{e}_z$  and  $\bar{e}_q$  point in the same direction, a sensor displacement  $q < 0$  corresponds to a tip movement towards the surface. Note that the tip centre position  $z_c$  cannot easily be set or determined as the static sensor displacement is governed by the a priori unknown force curve. Furthermore,  $q_s$  is usually so small that it is at or beyond the

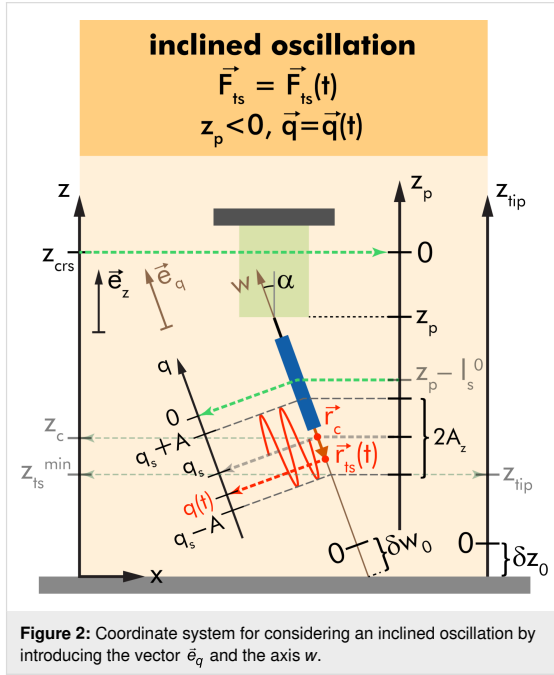
limit of detectability for most NC-AFM implementations. In dynamic NC-AFM operation, the sensor oscillates with an amplitude  $A$  symmetrical to the static displacement  $q_s$  with turning points  $q_s + A$  and  $q_s - A$  (Figure 1d). The momentary tip position at time  $t$  can either be described as the displacement  $q(t)$  or as the position  $z_{\text{ts}}(t)$ , whereby the lower turning point  $z_{\text{ts}}^{\text{min}}$  is the point of strongest tip–surface interaction.

While the tip position and sensor dynamics can principally be well described by the respective positions on the  $z$ -axis, this axis is practically of limited use as its zero point cannot be defined or determined in a reasonable way. This is due to the fact that neither  $z_{\text{crs}}$  nor  $l_s^0$  can be determined with atomic-scale precision, which would be needed for properly taking into account the force curve  $F_{\text{ts}}^z(z_{\text{ts}})$ . Furthermore, it is conceptually difficult to define the position of the surface at the atomic scale. As every force curve acquired on a surface diverges for  $z_{\text{ts}} \rightarrow 0$ , the natural choice of the  $z$ -axis origin would be the  $z$  value approached by the diverging force. This point is, however, experimentally not accessible. Instead, precise values for the piezo position  $z_p$  and the sensor displacement  $q(t)$  are experimentally available. To derive a force–distance curve experimentally, the usual procedure is therefore to apply dynamic AFM and to measure the distance-dependent shift in frequency,  $\Delta f(z_p)$ , of the sensor excitation frequency  $f_{\text{exc}}$  that results when phase resonance for the sensor oscillation is maintained throughout the measurement [19]. The resulting curve  $\Delta f(z_p)$  is a convolution of the covered part of the force curve  $F_{\text{ts}}^z(z_{\text{ts}})$  and a kernel depending on the stabilised sensor oscillation amplitude  $A$ . A sophisticated analysis of the  $\Delta f(z_p)$  curves measured with different oscillation amplitudes  $A$  yields a precise result [2] for the force curve, yet with an arbitrary origin along the  $z$ -axis. In theoretical modelling and analysis of tip–sample interactions, it has been established as a standard to represent force curves as  $F_{\text{ts}}^z = F_{\text{ts}}^z(z_{\text{ts}}^{\text{min}})$  [4,5]. As  $z_{\text{ts}}^{\text{min}}$  is practically not accessible, for the representation of force curves we introduce an axis  $z_{\text{tip}}$  that is identical to the  $z$ -axis except for an unknown offset  $\delta z_0$  for the tip starting position and describe a force curve resulting from the analysis of measured data as  $F_{\text{ts}}^z(z_{\text{tip}})$  where  $z_{\text{tip}} = z_{\text{ts}}^{\text{min}} - \delta z_0$ .

### Geometry for the inclined sampling path

A tip sampling path inclined relative to the  $z$ -axis implies that the direction of oscillation  $\bar{e}_q$  is tilted with respect to  $\bar{e}_z$  as illustrated in Figure 2. We introduce the inclined axis  $w$  parallel to the tip sampling path with  $\bar{e}_w$  pointing in the direction of  $\bar{e}_q$ . Assuming an inclination angle of  $\alpha$  (with  $0 \leq \alpha \leq \pi/2$ ) between  $\bar{e}_z$  and  $\bar{e}_q$ , any position on the  $w$ -axis can be expressed by the respective position on the  $z_{\text{tip}}$ -axis by a simple geometrical transformation. This implies that any sensor movement along  $z_p$  is not in line with the tip sampling path. Therefore, one has to

take into account that the inclined oscillatory motion of the sensor can invoke significant lateral movement of the tip when describing the  $\Delta f$  signal formation and force deconvolution. If the force field  $\vec{F}_{ts}(\vec{r}_{ts}) = \vec{F}_{ts}(x_{ts}, y_{ts}, z_{ts})$  above the surface is homogeneous and isotropic with respect to the lateral coordinates  $x_{ts}$  and  $y_{ts}$ , the inclined axis of sensor oscillation can be taken into account by using transformed position variables  $z_p \rightarrow z_p \cos \alpha$  or  $z_{tip} \rightarrow z_{tip} \cos \alpha$ .



If no such homogeneity is present, however, the  $w$ -axis has to be taken explicitly into account. The definition of a zero position of this  $w$ -axis goes along the same lines as the definition of zero  $\delta z_0$  for the  $z_{tip}$ -axis by introducing  $w_{ts}^{\min}$  and the uncertainty  $\delta w_0$ .

For the further discussion, we define the vectorial sensor displacement  $\vec{q}$  as

$$\vec{q}(t) = q(t) \cdot \vec{e}_q. \quad (1)$$

Within the harmonic approximation [3],  $q(t)$  is given as

$$q(t) = q_s + A \cdot \cos(2\pi f_{exc} t + \varphi) \quad (2)$$

with the static deflection  $q_s$ , the oscillation amplitude  $A$ , the excitation frequency  $f_{exc}$ , and the phase  $\varphi$  [3]. In its vectorial

form, the momentary position of the tip  $\vec{r}_{ts}(t)$  is given as

$$\vec{r}_{ts}(t) = \vec{r}_0 + \vec{r}_p + \vec{q}(t) \quad (3)$$

$$= \vec{r}_c + A \cdot \cos(2\pi f_{exc} t + \varphi) \cdot \vec{e}_q \quad (4)$$

with the centre position  $\vec{r}_c = \vec{r}_0 + \vec{r}_p + q_s \vec{e}_q$ , start position  $\vec{r}_0$ , and piezo position  $\vec{r}_p$ . These quantities generalise the previously introduced  $z$  coordinates  $z_c$ ,  $z_0$ , and  $z_p$ , respectively. We further introduce the reduced amplitude  $A_z$  as the projection of  $A$  on the surface normal [2]

$$A_z = A \cdot \cos \alpha. \quad (5)$$

### Equation of motion for the inclined sampling path

Next, we derive the three AFM equations [3] linking the AFM physical parameters with the experimental observables and excitation parameters for a straight tip sampling path with arbitrary oscillation direction. The starting point is the differential equation describing the displacement  $q(t)$  in presence of the tip-sample force field  $\vec{F}_{ts}(\vec{r}_{ts}, \dot{r}_{ts})$  and excitation force  $F_{exc}^q$  as follows

$$0 = -\frac{k_0}{(2\pi f_0)^2} \ddot{q} - k_0 q - \frac{k_0}{2\pi f_0 Q_0} \dot{q} + F_{exc}^q(t) + F_{ts}^q(q, \dot{q}) \quad (6)$$

with the sensor parameters fundamental eigenfrequency  $f_0$ , modal sensor stiffness  $k_0$  [18], and modal sensor quality factor  $Q_0$ . This equation of motion is a one-dimensional differential equation depending on the tip-sample force component  $F_{ts}^q = \vec{F}_{ts}(\vec{r}_{ts}, \dot{r}_{ts}) \cdot \vec{e}_q$ , following the description in [3,15,16]. The vectorial tip-sample force can generally be expressed by the sum of an even,  $\vec{F}_{even}$ , and an odd,  $\vec{F}_{odd}$ , component

$$F_{ts}^q = \vec{F}_{even} \cdot \vec{e}_q + \vec{F}_{odd} \cdot \vec{e}_q. \quad (7)$$

The deflection  $q$  is periodic with  $T_{exc} = f_{exc}^{-1}$  and the tip-sample force component  $F_{ts}^q$  can, therefore, be expressed by the Fourier sum

$$F_{ts}^q = F_{even}^{q,0} + \sum_{n=1}^{\infty} \left[ F_{even}^{q,n} \cos(2\pi f_{exc} t + \varphi) + F_{odd}^{q,n} \sin(2\pi f_{exc} t + \varphi) \right] \quad (8)$$

with the coefficient for  $n = 0$

$$F_{\text{even}}^{\text{q},0} = f_{\text{exc}} \int_0^{T_{\text{exc}}} \vec{F}_{\text{even}}(\vec{r}_{\text{ts}}(t), \dot{\vec{r}}_{\text{ts}}(t)) \cdot \vec{e}_q dt \quad (9)$$

and the coefficients for  $n \geq 1$

$$F_{\text{even}}^{\text{q},n} = 2f_{\text{exc}} \int_0^{T_{\text{exc}}} \vec{F}_{\text{ts}}(\vec{r}_{\text{ts}}(t), \dot{\vec{r}}_{\text{ts}}(t)) \cdot \vec{e}_q \cos(2\pi n f_{\text{exc}} t + \varphi) dt \quad (10)$$

$$F_{\text{odd}}^{\text{q},n} = 2f_{\text{exc}} \int_0^{T_{\text{exc}}} \vec{F}_{\text{ts}}(\vec{r}_{\text{ts}}(t), \dot{\vec{r}}_{\text{ts}}(t)) \cdot \vec{e}_q \sin(2\pi n f_{\text{exc}} t + \varphi) dt. \quad (11)$$

With the time average defined by [3]

$$\langle \vec{f} \cdot \vec{e}_q \rangle_t = \langle f^q \rangle_t = f_{\text{exc}} \int_0^{T_{\text{exc}}} f^q(t) dt = f_{\text{exc}} \int_0^{T_{\text{exc}}} \vec{f}(t) \cdot \vec{e}_q dt, \quad (12)$$

for an arbitrary function  $\vec{f}$  with projection  $f^q = \vec{f} \cdot \vec{e}_q$ , the Fourier coefficients for  $n \geq 1$  can be expressed in terms of time averages

$$F_{\text{even}}^{\text{q},0} = \langle \vec{F}_{\text{even}} \cdot \vec{e}_q \rangle_t = \langle F_{\text{even}}^q \rangle_t \quad (13)$$

$$F_{\text{even}}^{\text{q},n} = 2 \langle \vec{F}_{\text{ts}} \cdot \vec{e}_q \cos(2\pi n f_{\text{exc}} t + \varphi) \rangle_t \quad (14)$$

$$F_{\text{odd}}^{\text{q},n} = 2 \langle \vec{F}_{\text{ts}} \cdot \vec{e}_q \sin(2\pi n f_{\text{exc}} t + \varphi) \rangle_t. \quad (15)$$

### AFM equations for the inclined sampling path

The three AFM equations follow from evaluating the Fourier coefficients  $F_{\text{even}}^{\text{q},0}$ ,  $F_{\text{even}}^{\text{q},1}$ , and  $F_{\text{odd}}^{\text{q},1}$ . The first step is to calculate the time-averaged form of the three equations (see Appendix section for the derivations)

$$\langle \vec{F}_{\text{even}} \cdot \vec{e}_q \rangle_t = k_0 q_s \quad (16)$$

$$\langle \vec{F}_{\text{even}} \cdot \vec{e}_q (q - q_s) \rangle_t = \frac{k_0 A^2}{2} \left( 1 - \frac{f_{\text{exc}}^2}{f_0^2} \right) - \frac{A F_{\text{exc}}^q}{2} \cos \varphi \quad (17)$$

$$\langle \vec{F}_{\text{odd}} \cdot \vec{e}_q \dot{q} \rangle_t = \frac{\pi k_0 A^2 f_{\text{exc}}^2}{f_0 Q_0} + \pi f_{\text{exc}} A F_{\text{exc}}^q \sin \varphi. \quad (18)$$

In a next step, the time averages are transformed to spatial averages similar to the formerly introduced cup and cap average functionals [3].

The harmonic approximation constrains the tip movement within the  $(\vec{r}_{\text{ts}}, \dot{\vec{r}}_{\text{ts}})$  phase space to a closed trajectory. Consequently, the parametrisation with a spatial coordinate along this sampling path requires a parametrisation of the velocity by this coordinate as well. To reflect this dependency, we introduce the even force  $\vec{F}_{\text{even}}^\circ(\vec{r}_{\text{ts}})$ , formally defined by  $\vec{F}_{\text{even}}^\circ(\vec{r}_{\text{ts}}) = \vec{F}_{\text{even}}(\vec{r}_{\text{ts}}, \dot{\vec{r}}_{\text{ts}}(\vec{r}_{\text{ts}}))$  as the force along the tip sampling path. Then, we further define the projection of an arbitrary function  $\vec{f}^\circ$  along the tip sampling path on the oscillation direction  $\vec{e}_q$  as  $f^{\circ q} = \vec{f}^\circ \cdot \vec{e}_q$  and perform the integration along the sampling path symmetrically to the centre position  $\vec{r}_c$  of this projected quantity  $f^{\circ q}$ . The cup and cap averaging functionals are then written as

$$\begin{aligned} \langle \vec{f}^\circ \cdot \vec{e}_q \rangle_{\cup}(\vec{r}_c) &= \langle f^{\circ q} \rangle_{\cup}(\vec{r}_c) \\ &= \int_{-A}^A \vec{f}^\circ(\vec{r}_c + q' \vec{e}_q) \cdot \vec{e}_q \frac{1}{\pi \sqrt{A^2 - (q')^2}} dq' \quad (19) \end{aligned}$$

$$\begin{aligned} \langle \vec{f}^\circ \cdot \vec{e}_q \rangle_{\cap}(\vec{r}_c) &= \langle f^{\circ q} \rangle_{\cap}(\vec{r}_c) \\ &= \int_{-A}^A \vec{f}^\circ(\vec{r}_c + q' \vec{e}_q) \cdot \vec{e}_q \frac{2}{\pi A^2} \sqrt{A^2 - (q')^2} dq'. \quad (20) \end{aligned}$$

These averages have now the structure of line integrals along the tip sampling path parallel to  $\vec{e}_q$ , spanning the range  $-A$  to  $A$  as parameterised by  $q'$ .

We furthermore define the tip-sample force gradient along the oscillation path,  $\vec{k}_{\text{ts}}^\circ$ , by the derivation of the force along the oscillation direction, namely

$$\vec{k}_{\text{ts}}^\circ(\vec{r}_c + q' \vec{e}_q) = \frac{d}{dq'} \vec{F}_{\text{even}}^\circ(\vec{r}_c + q' \vec{e}_q). \quad (21)$$

The three AFM equations follow now from Equation 16, Equation 17, and Equation 18 as

$$\langle \vec{F}_{\text{even}}^\circ \cdot \vec{e}_q \rangle_{\cup}(\vec{r}_c) = k_0 q_s. \quad (22)$$

$$\langle \vec{k}_{\text{ts}}^\circ \cdot \vec{e}_q \rangle_{\cap}(\vec{r}_c) = k_0 \left( 1 - \frac{f_{\text{exc}}^2}{f_0^2} \right) - \frac{F_{\text{exc}}^q}{A} \cos \varphi \quad (23)$$

$$\left\langle \vec{\gamma}_{\text{ts}}^\circ \cdot \vec{e}_q \right\rangle_{\text{C}}(\vec{r}_{\text{c}}) = -\frac{k_0}{2\pi Q_0 f_0} - \frac{F_{\text{exc}}^q}{2\pi f_{\text{exc}} A} \sin \varphi \quad (24)$$

whereby the vectorial damping coefficient  $\vec{\gamma}_{\text{ts}}$  and the damping coefficient  $\vec{\gamma}_{\text{ts}}^\circ$  along the oscillation path have been introduced to write the odd force as

$$\vec{F}_{\text{odd}}(\vec{r}_{\text{ts}}, \dot{\vec{r}}_{\text{ts}}) = -\vec{\gamma}_{\text{ts}}(\vec{r}_{\text{ts}}, \dot{\vec{r}}_{\text{ts}}) \cdot \dot{\vec{q}} = \vec{\gamma}_{\text{ts}}^\circ(\vec{r}_{\text{ts}}) \cdot \dot{\vec{q}}. \quad (25)$$

### Force response for the inclined sampling path

By reinterpreting the cup and cap averaging functionals as line integrals along the inclined tip sampling path, three AFM equations were found that represent the general case for a probe oscillating in an arbitrary direction. A probe orientation different from the surface normal and its oscillation in the vector force field above the surface has important consequences on the measured force response and appropriate data analysis procedures.

We demonstrate these consequences by simulating the frequency shift  $\Delta f = f_{\text{exc}} - f_0$  in the frequency-modulated AFM mode for different cases using a Morse potential

$$V_{\text{Morse}}(d) = E_b \left[ -2 \exp^{-\kappa(d-\sigma_0)} + \exp^{-2\kappa(d-\sigma_0)} \right] \quad (26)$$

as a model that describes the interaction between two atoms at a distance  $d$  by the parameters  $E_b = 0.371$  aJ,  $\sigma_0 = 0.235$  nm, and  $\kappa = 4.25$  nm<sup>-1</sup> (adapted from [20]). We use this model for the pairwise interaction between a tip with a heterogeneous surface section. The surface section is built by arranging  $N_a = 5$  atoms at  $z_{\text{ts}} = 0$  nm along the  $x$ -axis (with unit vector  $\vec{e}_x$ ) at an atom–atom distance of  $d_a = 0.5$  nm. To model a second atomic species for the heterogeneous surface section,  $E_b$  of the central atom is scaled by a factor of four. A sixth probe atom at position  $\vec{r}_{\text{ts}}$  representing the tip is moved within the force field  $\vec{F}_{\text{ts}}(\vec{r}_{\text{ts}})$  calculated from

$$\vec{F}_{\text{ts}}(\vec{r}_{\text{ts}}) = -\nabla \sum_{i=1}^{N_a} V_{\text{Morse}}\left(\left|\vec{r}_{\text{ts}} - (\vec{r}_a + i d_a \vec{e}_x)\right|\right). \quad (27)$$

Vector  $\vec{r}_a$  defines the origin of the surface section. In the following, the central atom is placed at  $\vec{r}_a = (x_{\text{ts}}, y_{\text{ts}}, z_{\text{ts}}) = (0.35, 0, 0)$  nm. The potential  $V_{\text{Morse}}$  and the force components  $F_{\text{ts}}^x = \vec{F}_{\text{ts}} \cdot \vec{e}_x$  as well as  $F_{\text{ts}}^z = \vec{F}_{\text{ts}} \cdot \vec{e}_z$  are shown in Figure 3a, b,

and c, respectively. A vectorial representation of the force field in the  $x_{\text{ts}}-z_{\text{ts}}$  plane is included in Figure 3a.

To illustrate the effects resulting from an inclined tip oscillation, four cases are discussed. Common to all cases is that the data recording path, described by the oscillation centre positions  $\vec{r}_{\text{c}}$ , remains oriented parallel to the  $\vec{e}_z$ -axis, that is, perpendicular to the surface as indicated by the dotted lines in Figure 3b and Figure 3c. This represents the common experimental protocol. In turn, the sampling path describing the tip oscillation is inclined by different angles  $\alpha$  within the  $x_{\text{ts}}-z_{\text{ts}}$  plane with the normalised inclined oscillation vector  $\vec{e}_q = [\sin\alpha, 0, \cos\alpha]$ . The tip trajectories during single oscillation cycles at one fixed  $\vec{r}_{\text{c}}$  are indicated for each case by dashed lines in Figure 3b and Figure 3c.

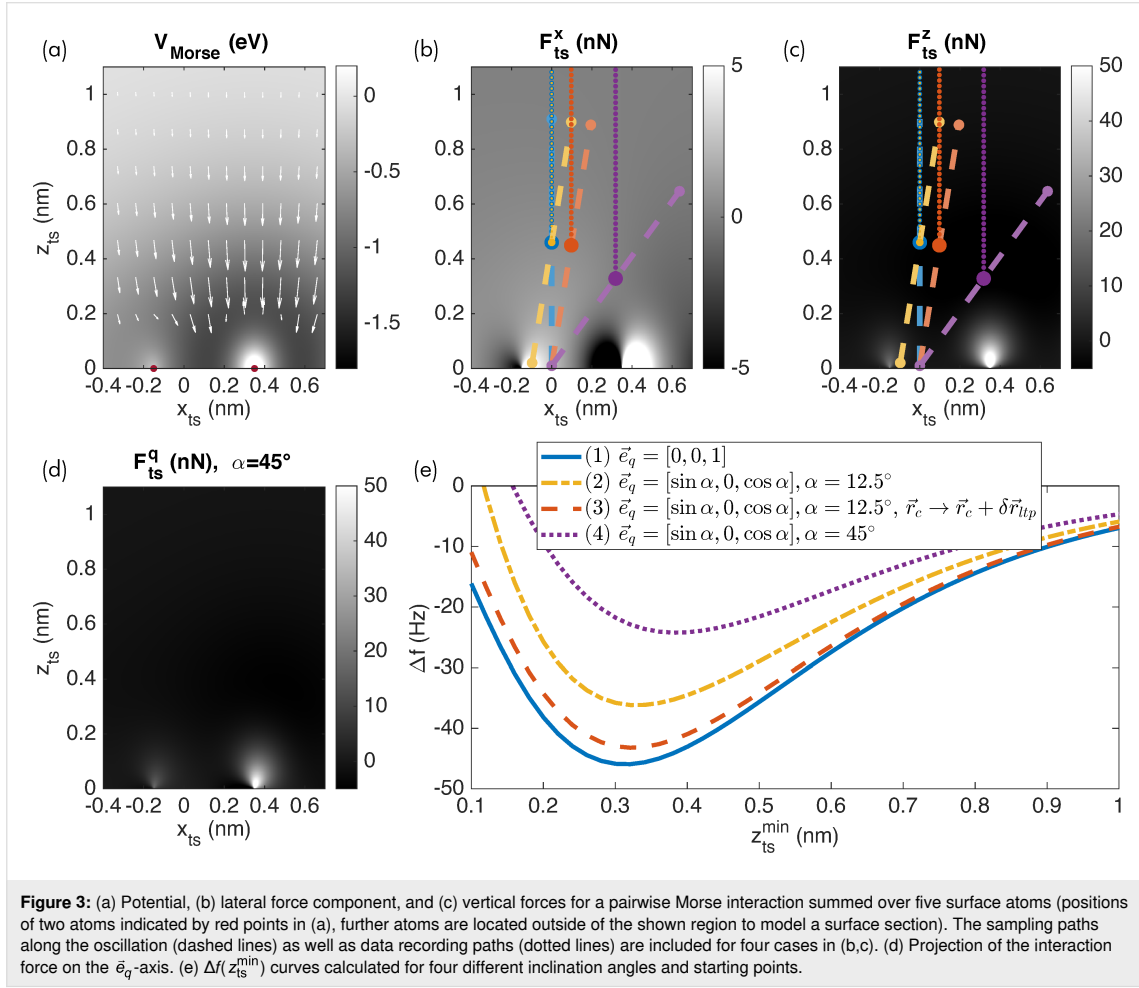
The force component  $F_{\text{ts}}^q$  along the tip path is a scalar quantity and shown for  $\alpha = 45^\circ$  in Figure 3d. Compared to the vertical component  $F_{\text{ts}}^z$  (see Figure 3c), the shape at the atom positions is asymmetric and the absolute contrast is diminished as a result of projecting the vectorial force  $\vec{F}_{\text{ts}}$  onto  $\vec{e}_q$ .

The force gradient  $k_{\text{ts}}^q$  along the tip path and projected to  $\vec{e}_q$  is calculated by numerical differentiation along  $\vec{e}_q$  of the  $F_{\text{ts}}^q$  force field. The result is used to calculate frequency shift  $\Delta f$  data from Equation 23 for  $\varphi = -\pi/2$ . As an example, we use parameters for a sensor often used in low-temperature environments (tuning fork sensor [21] with  $f_0 = 30$  kHz,  $k_0 = 1800$  N/m, and  $A = 0.45$  nm). However, similar effects can be present when using parameters for other sensors as well. Frequency shift  $\Delta f$  data are calculated with the piezo axis located at  $x_{\text{ts}} = y_{\text{ts}} = 0$  and moving the tip along  $z_p$  for data recording, while data are plotted as a function of  $z_{\text{ts}}^{\text{min}}$ .

The solid blue curve in Figure 3e represents case (1) of a perpendicular oscillation with  $\vec{e}_q = [0, 0, 1]$ . When positioning the tip along the  $\vec{e}_z$ -axis for data acquisition, this case allows for a reliable determination of the interaction force  $F_{\text{ts}}^z$  by applying known inversion strategies [2,4,5].

Next, the tip inclination is set to  $\alpha = 12.5^\circ$  within the  $x_{\text{ts}}-z_{\text{ts}}$  plane as case (2) shown in yellow in Figure 3b and Figure 3c. The corresponding  $\Delta f^{(2)}(z_{\text{ts}}^{\text{min}})$  curve (dash-dotted yellow in Figure 3e) is different from the blue  $\Delta f^{(1)}(z_{\text{ts}}^{\text{min}})$  curve. This is expected as the lower turning point moved sideways and the cap averaging is performed along a different path than in case (1). Note that in contrast to case (1), the tip sampling path has no overlapping segments when moving the tip along  $z_p$ . In case (3), the lateral movement of the lower turning point is compensated by subtracting the vector  $\delta\vec{r}_{\text{tip}} = [\Delta x, 0, \Delta z]$  with  $\Delta x = -A \sin\alpha$  and  $\Delta z = A(1 - \cos\alpha)$  from  $\vec{r}_{\text{c}}$ . The resulting  $\Delta f^{(3)}(z_{\text{ts}}^{\text{min}})$  data





included as a dashed red curve in Figure 3e deviates from all other curves.

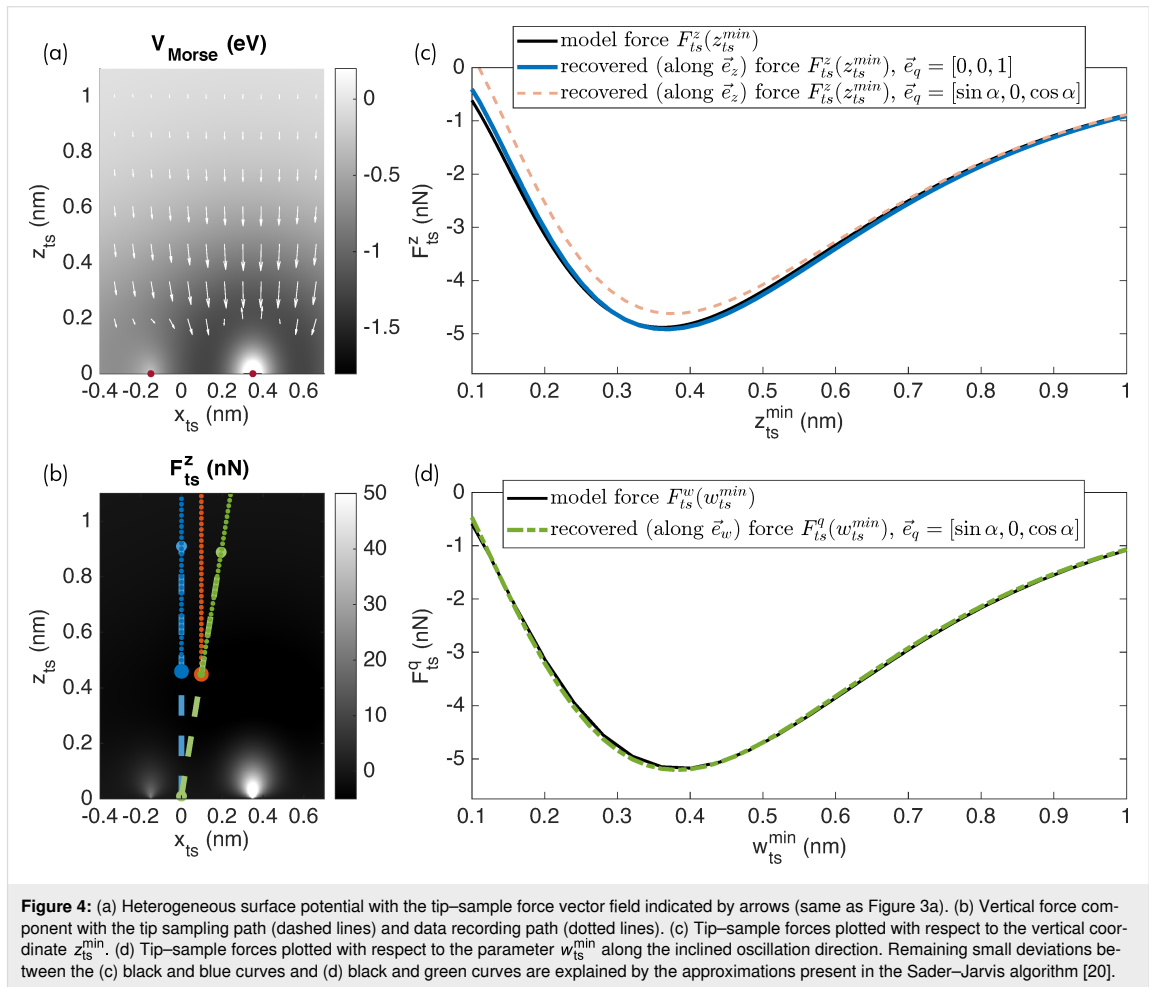
When further increasing the inclination angle  $\alpha$  as in case (4), the deviation becomes larger as presented by the violet dotted curve in Figure 3e for  $\alpha = 45^\circ$ . Last, we note that lateral components are virtually absent for large tip–sample distances in this model, leading to a convergence of the  $\Delta f(z_{ts}^{\min})$  curves in the regime  $z_{ts}^{\min} \gg 1$  nm.

### Force deconvolution for the inclined sampling path

The difference in the orientation of  $\vec{e}_q$  and  $\vec{e}_z$  violates a fundamental assumption of the commonly used inversion algorithms [4,5]: The tip sampling path segments are not overlapping when moving the tip along the data recording path for an inclined oscillation. The resulting error in the force recovery is shown in Figure 4c, where the red dashed curve presents the recovered

force for the case of an oscillation inclined by  $\alpha = 12.5^\circ$  and  $\Delta f$  data recorded along  $\vec{e}_z$ . As is apparent, the force curve does not match the model reference curve,  $F_{ts}^z(z_{ts}^{\min})$ , included as the solid black line. In contrast, the force curve recovered for the vertical oscillation and vertical data recording ( $\vec{e}_q = [0,0,1]$ , blue curve) matches the reference curve.

As a solution to this issue, we propose to orient the recording path for acquiring the AFM observables and parameters parallel to the tip sampling path  $\vec{e}_q$  describing the tip oscillation. This modification leads to an overlap of the tip sampling path segments for nearby positions along the data recording path. Therefore, the deconvolution using the known algorithms can be performed in the usual manner. Naturally, the result will not represent the perpendicular force  $F_{ts}^z$ , but rather describes the force component  $F_{ts}^q$  along the  $w$ -axis, parameterised by the scalar variable  $w_{ts}^{\min}$ . For a conservative force field, the vertical interaction force could in principle be calculated from this result.



Additionally, if the full force field is of interest, this can be extracted by systematic measurements of many  $\Delta f$  curves using the appropriate experimental procedures [22].

Simulation results for moving the tip along the inclined path during data acquisition and extracting the force along this path are presented in Figure 4d by the green curve. The force along this data recording path is correctly recovered as shown in Figure 4d where the green dash-dotted curve closely matches the model curve (in solid black) extracted along this path. Note that the force along an inclined  $w$ -axis is different from the vertical interaction force along  $z_{ts}^{\min}$ .

## Conclusion

Several conclusions can be drawn from extending the mathematical description of dynamic force microscopy by arbitrary tip sampling and data recording paths. For a typical inclination of  $\alpha = 12.5^\circ$ , the minimum force was calculated to differ by

more than 5% when compared to a result not taking the inclination into account. The magnitude of this difference depends on the model parameter choice and geometry: The difference can be amplified or reduced depending on the oscillation amplitude, on the interaction potential strength and decay, as well as on the atomic geometry. For example, edges of finite atomic slabs or larger atomic clusters generate significant effects. In practice, a model calculation is required to determine the uncertainty in the measured force due to the inclined tip oscillation.

Precise forces are measured if the data recording path, here introduced as the axis  $w$ , is aligned parallel to the tip sampling path, here described as the vector  $\vec{e}_q$ . The resulting measured force represents the component  $F_{ts}^q(w)$  of the tip-sample force along this direction. Despite the formal and quantitative difference from the commonly considered vertical component  $F_{ts}^z(z)$ , the component along  $w$  delivers identical physical insights into the tip-sample interaction.

## Appendix: Mathematical Derivations

### AFM Equation 1

The first AFM equation follows from evaluating the Fourier coefficient  $F_{\text{even}}^{q,0}$ , defined by

$$F_{\text{even}}^{q,0} = \langle \bar{F}_{\text{ts}} \cdot \bar{e}_q \rangle = \langle F_{\text{ts}}^q \rangle_t. \quad (28)$$

The tip–sample force can furthermore be written as a sum of an even and an odd force

$$= \langle \bar{F}_{\text{even}} \cdot \bar{e}_q \rangle_t + \langle \bar{F}_{\text{odd}} \cdot \bar{e}_q \rangle_t. \quad (29)$$

By definition of an odd force, the time average  $\langle \bar{F}_{\text{odd}} \cdot \bar{e}_q \rangle_t$  evaluates to zero. We compare this equation by introducing the equation of motion (Equation 6) for  $F_{\text{ts}}^q$  and using the fact that the time average is a linear functional

$$= \frac{k_0}{(2\pi f_0)^2} \langle \ddot{q} \rangle_t + k_0 \langle q \rangle_t + \frac{k_0}{2\pi f_0 Q_0} \langle \dot{q} \rangle_t - \langle F_{\text{exc}} \rangle_t. \quad (30)$$

With the harmonic approximation (Equation 2) it can directly be shown that  $\langle \dot{q} \rangle_t = \langle \ddot{q} \rangle_t = \langle F_{\text{exc}} \rangle_t = 0$  and  $q_s = \langle q \rangle_t$ . The first AFM equation directly follows as

$$\langle \bar{F}_{\text{even}} \cdot \bar{e}_q \rangle_t = k_0 q_s. \quad (31)$$

### AFM Equation 2

The Fourier coefficient  $F_{\text{even}}^{q,1}$  is defined as

$$F_{\text{even}}^{q,1} = 2 \langle \bar{F}_{\text{ts}} \cdot \bar{e}_q \cos(2\pi f_{\text{exc}} t + \varphi) \rangle_t. \quad (32)$$

Within the harmonic approximation (Equation 2), this term can be written as

$$= \frac{2}{A} \langle \bar{F}_{\text{ts}} \cdot \bar{e}_q (q - q_s) \rangle_t \quad (33)$$

and  $\bar{F}_{\text{ts}}$  be expressed by even and odd forces

$$= \frac{2}{A} \langle \bar{F}_{\text{even}} \cdot \bar{e}_q (q - q_s) \rangle_t + \frac{2}{A} \langle \bar{F}_{\text{odd}} \cdot \bar{e}_q (q - q_s) \rangle_t \quad (34)$$

whereby the average  $\langle \bar{F}_{\text{odd}} \cdot \bar{e}_q (q - q_s) \rangle_t$  evaluates to zero. Using the equation of motion (Equation 6), the Fourier coefficient can be written as

$$= \frac{2k_0}{A(2\pi f_0)^2} [\langle \ddot{q} \rangle_t - q_s \langle \ddot{q} \rangle_t] + \frac{2k_0}{A} [\langle q^2 \rangle_t - q_s \langle q \rangle_t] + \frac{2k_0}{A2\pi f_0 Q_0} [\langle \dot{q} \rangle_t - q_s \langle \dot{q} \rangle_t] - \frac{2}{A} [\langle F_{\text{exc}} q \rangle_t - q_s \langle F_{\text{exc}} \rangle_t]. \quad (35)$$

In full analogy to [3], this equation evaluates to

$$= k_0 A \left( 1 - \frac{f_{\text{exc}}^2}{f_0^2} \right) - F_{\text{exc}} \cos \varphi \quad (36)$$

whereby the identities  $\langle q \rangle_t = \langle \dot{q} \rangle_t = \langle \ddot{q} \rangle_t = \langle \dot{q} \dot{q} \rangle_t = \langle F_{\text{exc}} \rangle_t = 0$  are used.

### AFM Equation 3

The Fourier coefficient  $F_{\text{odd}}^{q,1}$  is defined as

$$F_{\text{odd}}^{q,1} = 2 \langle \bar{F}_{\text{ts}} \cdot \bar{e}_q \sin(2\pi f_{\text{exc}} t + \varphi) \rangle_t \quad (37)$$

which can be written as

$$= -\frac{2}{2\pi f_{\text{exc}} A} \langle \bar{F}_{\text{ts}} \cdot \bar{e}_q \dot{q} \rangle_t \quad (38)$$

by using the harmonic approximation, Equation 2. The force is again expressed as a sum of even and odd contributions

$$= -\frac{2}{2\pi f_{\text{exc}} A} [\langle \bar{F}_{\text{even}} \cdot \bar{e}_q \dot{q} \rangle_t + \langle \bar{F}_{\text{odd}} \cdot \bar{e}_q \dot{q} \rangle_t] \quad (39)$$

whereby  $\langle \bar{F}_{\text{even}} \cdot \bar{e}_q \dot{q} \rangle_t$  evaluates to zero. Using the equation of motion, Equation 6, this is equal to

$$= -\frac{2}{2\pi f_{\text{exc}} A} \left[ \frac{k_0}{(2\pi f_0)^2} \langle \ddot{q} \dot{q} \rangle_t + k_0 \langle \dot{q} \dot{q} \rangle_t + \frac{k_0}{2\pi f_0 Q_0} \langle \dot{q}^2 \rangle_t - \langle F_{\text{exc}} \dot{q} \rangle_t \right]. \quad (40)$$

With the identities  $\langle \ddot{q} \dot{q} \rangle_t = \langle \dot{q} \dot{q} \rangle_t = 0$ , this term evaluates to

$$= -\frac{k_0 A}{Q_0} \frac{f_{\text{exc}}}{f_0} - F_{\text{exc}} \sin \varphi. \quad (41)$$

## Acknowledgements

We are grateful to Ralf Bechstein and Hagen Söngen for stimulating discussions, especially on the difference between  $\bar{k}_{\text{ts}}$  and  $\bar{k}_{\text{ts}}^{\circ}$ .

## Funding

Financial support from the German Research Foundation (DFG) via grants RA2832/1-1, RE1186/21-1, and RE1186/23-1 are gratefully acknowledged.

## ORCID® iDs

Philipp Rahe - <https://orcid.org/0000-0002-2768-8381>  
 Daniel Heile - <https://orcid.org/0000-0002-2315-5633>  
 Reinhard Olbrich - <https://orcid.org/0000-0001-7765-393X>  
 Michael Reichling - <https://orcid.org/0000-0003-3186-9000>

## References

- Gross, L.; Schuler, B.; Pavliček, N.; Fatayer, S.; Majzik, Z.; Moll, N.; Peña, D.; Meyer, G. *Angew. Chem., Int. Ed.* **2018**, *57*, 3888–3908. doi:10.1002/anie.201703509
- Heile, D.; Olbrich, R.; Reichling, M.; Rahe, P. *Phys. Rev. B* **2021**, *103*, 075409. doi:10.1103/physrevb.103.075409
- Söngen, H.; Bechstein, R.; Kühnle, A. *J. Phys.: Condens. Matter* **2017**, *29*, 274001. doi:10.1088/1361-648x/aa6f8b
- Sader, J. E.; Jarvis, S. P. *Appl. Phys. Lett.* **2004**, *84*, 1801–1803. doi:10.1063/1.1667267
- Giessibl, F. J. *Appl. Phys. Lett.* **2001**, *78*, 123–125. doi:10.1063/1.1335546
- Heim, L.-O.; Kappl, M.; Butt, H.-J. *Langmuir* **2004**, *20*, 2760–2764. doi:10.1021/la036128m
- Hutter, J. L. *Langmuir* **2005**, *21*, 2630–2632. doi:10.1021/la047670t
- Gates, R. S. *Rev. Sci. Instrum.* **2017**, *88*, 123710. doi:10.1063/1.4986201
- Edwards, S. A.; Ducker, W. A.; Sader, J. E. *J. Appl. Phys.* **2008**, *103*, 064513. doi:10.1063/1.2885734
- Wang, F. J. *Appl. Phys.* **2009**, *106*, 096103. doi:10.1063/1.3257268
- Cannara, R. J.; Brukman, M. J.; Carpick, R. W. *Rev. Sci. Instrum.* **2005**, *76*, 053706. doi:10.1063/1.1896624
- Wang, C.; Sun, J.; Itoh, H.; Shen, D.; Hu, J. *Anal. Sci.* **2011**, *27*, 143–147. doi:10.2116/analsci.27.143
- Misaka, T.; Kajimoto, K.; Araki, K.; Otsuka, Y.; Matsumoto, T. *Jpn. J. Appl. Phys.* **2020**, *59*, 090906. doi:10.35848/1347-4065/abac6e
- Garrett, J. L.; Krayner, L. J.; Palm, K. J.; Munday, J. N. *Appl. Phys. Lett.* **2017**, *111*, 043105. doi:10.1063/1.4996720
- D'Amato, M. J.; Marcus, M. S.; Eriksson, M. A.; Carpick, R. W. *Appl. Phys. Lett.* **2004**, *85*, 4738–4740. doi:10.1063/1.1812839
- Marcus, M. S.; Carpick, R. W.; Sasaki, D. Y.; Eriksson, M. A. *Phys. Rev. Lett.* **2002**, *88*, 226103. doi:10.1103/physrevlett.88.226103
- Gretz, O.; Weymouth, A. J.; Holzmann, T.; Pürckhauer, K.; Giessibl, F. J. *Beilstein J. Nanotechnol.* **2021**, *12*, 517–524. doi:10.3762/bjnano.12.42
- Lübbe, J.; Doering, L.; Reichling, M. *Meas. Sci. Technol.* **2012**, *23*, 045401. doi:10.1088/0957-0233/23/4/045401
- Albrecht, T. R.; Grütter, P.; Horne, D.; Rugar, D. *J. Appl. Phys.* **1991**, *69*, 668–673. doi:10.1063/1.347347
- Welker, J.; Illek, E.; Giessibl, F. J. *Beilstein J. Nanotechnol.* **2012**, *3*, 238–248. doi:10.3762/bjnano.3.27
- Falter, J.; Stiefemann, M.; Langewisch, G.; Schurig, P.; Hölscher, H.; Fuchs, H.; Schirmeisen, A. *Beilstein J. Nanotechnol.* **2014**, *5*, 507–516. doi:10.3762/bjnano.5.59

- Rahe, P.; Schütte, J.; Schniederberend, W.; Reichling, M.; Abe, M.; Sugimoto, Y.; Kühnle, A. *Rev. Sci. Instrum.* **2011**, *82*, 063704. doi:10.1063/1.3600453

## License and Terms

This is an open access article licensed under the terms of the Beilstein-Institut Open Access License Agreement (<https://www.beilstein-journals.org/bjnano/terms>), which is identical to the Creative Commons Attribution 4.0 International License (<https://creativecommons.org/licenses/by/4.0>). The reuse of material under this license requires that the author(s), source and license are credited. Third-party material in this article could be subject to other licenses (typically indicated in the credit line), and in this case, users are required to obtain permission from the license holder to reuse the material.

The definitive version of this article is the electronic one which can be found at:

<https://doi.org/10.3762/bjnano.13.53>



## 7. Quantitative CFM theory

Charge force microscopy (CFM) is a method for the quantification of nanoscale charges on, in or above a the sample substrate. Its implementation is a major achievement of the present thesis. In its technical realisation, CFM is similar to FM-CL-KPFM. However, the quantitative signal evaluation in CFM is based on the electrostatic model introduced in chapter 2.3.2 and therefore does account for all charges located in the tip-sample capacitor. As the classical KPFM theory only considers the contact potential difference voltage  $V_{\text{CPD}}$ , it is the fringe case of CFM theory if no charges are located in the considered tip-sample capacitor. In this chapter, the full formal derivation of the quantitative CFM theory is presented [68, 69, 70].

For formally describing a CFM experiment, the AFM theory has to be expanded to consider additional spectral components in the displacement spectrum  $\mathcal{F}[q(t)]$  which are due to the electrostatic interaction caused by modulation of the potential difference  $V$  between tip and back electrode with frequency  $f_{\text{el}}$ . To include that electrostatic interaction in the equation of motion of the tip (4.3.17), the tip-sample force  $F_{\text{ts}}^z(z_{\text{ts}}(t), \dot{z}_{\text{ts}}(t))$  is expanded by the electrostatic force (2.3.29) derived from the model introduced in section 2.3.2. Considering the resulting tip-sample force  $F_{\text{ts}}^z(z_{\text{ts}}(t), \dot{z}_{\text{ts}}(t), V)$  within the equation of motion of the tip (4.3.17) in case of a modulation of  $V$  with frequency  $f_{\text{el}}$  yields all additional spectral components in the displacement  $q(t)$  occurring in a CFM experiment. Limiting the harmonic approximation to the tip movement only and allowing the displacement  $q(t)$  to remain an arbitrary function of time, allows to solve the resulting equation of motion and to obtain a quantitative description of the full displacement spectrum  $\mathcal{F}[q(t)]$  of a CFM experiment containing different mixtures of both frequencies  $f_{\text{exc}}$  and  $f_{\text{el}}$ .

For a shorter notation, in this chapter,  $F_{\text{el}}$  represents the force  $F_{\text{el}}^{\text{body}}$  describing the electrostatic body-body interaction between the conductive tip and the metallic sample support as introduced in section 2.3.2.

## 7.1. Modulated electrostatic force contribution to the tip-sample force

Consider the electrostatic tip-sample force (2.3.29) during an CFM experiment as described in section 3.3 where a modulated external voltage (3.3.10) is applied between the tip and the metallic back electrode of the sample. Based on the electrostatic model introduced in section 2.3.2 the voltage  $V$ , between tip and sample support generally is given by relation (2.3.16), where inserting the modulated external voltage (3.3.10) provides

$$V = -V_{\text{CPD}} + V_{\text{bias}} + V_{\text{el}} \cos(2\pi f_{\text{el}} t) \quad (7.1.1)$$

Inserting this into the electrostatic tip-sample force (2.3.29) and rewriting the resulting relation by further using the theorem  $\cos(x)^2 = \frac{1}{2}(1 + \cos(2x))$  yields the relation for the electrostatic force in the CFM experiment [70]

$$\begin{aligned} F_{\text{el}}(z_{\text{ts}}, V) = & F_{\text{el,a}}(z_{\text{ts}}) \\ & + F_{\text{el,b}}(z_{\text{ts}}) \cos(2\pi f_{\text{el}} t) \\ & + F_{\text{el,c}}(z_{\text{ts}}) \cos(2\pi(2f_{\text{el}})t) \end{aligned} \quad (7.1.2)$$

where

$$\begin{aligned} F_{\text{el,a}}(z_{\text{ts}}) = & \frac{1}{2} \frac{\partial C_{\text{void}}}{\partial z_{\text{ts}}} \left[ (V_{\text{bias}} - V_{\text{CPD}})^2 + \frac{1}{2} V_{\text{el}}^2 \right] \\ & - (V_{\text{bias}} - V_{\text{CPD}}) \sum_{i=1}^N q_i \frac{\partial \hat{\Phi}_{\text{void}}(\mathbf{r}_i)}{\partial z_{\text{ts}}} \\ & - \frac{1}{2\epsilon_0} \sum_{i=1}^N \sum_{j=1}^N q_i q_j \frac{\partial \phi_{\text{ind}}(\mathbf{r}_i, \mathbf{r}_j)}{\partial z_{\text{ts}}} \end{aligned} \quad (7.1.3)$$

$$F_{\text{el,b}}(z_{\text{ts}}) = V_{\text{el}} \left[ \frac{\partial C_{\text{void}}}{\partial z_{\text{ts}}} (V_{\text{bias}} - V_{\text{CPD}}) - \sum_{i=1}^N q_i \frac{\partial \hat{\Phi}_{\text{void}}(\mathbf{r}_i)}{\partial z_{\text{ts}}} \right] \quad (7.1.4)$$

$$F_{\text{el,c}}(z_{\text{ts}}) = \frac{1}{4} \frac{\partial C_{\text{void}}}{\partial z_{\text{ts}}} V_{\text{el}}^2 \quad (7.1.5)$$

Due to the externally applied modulated voltage (3.3.10) the electrostatic force exhibits three spectral components related to the modulation frequency  $f_{\text{el}}$ . The term  $F_{\text{el,a}}$  describes the static part of  $F_{\text{el}}$ , the second term  $F_{\text{el,b}}$  is the first harmonic in respect to  $f_{\text{el}}$  and  $F_{\text{el,c}}$  is the second harmonic of the modulation at frequency  $2f_{\text{el}}$ . However, these spectral components of  $F_{\text{el}}$  only apply for a static tip ( $f_{\text{exc}} = 0$ ) at a fixed tip-sample distance  $z_{\text{ts}}$ . In a dynamic AFM experiment there will be

### 7.1. Modulated electrostatic force contribution to the tip-sample force

more spectral components due to the additional oscillation of the tip  $z_{\text{ts}}(t)$ . For obtaining these spectral components, it is required to consider the modulated electrostatic force (7.1.2) as an additional contribution to the general tip-sample force  $F_{\text{ts}}^z(z_{\text{ts}}(t), \dot{z}_{\text{ts}}(t))$  in the equation of motion (4.3.17) describing the tip oscillation in the interaction field of the sample. Therefore the tip-sample force is written analogous to (7.1.2) as [70]

$$\begin{aligned} F_{\text{ts}}^z(z_{\text{ts}}(t), \dot{z}_{\text{ts}}(t), V) = & F_{\text{ts,a}}^z(z_{\text{ts}}(t), \dot{z}_{\text{ts}}(t)) \\ & + F_{\text{ts,b}}^z(z_{\text{ts}}(t), \dot{z}_{\text{ts}}(t)) \cos(2\pi f_{\text{el}}t) \\ & + F_{\text{ts,c}}^z(z_{\text{ts}}(t), \dot{z}_{\text{ts}}(t)) \cos(2\pi(2f_{\text{el}})t) \end{aligned} \quad (7.1.6)$$

Where  $F_{\text{ts,a}}^z$  includes all voltage-independent contributions to the interaction force and  $F_{\text{el,a}}$ . Hence this term is equal to the tip-sample force considered generally in the previous chapter 4, but is now extended by the static electrostatic interaction term  $F_{\text{el,a}}$  of equation (7.1.2). In return, this means, that  $F_{\text{el,a}}$  cannot a priori be distinguished from all other tip-sample interaction forces by measuring  $f_{\text{exc}}$ . The other two terms are due to the modulation of the voltage  $V$  between tip and sample support by  $f_{\text{el}}$  and thus exclusively describe electrostatic interactions which provides the identities  $F_{\text{ts,b}}^z = F_{\text{el,b}}$  and  $F_{\text{ts,c}}^z = F_{\text{el,c}}$ . Because the electrostatic force (2.3.29) is conservative, it does not depend on the tip velocity  $\dot{z}_{\text{ts}}$  in contrast to some force contributions of  $F_{\text{ts,a}}^z$ . Hence  $F_{\text{ts,a}}^z$  is a function of both, tip-sample distance and tip velocity  $F_{\text{ts,a}}^z = F_{\text{ts,a}}^z(z_{\text{ts}}(t), \dot{z}_{\text{ts}}(t))$ , while  $F_{\text{el,b}}$  and  $F_{\text{el,c}}$  only depend on the tip-sample distance  $z_{\text{ts}}(t)$ . Consequently, the tip-sample force containing the modulated electrostatic interaction (7.1.2) can be represented as

$$\begin{aligned} F_{\text{ts}}^z(z_{\text{ts}}(t), \dot{z}_{\text{ts}}(t), V) = & F_{\text{ts,a}}^z(z_{\text{ts}}(t), \dot{z}_{\text{ts}}(t)) \\ & + F_{\text{el,b}}(z_{\text{ts}}(t)) \cos(2\pi f_{\text{el}}t) \\ & + F_{\text{el,c}}(z_{\text{ts}}(t)) \cos(2\pi(2f_{\text{el}})t) \end{aligned} \quad (7.1.7)$$

Inserting this result into the equation of motion (4.3.17), yields an relation describing movement of the tip in interacting with the sample force field and the modulated electrostatic force applied for CFM detection as

$$\begin{aligned} \frac{k_0}{(2\pi f_0)^2} \ddot{q}(t) = & -k_0 q(t) - \frac{k_0}{2\pi f_0 Q_0} \dot{q}(t) \\ & + F_{\text{exc}}(t) \\ & + F_{\text{ts,a}}^z(z_{\text{ts}}(t), \dot{z}_{\text{ts}}(t)) \\ & + F_{\text{el,b}}(z_{\text{ts}}(t)) \cos(2\pi f_{\text{el}}t) \\ & + F_{\text{el,c}}(z_{\text{ts}}(t)) \cos(2\pi(2f_{\text{el}})t) \end{aligned} \quad (7.1.8)$$

As explained in section 4.3.1 an analytical solution of equation (7.1.8) is generally not possible, because the unknown tip-sample force  $F_{\text{ts,a}}^z$  and the electrostatic contributions  $F_{\text{el,b}}$  and  $F_{\text{el,c}}$  are dependent on the tip-sample distance  $z_{\text{ts}}(t)$ , which in



## 7. Quantitative CFM theory

return is a function of the sensor displacement  $q(t)$  (see section 4.1). In the chapter (4) the harmonic approximation is employed by consequently replacing  $q(t)$  with  $\tilde{q}(t)$  and  $z_{\text{ts}}(t)$  by  $\tilde{z}_{\text{ts}}(t)$  for solving the equation of motion. However, for describing a CFM experiment based on the equation of motion (7.1.8) this approach would not be expedient, as it would eliminate all spectral components other than the static deflection  $q_s$  and the first harmonic at frequency  $f_{\text{exc}}$  from the solution. To prevent this, the application of the harmonic approximation has to be modified in the following calculation.

### 7.2. Harmonic approximation in CFM

For enabling arbitrary spectral components in  $q(t)$ , the harmonic approximation is only employed on the tip movement in the force field, but not the sampled interaction. By doing so, the tip is allowed to sample any spectral component due to the interaction in  $q(t)$  while moving on the fixed path defined by  $\tilde{z}_{\text{ts}}(t)$  and  $\dot{\tilde{z}}_{\text{ts}}(t)$ . Formally, this means replacing  $F_{\text{ts,a}}^z(z_{\text{ts}}(t), \dot{z}_{\text{ts}}(t))$ ,  $F_{\text{el,b}}(z_{\text{ts}}(t))$  and  $F_{\text{el,c}}(z_{\text{ts}}(t))$  by  $F_{\text{ts,a}}^z(\tilde{z}_{\text{ts}}(t), \dot{\tilde{z}}_{\text{ts}}(t))$ ,  $F_{\text{el,b}}(\tilde{z}_{\text{ts}}(t))$  and  $F_{\text{el,c}}(\tilde{z}_{\text{ts}}(t))$  while keeping  $q(t)$  as an arbitrary function of time. Employing the harmonic approximation in that way, the equation of motion (7.1.8) is transformed to

$$\begin{aligned} \frac{k_0}{(2\pi f_0)^2} \ddot{q}(t) = & -k_0 q(t) - \frac{k_0}{2\pi f_0 Q_0} \dot{q}(t) \\ & + \tilde{F}_{\text{exc}}(t) \\ & + F_{\text{ts,a}}^z(\tilde{z}_{\text{ts}}(t), \dot{\tilde{z}}_{\text{ts}}(t)) \\ & + F_{\text{el,b}}(\tilde{z}_{\text{ts}}(t)) \cos(2\pi f_{\text{el}} t) \\ & + F_{\text{el,c}}(\tilde{z}_{\text{ts}}(t)) \cos(2\pi(2f_{\text{el}}) t) \end{aligned} \quad (7.2.9)$$

Where the displacement  $q(t)$  can contain any spectral component additional to  $f_{\text{exc}}$  while the tip moves in the force field on the fixed path given by  $\tilde{z}_{\text{ts}}(t)$  and  $\dot{\tilde{z}}_{\text{ts}}(t)$  which are well defined by (4.3.20) and (4.3.21). Note, that  $z_{\text{ts}}(t)$  is a function of  $q(t)$  (see Sec. 4.1), hence, it has to be assumed here that the deflection  $q(t)$  behaves harmonically and its additional spectral components do not significantly affect the sampling path of the tip  $[\tilde{z}_{\text{ts}}(t), \dot{\tilde{z}}_{\text{ts}}(t)]$ . Based on this assumption, the equation of motion (7.2.9) can be solved and all spectral components occurring in a CFM experiment can be derived.

### 7.3. Fourier series development of the periodically sampled force contributions

The tip-sample force (7.1.7) is sampled periodically due to its dependency on the harmonically oscillating tip-sample distance  $\tilde{z}_{\text{ts}}(t)$ . Therefore, its contributions  $F_{\text{ts,a}}^z(\tilde{z}_{\text{ts}}(t), \dot{\tilde{z}}_{\text{ts}}(t))$ ,  $F_{\text{el,b}}(\tilde{z}_{\text{ts}}(t))$  and  $F_{\text{el,c}}(\tilde{z}_{\text{ts}}(t))$  are periodic functions as well, having a cycle time  $T = 1/f_{\text{exc}}$  and phase  $\varphi$  in respect to the excitation  $\tilde{F}_{\text{exc}}(t)$ . All the periodic functions (due to the dependency on  $\tilde{z}_{\text{ts}}(t)$ ) can be developed in Fourier series for solving equation (7.2.9) in an ansatz similar to that presented in section 4.3.3.

Here, the tip-sample force  $F_{\text{ts,a}}^z(\tilde{z}_{\text{ts}}(t), \dot{\tilde{z}}_{\text{ts}}(t))$  is equal to the tip-sample force considered in the AFM chapter 4 containing all voltage-independent tip-sample interactions but also  $F_{\text{el,a}}(\tilde{z}_{\text{ts}}(t))$ . Consequently  $F_{\text{ts,a}}^z(\tilde{z}_{\text{ts}}(t), \dot{\tilde{z}}_{\text{ts}}(t))$  can be generally decomposed into an even and odd part  $F_{\text{ts,a}}^z(\tilde{z}_{\text{ts}}(t), \dot{\tilde{z}}_{\text{ts}}(t)) = F_{\text{even,a}}(\tilde{z}_{\text{ts}}(t), \dot{\tilde{z}}_{\text{ts}}(t)) + F_{\text{odd,a}}(\tilde{z}_{\text{ts}}(t), \dot{\tilde{z}}_{\text{ts}}(t))$  in respect to the tip-velocity  $\dot{\tilde{z}}_{\text{ts}}$  (see section 4.3.2 for example). The complete force contribution  $F_{\text{ts,a}}^z(\tilde{z}_{\text{ts}}(t), \dot{\tilde{z}}_{\text{ts}}(t))$  can be developed in an Fourier series equal to relation (4.2.5) yielding

$$F_{\text{ts,a}}^z(\tilde{z}_{\text{ts}}, \dot{\tilde{z}}_{\text{ts}}) = F_{\text{even,a}}^{(0)} + \sum_{n=1}^{\infty} F_{\text{even,a}}^{(n)} \cos(2\pi n f_{\text{exc}} t + \varphi) \quad (7.3.10)$$

$$+ \sum_{n=1}^{\infty} F_{\text{odd,a}}^{(n)} \sin(2\pi n f_{\text{exc}} t + \varphi)$$

where  $F_{\text{even,a}}^{(0)}$  is the static force and the Fourier coefficients for  $n \geq 1$  can be expressed as

$$F_{\text{even,a}}^{(n)} = 2 \left\langle F_{\text{ts,a}}^z(\tilde{z}_{\text{ts}}(t), \dot{\tilde{z}}_{\text{ts}}(t)) \cos(2\pi n f_{\text{exc}} t + \varphi) \right\rangle_t \quad (7.3.11)$$

$$F_{\text{odd,a}}^{(n)} = 2 \left\langle F_{\text{ts,a}}^z(\tilde{z}_{\text{ts}}(t), \dot{\tilde{z}}_{\text{ts}}(t)) \sin(2\pi n f_{\text{exc}} t + \varphi) \right\rangle_t \quad (7.3.12)$$

using the definition of the time average (4.3.32) for functions periodic in  $1/f_{\text{exc}}$ . In the same manner, the periodic electrostatic contributions  $F_{\text{el,b}}(\tilde{z}_{\text{ts}}(t))$  and  $F_{\text{el,c}}(\tilde{z}_{\text{ts}}(t))$  can be developed. However, as the electrostatic model (see section 2.3.2) provides a purely conservative force (2.3.29), also its components  $F_{\text{el,b}}(\tilde{z}_{\text{ts}}(t))$  and  $F_{\text{el,c}}(\tilde{z}_{\text{ts}}(t))$  are conservative and, hence, independent of the tip-velocity  $\dot{z}_{\text{ts}}$ . For that reason, both contributions  $F_{\text{el,b}}(\tilde{z}_{\text{ts}}(t))$  and  $F_{\text{el,c}}(\tilde{z}_{\text{ts}}(t))$  are even in respect to  $\dot{\tilde{z}}_{\text{ts}}$  and consequently their Fourier series exclusively consider even contributions as

$$F_{\text{el,b}}(\tilde{z}_{\text{ts}}) = F_{\text{el,b}}^{(0)} + \sum_{n=1}^{\infty} F_{\text{el,b}}^{(n)} \cos(2\pi n f_{\text{exc}} t + \varphi) \quad (7.3.13)$$

$$F_{\text{el,c}}(\tilde{z}_{\text{ts}}) = F_{\text{el,c}}^{(0)} + \sum_{n=1}^{\infty} F_{\text{el,c}}^{(n)} \cos(2\pi n f_{\text{exc}} t + \varphi) \quad (7.3.14)$$

## 7. Quantitative CFM theory

where the Fourier coefficients for  $n \geq 1$  are given by

$$F_{\text{el,b}}^{(n)} = 2 \langle F_{\text{el,b}}(\tilde{z}_{\text{ts}}) \cos(2\pi n f_{\text{exc}} t + \varphi) \rangle_t \quad (7.3.15)$$

$$F_{\text{el,c}}^{(n)} = 2 \langle F_{\text{el,c}}(\tilde{z}_{\text{ts}}) \cos(2\pi n f_{\text{exc}} t + \varphi) \rangle_t \quad (7.3.16)$$

As in the considerations of chapter 4, the time-averages over one oscillation cycle  $1/f_{\text{exc}}$  have to be transformed into spatial-averages along the tip-sampling path  $[z_{\text{c}} - A, z_{\text{c}} + A]$ . This is the next step for deriving the CFM relevant spectral components of the deflection  $q(t)$ .

## 7.4. Application of the AFM averaging functions

Within the harmonic approximation, Fourier series (7.3.10), (7.3.13) and (7.3.14) are truncated after  $n = 1$ . Further projecting the time-averages of the remaining coefficients to the tip-sampling path parallel to  $z_{\text{ts}}$  and inserting these into the respective Fourier series by also using identities

$$\cos(2\pi f_{\text{exc}} t + \varphi) = \frac{1}{A} (\tilde{z}_{\text{ts}}(t) - z_{\text{c}}) \quad (7.4.17)$$

and

$$\sin(2\pi f_{\text{exc}} t + \varphi) = -\frac{1}{2\pi f_{\text{exc}}} \dot{\tilde{z}}_{\text{ts}} \quad (7.4.18)$$

yields the relations

$$F_{\text{ts,a}}^z(\tilde{z}_{\text{ts}}, \dot{\tilde{z}}_{\text{ts}}) \approx \langle F_{\text{even,a}}^{\circ} \rangle_{\cup}(z_{\text{c}}) + \langle k_{\text{ts,a}}^{\circ} \rangle_{\cap}(z_{\text{c}}) \cdot (\tilde{z}_{\text{ts}}(t) - z_{\text{c}}) - \langle \gamma_{\text{ts,a}}^{\circ} \rangle_{\cap}(z_{\text{c}}) \cdot \dot{\tilde{z}}_{\text{ts}} \quad (7.4.19)$$

$$F_{\text{el,b}}(\tilde{z}_{\text{ts}}) \approx \langle F_{\text{el,b}}^{\circ} \rangle_{\cup}(z_{\text{c}}) + \langle k_{\text{el,b}}^{\circ} \rangle_{\cap}(z_{\text{c}}) \cdot (\tilde{z}_{\text{ts}}(t) - z_{\text{c}}) \quad (7.4.20)$$

$$F_{\text{el,c}}(\tilde{z}_{\text{ts}}) \approx \langle F_{\text{el,c}}^{\circ} \rangle_{\cup}(z_{\text{c}}) + \langle k_{\text{el,c}}^{\circ} \rangle_{\cap}(z_{\text{c}}) \cdot (\tilde{z}_{\text{ts}}(t) - z_{\text{c}}) \quad (7.4.21)$$

The respective calculations are similar to the derivations carried out in chapter 4 and appendix A.6. The tip-sample force  $F_{\text{even,a}}^{\circ}(\tilde{z}_{\text{ts}}(t))$  and the electrostatic contributions  $F_{\text{el,b}}^{\circ}(\tilde{z}_{\text{ts}}(t))$  and  $F_{\text{el,c}}^{\circ}(\tilde{z}_{\text{ts}}(t))$  along the tip-sampling path are introduced analogous to equation (4.5.38). Further, the tip-sample force gradient  $k_{\text{ts,a}}^{\circ}$  and the electrostatic force gradients  $k_{\text{el,b}}^{\circ}$  and  $k_{\text{el,c}}^{\circ}$  along the sampling path are introduced analogously to equation (4.5.48) as

$$k_{\text{ts,a}}^{\circ} = \frac{\partial F_{\text{even,a}}^{\circ}(z_{\text{c}} + z)}{\partial z} = \frac{\partial F_{\text{even,a}}^{\circ}(z_{\text{ts}})}{\partial z_{\text{ts}}} \quad (7.4.22)$$

$$k_{\text{el,b}}^{\circ} = \frac{\partial F_{\text{el,b}}^{\circ}(z_{\text{c}} + z)}{\partial z} = \frac{\partial F_{\text{el,b}}^{\circ}(z_{\text{ts}})}{\partial z_{\text{ts}}} \quad (7.4.23)$$

$$k_{\text{el,c}}^{\circ} = \frac{\partial F_{\text{el,c}}^{\circ}(z_{\text{c}} + z)}{\partial z} = \frac{\partial F_{\text{el,c}}^{\circ}(z_{\text{ts}})}{\partial z_{\text{ts}}} \quad (7.4.24)$$

#### 7.4. Application of the AFM averaging functions

As the parameter  $z$  describes sampling along  $z_{ts}$  within the oscillation range  $z_c - A$  and  $z_c + A$ , the derivation in respect to  $z$  is effectively an derivation in respect to  $z_{ts}$ . Hence, the electrostatic force gradients  $k_{el,b}^\circ$  and  $k_{el,c}^\circ$  are directly given by derivation of the modulated electrostatic force (7.1.2) in respect to  $z_{ts}$ . Furthermore, the odd force is described by

$$F_{\text{odd},a}(\tilde{z}_{ts}(t), \dot{\tilde{z}}_{ts}(t)) = -\gamma_{ts,a}(\tilde{z}_{ts}(t), \dot{\tilde{z}}_{ts}(t)) \cdot \ddot{\tilde{z}}_{ts}(t) \quad (7.4.25)$$

in analogy to relation (4.5.39), where  $\gamma_{ts,a}(\tilde{z}_{ts}(t), \dot{\tilde{z}}_{ts}(t))$  is the tip-sample damping which is even in respect to  $\dot{\tilde{z}}_{ts}$ . Based on this, the tip-sample damping along the tip-sampling path  $\gamma_{ts,a}^\circ(\tilde{z}_{ts}(t))$  can be introduced similar to relation (4.5.40). Note, however, that the direct derivation of the AFM equations by evaluating  $F_{\text{even},a}^{(0)}$ ,  $F_{\text{even},a}^{(1)}$ ,  $F_{\text{odd},a}^{(1)}$  with the the equation of motion (7.2.9) is not possible here due to the unknown deflection  $q(t)$  and the additional electrostatic interaction terms  $F_{el,b}$  and  $F_{el,c}$ . Consequently the terms  $\langle F_{\text{even},a}^\circ \rangle_{\cup}$ ,  $\langle k_{ts,a}^\circ \rangle_{\cap}$  and  $\langle \gamma_{ts,a}^\circ \rangle_{\cap}$  will generally not be equal to the AFM equations (4.5.45), (4.5.46) and (4.5.47) as they contain additional contributions of the modulated electrostatic force. These results are valid under the assumption that the electrostatic modulation does not affect the tip-sampling path but the spectral components of it appear in the harmonic displacement  $q(t)$ . In other words, the electrostatic modulation contributions to the tip-sample interaction detected at  $f_{\text{exc}}$  are miniscule so that the AFM equations (4.5.45)-(4.5.47) describe the interaction in good approximation.

## 7.5. Solution of the equation of motion

Inserting relations (7.4.19)-(7.4.21) and the harmonic excitation (4.3.18) into relation (7.2.9) and, further, using the identity  $\cos(x) \cos(y) = \frac{1}{2} (\cos(x-y) + \cos(x+y))$  yields

$$\begin{aligned}
\frac{k_0}{(2\pi f_0)^2} \ddot{q}(t) \approx & - \left( k_0 - \langle k_{ts,a}^\circ \rangle_\cap (z_c) \right) q(t) \\
& - \left( \frac{k_0}{2\pi f_0 Q_0} + \langle \gamma_{ts,a}^\circ \rangle_\cap (z_c) \right) \dot{q}(t) \\
& + F_0 \cos(2\pi f_{exc} t) \\
& + \langle F_{even,a}^\circ \rangle_\cup (z_c) - \langle k_{ts,a}^\circ \rangle_\cap q_s \\
& + \langle F_{el,b}^\circ \rangle_\cup (z_c) \cos(2\pi f_{el} t) \\
& + \langle F_{el,c}^\circ \rangle_\cup (z_c) \cos(2\pi(2f_{el})t) \\
& + \frac{A}{2} \langle k_{el,b}^\circ \rangle_\cap (z_c) \cos(2\pi(f_{exc} + f_{el})t + \varphi) \\
& + \frac{A}{2} \langle k_{el,b}^\circ \rangle_\cap (z_c) \cos(2\pi(f_{exc} - f_{el})t + \varphi) \\
& + \frac{A}{2} \langle k_{el,c}^\circ \rangle_\cap (z_c) \cos(2\pi(f_{exc} + 2f_{el})t + \varphi) \\
& + \frac{A}{2} \langle k_{el,c}^\circ \rangle_\cap (z_c) \cos(2\pi(f_{exc} - 2f_{el})t + \varphi)
\end{aligned} \tag{7.5.26}$$

Where the approximations  $\tilde{z}_{ts}(t) - z_c \approx q(t) - q_s$  and  $\dot{\tilde{z}}_{ts}(t) \approx \dot{q}(t)$  are used. These are due to the way the harmonic approximation is employed here. As it is considered, that the main sampling path  $\tilde{z}_{ts}(t)$  of the tip is not affected by the modulated electrostatic contribution, the deflection  $q(t)$  will mainly follow that path whereby the modulation causes small additional spectral components. In analogy to the equation of motion solution with the AFM equations as shown in section A.7, the terms

$$k'_a = k_0 - \langle k_{ts,a}^\circ \rangle_\cap (z_c) \tag{7.5.27}$$

$$\gamma'_a = \frac{k_0}{2\pi f_0 Q_0} + \langle \gamma_{ts,a}^\circ \rangle_\cap (z_c) \tag{7.5.28}$$

$$F'_{s,a} = \langle F_{even,a}^\circ \rangle_\cup (z_c) - \langle k_{ts,a}^\circ \rangle_\cap q_s \tag{7.5.29}$$

can be considered as effective spring constant  $k'_a$ , effective damping  $\gamma'_a$  and effective force offset  $F'_{s,a}$  of the harmonic oscillator in the force field of the sample with the additional electrostatic contribution. Inserting these into the equation of motion (7.5.26) directly shows, that the tip movement in the force field of the sample with additional contributions of the modulated electrostatic force can be described

within the harmonic approximation by a freely oscillating tip with effective parameters. Contributions due to the modulated electrostatic force (7.1.2) are considered as additional parts of the excitation force. Thus, while the tip is mainly driven to oscillate at  $f_{\text{exc}}$  it experiences additional driving forces at distinct frequencies given by the contributions in (7.5.26) which are due to the electrostatic force modulation. As these contributions are now independent of  $\tilde{z}_{\text{ts}}(t)$  but depend on  $z_c$  due to the cup and cap averages, the approximated equation of motion (7.5.26) can be solved analytically for the resulting deflection  $q(t)$  in an analogous manner as presented in section 4.2. Therefore, using the Fourier transformation (4.2.5) with the identities (4.2.7) and (4.2.8) leads to

$$\begin{aligned} \mathcal{F}[q(t)] = G'_{\text{ho,a}}(f) \mathcal{F} \left[ +F'_{\text{s,a}} \right. & \quad (7.5.30) \\ & + F_0 \cos(2\pi f_{\text{exc}} t) \\ & + \left\langle F_{\text{el,b}}^{\circ} \right\rangle_{\cup} (z_c) \cos(2\pi f_{\text{el}} t) \\ & + \left\langle F_{\text{el,c}}^{\circ} \right\rangle_{\cup} (z_c) \cos(2\pi(2f_{\text{el}}) t) \\ & + \frac{A}{2} \left\langle k_{\text{el,b}}^{\circ} \right\rangle_{\cap} (z_c) \cos(2\pi(f_{\text{exc}} + f_{\text{el}}) t + \varphi) \\ & + \frac{A}{2} \left\langle k_{\text{el,b}}^{\circ} \right\rangle_{\cap} (z_c) \cos(2\pi(f_{\text{exc}} - f_{\text{el}}) t + \varphi) \\ & + \frac{A}{2} \left\langle k_{\text{el,c}}^{\circ} \right\rangle_{\cap} (z_c) \cos(2\pi(f_{\text{exc}} + 2f_{\text{el}}) t + \varphi) \\ & \left. + \frac{A}{2} \left\langle k_{\text{el,c}}^{\circ} \right\rangle_{\cap} (z_c) \cos(2\pi(f_{\text{exc}} - 2f_{\text{el}}) t + \varphi) \right] \end{aligned}$$

where

$$G'_{\text{ho,a}}(f) = \frac{1}{\left( k'_a - k_0 \frac{f^2}{f_0^2} \right) + 2\pi f i \gamma'_a} = |G'_{\text{ho,a}}(f)| \exp(i\varphi'_{\text{ho,a}}(f)) \quad (7.5.31)$$

is the corresponding complex amplitude transfer function of the driven harmonic oscillator in interaction with the sample force field and the modulated electrostatic force. At the current excitation frequency  $f$ ,  $|G'_{\text{ho,a}}(f)|$  is the length of a vector in the complex plane pointing in the direction of the corresponding phase angle  $\varphi'_{\text{ho,a}}(f)$ . Both quantities can be calculated analogously as shown in section 4.2 considering the real and imaginary part of  $G'_{\text{ho,a}}(f)$ . The phase angle  $\varphi'_{\text{ho,a}}(f)$  is analogue to (A.7.119) but here dependent on  $k'_a$  and  $\gamma'_a$  instead. Considering equation (7.5.30), all spectral components of the sensor deflection  $\mathcal{F}[q(t)](f)$  are directly linked via the transfer function  $G'_{\text{ho,a}}(f)$  to the spectral components of the excitation force and thus are given by

- a static deflection due to the static force components in  $F'_{\text{s,a}}$ ,
- a first harmonic mode following the external excitation with  $f_{\text{exc}}$ ,

## 7. Quantitative CFM theory

- a first and second harmonic of the electrostatic modulation at the frequencies  $f_{\text{el}}$  and  $2f_{\text{el}}$ ,
- and the sidebands  $f_{\text{exc}} \pm f_{\text{el}}$  and  $f_{\text{exc}} \pm 2f_{\text{el}}$

Each of these spectral components can be experimentally measured if a modulated external voltage (3.3.10) is applied between tip and sample support. In CFM the spectral components at both sideband frequencies are detected and evaluated.

### 7.6. CFM detection

A Lock-In amplifier detects a Fourier component  $\mathcal{F}[V_s](f)$  of its input signal  $V_s$  at a fixed frequency  $f$  within a given bandwidth while filtering noise. For that the Lock-In requires an additional, well-defined reference signal  $V_r$ , which determines the evaluated frequency  $f$ . The Fourier component of the input signal is defined on the complex plane as

$$\mathcal{F}[V_s](f) = |\mathcal{F}[V_s](f)| \exp(i\Delta\varphi(f)) \quad (7.6.32)$$

$$= A(f) \exp(i\Delta\varphi(f)) \quad (7.6.33)$$

where  $A(f) = |\mathcal{F}[V_s](f)|$  is the real amplitude and  $\Delta\varphi(f)$  the real phase shift of the input signal  $V_s$  in relation to the reference  $V_r$  at the frequency  $f$  which are output by the Lock-In amplifier. Considering the sensor displacement  $q(t)$  as the input signal for a Lock-in amplifier in baseband detection, any of its spectral components  $\mathcal{F}[q(t)](f)$  given in equation (7.5.30) can be quantitatively measured by setting the frequency  $f$  of the reference signal accordingly. Thereby the Lock-in detected amplitude and phase of the Fourier component  $\mathcal{F}[q(t)](f)$  at frequency  $f$  will be dependent on the transfer function  $G'_{\text{ho,a}}(f)$  and the spectral component of excitation force at the same frequency. For CFM, the spectral components of the displacement  $q(t)$  at frequencies  $f_{\text{exc}} \pm f_{\text{el}}$  and  $f_{\text{exc}} \pm 2f_{\text{el}}$  are detected using two separate Lock-In amplifiers for side-band detection<sup>1</sup>. The signal within Lock-in detection at frequency  $f_{\text{exc}} \pm f_{\text{el}}$  is given by

$$\mathcal{F}[q(t)](f_{\text{exc}} \pm f_{\text{el}}) = A(f_{\text{exc}} \pm f_{\text{el}}) \exp(i\Delta\varphi(f_{\text{exc}} \pm f_{\text{el}})) \quad (7.6.36)$$

---

<sup>1</sup>Note here, that in an experimental FM-CL-KPFM setup the spectral components  $\mathcal{F}[q(t)](f_{\text{exc}} \pm f_{\text{el}})$  and  $\mathcal{F}[q(t)](f_{\text{exc}} \pm 2f_{\text{el}})$  typically are not directly detected from the deflection signal  $q(t)$ . Instead the deflection signal  $q(t)$  is demodulated at the excitation frequency  $f_{\text{exc}}$  by multiplying it with a reference oscillation  $\cos(2\pi f_{\text{exc}} t)$  from the PLL before it is given as input signal to the Lock-In amplifiers. Effectively that demodulation resembles a shift of all spectral components of the deflection by  $f_{\text{exc}}$ . Hence the Lock-in detection of spectral components in the demodulated signal  $q(t) \cos(2\pi f_{\text{exc}} t)$  at reference frequencies  $f_{\text{el}}$  and  $2f_{\text{el}}$  is equivalent to detecting the spectral components of the deflection  $q(t)$  at frequencies  $f_{\text{exc}} + f_{\text{el}}$  and  $f_{\text{exc}} + 2f_{\text{el}}$

where

$$A(f_{\text{exc}} \pm f_{\text{el}}) = \left| G'_{\text{ho,a}}(f_{\text{exc}} \pm f_{\text{el}}) \right| \cdot \frac{A}{2} \left| \langle k_{\text{el,b}}^{\circ} \rangle_{\cap} \right| \quad (7.6.37)$$

and

$$\Delta\varphi(f_{\text{exc}} \pm f_{\text{el}}) = \varphi'_{\text{ho,a}}(f_{\text{exc}} \pm f_{\text{el}}) + \pi H_{\text{step}}(-\langle k_{\text{el,b}}^{\circ} \rangle_{\cap}) \quad (7.6.38)$$

are the amplitude and phase shift output by the Lock-In amplifier. It is assumed, that the frequencies of all other spectral components near  $f_{\text{exc}} \pm f_{\text{el}}$  are outside of the set bandwidth of the Lock-in amplifier and, therefore, are completely filtered out. The amplitude  $A(f_{\text{exc}} \pm f_{\text{el}})$  of the spectral component of the deflection at excitation frequency  $f_{\text{exc}} \pm f_{\text{el}}$  detected by the Lock-in amplifier is given by the product between the transfer function absolute  $\left| G'_{\text{ho,a}}(f_{\text{exc}} \pm f_{\text{el}}) \right|$  as gain and the magnitude of the first spectral component of electrostatic force gradient  $\left| \langle k_{\text{el,b}}^{\circ} \rangle_{\cap} \right|$  times  $A/2$ . The evaluation of the phase shift  $\Delta\varphi(f_{\text{exc}} + f_{\text{el}})$  provides information about the sign of the corresponding spectral component. It consists of the phase shift of the harmonic oscillator in interaction  $\varphi'_{\text{ho,a}}(f_{\text{exc}} \pm f_{\text{el}})$  and an additional phase shift which is  $\pi$  in case that tip-sample force gradient is negative  $\langle k_{\text{el,b}}^{\circ} \rangle_{\cap} < 0$  and zero all other cases. In the equation this additional phase shift therefore is considered as product with the Heaviside step function  $H_{\text{step}}(-\langle k_{\text{el,b}}^{\circ} \rangle_{\cap})$ .

The second Lock-In detects the signal at frequency  $f_{\text{exc}} \pm 2f_{\text{el}}$  which is given by

$$\mathcal{F}[q(t)](f_{\text{exc}} \pm 2f_{\text{el}}) = A(f_{\text{exc}} + 2f_{\text{el}}) \exp(i\Delta\varphi(f_{\text{exc}} + 2f_{\text{el}})) \quad (7.6.39)$$

with

$$A(f_{\text{exc}} \pm 2f_{\text{el}}) = \left| G'_{\text{ho,a}}(f_{\text{exc}} \pm 2f_{\text{el}}) \right| \cdot \frac{A}{2} \left| \langle k_{\text{el,c}}^{\circ} \rangle_{\cap} \right| \quad (7.6.40)$$

$$\Delta\varphi(f_{\text{exc}} \pm 2f_{\text{el}}) = \varphi'_{\text{ho,a}}(f_{\text{exc}} \pm 2f_{\text{el}}) + \pi H_{\text{step}}(-\langle k_{\text{el,c}}^{\circ} \rangle_{\cap}) \quad (7.6.41)$$

where the Lock-in detected amplitude  $A(f_{\text{exc}} \pm 2f_{\text{el}})$  and phase shift  $\Delta\varphi(f_{\text{exc}} \pm 2f_{\text{el}})$  contain information about  $\langle k_{\text{el,c}}^{\circ} \rangle_{\cap}$ . By this approach both spectral components of the electrostatic force gradient  $\langle k_{\text{el,b}}^{\circ} \rangle_{\cap}$  and  $\langle k_{\text{el,c}}^{\circ} \rangle_{\cap}$  at frequencies  $f_{\text{exc}} + f_{\text{el}}$  and  $f_{\text{exc}} + 2f_{\text{el}}$  are obtained in a CFM experiment.

---

which means

$$\mathcal{F}[q(t) \cos(2\pi f_{\text{exc}} t)](f_{\text{el}}) \Leftrightarrow \mathcal{F}[q(t)](f_{\text{exc}} \pm f_{\text{el}}) \quad (7.6.34)$$

$$\mathcal{F}[q(t) \cos(2\pi f_{\text{exc}} t)](2f_{\text{el}}) \Leftrightarrow \mathcal{F}[q(t)](f_{\text{exc}} \pm 2f_{\text{el}}) \quad (7.6.35)$$

As the outcome is equal independent of the exact detection approach [70], this rather technical detail is left out here for a better readability.



## 7.7. Interpretation of CFM signals

In CFM, the bias voltage  $V_{\text{bias}}$  is adjusted in a feedback loop to equalize the Lock-In detected amplitude (7.6.37) of the spectral component of the deflection signal at frequency  $f_{\text{exc}} \pm f_{\text{el}}$ . The adjusted bias voltage  $V_{\text{bias}}$  which minimizes the amplitude  $A(f_{\text{exc}} + f_{\text{el}})$  of that spectral component is the resulting CFM signal  $V_{\text{bias}}^{\text{min}}$ . For an active feedback loop ideally adjusting  $V_{\text{bias}} = V_{\text{bias}}^{\text{min}}$  the spectral components (7.6.36) vanish as shown in Figure 3.4(b), which yields

$$\mathcal{F}[q(t) \cos(2\pi f_{\text{exc}} t)](f_{\text{el}}) = 0 \quad (7.7.42)$$

$$\Leftrightarrow \mathcal{F}[q(t)](f_{\text{exc}} \pm f_{\text{el}}) = 0 \quad (7.7.43)$$

$$\Leftrightarrow A(f_{\text{exc}} \pm f_{\text{el}}) = 0 \quad (7.7.44)$$

$$\Leftrightarrow \langle k_{\text{el,b}}^{\circ} \rangle_{\square} = 0 \quad \text{for} \quad V_{\text{bias}} = V_{\text{bias}}^{\text{min}} \quad (7.7.45)$$

Considering the contributions in CFM detection, the spectral component (7.6.36) only can be minimized if the electrostatic force gradient vanishes due to the adjusted bias voltage  $V_{\text{bias}} = V_{\text{bias}}^{\text{min}}$ . Thus, based on equation (7.1.4) and (7.4.23), a relation for the CFM signal  $V_{\text{bias}}^{\text{min}}$  can be derived as

$$V_{\text{bias}}^{\text{min}} = V_{\text{CPD}} + \sum_{i=1}^N q_i \frac{\left\langle \frac{\partial^2 \hat{\Phi}_{\text{void}}(\mathbf{r}_i)}{\partial z_{\text{ts}}^2} \right\rangle_{\square}}{\left\langle \frac{\partial^2 C_{\text{void}}}{\partial z_{\text{ts}}^2} \right\rangle_{\square}} \quad (7.7.46)$$

By introducing the weight function for charges  $W_q(\mathbf{r}_i)$  [69] evaluated at the charge position  $\mathbf{r}_i$ , the relation (7.7.46) can be written in the compact form

$$V_{\text{bias}}^{\text{min}} = V_{\text{CPD}} + \sum_{i=1}^N q_i W_q(\mathbf{r}_i) \quad (7.7.47)$$

The CFM signal  $V_{\text{bias}}^{\text{min}}$  is the voltage which nullifies the cap-averaged electrostatic force gradient  $\langle k_{\text{el,b}}^{\circ} \rangle_{\square}$  detected at frequency  $f_{\text{exc}} \pm f_{\text{el}}$ . In terms of the cycle-averaged force  $F_{\text{el,b}}$ ,  $V_{\text{bias}}^{\text{min}}$  represents the bias voltage where the repulsive charge-dependent force best counteracts the capacitive force. Hence voltage  $V_{\text{bias}}^{\text{min}}$  defines the point of minimum attractive cycle-averaged electrostatic force  $\langle F_{\text{el,b}} \rangle_{\square}$ .

The voltage  $V_{\text{bias}}^{\text{min}}$  contains information on the charges  $q_i$  located in the tip-sample capacitor and the contact potential difference  $V_{\text{CPD}}$  between the tip and the sample support. Therefore, the voltage  $V_{\text{bias}}^{\text{min}}$  measured in presence of any charge  $q_i$  in the tip-sample capacitor will not be equal to  $V_{\text{CPD}}$ . The correct evaluation of  $V_{\text{bias}}^{\text{min}}$  data requires the precise calculation of the weight function  $W_q(\mathbf{r}_i)$  at each charge position

$\mathbf{r}_i$ . This, in return, requires precise characterisation of the tip-sample capacitor geometry and its description by accurate tip-geometry models for calculating the electrostatic capacitance  $C_{\text{void}}(z_{\text{ts}})$  and potential  $\hat{\Phi}_{\text{void}}(z_{\text{ts}})$ . In chapter 8, different tip-geometry models are analysed and important model parameter influences on the voltage  $V_{\text{bias}}^{\text{min}}$  are identified. For a given electrostatic model, the charges  $q_i$  and the contact potential difference  $V_{\text{CPD}}$  present in the tip-sample capacitor can be quantitatively retrieved from distant-dependent  $V_{\text{bias}}^{\text{min}}(z_{\text{ts}})$  data (see chapter 8).

While in model calculations the parameters describing tip-sample properties are well defined and known, in experiments, the parameters required for the considered model for representing the tip-sample capacitor have to be retrieved from experimental data. This leads to the second important signal required for the interpretation of experimental CFM data, which is the spectral component (7.6.39) at frequency  $f_{\text{exc}} \pm 2f_{\text{el}}$  detected by a second Lock-In. Considering equation (7.6.40) with relations (7.1.5) and (7.4.24) provides the relation

$$A(f_{\text{exc}} \pm 2f_{\text{el}}) = \left| G'_{\text{ho,a}}(f_{\text{exc}} \pm 2f_{\text{el}}) \right| \frac{A}{8} V_{\text{el}}^2 \left\langle \frac{\partial^2 C_{\text{void}}}{\partial z_{\text{ts}}^2} \right\rangle_{\cap} \quad (7.7.48)$$

for the amplitude of each spectral component at frequencies  $f_{\text{exc}} \pm 2f_{\text{el}}$ . As the sum of both amplitudes is measured, the full amplitude at frequency  $f_{\text{exc}} + 2f_{\text{el}}$  is given by

$$A_{2f_{\text{el}}} = A(f_{\text{exc}} + 2f_{\text{el}}) = \left| G'_{\text{ho,a}}(f_{\text{exc}} \pm 2f_{\text{el}}) \right| \frac{A}{4} V_{\text{el}}^2 \left\langle \frac{\partial^2 C_{\text{void}}}{\partial z_{\text{ts}}^2} \right\rangle_{\cap} \quad (7.7.49)$$

Hence, the signal  $A_{2f_{\text{el}}}$  yields information on the capacitance  $C_{\text{void}}$  of the tip-sample system. Measuring  $A_{2f_{\text{el}}}$  and  $V_{\text{bias}}^{\text{min}}$  as function of  $z_{\text{ts}}$  allows the quantification of charges  $q_i$  located in the tip-sample capacitor on the foundation of a sufficiently precise electrostatic tip-geometry model in two consecutive evaluation steps (see chapter 9).



## 8. Modelling nanoscale charge measurements

Here, a detailed investigation of numerous factors that contribute to the measurement observable  $V_{\text{bias}}^{\text{min}}$  are presented which, consequently, need to be considered when aiming for quantitative charge measurements. In particular, a dependence on the oscillation amplitude is unravelled and the influence of the tip geometry and system parameters such as the dielectric constant are analysed. Furthermore, the influence of charges depending on their lateral and vertical position is discussed. As CFM is a non-local technique, it can be shown that charges far away from the tip position still give a contribution. The conclusive findings are, that charge quantification from regular imaging bears many ambiguities, while mapping the progress of  $V_{\text{bias}}^{\text{min}}$  with respect to the vertical tip position  $z_{\text{ts}}^{\text{min}}$  allows to untangle many of these contributions on the path to charge quantification.

The following work initially was published in [143].

## Modeling nanoscale charge measurements

Daniel Heile , Reinhard Olbrich , Michael Reichling , and Philipp Rahe \*

Fachbereich Mathematik/Informatik/Physik, Universität Osnabrück, BarbarasträÙe 7, 49076 Osnabrück, Germany



(Received 23 November 2022; revised 4 June 2023; accepted 5 June 2023; published 15 August 2023)

The quantitative measurement of charges at the nanoscale yields important insights into fundamental physical, chemical, or biological processes. In principle, charges can be probed by the sharp tip of a dynamic atomic force microscope, however, quantitative measurements are still a challenge as a large number of parameters and effects contribute to the measured signal. Here, we introduce the fundamental framework for charge force microscopy (CFM) and investigate charges located in, on, or above the surface of a dielectric substrate supported by a metal electrode. We present a comprehensive analysis of CFM signal generation and, in particular, unravel the dependency of the CFM signal on the probe oscillation amplitude, on system parameters such as the substrate dielectric constant or the tip geometry, and on the vertical and lateral position of charges. Most importantly, we untangle the influence from nearby charges when quantifying the magnitude of a central charge of interest in presence of many surrounding charges. We find that charge quantification from regular imaging bears many ambiguities, while mapping the CFM signal perpendicular to the sample surface allows to untangle many signal contributions. Thus, by accounting for measurement parameters and nonlocal influences, quantitative measurements are possible with CFM.

DOI: [10.1103/PhysRevB.108.085420](https://doi.org/10.1103/PhysRevB.108.085420)

### I. INTRODUCTION

Measuring and controlling the charge state of nanoscale objects is paramount in a large number of research fields including catalysis, organic and molecular electronics, quantum sensors, or energy storage [1–3]. A *change* in the charge state of a nano-object can well be detected by dynamic techniques of measuring forces between a fine tip and the object of interest with a sensitivity down to single electrons [4–8] and atomic-scale resolution has been achieved [9,10]. In contrast, the *quantification* of the static charge magnitude accumulated in a nano-object is still most challenging [11]. In addition to the long-range character of the electrostatic force, the electric potential distribution governing the tip-surface interaction critically depends on the nanoscale size and shape of the tip that can hardly be produced or characterized with the desired precision.

Here, we address fundamental aspects for an experimental quantification of charges below, on, or above the surface of an electrically insulating substrate. Charge measurements are implemented using the technology of frequency-modulated (FM) closed-loop (CL) Kelvin probe force microscopy (KPFM), a nanoscale imaging technique that is rooted in the measurement of the work function difference between tip and sample for metal and semiconductor surfaces [12–14]. The KPFM measurement signal is generally referred to as the contact potential difference (CPD) [15] and the spatial resolution power is reflected by introducing the concept of both a *local* work function [16] as well as a *local* contact potential difference [15]. The central measurement parameter in KPFM is the

bias voltage  $V_{\text{bias}}$  applied between the electrically conducting tip and the conducting sample.

In this work, we investigate charges near a dielectric support and  $V_{\text{bias}}$  refers to the voltage applied between the tip and a metallic counter electrode. The primary outcome of a charge measurement experiment is the force-minimizing bias voltage  $V_{\text{bias}}^{\text{min}}$  that is the response in the FM-CL force measurement. For our analysis, we build on previous work where a formalism was outlined allowing a simple representation of  $V_{\text{bias}}^{\text{min}}$  in terms of the charges  $q_i$  and the weighted average of the second derivatives of the tip-surface electric potential  $\Phi_{\text{void}}$  at the charge positions  $\vec{r}_i$  as well as the weighted average of the second derivative of the void capacitance  $C_{\text{void}}$  along the tip-sampling path [17]. Together, these averages provide a weight function  $W_q(\vec{r}_i)$  [18], which determines the contribution of the respective charge to the  $V_{\text{bias}}^{\text{min}}$  voltage signal. For a valid interpretation of measurement data, the contact potential difference between tip and sample support  $V_{\text{CPD}}$  that is part of the measured signal  $V_{\text{bias}}^{\text{min}}$  has to be taken into account. Measuring  $V_{\text{bias}}^{\text{min}}$  is further on referred to as the method of charge force microscopy (CFM).

Here, we investigate by extensive modeling how a static charge magnitude can be measured by monitoring the CFM voltage  $V_{\text{bias}}^{\text{min}}$  when approaching the tip to the surface in the vicinity of the charge. In particular, we use three different geometric models for the tip and investigate  $V_{\text{bias}}^{\text{min}}$  for different oscillation amplitudes, different dielectric properties of the substrate, different charge positions, and different charge distributions around a central charge of interest. We find that the CFM voltage acquired as a function of the tip-sample distance  $z_{\text{ts}}$  is key to charge quantification, while commonly used imaging bears many ambiguities.

The paper is organized as follows: In Sec. II we review the physical model, introduce three tip geometries that are used

\*prahe@uos.de

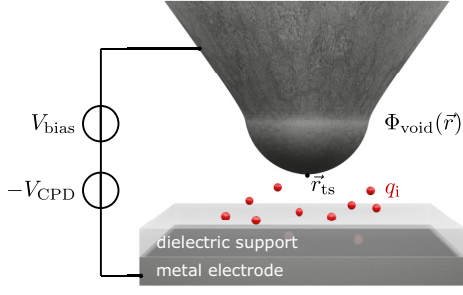


FIG. 1. Geometry of a tip in proximity of a dielectric support fixed on a metallic counter electrode. Point charges  $q_i$  (red spheres) are located between tip and metal electrode. The void (charge-free) tip-sample capacitor is physically described by the electrostatic potential  $\Phi_{\text{void}}(\vec{r})$ . An external voltage  $V_{\text{bias}}$  is applied between tip and metal counter electrode, while a voltage  $-V_{\text{CPD}}$  is generated upon electrical contact between the two metals. The vector  $\vec{r}_{\text{ts}} = [x_{\text{ts}}, y_{\text{ts}}, z_{\text{ts}}]$  describes the momentary tip position with  $z_{\text{ts}}$  being the tip-sample distance.

for the simulations, and discuss the electrostatic quantities relevant for  $W_q(\vec{r}_i)$ . The influence of the probe oscillation amplitude  $A$ , the impact of the dielectric constant  $\epsilon_s$  of the substrate, and effects of the tip geometry on the charge measurement are analysed in Sec. III. In Sec. IV, we investigate the influence of the lateral and vertical positions of a single point charge on the distance-dependent CFM signal. Section V addresses charge quantification by introducing a methodology to retrieve the charge of a central pointlike object in the vicinity of secondary charges from  $V_{\text{bias}}^{\text{min}}$  data. We conclude in Sec. VI with a summary of major results and propositions for a successful implementation of CFM measurements.

## II. ELECTROSTATIC MODEL AND CFM FUNDAMENTALS

A model representation of the tip-sample geometry is shown in Figs. 1 and 2. The system is described in the sample coordinate system  $\vec{r} = (x, y, z)$  where the tip is positioned at  $\vec{r}_{\text{ts}} = [x_{\text{ts}}, y_{\text{ts}}, z_{\text{ts}}]$ . Following previously outlined definitions [19], the  $z$  axis is perpendicular to the substrate surface, its origin  $z = 0$  is at the surface, and  $z_{\text{ts}}$  is the closest

tip-sample distance during one tip oscillation cycle. The tip is brought into close proximity to the surface of a thick dielectric support with relative permittivity  $\epsilon_s$  that is fixed on a metal plate acting as the counter electrode with respect to the tip. Charges  $q_i$  placed at positions  $\vec{r}_i$  in, on, or above the dielectric support represent point charges or charged nanoscale objects that are subject of investigation. The model works under the assumption that the tip is an ideal metal free of excess charge. The surface of the tip is assumed to be smooth as well as bare of atomic structure and the tip can be described by a macroscopic model [20]. A variable voltage  $V_{\text{bias}}$  is applied between tip and counter electrode, while the voltage  $-V_{\text{CPD}}$  appears upon establishing electrical contact between tip and counter electrode.

The electrostatic force  $F_{\text{el}}$  acting on the probing tip is the central quantity for charge quantification as it is fundamental for determining the voltage  $V_{\text{bias}}^{\text{min}}$ . This force can be calculated from the electrostatic energy of the full physical setup, whereby the tip-sample system, the point charges, as well as the external bias supply have to be taken into account. For the tip-sample system, the electrostatic energy can be calculated from solving the electrostatic problem for the given tip and sample geometry including the point charges and the dielectric support. Additionally, the work performed by the external bias supply has to be taken into account in the energy calculation. A solution of the more general electrostatic problem, namely, a system containing an arbitrary number of metal objects and point charges with an external battery, has been given before [21]. For our purpose, this analysis has been reduced to the case of two metals, one representing the tip and the second the counter electrode, as well as  $N$  point charges [17]. This allows to write the total electrostatic energy  $U_{\text{el}}$  as a sum of four contributions [22], namely,

$$U_{\text{el}} = U_C + U_{\text{q-c}} + U_{\text{q-q}} + U_{\text{im}}. \quad (1)$$

The first term  $U_C$  describes the capacitive interaction between tip and metal electrode with an interjacent dielectric medium. This energy is independent of the point charges, but establishes the quadratical dependence of the interaction force on  $V_{\text{bias}}$ . The quantity governing this contribution is the void capacitance  $C_{\text{void}}(\vec{r}_{\text{ts}})$ , where  $\vec{r}_{\text{ts}}$  is the momentary tip position. By *void* we denote all quantities of the charge-free system.

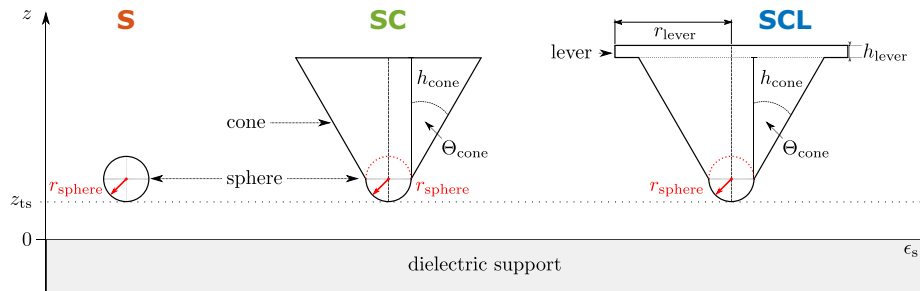


FIG. 2. Cross sections of the three model tips and system geometries: sphere (S), half-sphere and cone (SC), as well as half-sphere and cone with lever (SCL). The sphere is parametrized by the radius  $r_{\text{sphere}}$ , the cone by the cone height  $h_{\text{cone}}$  and half opening angle  $\Theta_{\text{cone}}$ , and the lever by the radius  $r_{\text{lever}}$  and the thickness  $h_{\text{lever}}$ . The tip-sample distance  $z_{\text{ts}}$  (marked by the dotted line) is defined as the distance between the surface of the dielectric support with relative permittivity  $\epsilon_s$  and the point of the tip closest to the surface.

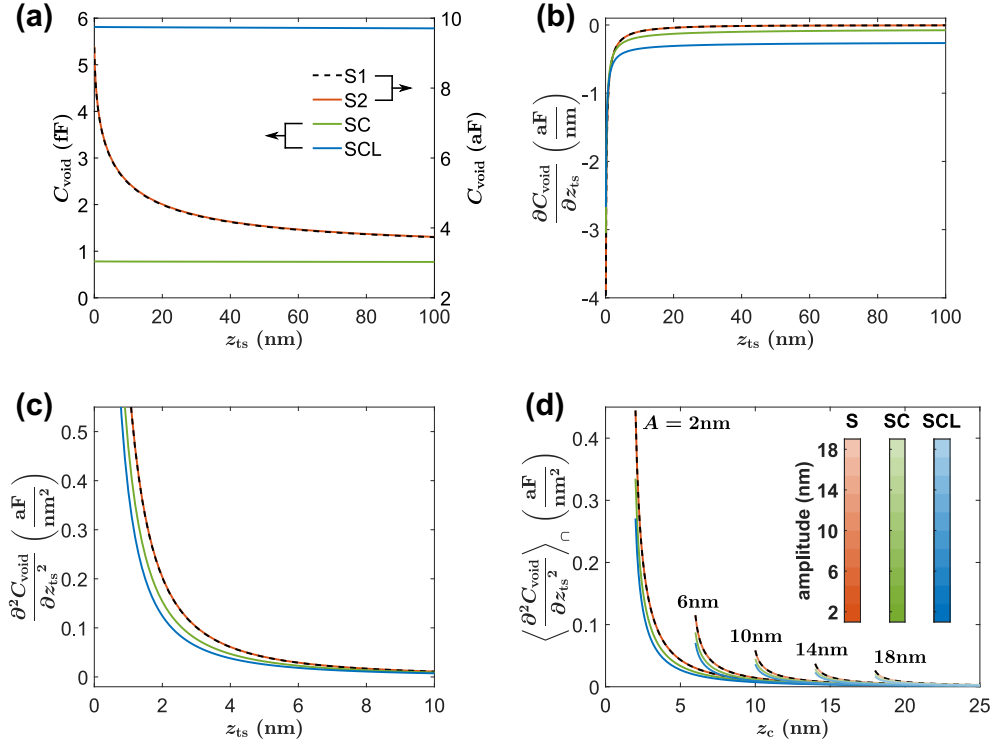


FIG. 3. (a) Capacitance  $C_{\text{void}}$  as well as (b) first, (c) second, and (d) cap-averaged second derivative of the capacitance for tip models S, SC, and SCL. Data in (a)–(c) are plotted with respect to the tip-sample distance  $z_{\text{ts}}$ , while data in (d) are plotted with respect to the tip oscillation center position  $z_c$  [19] for oscillation amplitudes  $A$  in the range of 2 to 18 nm. Tip model parameters listed in Table I and  $\epsilon_s = 24$  are used in the calculation. For geometry S, results calculated by the analytical [25] (S1) and numerical [24] (S2) codes are depicted by black dashed and straight red lines, respectively. Results for the SC and SCL models are depicted in green and blue, respectively.

The system is modeled by two metals representing the tip and the counter electrode with the potential difference  $V$  between these two metals. Further analysis shows that the capacitive term is an important experimental parameter but not directly relevant for charge measurements. Instead, the second energy contribution  $U_{q-c}$  is central for charge quantification as this term describes the energy required to bring the point charges  $q_i$  into the capacitor at positions  $\vec{r}_i$ . In particular, the energy for each point charge  $i$  can be expressed by a product between the point-charge magnitude  $q_i$  and the electrostatic potential of the point-charge free capacitor  $\Phi_{\text{void}}(\vec{r}_{\text{ts}}, \vec{r}_i)$  for a given tip position  $\vec{r}_{\text{ts}}$  and at the position of the charge  $\vec{r}_i$ . For the ease of calculation, the electrostatic potential is normalized by the potential difference  $V$ , resulting in the normalized electrostatic potential  $\hat{\Phi}_{\text{void}} = \Phi_{\text{void}}/V$ . The Coulomb interaction between the point charges is described by the third term  $U_{q-q}$ . Descriptively, this is the energy required to introduce each point charge into the field of the other point charges. The fourth term  $U_{\text{im}}$  describes the energy contribution of all image charges at the metal surfaces that are generated by the point charges.

Using Eq. (1), the electrostatic force  $F_{\text{el}}$  is calculated from the negative derivative of the total energy  $U_{\text{el}}$  with respect to the tip-sample distance  $z_{\text{ts}}$ . The restriction of the derivative to the coordinate  $z_{\text{ts}}$  is justified by the constraint of the probe solely oscillating along  $z_{\text{ts}}$  without any other degree

of freedom. The electrostatic force consists of four terms, namely [22],

$$F_{\text{el}}(z_{\text{ts}}, V) = \frac{1}{2} \frac{\partial C_{\text{void}}}{\partial z_{\text{ts}}} V^2 - \sum_{i=1}^N q_i \frac{\partial \hat{\Phi}_{\text{void}}(\vec{r}_i)}{\partial z_{\text{ts}}} V - \frac{\partial U_{q-q}}{\partial z_{\text{ts}}} - \frac{1}{2} \sum_{i=1}^N q_i \frac{\partial \Phi_{\text{im}}(\vec{r}_i)}{\partial z_{\text{ts}}}. \quad (2)$$

The first term follows from the capacitive contribution to the electrostatic force and is always attractive as  $\frac{\partial C_{\text{void}}}{\partial z_{\text{ts}}} < 0$  as shown in Fig. 3(b). This term enables the measurement of the voltage  $V_{\text{CPD}}$  in KPFM experiments [14]. The second term is the key contribution to CFM measurements as it describes the force acting between the charges and the metal objects. The third term vanishes ( $\frac{\partial U_{q-q}}{\partial z_{\text{ts}}} = 0$ ) as electrostatic forces and counterforces compensate each other in an ensemble of charges held at fixed positions. The fourth term is caused by charge redistribution on the metal surfaces, commonly referred to as the image charge. The related potential  $\Phi_{\text{im}}$  is independent of the potential difference  $V$  and, therefore, does not contribute to  $V_{\text{bias}}^{\text{min}}$  as the force minimizing bias voltage is derived from the derivation with respect to  $V$ .

The basic principle of CFM is the variation of  $V_{\text{bias}}$  to find the point of minimum attractive force at  $V_{\text{bias}}^{\text{min}}$  where the repulsive charge-dependent force best counteracts the

TABLE I. Parameters for the tip models S, SC, and SCL utilized for all calculations unless otherwise noted.

| Model | $r_{\text{sphere}}$<br>(nm) | $\Theta_{\text{cone}}$<br>(deg) | $h_{\text{cone}}$<br>( $\mu\text{m}$ ) | $r_{\text{lever}}$<br>( $\mu\text{m}$ ) | $h_{\text{lever}}$<br>( $\mu\text{m}$ ) |
|-------|-----------------------------|---------------------------------|--|---|---|
| S     | 30.0                        |                                 |  |   |   |
| SC    | 30.0                        | 23.3                            | 12.5                                   |   |   |
| SCL   | 30.0                        | 23.3                            | 12.5                                   | 34.6                                    | 4.0                                     |

attractive capacitive force under conditions of a dynamic measurement. For a measurement with frequency modulation and closed-loop force minimization, the total potential difference  $V$  between tip and sample is represented as

$$V = V_{\text{bias}} - V_{\text{CPD}} + V_{\text{el}} \cos(2\pi f_{\text{el}} t) \quad (3)$$

with the contact potential difference  $V_{\text{CPD}}$ , the bias voltage  $V_{\text{bias}}$ , and a bias modulation with amplitude  $V_{\text{el}}$  and frequency  $f_{\text{el}}$ . The negative sign for  $V_{\text{CPD}}$  is used to follow the common convention in the KPFM literature [15]. As a result of the bias modulation, the electrostatic force measured by the tip is a modulated signal with spectral components at  $f_{\text{el}}$  and  $2f_{\text{el}}$ , namely [22],

$$F_{\text{el}} = F_{\text{el,a}} + F_{\text{el,b}} \cos(2\pi f_{\text{el}} t) + F_{\text{el,c}} \cos(2\pi 2f_{\text{el}} t). \quad (4)$$

Terms  $F_{\text{el,a}}$  and  $F_{\text{el,c}}$  are given in Ref. [22]. The term

$$F_{\text{el,b}} = V_{\text{el}} \left( \frac{\partial C_{\text{void}}}{\partial z_{\text{ts}}} (V_{\text{bias}} - V_{\text{CPD}}) - \sum_{i=1}^N q_i \frac{\partial \hat{\Phi}_{\text{void}}(\vec{r}_i)}{\partial z_{\text{ts}}} \right) \quad (5)$$

is relevant for CFM as this component contains the full information on the charge distribution. It can be shown [22] that the dynamic measurement with FM detection yields a signal proportional to the cycle-averaged force gradient

$$\left\langle \frac{\partial F_{\text{el,b}}}{\partial z_{\text{ts}}} \right\rangle_{\cap} = V_{\text{el}} \left( \left\langle \frac{\partial^2 C_{\text{void}}}{\partial z_{\text{ts}}^2} \right\rangle_{\cap} (V_{\text{bias}} - V_{\text{CPD}}) - \sum_{i=1}^N q_i \left\langle \frac{\partial^2 \hat{\Phi}_{\text{void}}(\vec{r}_i)}{\partial z_{\text{ts}}^2} \right\rangle_{\cap} \right), \quad (6)$$

whereby  $\langle \dots \rangle_{\cap}$  denotes the cap-weighted average function [23]

$$\langle f \rangle_{\cap}(z_c) = \frac{2}{\pi A^2} \int_{-A}^A f(z_c + z) \sqrt{A^2 - z^2} dz \quad (7)$$

with the tip oscillation center position  $z_c$  and the oscillation amplitude  $A$  as introduced in Ref. [19]. The CFM signal voltage  $V_{\text{bias}}^{\text{min}}$  directly follows from setting Eq. (6) to be equal

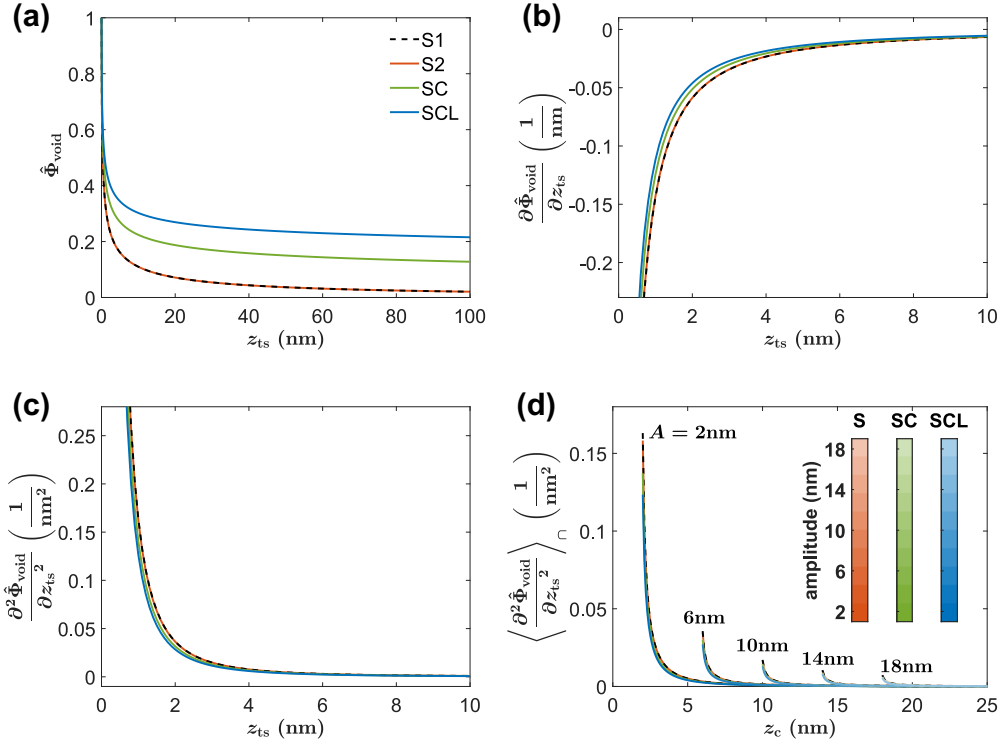


FIG. 4. (a) Normalized electrostatic potential  $\hat{\Phi}_{\text{void}}$  as well as (b) first, (c) second, and (d) cap-averaged second derivative of the normalized electrostatic potential evaluated at position  $\vec{r}_0 = [0, 0, 0]$  for tip models S, SC, and SCL. Data in (a)–(c) are plotted with respect to the tip-sample distance  $z_{\text{ts}}$ , while data in (d) are plotted with respect to the tip oscillation center position  $z_c$  [19] for oscillation amplitudes  $A$  in the range of 2 to 18 nm. Tip-model parameters listed in Table I and  $\epsilon_s = 24$  are used in the calculation. For geometry S, results calculated by the analytical [25] (S1) and numerical [24] (S2) codes are depicted by black dashed and straight red lines, respectively. Results for the SC and SCL models are depicted in green and blue, respectively.



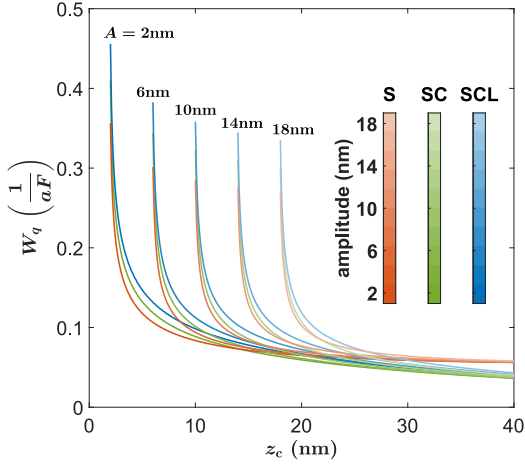


FIG. 5. Weight function  $W_q$  as a function of the tip oscillation center position  $z_c$  [19] calculated at the position  $\vec{r}_0 = [0, 0, 0]$  for models S, SC, and SCL as well as for amplitudes  $A$  in the range from 2 to 18 nm. Increasing amplitudes are represented by successively tinted colors (colors with increased lightness) as indicated by the color bars.

to zero. Technically, this is usually realized by a feedback loop adjusting  $V_{\text{bias}}$  to the point of vanishing signal  $\langle \frac{\partial F_{\text{elb}}}{\partial z_{\text{ts}}} \rangle_{\square}$  with respect to  $V_{\text{bias}}$ ; this signal can be measured from the  $f_{\text{el}}$  component in the frequency-shift signal  $\Delta f$ . Narrow-band and phase-sensitive detection of this component yields a high signal-to-noise ratio for measuring  $V_{\text{bias}}^{\text{min}}$  as the small voltage modulation amplitude  $V_{\text{el}}$  effectively produces a differentia-

tion with respect to  $V_{\text{bias}}$ . The CFM signal then reads as [17]

$$V_{\text{bias}}^{\text{min}} = V_{\text{CPD}} + \sum_{i=0}^N q_i \frac{\left\langle \frac{\partial^2 \hat{\Phi}_{\text{void}}(\vec{r}_i)}{\partial z_{\text{ts}}^2} \right\rangle_{\square}}{\left\langle \frac{\partial^2 C_{\text{void}}}{\partial z_{\text{ts}}^2} \right\rangle_{\square}}. \quad (8)$$

This equation can be written in a compact form by introducing the weight function for charges  $W_q(\vec{r}_i)$  [18] evaluated at the charge position  $\vec{r}_i$ :

$$V_{\text{bias}}^{\text{min}} = V_{\text{CPD}} + \sum_{i=0}^N q_i W_q(\vec{r}_i) \quad \text{with} \quad W_q(\vec{r}_i) = \frac{\left\langle \frac{\partial^2 \hat{\Phi}_{\text{void}}(\vec{r}_i)}{\partial z_{\text{ts}}^2} \right\rangle_{\square}}{\left\langle \frac{\partial^2 C_{\text{void}}}{\partial z_{\text{ts}}^2} \right\rangle_{\square}}. \quad (9)$$

Two electrostatic quantities contribute to the weight function  $W_q$ , namely, the normalized electrostatic potential  $\hat{\Phi}_{\text{void}}$  evaluated at charge positions  $\vec{r}_i$  and the capacitance  $C_{\text{void}}$ , both for the given tip position  $\vec{r}_{\text{ts}}$ . To evaluate these quantities, the tip-sample system has to be defined in all details, namely, the tip geometry (formally described by a set of parameters  $\{p_{\text{tip}}\}$ ), the tip position  $\vec{r}_{\text{ts}} = [x_{\text{ts}}, y_{\text{ts}}, z_{\text{ts}}]$ , the dielectric constant  $\epsilon_s$  of the dielectric support, and the tip oscillation amplitude  $A$  via the cap-average  $\langle \dots \rangle_{\square}$ . The vertical tip position of the averaged quantities is parametrized by either the tip oscillation center position  $z_c$  or the position of the lower turning point during the oscillation cycle  $z_{\text{ts}}^{\text{min}} = z_c - A$  [19]. Taking

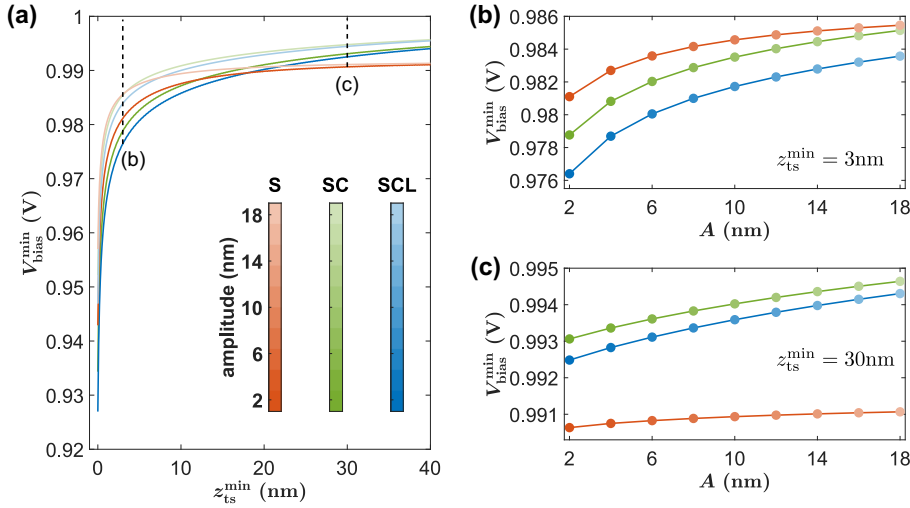


FIG. 6.  $V_{\text{bias}}^{\text{min}}$  voltage calculated for models S, SC, and SCL as a function of (a)  $z_{\text{ts}}^{\text{min}}$  for amplitudes  $A$  in the range from 2 to 18 nm as well as (b), (c) as a function of the oscillation amplitude  $A$  at fixed minimum tip-sample distances of (b) 3 nm and (c) 30 nm. Equation (8) is evaluated at  $\vec{r}_0 = [0, 0, 0]$  for a single point charge  $q = -e$  (with the elementary charge  $e > 0$ ) located at this position. Tip-model parameters listed in Table I,  $\epsilon_s = 24$ , and  $V_{\text{CPD}} = 1$  V are used in the calculation. Increasing amplitudes are represented by successively tinted colors [see color bars in (a)]. For clarity, only the  $V_{\text{bias}}^{\text{min}}$  curves for the smallest and largest amplitudes are depicted in (a).

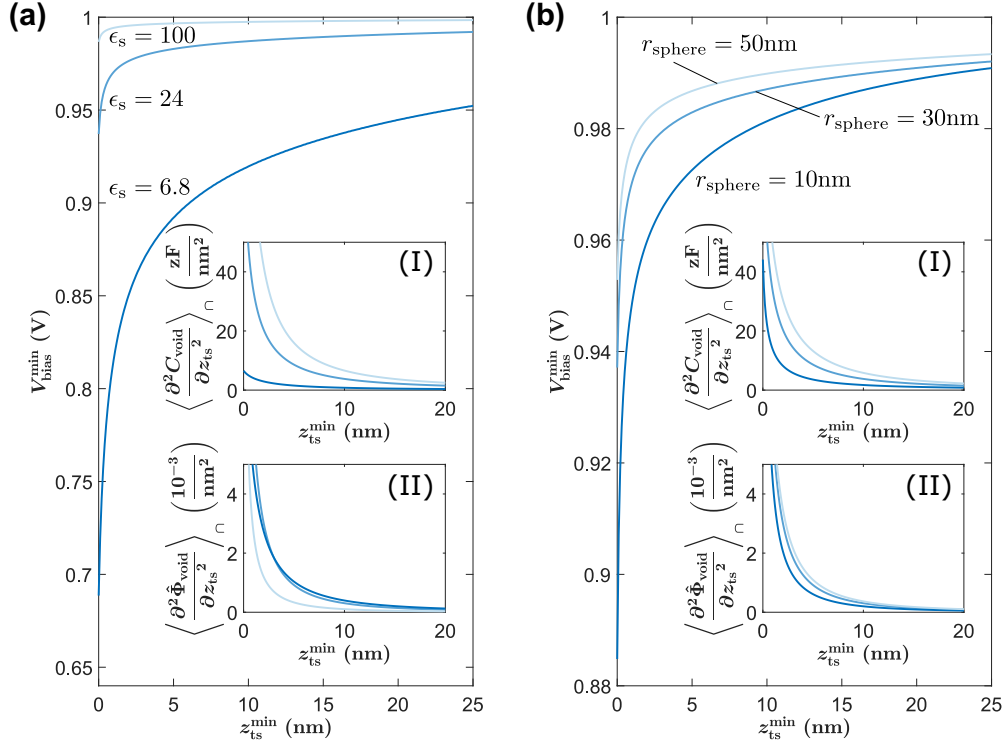


FIG. 7. Dependency of  $V_{\text{bias}}^{\min}(z_{\text{ts}}^{\min})$  on (a) the sample permittivity  $\epsilon_s$  with  $r_{\text{sphere}} = 30$  nm and on (b) the sphere radius  $r_{\text{sphere}}$  with  $\epsilon_s = 24$ , both for the SCL model. An oscillation amplitude  $A = 5$  nm, parameters from Table I,  $\epsilon_s = 24$ , and  $V_{\text{CPD}} = 1$  V are used. One negative charge  $q = -e$  is placed at  $\vec{r}_0 = [0, 0, 0]$ . The successive tint of the line colors represents (a) the different permittivity values ( $\epsilon_s = 6.8, 24$ , and  $100$ ) or (b) the different sphere radii ( $r_{\text{sphere}} = 10, 30$ , and  $50$  nm). Insets show the corresponding cap-averaged second derivatives of (I) the capacitance and (II) the normalized electrostatic potential.

account of all parameters, we find

$$\langle C_{\text{void}} \rangle_{\cap} = \langle C_{\text{void}} \rangle_{\cap}(x_{\text{ts}}, y_{\text{ts}}, z_c, \epsilon_s, \{p_{\text{tip}}\}, A), \quad (10)$$

$$\langle \hat{\Phi}_{\text{void}} \rangle_{\cap} = \langle \hat{\Phi}_{\text{void}} \rangle_{\cap}(\vec{r}_i, x_{\text{ts}}, y_{\text{ts}}, z_c, \epsilon_s, \{p_{\text{tip}}\}, A), \quad (11)$$

$$W_q(\vec{r}_i) = W_q(\vec{r}_i, x_{\text{ts}}, y_{\text{ts}}, z_c, \epsilon_s, \{p_{\text{tip}}\}, A). \quad (12)$$

For homogeneous, atomically flat surfaces, the vector  $\vec{r}_{\text{ts}}$  in Eqs. (10)–(12) could be substituted by the scalar coordinate  $z_{\text{ts}}$ . However, for the general case of a structured surface, the lateral tip position has to be taken into account. Depending on the context, different parameters for the electrostatic quantities will be relevant in the following sections. To highlight the respective relevant dependency for the different cases, we refrain in the following from explicitly listing the full parameter list for the quantities in Eqs. (10)–(12), but give the relevant ones instead.

For the evaluation of the electrostatic model for the void system, we consider three model tip geometries as sketched in Fig. 2: a tip consisting of a sphere with radius  $r_{\text{sphere}}$  (denoted by S), a half-sphere with radius  $r_{\text{sphere}}$  attached to a cone with height  $h_{\text{cone}}$  and half opening angle  $\Theta_{\text{cone}}$  (denoted by SC), and a half-sphere and a cone, as in the SC model, attached to a lever with area  $A_{\text{lever}}$  and thickness  $h_{\text{lever}}$  (denoted by SCL). The model tips have different sets of parameters  $\{p_{\text{tip}}\}$ , but all bear rotational symmetry with respect to the  $z$  axis. To

maintain this symmetry, the lever in geometry SCL is modeled by a disk of radius  $r_{\text{lever}}$  with an area  $A_{\text{lever}} = \pi r_{\text{lever}}^2$  chosen to be the same as the one of a typical rectangular cantilever. As the sensitivity to the cantilever size is neglectable when using FM detection [24], we do not consider the different oscillation amplitudes of the elements along the one-side clamped cantilever beam [20], but assume that the beam oscillates as one element. We apply two algorithms to numerically evaluate  $\hat{\Phi}_{\text{void}}$  and  $C_{\text{void}}$ , namely, an implementation of the analytical model originally calculated by Smythe [25] for geometry S as well as the CAPSOL code [24] for geometries S, SC, and SCL. To check the consistency of our methods, we perform calculations using both the Smythe (denoted by S1) [25] and CAPSOL (denoted by S2) [24] methods for the sphere model and find perfect agreement. Note that the Smythe method assumes a dielectric half-space, while we choose 1 mm thickness of the dielectric support for calculations based on the CAPSOL code. Assuming a finite dimension for the dielectric support has negligible effect on the results as the length scale of the relevant interactions is orders of magnitudes smaller than 1 mm.

Clearly, geometry SCL is expected to resemble the experimental situation closest and, therefore, is expected to yield the best results. However, the comparative evaluation of geometries S, SC, and SCL yields insights into the relevance of the tip parameter set for the evaluation of  $V_{\text{bias}}^{\min}$ . We

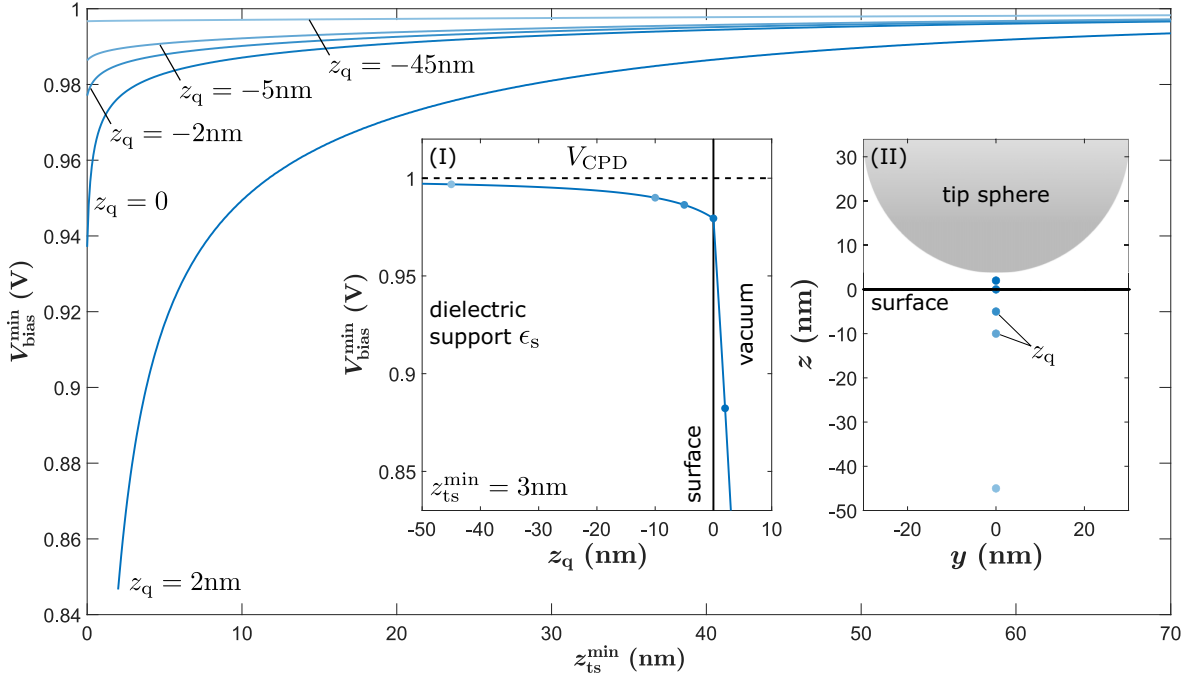


FIG. 8.  $V_{\text{bias}}^{\text{min}}$  as a function of the tip-sample distance  $z_{\text{ts}}^{\text{min}}$  for different vertical charge positions  $z_q$  of a single point charge  $q = -e$  (with the elementary charge  $e > 0$ ) located at  $\vec{r} = [0, 0, z_q]$  with the tip positioned at  $x_{\text{ts}} = y_{\text{ts}} = 0$ . Vertical charge positions  $z_q$  are chosen in the range from  $-45$  to  $2$  nm. The SCL model, an oscillation amplitude of  $A = 5$  nm, tip-model parameters listed in Table I,  $\epsilon_s = 24$ , as well as  $V_{\text{CPD}} = 1$  V are used in the simulation. Inset (I) represents  $V_{\text{bias}}^{\text{min}}$  as a function of the vertical charge position  $z_q$  at constant minimum tip height  $z_{\text{ts}}^{\text{min}} = 3$  nm, while inset (II) is a sketch of the tip geometry and the charge positions.

start the exploration by performing the intermediate steps of calculating quantities  $\langle \frac{\partial^2 C_{\text{void}}}{\partial z_{\text{ts}}^2} \rangle_{\cap}(z_c)$  and  $\langle \frac{\partial^2 \Phi_{\text{void}}}{\partial z_{\text{ts}}^2} \rangle_{\cap}(z_c)$  for the different models and by investigating contributions of the different tip elements to these quantities. The dimensions listed in Table I are adapted from commercially available cantilevers with metal coating that are commonly employed for KPFM experiments and are, unless otherwise noted, used for the following numerical evaluations. The results for the capacitance and electrostatic potential including their gradients and respective weighted averages along the tip oscillation path are presented in Figs. 3 and 4, respectively, for  $\epsilon_s = 24$ . The averages are plotted as a function of the tip oscillation center position  $z_c$  [19]. The colors correspond to the tip geometries: S in red, SC in green, and SCL in blue, while the different tint of these colors indicate the respective amplitude as depicted by the color bars in Figs. 3(d) and 4(d).

Naturally, the capacitance  $C_{\text{void}}(z_{\text{ts}})$  as a function of the tip-sample distance  $z_{\text{ts}}$  is found to be a monotonically decreasing function and capacitance values of the sphere model tip (S) are several orders of magnitude smaller than those of the SC and SCL model tips [see Fig. 3(a)]. The focus here is calculating the weight functions  $W_q(\vec{r}_i)$ , where rather the curvature than the absolute value of the capacitance is relevant. With each step of differentiation with respect to  $z_{\text{ts}}$ , the curves for the different models come closer to each other [see Figs. 3(b) and 3(c)]. The differences are further reduced when calculating  $\langle \frac{\partial^2 C_{\text{void}}}{\partial z_{\text{ts}}^2} \rangle_{\cap}(z_c)$  as shown in Fig. 3(d) for a series of oscillation amplitudes.

The normalized electrostatic potential  $\hat{\Phi}_{\text{void}}(\vec{r}_i)$ , evaluated at  $\vec{r}_i = \vec{r}_0 = [0, 0, 0]$  for the tip at  $\vec{r}_{\text{ts}} = [0, 0, z_{\text{ts}}]$ , shown in Fig. 4 as a function of the tip-sample distance  $z_{\text{ts}}$ , exhibits a decaying behavior. Here, potential values are of the same order of magnitude for the different tip models, yet, we find qualitative differences. While  $\hat{\Phi}_{\text{void}}(z_{\text{ts}})$  for model S quickly decays towards zero over the shown range, the decay of the other models is much slower. However, differences between the models vanish upon differentiation. Notably, the cap-averaged second derivatives  $\langle \frac{\partial^2 \hat{\Phi}_{\text{void}}}{\partial z_{\text{ts}}^2} \rangle_{\cap}(z_c)$  shown in Fig. 4(d) are almost identical for the different tip geometries.

To explore the situation relevant for a CFM measurement, we now assume that a charge is placed at the position  $\vec{r}_i = \vec{r}_0$  and the tip oscillates along the  $z$ -axis symmetrically to  $z_c$ . The weight function  $W_q$  at the position  $\vec{r}_0$  as a function of  $z_c$  is calculated for models S, SC, and SCL and for amplitudes  $A$  varied in the range from 2 to 18 nm with results shown in Fig. 5. A strong dependency of  $W_q$  on the oscillation amplitude and on the tip model is apparent and further dependencies will be investigated in the following sections. These dependencies will directly translate into the CFM signal  $V_{\text{bias}}^{\text{min}}$  via Eq. (9) and it is, therefore, evident that  $V_{\text{bias}}^{\text{min}}$  values determined with different oscillation amplitudes or under otherwise different conditions cannot be compared to each other.

In summary, when calculating properties along the surface normal through the tip center, the cap-averaged capacitance gradient exhibits a more critical dependence on the tip model

than the cap-averaged electrostatic potential gradient. As modeling a realistic tip at the nanoscale is a most difficult endeavor, for the practical exploitation of the CFM method, it would be most desirable to determine  $\langle \frac{\partial^2 C_{\text{void}}}{\partial z_{\text{ts}}^2} \rangle_{\cap}(z_c)$  directly from the experiment rather from a model. Furthermore, the cap-averaged second derivatives of the electrostatic capacitance [Fig. 3(d)] and the normalized potential [Fig. 4(d)] both exhibit a strong dependency on the oscillation amplitude  $A$ , translating into a strong amplitude dependency of the CFM signal  $V_{\text{bias}}^{\text{min}}$ .

### III. PARAMETERS DETERMINING THE CFM VOLTAGE

Now, we investigate the dependency of  $V_{\text{bias}}^{\text{min}}$  on experimental and material parameters for the case of a negative charge  $q = -e$  (with  $e > 0$ ) positioned at  $\vec{r}_0 = [0, 0, 0]$ . In particular, the CFM voltage  $V_{\text{bias}}^{\text{min}}$  is calculated as a function of the tip position along the  $z$  axis with  $\vec{r}_{\text{ts}} = [0, 0, z_{\text{ts}}]$  for  $\epsilon_s = 24$  and  $V_{\text{CPD}} = 1$  V unless otherwise noted.

#### A. Oscillation amplitude

We start by investigating the dependency of  $V_{\text{bias}}^{\text{min}}$  on the oscillation amplitude  $A$  that is varied in the range of 2 to 18 nm.  $V_{\text{bias}}^{\text{min}}$  is plotted in Fig. 6 as a function of (a) the minimum tip-sample distance  $z_{\text{ts}}^{\text{min}}$  for different oscillation amplitudes and (b), (c) as a function of the oscillation amplitude  $A$  at fixed minimum tip-sample distances  $z_{\text{ts}}^{\text{min}} = 3$  nm and  $z_{\text{ts}}^{\text{min}} = 30$  nm, respectively. The position  $z_{\text{ts}}^{\text{min}} = z_c - A$  represents the minimum tip-sample distance during the oscillation cycle and can be chosen to be zero as  $W_q$  always attains a finite value at  $z_{\text{ts}}^{\text{min}} = 0$ .

The CFM voltage exhibits the largest deviation from  $V_{\text{CPD}}$  at very small tip-sample distances [see Fig. 6(b)], while the deviation for the sphere  $S$  is largest at large tip-sample distances [see Fig. 6(c)]. We attribute this behavior to the simplicity of the sphere tip model creating an electric field that is qualitatively different from the more realistic tip models SC and SCL. As the central result, we find a scaling of  $V_{\text{bias}}^{\text{min}}$  with the oscillation amplitude  $A$  over a large range of  $z_{\text{ts}}^{\text{min}}$ . Consequently, the oscillation amplitude  $A$  is a critical parameter for CFM measurements and it is important to experimentally determine this parameter for CFM measurements [26–28]. All further analysis will be focused on the SCL tip model.

#### B. Substrate dielectric constant

Results in Fig. 7(a) highlight the influence of the substrate dielectric constant  $\epsilon_s$  on  $V_{\text{bias}}^{\text{min}}$ . While keeping all other parameters constant, we vary the relative permittivity to  $\epsilon_s = 6.8, 24, \text{ and } 100$  to cover the range from insulating to almost metallic samples. As expected,  $V_{\text{bias}}^{\text{min}}$  values are close to  $V_{\text{CPD}}$  for large  $\epsilon_s$ . This corresponds to the situation of a Kelvin probe measurement on an electrical conductor, where a single charge present at the surface has only a minute effect on the work function measurement. The deviation of  $V_{\text{bias}}^{\text{min}}$  from  $V_{\text{CPD}}$  is increasing with decreasing  $\epsilon_s$  and we yield the plausible result that most sensitive charge measurements are possible on a strongly insulating substrate. This behavior is qualitatively the same for the other tip geometries as shown in Appendix A

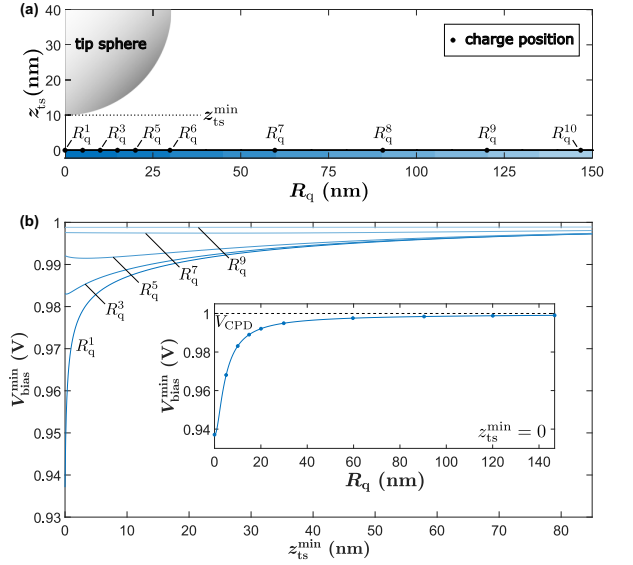


FIG. 9. Effect of the lateral charge position on  $V_{\text{bias}}^{\text{min}}$ . (a) Model geometry including charges at radial positions  $R_q^i = \sqrt{(x_{q,i})^2 + (y_{q,i})^2}$  for  $z_q = 0$  and the tip at position  $\vec{r}_{\text{ts}} = [0, 0, z_{\text{ts}}^{\text{min}}]$ . (b)  $V_{\text{bias}}^{\text{min}}$  data as a function of the tip-sample distance  $z_{\text{ts}}^{\text{min}}$  for single point charges  $q = -e$  at selected radial positions  $R_q^i$ . The SCL tip model, an oscillation amplitude of  $A = 5$  nm, parameters from Table I,  $\epsilon_s = 24$ , and  $V_{\text{CPD}} = 1$  V are used for the simulation. The inset in (b) represents  $V_{\text{bias}}^{\text{min}}$  as a function of the radial displacement  $R_q$  at  $z_{\text{ts}}^{\text{min}} = 0$ .

[Fig. 13(a)] and can be traced to an increased sensitivity of the cap-averaged second capacitance gradient to  $\epsilon_s$  [see inset (I) in Fig. 7(a)]. As the actual  $\epsilon_s$  of the substrate is often not well known, this finding points to the importance of an experimental determination of  $\langle \frac{\partial^2 C_{\text{void}}}{\partial z_{\text{ts}}^2} \rangle_{\cap}(z_{\text{ts}})$ .

#### C. Sphere radius

The impact of the sphere radius  $r_{\text{sphere}}$  on  $V_{\text{bias}}^{\text{min}}$  is shown in Fig. 7(b). When exploring  $V_{\text{bias}}^{\text{min}}$  within realistic ranges of  $\{p_{\text{tip}}\}$ , we find that the sphere radius is the most critical parameter of the tip geometry, while a change of cone and lever dimensions within the same order of magnitude has a significantly smaller effect (data not shown). Larger deviations of  $V_{\text{bias}}^{\text{min}}$  from  $V_{\text{CPD}}$  are found for smaller sphere radii. Furthermore, a rapid decay of  $V_{\text{bias}}^{\text{min}}$  with increasing  $z_{\text{ts}}^{\text{min}}$  is found for large tip radii  $r_{\text{sphere}}$ , yet the absolute signal is smaller. This behavior is attributed to strong lateral averaging of a large tip [29] and the differences highlight that the tip radius is a critical parameter for charge quantification.

### IV. CFM VOLTAGE AS A FUNCTION OF THE CHARGE POSITION

Aside from the system parameters, the magnitude of  $V_{\text{bias}}^{\text{min}}$  has a clear dependency on the charge position relative to the lateral position  $(x_{\text{ts}}, y_{\text{ts}})$  and the lower turning point  $z_{\text{ts}}^{\text{min}}$  of the tip oscillation. In particular, the following analysis will highlight the nonlocal character of the CFM detection principle.

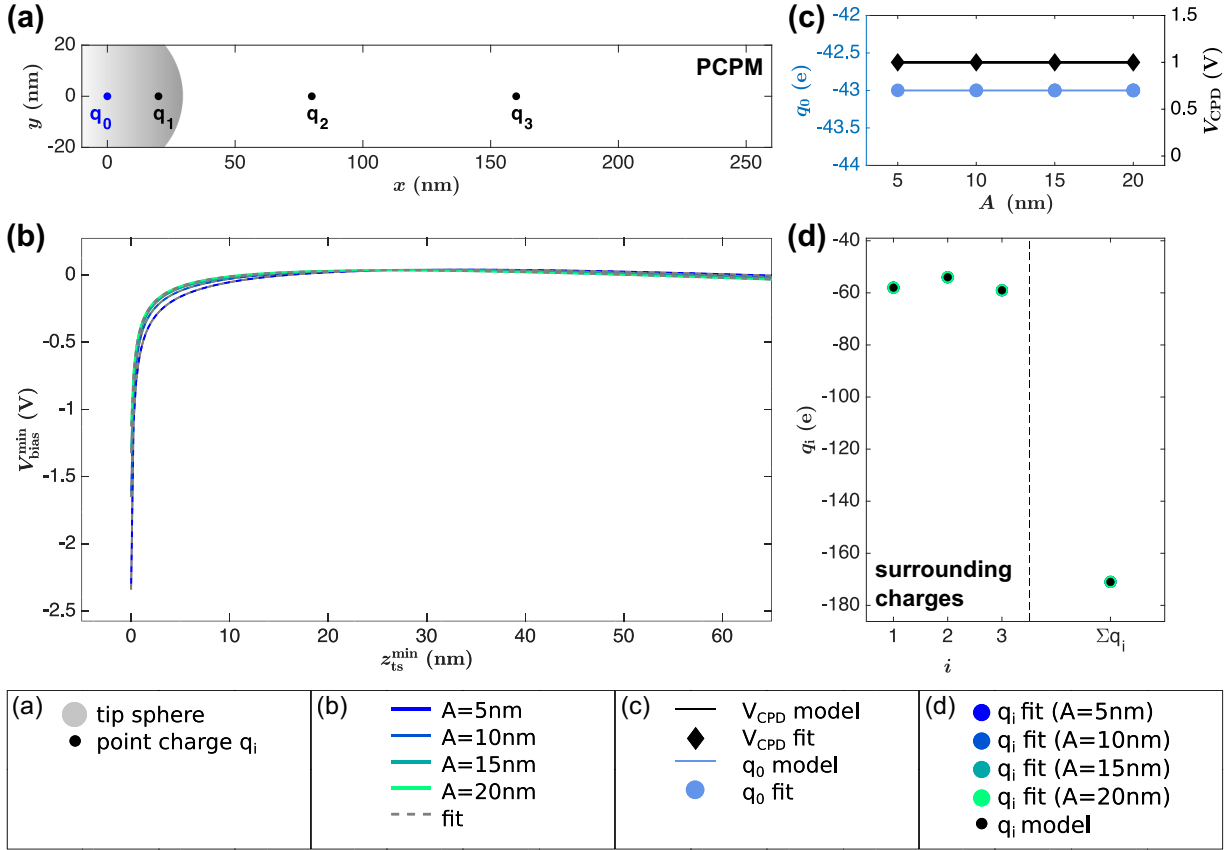


FIG. 10. Results of the optimization routine for a charge distribution with three point charges  $q_1$ ,  $q_2$ , and  $q_3$  at different distances to the central charge of interest  $q_0$ . (a) Point-charge position map (PCPM) illustrating the charge positions. (b) Artificially generated measurement data  $V_{\text{bias, meas}}^{\text{min}}$  as a function of the tip-sample distance  $z_{\text{ts}}^{\text{min}}$ . The curves are generated for oscillation amplitudes  $A = 5$  nm (dark blue), 10 nm (lighter blue), 15 nm (dark green), and 20 nm (light green) using  $\epsilon_s = 24$ ,  $V_{\text{CPD}} = 1$  V, and parameters from Table I. The  $V_{\text{bias}}^{\text{min}}$  curves fitted to these data by the optimization algorithm are depicted by gray dashed lines. (c) Model and resulting values for the fit parameters  $q_0$  and  $V_{\text{CPD}}$  as a function of the amplitude  $A$ . (d) Model and resulting values for the surrounding charges  $q_i$  ( $i = 1, 2, 3$ ) and their sum for the different amplitudes  $A$  indicated by the same colors of the points as in (b).

### A. Vertical charge position

First, the CFM signal  $V_{\text{bias}}^{\text{min}}$  is investigated with respect to the tip-sample distance  $z_{\text{ts}}^{\text{min}}$  for a single point charge located at different central vertical positions with results presented in Fig. 8. Vertical charge positions  $z_q$  in the range from  $-45$  to  $2$  nm for the SCL model (see inset II in Fig. 8 for a sketch of the geometry) and an oscillation amplitude of  $A = 5$  nm are chosen. The vertical position range includes the dielectric boundary and extends along the negative direction up to a vertical distance of more than the tip radius. In all cases, the  $V_{\text{bias}}^{\text{min}}(z_{\text{ts}}^{\text{min}})$  curves exhibit the largest deviation from  $V_{\text{CPD}}$  at small tip-sample distances and approach  $V_{\text{CPD}}$  for large  $z_{\text{ts}}^{\text{min}}$ . The CFM voltage as a function of the charge position  $z_q$  but at a fixed tip height of  $z_{\text{ts}}^{\text{min}} = 3$  nm is presented in inset (I) of Fig. 8. The slope with respect to  $z_q$  differs on either side of the dielectric boundary: Due to the high electric field at the tip apex, a large slope of  $V_{\text{bias}}^{\text{min}}(z_{\text{ts}}^{\text{min}})$  is present in the gap between tip and dielectric. The polarization of the dielectric medium surrounding the point charge at  $z_q < 0$  leads to a

slow decay towards  $V_{\text{CPD}}$  for large  $z_q$ . A similar behavior is found for the S and SC tip models (see Appendix A, Fig. 14). This example particularly shows that charges buried inside the dielectric substrate, such as charged defects or vacancy sites, contribute to the  $V_{\text{bias}}^{\text{min}}$  voltage and, therefore, can compromise the CFM measurement of charges of interest.

### B. Lateral charge position

Second, the CFM signal  $V_{\text{bias}}^{\text{min}}(z_{\text{ts}}^{\text{min}})$  is evaluated for different lateral point charge positions at the substrate surface ( $z_q = 0$ ) with results shown in Fig. 9. Since the SCL tip model bears rotational symmetry along the  $z$  axis, any lateral charge position  $(x_q, y_q)$  can be mapped to one radial coordinate  $R_q = \sqrt{x_q^2 + y_q^2}$  measured from the lateral tip position. Consequently, with a rotational symmetric tip, it is not possible to distinguish between charges present at different lateral positions of identical radial distance  $R_q$ . Instead, the  $V_{\text{bias}}^{\text{min}}$  voltage of several charges located at the same radial distance  $R_q$

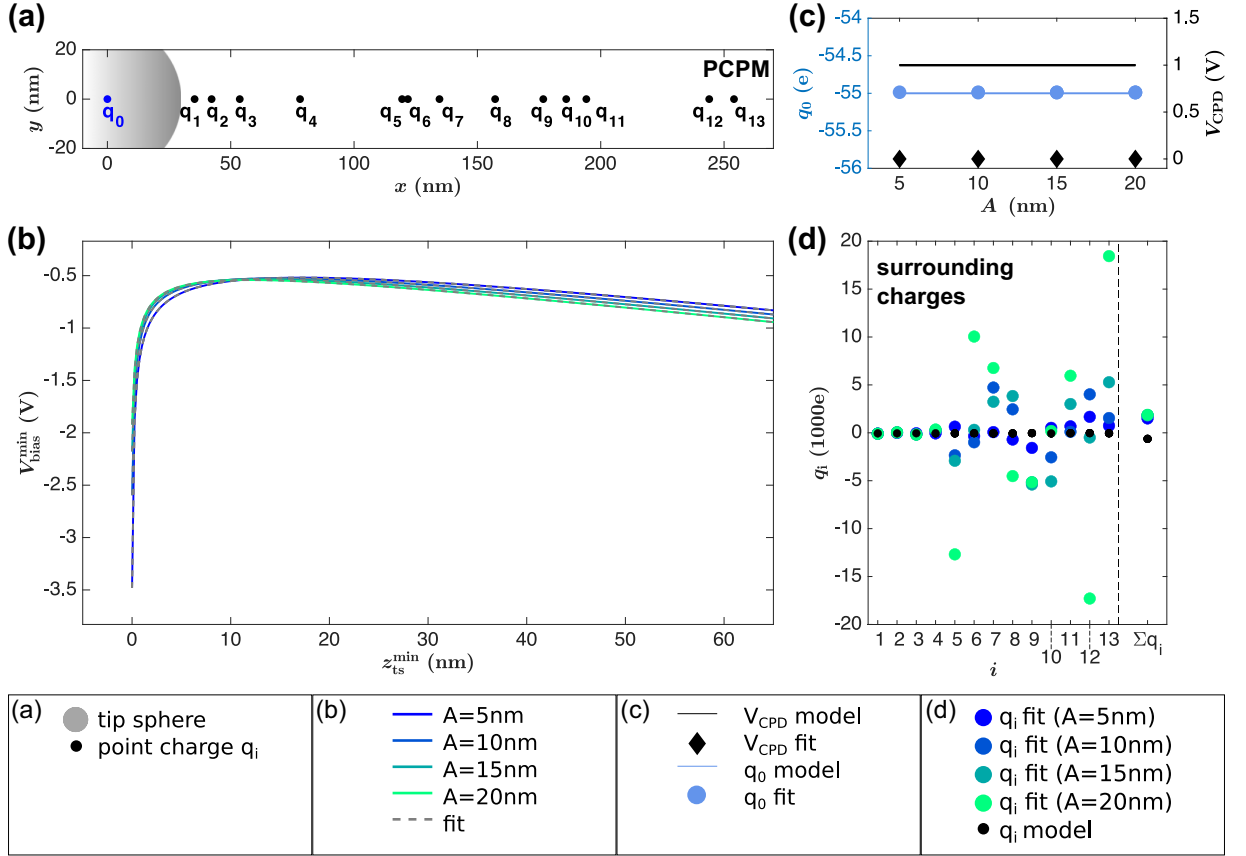


FIG. 11. Results of the optimization routine for a complex charge distribution with 13 point charges  $q_i$  surrounding a central charge of interest  $q_0$ . (a) Point-charge position map (PCPM) illustrating the charge positions. (b)  $V_{\text{bias, meas}}^{\text{min}}$  data as a function of the tip-sample distance  $z_{\text{ts}}^{\text{min}}$ . The curves are generated for oscillation amplitudes  $A = 5$  nm (dark blue), 10 nm (lighter blue), 15 nm (dark green), and 20 nm (light green) using  $\epsilon_s = 24$ ,  $V_{\text{CPD}} = 1$  V, and parameters from Table I.  $V_{\text{bias}}^{\text{min}}$  curves fitted to these data by the optimization algorithm are depicted by gray dashed lines. (c) Model and resulting values for the fit parameters  $q_0$  and  $V_{\text{CPD}}$  as a function of the amplitude  $A$ . (d) Model and resulting values for the surrounding charges  $q_i$  ( $i = 1, \dots, 13$ ) for the different amplitudes  $A$  indicated by the same colors of the points as in (b).

are equal to the  $V_{\text{bias}}^{\text{min}}$  voltage corresponding to the sum of their charge magnitudes. We expect that the rotational symmetry is a reasonable approximation for experiments as AFM tips are usually fabricated with the aim to being rather symmetric. Figure 9(a) visualizes the tip geometry and the model charge positions on the radial axis with charges positioned within ( $i = 1 \dots 6$ ) and beyond ( $i = 7 \dots 10$ ) the  $xy$ -projected tip sphere.  $V_{\text{bias}}^{\text{min}}(z_{\text{ts}}^{\text{min}})$  curves calculated for exemplary individual charges are shown in Fig. 9(b) whereby the charges are named by their radial positions  $R_q^i$ .

All curves exhibit their maximum deviation from  $V_{\text{CPD}}$  at or close to  $z_{\text{ts}}^{\text{min}} = 0$ . The CFM voltage at  $z_{\text{ts}}^{\text{min}} = 0$  is closer to  $V_{\text{CPD}}$  for large radial charge positions. This is in agreement with a reduced sensitivity to a point charge located far away from the lateral tip position as is further highlighted by the inset in Fig. 9(b), where  $V_{\text{bias}}^{\text{min}}(z_{\text{ts}}^{\text{min}} = 0)$  is plotted as a function of the radial charge position  $R_q$ .

At larger tip-sample distances,  $V_{\text{bias}}^{\text{min}}$  voltages approach  $V_{\text{CPD}}$ , however,  $V_{\text{bias}}^{\text{min}}(z_{\text{ts}}^{\text{min}})$  does not converge against  $V_{\text{CPD}}$  within the investigated tip-sample distance regime. Instead, the  $V_{\text{bias}}^{\text{min}}$  voltages differ, depending on the lateral charge

position, by several mV from  $V_{\text{CPD}}$  even at  $z_{\text{ts}}^{\text{min}} = 80$  nm. Moreover, not all  $V_{\text{bias}}^{\text{min}}(z_{\text{ts}}^{\text{min}})$  curves are strictly monotonic with respect to  $z_{\text{ts}}^{\text{min}}$ , but may exhibit an intermediate extremum [see, for example,  $V_{\text{bias}}^{\text{min}}(z_{\text{ts}}^{\text{min}})$  data for  $R_q^5$  in Fig. 9(b)]. The positions of these extrema shift towards larger  $z_{\text{ts}}^{\text{min}}$  with larger radial charge position  $R_q$  what can be explained by the form of the weight function for charges  $W_q$ , specifically by the transition in the electrostatic quantities between the sphere-dominated and the cone-influenced regimes. An intermediate extremum, and a qualitative agreement with all other observations discussed in this section, is also observed for the other tip geometries S and SC as shown in Appendix A, Fig. 15.

As expected, the strongest contribution of a point charge to  $V_{\text{bias}}^{\text{min}}$  is found for positions close to the tip apex, while the influence diminishes for positions further away. However, even charges located at radial distances of  $R_q \geq 100$  nm contribute to the  $V_{\text{bias}}^{\text{min}}$  signal. As is apparent for  $R_q^7$  or  $R_q^9$  in Fig. 9(b), the contribution is rather constant with respect to the tip-sample distance  $z_{\text{ts}}^{\text{min}}$  and effectively appears as an offset to  $V_{\text{bias}}^{\text{min}}$ . Consequently, if multiple charges are present

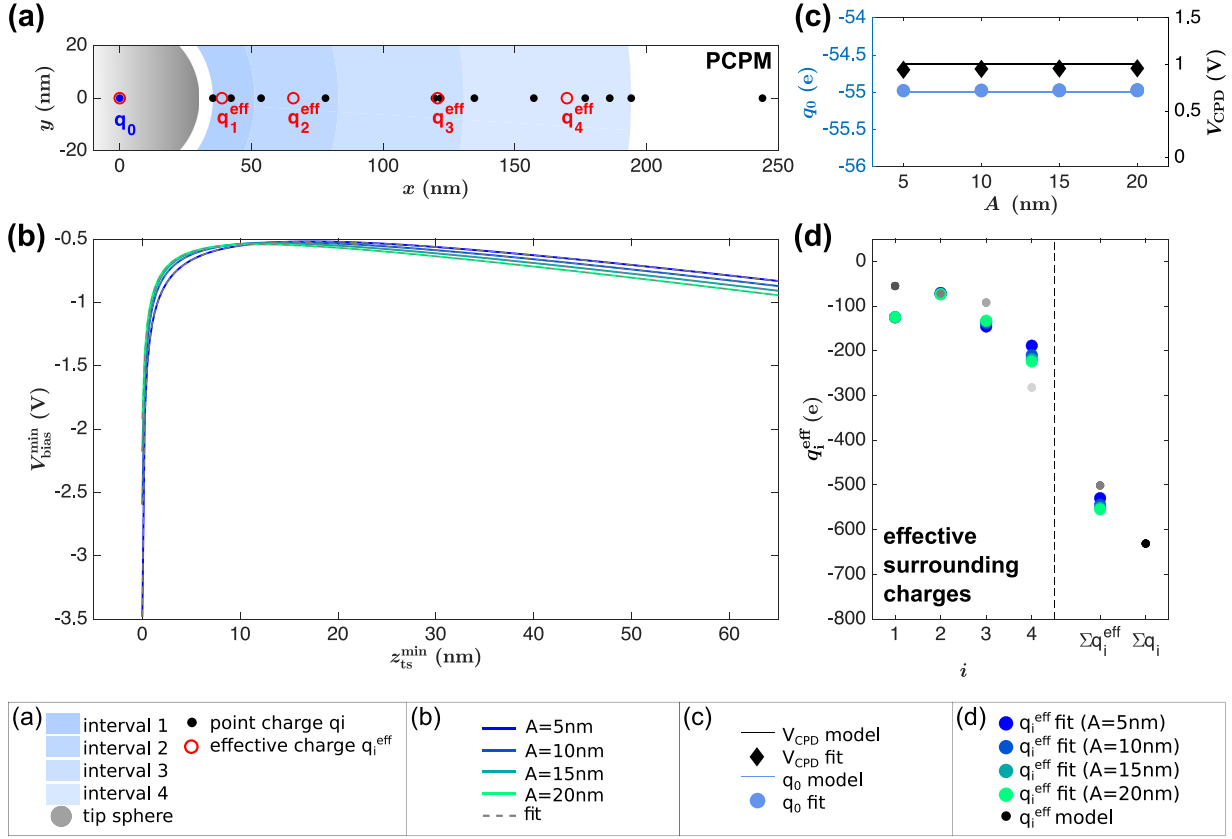


FIG. 12. Introduction of effective charges  $q_i^{\text{eff}}$  for the charge distribution in Fig. 11. (a) Point-charge position map (PCPM) showing the full charge distribution with point charges  $q_i$  (black points, identical positions, and magnitudes as in Fig. 11) used for  $V_{\text{bias, meas}}^{\text{min}}(z_{\text{ts}}^{\text{min}})$  data generation as well as the effective charges  $q_i^{\text{eff}}$  (red circles) used as parameters for the fitting routine. The blue segments represent the different ranges in which the effective charges  $q_i^{\text{eff}}$  are placed. (b)  $V_{\text{bias, meas}}^{\text{min}}$  data as a function of the minimum tip-sample distance  $z_{\text{ts}}^{\text{min}}$ . The simulation is performed for oscillation amplitudes  $A = 5$  nm (dark blue), 10 nm (lighter blue), 15 nm (dark green), and 20 nm (light green) as well as for  $\epsilon_s = 24$ ,  $V_{\text{CPD}} = 1$  V, and parameters from Table I. The corresponding  $V_{\text{bias}}^{\text{min}}$  curves resulting from the optimization algorithm are depicted by gray dashed lines. (c) Model and resulting values for the fit parameters  $q_0$  and  $V_{\text{CPD}}$  as a function of the amplitude  $A$ . (d) Model and resulting values for the surrounding effective charges  $q_i^{\text{eff}}$  ( $i = 1, 2, 3, 4$ ) and their sum for the different amplitudes  $A$  indicated by the same colors of the points as in (b).

in the system, it is likely that these have to be considered when determining the magnitude of a point charge centered underneath the tip and that their contribution can hardly be distinguished from  $V_{\text{CPD}}$ . These observations underline the necessity of performing charge quantification by distance-dependent measurements on a central charge while taking the surrounding charges into account.

## V. CHARGE QUANTIFICATION

Based on the previous understanding of the CFM voltage, we introduce in this section an approach to determine the charge state of a central charge  $q_0$  positioned at  $\vec{r}_0 = [0, 0, 0]$ . In particular, we demonstrate that the central charge  $q_0$  can be retrieved with high accuracy even if a number of surrounding point charges  $q_i$  are present, a situation frequently given in experiments.

### A. Optimization algorithm

The central approach for charge determination lies in the fitting of  $V_{\text{bias}}^{\text{min}}(z_{\text{ts}}^{\text{min}})$  data with the charge magnitudes and the contact potential difference as free fit parameters. Here, we demonstrate the robustness of this approach by numerical simulations. Along these lines, we implement an optimization algorithm for fitting Eq. (8) to  $V_{\text{bias, meas}}^{\text{min}}(z_{\text{ts}}^{\text{min}})$  data of a simulated measurement of a charge distribution with  $N + 1$  point charges  $q_i$  at positions  $\vec{r}_i$ . The MATLAB<sup>®</sup> function `fminsearch` is used to iteratively reduce the root-mean-square (rms) difference between the measured  $V_{\text{bias, meas}}^{\text{min}}(z_{\text{ts}}^{\text{min}})$  and calculated  $V_{\text{bias}}^{\text{min}}(z_{\text{ts}}^{\text{min}})$  data with  $q_i$  ( $i = 0 \dots N$ ) and  $V_{\text{CPD}}$  as fit parameters. We consider charge distributions of different complexity and generate corresponding artificial  $V_{\text{bias, meas}}^{\text{min}}(z_{\text{ts}}^{\text{min}})$  data. These data shall represent experimental situations where a nano-object like a metal cluster is charged by some or some 10 elementary charges. For testing the optimization routine, we utilize tip model S evaluated by the Smythe formulas [25].

Tip model S is chosen here to reduce computational time, yet other reasonable tip models are expected to work as well.

First, we introduce a charge distribution consisting of a central charge  $q_0$  at  $\vec{r}_0 = [0, 0, 0]$  and three surrounding charges  $q_1$ ,  $q_2$ , and  $q_3$  placed at radial positions  $R_q^1 = 20$  nm,  $R_q^2 = 80$  nm, and  $R_q^3 = 160$  nm, all at  $z_q = 0$ . The geometry of this distribution including the tip sphere is shown in top view in Fig. 10(a) what we further on denote as the point-charge position map (PCPM). Charge magnitudes  $q_i$  are randomly chosen in the interval between  $-30e$  and  $-60e$  (with the elementary charge  $e > 0$ ). We do not see any fundamental limitation of the charge magnitude in further simulations with different charge magnitudes (see Appendix B, Fig. 16 for one example with smaller charge magnitudes). The distance-dependent data are calculated for the given charge distribution using amplitude values  $A = 5, 10, 15$ , and  $20$  nm parameters listed in Table I,  $\epsilon_s = 24$ , and  $V_{\text{CPD}} = 1$  V. The resulting  $V_{\text{bias, meas}}^{\text{min}}(z_{\text{ts}}^{\text{min}})$  curves are depicted in Fig. 10(b). Note that for a simulation with all  $q_i$  having the same sign, the nonmonotonic behavior in the CFM data is characteristic to the S model tip and does not represent a physical property of the distribution of charges under investigation.

Second, we test the optimization routine by recovering the “unknown” charge magnitudes  $q_0, q_1, q_2$ , and  $q_3$  as well as  $V_{\text{CPD}}$  by fitting  $V_{\text{bias}}^{\text{min}}(z_{\text{ts}}^{\text{min}})$  to the data generated in the first step. Starting values are chosen for  $V_{\text{CPD}}$  as zero and for  $q_i$  as one negative elementary charge. The optimization is performed until one of the two following termination criteria is reached: (1) The optimization exceeds 5000 iterations, (2) the difference (To1X) in  $q_i/e$  and  $V_{\text{CPD}}/V$  between two subsequent optimization steps is less than  $10^{-6}$  and the change (To1Fun) in the rms difference between  $V_{\text{bias, meas}}^{\text{min}}(z_{\text{ts}}^{\text{min}})$  and  $V_{\text{bias}}^{\text{min}}(z_{\text{ts}}^{\text{min}})$  is less than 1 pV for two subsequent iteration steps. For a reliable charge quantification it is necessary to reach criterion (2). The resulting  $V_{\text{bias}}^{\text{min}}(z_{\text{ts}}^{\text{min}})$  curves are included in Fig. 10(b) as dashed gray lines and perfectly match the original  $V_{\text{bias, meas}}^{\text{min}}(z_{\text{ts}}^{\text{min}})$  data. Correspondingly, the values for quantities  $q_0, q_1, q_2$ , and  $q_3$  as well as  $V_{\text{CPD}}$  are retrieved with high accuracy for all amplitudes as shown in Figs. 10(c) and 10(d). Thus, for a central charge and a small number of surrounding charges, the optimization routine perfectly recovers the charge magnitudes.

### B. Concept of effective charges

Much less favorable results are obtained when increasing the number of surrounding charges; in this case the optimization problem is overdetermined. We first illustrate this challenge by a model calculation for an extended charge distribution and in a second step introduce the concept of effective surrounding charges as a solution.

First, 13 point charges  $q_i$  are randomly placed in the simulation at radial distances  $R_q^i$  ranging from 25 nm to more than 230 nm, in addition to the central charge  $q_0$ . Charge magnitudes are randomly chosen between  $-30e$  and  $-60e$  and the corresponding PCPM is presented in Fig. 11(a). The generated  $V_{\text{bias, meas}}^{\text{min}}(z_{\text{ts}}^{\text{min}})$  curve data including the  $V_{\text{bias}}^{\text{min}}(z_{\text{ts}}^{\text{min}})$  fits for different amplitudes are shown in Fig. 11(b). The fits are in excellent agreement with the simulated  $V_{\text{bias}}^{\text{min}}(z_{\text{ts}}^{\text{min}})$  data and the central charge  $q_0$  is accurately determined for

all oscillation amplitudes as shown in Fig. 11(c). In contrast, the quantity  $V_{\text{CPD}}$  [see Fig. 11(c)] as well as most of the surrounding charges  $q_i$  [see Fig. 11(d)] strongly deviate from the original values and the sum of surrounding charges is not reproduced correctly [see Fig. 11(d)]. These observations can be traced to the properties of the weight function for charges  $W_q$  averaging over charges in near proximity to each other and the subsequent overdetermination of the optimization problem.

A particularly illustrative example for the insensitivity of  $W_q$  to neighboring charges can be identified from charges  $q_5$  and  $q_6$ . As both charges are placed in close proximity to each other at large  $R_q$ , their specific contribution to  $V_{\text{bias}}^{\text{min}}(z_{\text{ts}}^{\text{min}})$  via their respective  $W_q(\vec{r}_i)$  function is virtually indistinguishable. Consequently, the large negative charge of  $q_5$  is counterbalanced by the large positive charge  $q_6$  and the fit routine aborts after reaching the maximum number of allowed iterations. Furthermore, we find that the  $z_{\text{ts}}^{\text{min}}$  dependence of  $W_q$  is not significant for charges positioned at  $R_q^i > 100$  nm. In the current example, the fit routine finds a solution with charges at  $R_q^i > 200$  nm having very large magnitudes while  $V_{\text{CPD}}$  is set to a value close to zero.

Note, however, that the magnitude of the central charge of interest is nonetheless well reproduced. This result suggests that  $q_0$  yields the key contribution to  $V_{\text{bias}}^{\text{min}}$  with a  $z_{\text{ts}}^{\text{min}}$  dependence that is characteristic enough to provide the correct result for the central charge. Based on this finding, we seek for a stable solution yielding more realistic results for the surrounding charges. To remove surplus fit variables, we reduce the number of surrounding charges by replacing them with effective point charges. In particular, all point charges at  $R_q^i > 200$  nm are excluded as their contribution is small and indistinguishable from  $V_{\text{CPD}}$ . The remaining point charges are subsumed into segments along the  $R_q$  axis and reduced to effective charges. Positions of these effective charges are determined as follows: The range  $\Delta R_q = R_q^{\text{max}} - R_q^{\text{min}}$  is calculated from the two point charges positioned at the minimum radial distance  $R_q^{\text{min}}$  and at the maximum radial distance  $R_q^{\text{max}} \leq 200$  nm. Next, this range is segmented into four intervals of increasing width, namely, of  $0.1\Delta R_q$ ,  $0.2\Delta R_q$ ,  $0.3\Delta R_q$ , and  $0.4\Delta R_q$ . Finally, one effective point charge is placed in each of these segments at the average radial distance of point charges within the respective segment. The use of an averaged position is most reliable if the charges are of the same order of magnitude.

For the example in Fig. 11, the reduced PCPM is shown in Fig. 12(a), consisting of the central charge and four effective surrounding charges (in red). This PCPM is used to fit the  $V_{\text{bias, meas}}^{\text{min}}(z_{\text{ts}}^{\text{min}})$  data calculated for the complete charge distribution. As depicted in Fig. 12(b), fit results based on the effective PCPM perfectly match the  $V_{\text{bias, meas}}^{\text{min}}(z_{\text{ts}}^{\text{min}})$  curves calculated for the full PCPM. Most importantly, the central charge  $q_0$  is determined as  $-54.98e$  [see Fig. 12(c)], in excellent agreement with the actual value of  $-55.00e$ , while  $V_{\text{CPD}}$  is found to be 0.96 V, with a deviation of less than 5% to the actual value of 1 V [see also Fig. 12(c)]. Due to neglecting the charges at  $R_q > 200$  nm, the latter deviation is expected. Values for the charge magnitudes  $q_i^{\text{eff}}$  are presented in Fig. 12(d), together with the values of  $q_{i, \text{model}}^{\text{eff}}$  that were



calculated from the sum of all charges  $q_i$  in the corresponding interval. Both quantities are in good agreement for the inner segments, while they deviate stronger for the outer segments. This results in a slight overestimation of the sum of effective charges  $\sum q_i^{\text{eff}}$  compared to the sum  $\sum q_{i,\text{model}}^{\text{eff}}$ . We explain these observations in particular by the effective charge  $q_4^{\text{eff}}$  and the  $V_{\text{CPD}}$  value both compensating for the omitted charges at  $R_q > 200$  nm. By testing different tip models and by performing cross-check calculations covering a large set of charge numbers and positions, we find that four effective charges positioned as described yield the most reliable results.

In conclusion, the introduction of effective charges to reduce the number of dependent parameters to avoid unphysical results is a robust approach for the quantification of the central charge. For the herein presented model data, the reduction of the 13 surrounding charges  $q_i$  to four effective charges  $q_i^{\text{eff}}$  as shown in Fig. 12 is found to give the best result. While less effective charges reduce the fit quality, more charges lead to the described effects of dependent fit parameters. The determination of the central charge magnitude  $q_0$  proved to be robust in all trials, even if a single charge is located nearby the central charge for a small number of surrounding charges (see Appendix C, Fig. 17). Be aware that finding a stable solution for difficult cases can necessitate a modification of the starting parameters for the optimization routine. However, the selection does not lead to a bias in the resulting values. Instead, unphysical solutions are easily identified from comparing the results for different probe oscillation

amplitudes: if the optimization algorithm is stuck in a local minimum, single outliers are present for specific amplitudes.

## VI. SUMMARY AND CONCLUSIONS

The analysis in this work identifies a number of parameters that influence the absolute value of the  $V_{\text{bias}}^{\text{min}}$  voltage in a charge force microscopy (CFM) experiment. It is found that the CFM voltage signal is dependent on the oscillation amplitude and the CFM technique yields best results for tips with a small radius as well as substrates with a small dielectric constant. Furthermore, the analysis confirms a substantial contribution of charges in close vicinity of the tip apex to the  $V_{\text{bias}}^{\text{min}}$  signal, while the effect of charges far away from the tip apex (including charges buried inside the dielectric sample) are likely to appear as an offset to the contact potential difference in the  $V_{\text{bias}}^{\text{min}}$  signal.

First and foremost, it becomes clear from this analysis that taking a *lateral* map of  $V_{\text{bias}}^{\text{min}}$  is insufficient for charge quantification. Instead, the acquisition of *vertical*  $V_{\text{bias}}^{\text{min}}(z_{\text{ts}}^{\text{min}})$  data is necessary for obtaining reliable CFM results. For the general case of a complex charge distribution at the surface or within a sample, charge quantification can be realized by the following four steps: First, the electrostatic model is determined, for example, by a measurement of the cap-averaged second capacitance gradient, to yield the weight function for charges. Second, the point-charge positions are identified from image data and the effective charge distribution is determined

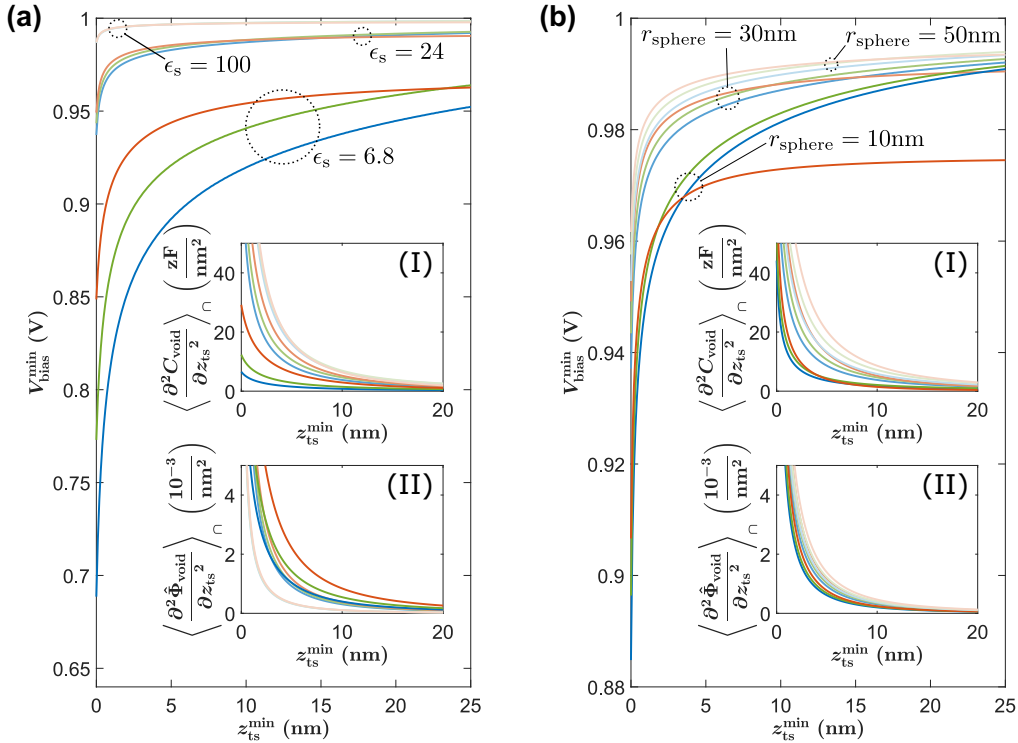


FIG. 13. Extended version of Fig. 7 highlighting the dependence of  $V_{\text{bias}}^{\text{min}}$  on (a) the relative dielectric permittivity  $\epsilon_s$  and (b) the tip radius  $r_{\text{sphere}}$ . Data for models S (SC) are presented in red (green) while data for model SCL are depicted in blue. Tinted colors are used to express the respective parameter modification. Parameters are otherwise identical to those of Fig. 7.

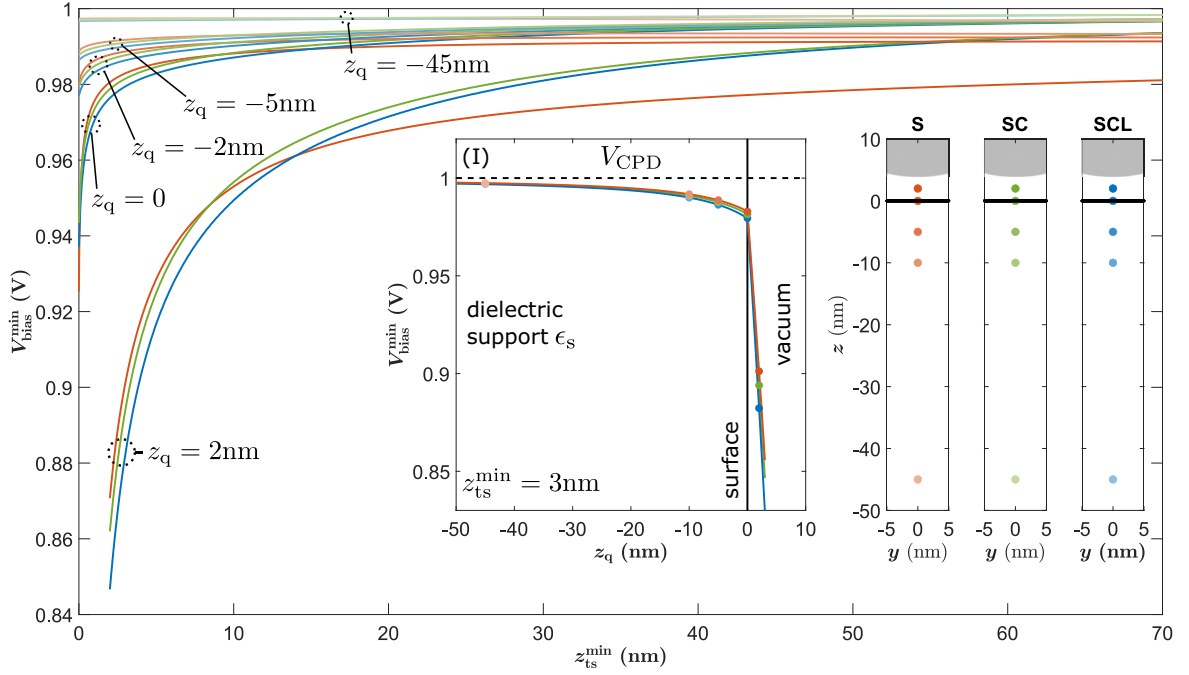


FIG. 14. Extended version of Fig. 8 highlighting the effect of the vertical charge position on  $V_{\text{bias}}^{\text{min}}$ . Data for models S (SC) are presented in red (green) while data for model SCL are depicted in blue. Tinted colors are used to express the different vertical position values. Parameters are otherwise identical to those of Fig. 8.

from these data. Third,  $V_{\text{bias}}^{\text{min}}(z_{\text{ts}}^{\text{min}})$  data are systematically acquired at the position of the charge of interest for different amplitudes of the cantilever oscillation. This approach enables an inherent consistency check. Fourth, an optimization routine is used to fit  $V_{\text{bias}}^{\text{min}}$  curve data to the measurement results with the charge magnitudes  $q_i$  as well as  $V_{\text{CPD}}$  as fit parameters.

In conclusion, the CFM method holds the strong promise to offer charge quantification in numerous systems of fundamental and applied research, and by further refinement of this method, it can be expected to obtain accurate results for all relevant experimental situations.

#### ACKNOWLEDGMENTS

Financial support by the Deutsche Forschungsgemeinschaft via Grants No. RA2832/1-1, No. RE1186/21-1, and No. RE1186/23-1 is gratefully acknowledged. We thank C. Barth for stimulating discussions. HPC infrastructure used for the simulations is funded by the Deutsche Forschungsgemeinschaft via Grant No. 456666331.

#### APPENDIX A: PARAMETER ANALYSIS FOR FURTHER TIP GEOMETRIES

Simulation results for the S and SC model in addition to the SCL geometry are presented in Figs. 13–15. In particular, Fig. 13 presents the dependency of  $V_{\text{bias}}^{\text{min}}$  on the dielectric constant of the substrate  $\epsilon_s$ , and on the tip sphere radius  $r_{\text{sphere}}$ . Data for only the SCL model are shown in Fig. 7 in the main text. In Fig. 14, the  $V_{\text{bias}}^{\text{min}}$  signal is evaluated for different vertical charge positions and for the S, SC, and SCL models. This

figure is a generalisation of Fig. 8 in the main text. Figure 15 shows  $V_{\text{bias}}^{\text{min}}$  for different lateral charge positions, also for the S, SC, and SCL models as an extension of Fig. 9 in the main text.

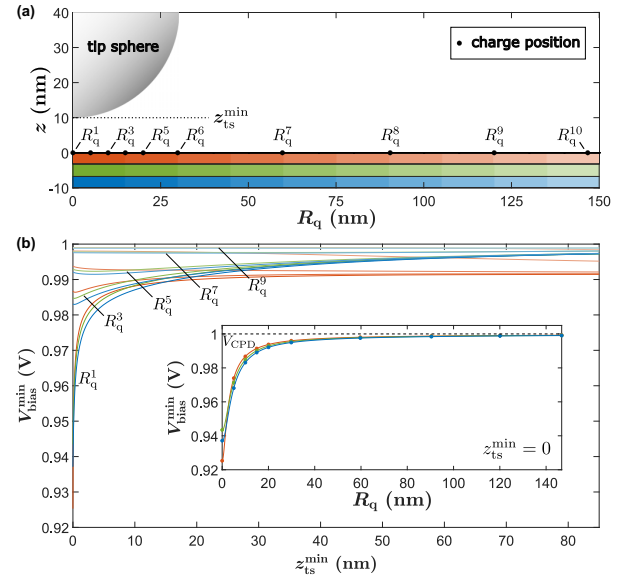


FIG. 15. Extended version of Fig. 9 highlighting the effect of the lateral charge position on  $V_{\text{bias}}^{\text{min}}$ . Data for models S (SC) are presented in red (green) while data for model SCL are depicted in blue. Tinted colors are used to express the lateral position values. Parameters are otherwise identical to those of Fig. 9.

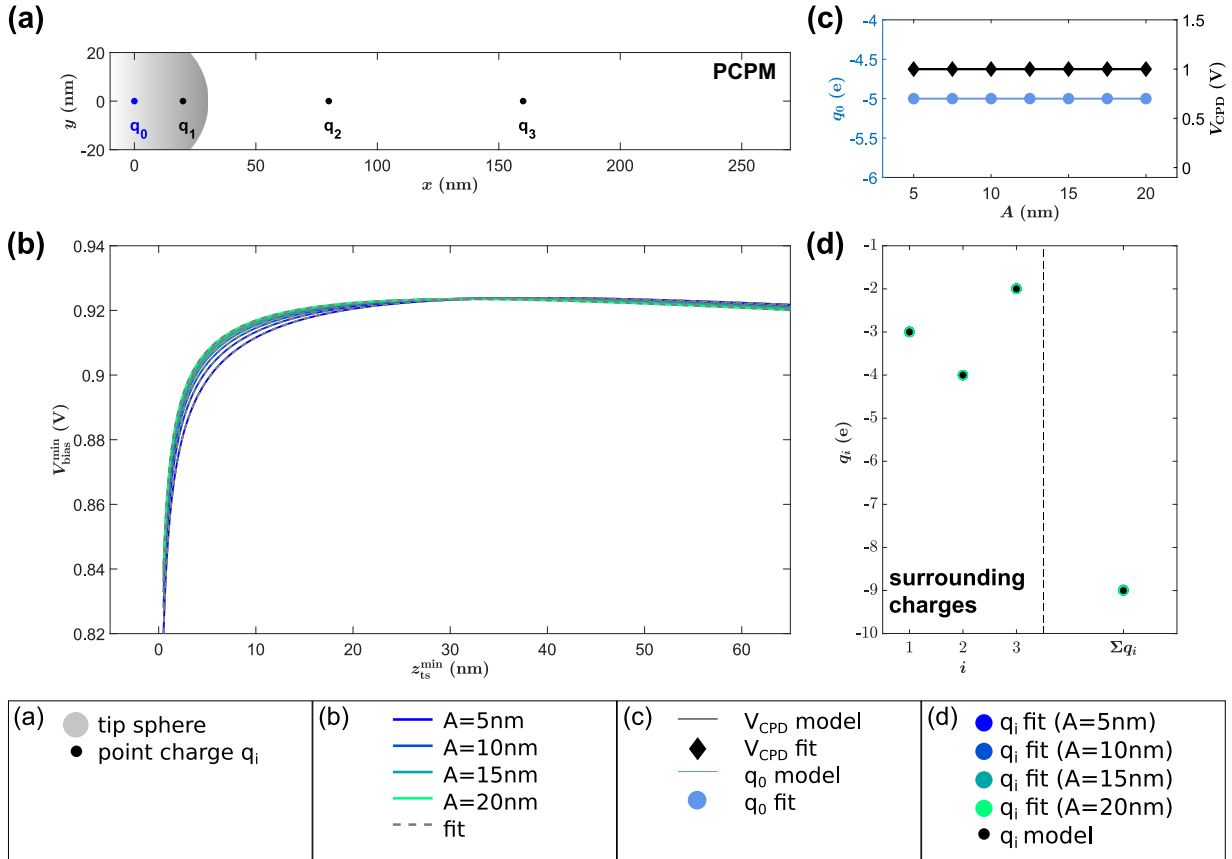


FIG. 16. Exemplary CFM experiment simulation with point charges in the range of  $-1e$  to  $-5e$ . (a) Point-charge position map (PCPM), (b)  $V_{\text{bias, meas}}^{\text{min}}$  data as a function of the minimum tip-sample distance  $z_{\text{ts}}^{\text{min}}$ , (c) model and resulting values for the fit parameters  $q_0$  and  $V_{\text{CPD}}$  as a function of the amplitude  $A$  and (d) model and resulting values for the surrounding charges  $q_i$  ( $i = 1, 2, 3$ ) and their sum as a function of the amplitude  $A$ .

#### APPENDIX B: SIMULATION WITH SMALL CHARGE MAGNITUDES

Figure 16 presents one example of a simulated CFM experiment with point-charge magnitudes randomly chosen in the range of  $-1e$  to  $-5e$ . Excellent fit results are obtained.

#### APPENDIX C: SENSITIVITY TO NEARBY CHARGES

As shown in Fig. 17, CFM delivers excellent fit results for few charges located nearby the tip even if these charges are separated by only 2 nm.

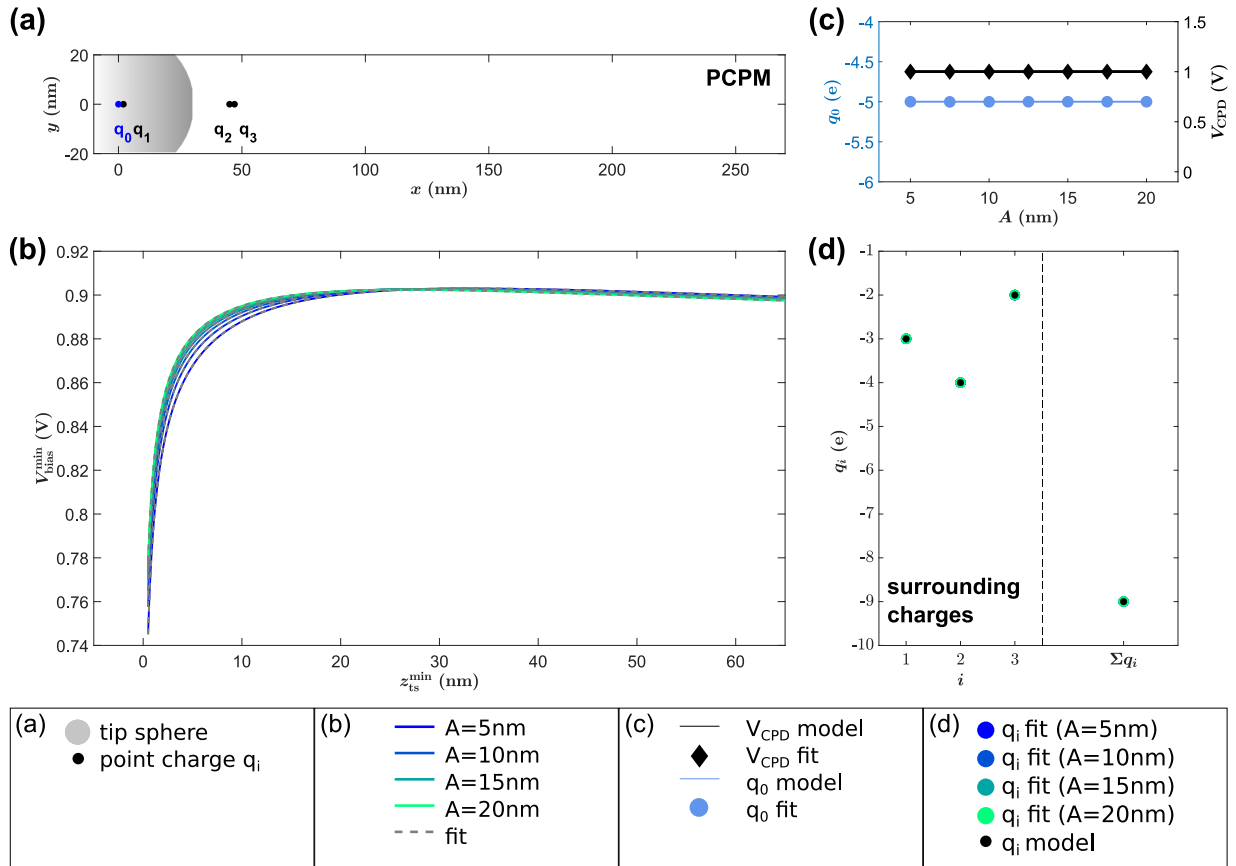


FIG. 17. Sensitivity to nearby charges. (a) Point-charge position map (PCPM), (b)  $V_{\text{bias, meas}}^{\text{min}}$  data as a function of the minimum tip-sample distance  $z_{\text{ts}}^{\text{min}}$ , (c) model and resulting values for the fit parameters  $q_0$  and  $V_{\text{CPD}}$  as a function of the amplitude  $A$ , (d) model and resulting values for the surrounding charges  $q_i$  ( $i = 1, 2, 3$ ) and their sum as a function of the amplitude  $A$ .

- [1] M. Mas-Torrent, C. Rovira, and J. Veciana, Surface-confined electroactive molecules for multistate charge storage information, *Adv. Mater.* **25**, 462 (2013).
- [2] Y. Adachi, J. Brndiar, H. F. Wen, Q. Zhang, M. Miyazaki, S. Thakur, Y. Sugawara, H. Sang, Y. Li, I. Štich, and L. Kantorovich, Electron dynamics of tip-tunable oxygen species on  $\text{TiO}_2$  surface, *Commun. Mater.* **2**, 71 (2021).
- [3] K. Bian, W. Zheng, X. Zeng, X. Chen, R. Stöhr, A. Denisenko, S. Yang, J. Wrachtrup, and Y. Jiang, Nanoscale electric-field imaging based on a quantum sensor and its charge-state control under ambient condition, *Nat. Commun.* **12**, 2457 (2021).
- [4] P. Rahe, R. P. Steele, and C. C. Williams, Consecutive charging of a molecule-on-insulator ensemble using single electron tunnelling methods, *Nano Lett.* **16**, 911 (2016).
- [5] S. Fatayer, B. Schuler, W. Steurer, I. Scivetti, J. Repp, L. Gross, M. Persson, and G. Meyer, Reorganization energy upon charging a single molecule on an insulator measured by atomic force microscopy, *Nat. Nanotechnol.* **13**, 376 (2018).
- [6] Y. Adachi, H. F. Wen, Q. Zhang, M. Miyazaki, Y. Sugawara, J. Brndiar, L. Kantorovich, I. Štich, and Y. J. Li, Charge state tristability of oxygen adatom on a rutile  $\text{TiO}_2(110)-(1 \times 1)$  surface controlled by atomic force microscopy, *J. Phys. Chem. C* **126**, 5064 (2022).
- [7] L. Gross, F. Mohn, P. Liljeroth, J. Repp, F. J. Giessibl, and G. Meyer, Measuring the charge state of an adatom with noncontact atomic force microscopy, *Science* **324**, 1428 (2009).
- [8] F. Albrecht, J. Repp, M. Fleischmann, M. Scheer, M. Ondráček, and P. Jelínek, Probing Charges on the Atomic Scale by Means of Atomic Force Microscopy, *Phys. Rev. Lett.* **115**, 076101 (2015).
- [9] C. Wagner, M. F. B. Green, M. Maiworm, P. Leinen, T. Esat, N. Ferri, N. Friedrich, R. Findeisen, A. Tkatchenko, R. Temirov, and F. S. Tautz, Quantitative imaging of electric surface potentials with single-atom sensitivity, *Nat. Mater.* **18**, 853 (2019).
- [10] F. Mohn, L. Gross, N. Moll, and G. Meyer, Imaging the charge distribution within a single molecule, *Nat. Nanotechnol.* **7**, 227 (2012).

- [11] J. F. Gonzalez, A. M. Somoza, and E. Palacios-Lidón, Charge distribution from SKPM images, *Phys. Chem. Chem. Phys.* **19**, 27299 (2017).
- [12] L. Kelvin, Contact electricity of metals, *Philos. Mag. Ser. 5* **46**, 82 (1898).
- [13] W. A. Zisman, A new method of measuring contact potential differences in metals, *Rev. Sci. Instrum.* **3**, 367 (1932).
- [14] M. Nonnenmacher, M. P. O'Boyle, and H. K. Wickramasinghe, Kelvin probe force microscopy, *Appl. Phys. Lett.* **58**, 2921 (1991).
- [15] W. Melitz, J. Shen, A. C. Kummel, and S. Lee, Kelvin probe force microscopy and its application, *Surf. Sci. Rep.* **66**, 1 (2011).
- [16] K. Wandelt, The local work function: Concept and implications, *Appl. Surf. Sci.* **111**, 1 (1997).
- [17] J. L. Neff and P. Rahe, Insights into Kelvin probe force microscopy data of insulator-supported molecules, *Phys. Rev. B* **91**, 085424 (2015).
- [18] H. Söngen, P. Rahe, J. L. Neff, R. Bechstein, J. Ritala, A. S. Foster, and A. Kühnle, The weight function for charges - a rigorous theoretical concept for Kelvin probe force microscopy, *J. Appl. Phys.* **119**, 025304 (2016).
- [19] P. Rahe, D. Heile, R. Olbrich, and M. Reichling, Quantitative dynamic force microscopy with inclined tip oscillation, *Beilstein J. Nanotechnol.* **13**, 610 (2022).
- [20] E. Bonaccorso, F. Schönfeld, and H.-J. Butt, Electrostatic forces acting on tip and cantilever in atomic force microscopy, *Phys. Rev. B* **74**, 085413 (2006).
- [21] L. N. Kantorovich, A. I. Livshits, and M. Stoneham, Electrostatic energy calculation for the interpretation of scanning probe microscopy experiments, *J. Phys.: Condens. Matter* **12**, 795 (2000).
- [22] P. Rahe and H. Söngen, Imaging static charge distributions: A comprehensive KPFM theory, in *Kelvin Probe Force Microscopy: From Single Charge Detection to Device Characterization*, edited by S. Sadewasser and T. Glatzel (Springer, Cham, 2018), pp. 147–170.
- [23] H. Söngen, R. Bechstein, and A. Kühnle, Quantitative atomic force microscopy, *J. Phys.: Condens. Matter* **29**, 274001 (2017).
- [24] A. Sadeghi, A. Baratoff, S. A. Ghasemi, S. Goedecker, T. Glatzel, S. Kawai, and E. Meyer, Multiscale approach for simulations of Kelvin probe force microscopy with atomic resolution, *Phys. Rev. B* **86**, 075407 (2012).
- [25] W. R. Smythe, *Static and Dynamic Electricity* (Taylor & Francis, London, 1989).
- [26] D. Heile, R. Olbrich, M. Reichling, and P. Rahe, Alignment method for the accurate and precise quantification of tip-surface forces, *Phys. Rev. B* **103**, 075409 (2021).
- [27] Y. Sugimoto, Y. Nakajima, D. Sawada, K. Morita, M. Abe, and S. Morita, Simultaneous AFM and STM measurements on the Si(111)-(7 × 7) surface, *Phys. Rev. B* **81**, 245322 (2010).
- [28] G. H. Simon, M. Heyde, and H.-P. Rust, Recipes for cantilever parameter determination in dynamic force spectroscopy: Spring constant and amplitude, *Nanotechnology* **18**, 255503 (2007).
- [29] T. Glatzel, L. Zimmerli, S. Koch, B. Such, S. Kawai, and E. Meyer, Determination of effective tip geometries in Kelvin probe force microscopy on thin insulating films on metals, *Nanotechnology* **20**, 264016 (2009).

## 9. Nanoscale charge quantification using CFM

The capability of CFM for charge quantification using a two-step procedure is demonstrated by measuring the static charge state of a gold nano-particle supported by a  $\text{CeO}_2(111)$  substrate. Therefore distant-dependent  $A_{2\text{fel}}(z_{\text{ts}})$  and  $V_{\text{bias}}^{\text{min}}(z_{\text{ts}})$  data are systematically measured above the particle position (onP) and an empty terrace (offP) for a set of oscillation amplitudes using the FCA method and post-processed by the two-step procedure. In the first step, the  $A_{2\text{fel}}(z_{\text{ts}})$  data is evaluated giving the parameters for the electrostatic model. In the second step, the electrostatic model is used for evaluating the  $V_{\text{bias}}^{\text{min}}(z_{\text{ts}})$  data yielding the charge contained within the investigated gold nano-particle.

The results discussed in the following are currently in preparation for submission, the shown manuscript is a preliminary version from 22.06.2023.

## Nanoscale charge quantification with charge force microscopy

Daniel Heile,\* Reinhard Olbrich,\* Michael Reichling, and Philipp Rahe†

*Fachbereich Mathematik/Informatik/Physik, Universität Osnabrück, Barbarastraße 7, 49076 Osnabrück, Germany*

(Dated: June 22, 2023)

The static charge of a ceria supported Au nano-particle is determined using charge force microscopy (CFM) performed with the tip of a non-contact atomic force microscope as the force probe. The charge is retrieved from systematically acquired measurements of the CFM signal as a function of tip-surface distance. Being a dynamic method involving the oscillation of the force probe as well as an oscillating bias voltage, CFM allows charge quantification in a two-step procedure by side-band detection at the bias voltage oscillation frequency and its first harmonic. In the first step, distance-dependent data of the tip-surface capacitance signal are retrieved from analysing the signal at the first harmonic of the bias modulation frequency. These data yield parameters for the electrostatic model. In the second step, the weight function for charges is calculated from the electrostatic model and the charge of the nano-particle of interest is retrieved from a fit of the weight function to the CFM signal measured at the bias modulation frequency. The technique is demonstrated for the measurement of the charge of a gold cluster on the surface of a heavily reduced ceria substrate that is surrounded by further similar gold clusters. While the procedure yields a negative charge for the central and surrounding nano-particles, the surface nearby the particles is found to accumulate a positive charge. This directly demonstrates charge transfer from the substrate to the nano-particles.

As a key enabler of catalytic activity, metal nano-particles on reducible oxides are of critical importance in catalytic research and application [1, 2]. Particularly with regard to the catalytic capabilities, the material, size and shape [3] as well as the charge state [4] of the metal nano-particles have a strong influence. Among the particle-supporting materials, cerium oxide (ceria,  $\text{CeO}_2$ ) is central in heterogeneous catalysis with the well known redox properties [5] following from the  $\text{Ce}^{3+}$ - $\text{Ce}^{4+}$  switch of the cations [6]. In particular, gold/ceria catalysts are exploited for many reactions, including low-temperature CO oxidation [7], water-gas shift reactions [8], or hydrogenation of  $\text{CO}_2$  to methanol [9]. For this system, the excess charges of oxygen vacancies that are always present in reduced ceria at (sub-)surface positions [10–12] strongly influence the nano-particle charge state and, thus, the reactivity of gold nano-particles [13]. Consequently, a local measurement of the charge state is key for understanding the catalytic activity of these metal nano-particles [14–19].

First approaches to experimentally quantify the total charge in metal nano-particles have been pursued by means of electron holography with transmission electron microscopy [20] as well as by photoelectron spectroscopy [4]. Additionally, it is common practice to image oxide surfaces covered with metal nano-particles by both scanning probe microscopy (SPM) to investigate structural characteristics [21] and Kelvin Probe Force Microscopy (KPFM) to map electric properties [22]. However, the surprisingly little consistency in KPFM data for metal nano-particles on surfaces [18, 23] can directly be explained by the large number of contributing factors, including the cantilever dynamics [24, 25], the tip-

sample geometry [26], and the measurement parameters [27]. An approach to describe the KPFM detection in terms of a point spread function has recently been proposed [28, 29], but it became clear that an extensive model is required when aiming for quantitative measurements [30, 31]. Very recently, charge force microscopy (CFM) has been proposed to challenge these difficulties [27].

Here, we experimentally apply CFM to a metal nano-particle/oxide system and develop a two-step procedure for charge quantification. Fundamental to CFM is the measurement of distance- and amplitude-dependent data. In the first step, system parameters are determined from these data that describe the tip geometry and enable the evaluation of the electrostatic quantities. These parameters serve for the determination of the charge magnitude of a single gold nano-particle in presence of the support and further surrounding nano-particles in the second step. We find that the introduction of a positive charge in the vicinity of the nano-particle of interest is required to match the experimental data by the model.

The target quantity in CFM is the bias voltage  $V_{\text{bias}}^{\text{min}}$  measured upon minimising the electrostatic interaction in non-contact atomic force microscopy (NC-AFM) [27, 30, 31]. While the experimental detection scheme of CFM is adapted from KPFM [32], the signal interpretation in CFM relies on a description of the sample system in terms of metal electrodes and point charges [27, 30, 31, 33]. This is different to measuring work function differences with the Kelvin Probe technique [34]. A general equation for  $V_{\text{bias}}^{\text{min}}$  of a system containing  $N$  fixed point charges  $q_i$  at positions  $\vec{r}_i$  at the surface of a dielectric substrate and a contact potential difference  $V_{\text{CPD}}$  between the substrate back contact and the metallic tip is given by using the

\* These two authors contributed equally

† prahe@uos.de

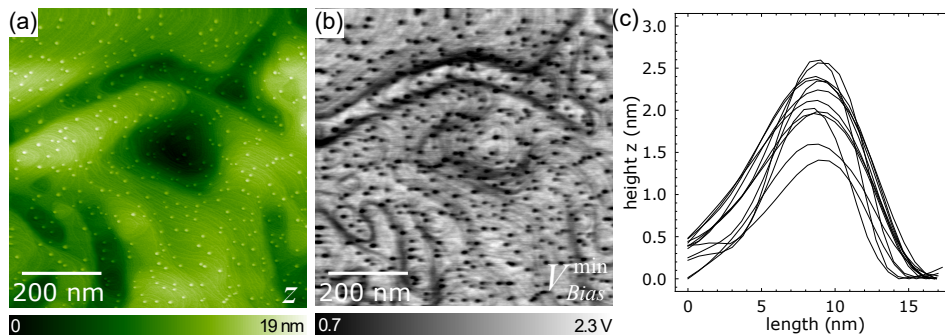


FIG. 1. Images of the ceria  $\text{CeO}_2(111)$  surface with gold nano-particles after the post-annealing step. (a) Topographic ( $z_p$ ) NC-AFM image and (b) corresponding  $V_{\text{bias}}^{\text{min}}$  data. (c) Line profiles extracted across 13 exemplary nano-particles from panel (a). A typical height of the gold nano-particles of  $(2.0 \pm 0.5)$  nm is found.

weight function for charges  $W_q$  [30, 31]

$$V_{\text{bias}}^{\text{min}} = V_{\text{CPD}} + \sum_{i=1}^N q_i W_q(\vec{r}_i). \quad (1)$$

with

$$W_q(\vec{r}_i) = \frac{\left\langle \frac{\partial^2 \hat{\Phi}_{\text{void}}(\vec{r}_i)}{\partial z_{\text{ts}}^2} \right\rangle_{\square}}{\left\langle \frac{\partial^2 C_{\text{void}}}{\partial z_{\text{ts}}^2} \right\rangle_{\square}} \quad (2)$$

depending on the normalised electrostatic potential  $\hat{\Phi}_{\text{void}}$  and the capacitance  $C_{\text{void}}$  of the void (charge free) tip-sample system as well as the tip-surface distance that is the probe oscillation centre position  $z_c$  for the dynamic measurement. Note that the weight function for charges  $W_q(\vec{r}_i)$  is evaluated at the position of each point charge position  $\vec{r}_i$ , but depends on the electrostatic model of the point-charge free (void) system.

The central challenge for quantitative charge measurements with CFM is an accurate characterization of the experimental tip-sample system to evaluate the weight function for charges  $W_q$ . Here, we exploit the signal  $A_{2\text{fel}}$  measured at twice the bias modulation frequency,  $2f_{\text{el}}$ , for the determination of the electrostatic model. As shown in the appendix Sec. A, this signal is given by

$$A_{2\text{fel}} = |G'_{\text{ho}}(f_{\text{exc}} + 2f_{\text{el}})| \frac{A}{4} V_{\text{el}}^2 \left\langle \frac{\partial^2 C_{\text{void}}}{\partial z_{\text{ts}}^2} \right\rangle_{\square} \quad (3)$$

with the transfer function of the harmonic oscillator when interacting with the sample  $G'_{\text{ho}}$  [35], the sensor excitation frequency  $f_{\text{exc}}$ , the bias modulation voltage  $V_{\text{el}}$  and the oscillation amplitude  $A$ . Within the harmonic approximation, the transfer function  $G'_{\text{ho}}$  can be approximated by the undisturbed version  $G_{\text{ho}}$  that is directly given from the sensor properties [35]. Central to Eqs. 2

and 3 is the cap averaging function  $\langle \cdot \rangle_{\square}$  defined by [35]

$$\langle f \rangle_{\square}(z_c) = \frac{2}{\pi A^2} \int_{-A}^A f(z_c + z) \sqrt{A^2 - z^2} dz, \quad (4)$$

which describes the averaging of the physical quantities due to the movement of the oscillating tip. Furthermore, Eqs. 1 and 2 highlight that the CFM voltage  $V_{\text{bias}}^{\text{min}}$  has a complex dependency on electrostatic and sensor parameters. A detailed analysis of these dependencies can be found in [27].

The fundamental approach in this work is to determine the electrostatic model parameters from fitting the electrostatic model to experimental data  $A_{2\text{fel}}(z_p)$  (The experimental adjustment parameter  $z_p$  describes the piezo position, which is identical to the tip oscillation centre position  $z_c$  except for the zero point of the coordinate axis and the static sensor deflection [36]) We use an electrostatic model [25] for calculating  $C_{\text{void}}$  and  $\hat{\Phi}_{\text{void}}$  that describes the tip as a combination of a half-sphere, a cone, and a disk as well as the sample as a dielectric slab of 1 mm thickness with dielectric constant  $\epsilon_s$ . The robustness of our approach and the reliability of the resulting parameters is confirmed by analysing data for different oscillation amplitudes [37] and at two different lateral surface positions, namely at the position of the particle of interest (“onP”) and on a particle-free terrace (“offP”).

Surface preparation and CFM measurements are performed under ultra-high vacuum conditions (base pressure  $< 1 \times 10^{-10}$  mbar). First, clean  $\text{CeO}_2(111)$  surfaces are prepared by sputter/anneal cycles. Second, gold material is deposited from an electron beam evaporator (type EFM 3i from Focus GmbH) on the sample held at room temperature. Third, small Au nano-particles are formed in a post-deposition annealing step. NC-AFM imaging and CFM charge quantification measurements are conducted with Ar-sputtered Si and PtIr-coated Si tips, respectively. CFM measurements are performed in the frequency-modulated closed-loop (FM-CL) mode [38] and the data acquisition of distance-dependent  $\Delta f(z_p)$ ,



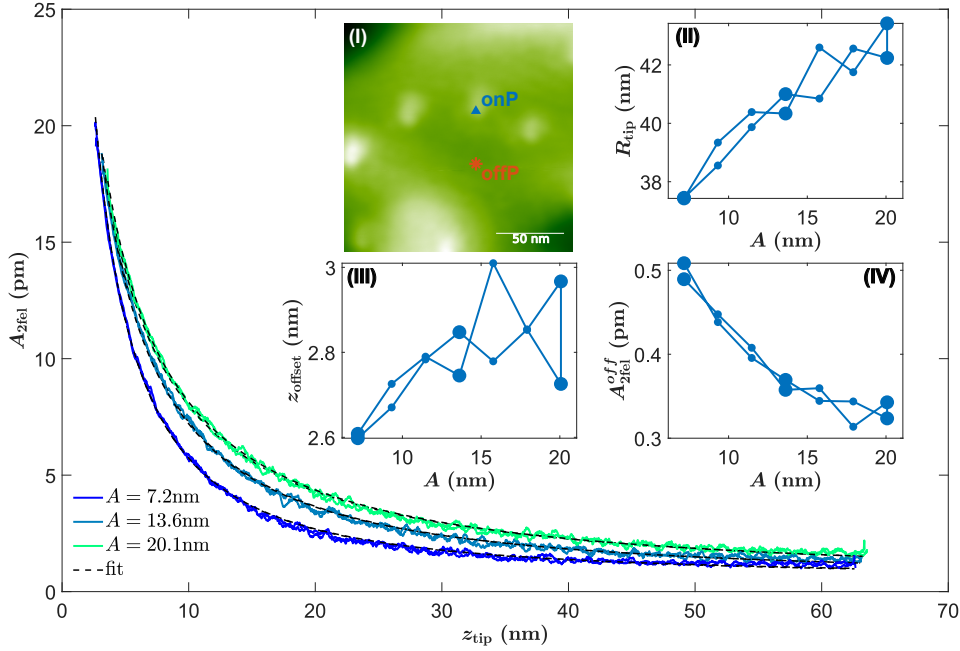


FIG. 2. Determination of the electrostatic model parameters with distance-dependent  $A_{2fel}$  data acquired on a single gold nanoparticle (position onP marked in inset (I)). A total of 14  $A_{2fel}(z_{tip})$  curves are acquired using 7 different oscillation amplitudes (data for three oscillation amplitudes shown, see appendix Sec. B for experimental details). Data are fitted (dashed black lines) using Eq. 3 with  $\epsilon_s = 24$  and three fit parameters  $R_{tip}$  (see inset II),  $z_{offset}$  (see inset III), and  $A_{2fel}^{offset}$  (see inset IV).

$V_{bias}^{min}(z_p)$ , and  $A_{2fel}(z_p)$  data using different sensor oscillation amplitudes  $A$  is executed at the two sample positions onP and offP. Seven increasing and decreasing oscillation amplitudes are used for pre-processing by the *force curve alignment (FCA)* [37] method. With this method, the oscillation amplitude  $A$  is precisely determined and thermal drift is corrected, ensuring a precise relative alignment of all curve data along the  $z_p$  axis and allowing to plot data against the coordinate of the lower tip oscillation turning point  $z_{tip}$  [36]. Further experimental details are given in appendix section B.

The topographic overview image in Fig. 1(a) shows the ceria surface after completing the sample preparation. The image reveals the surface step edges and many small terraces having a width between 5 nm and 60 nm. Single gold nanoparticles are identified as bright protrusions and are distributed homogeneously over the surface although a tendency for nucleation at or nearby step edges is observed. The line profiles of selected nanoparticles are shown in Fig. 1(c). In the corresponding  $V_{bias}^{min}$  data (tip bias, see Fig. 1(b)), dark spots are visible at the particle positions. The  $V_{bias}^{min}$  voltage is similar for all particles, highlighting that they have similar properties. In addition, the  $\text{CeO}_2(111)$  step edges appear as dark lines in the  $V_{bias}^{min}$  data. We note in passing that the difference in  $V_{bias}^{min}$  at step edges on the related  $\text{CaF}_2(111)$  surface has been explained by the different

step orientation [39]. While the more negative voltage suggest negatively-charged nano-particles and step edges, we need to highlight that the absolute values are strongly dependent on the imaging and system parameters [27]. Thus, an interpretation first requires a determination of the electrostatic model parameters.

In the first step of the charge quantification procedure, the measured and FCA-corrected  $A_{2fel}(z_p)$  data acquired at the position of one single gold nanoparticle are fitted with Eq. 3 using three fit parameters: the tip radius  $R_{tip}$ , the offset  $z_{offset}$  along the  $z$  axis relating the experimental piezo position  $z_p$  to the model coordinate system, and the amplitude-dependent offset  $A_{2fel}^{offset}$  which is an effect of the lock-in detection of the modulated  $A_{2fel}$ -signal in presence of measurement noise (see appendix Sec. C). While FCA ensures a correct *relative* alignment within a set of force-distance curves, the parameter  $z_{offset}$  determines the *absolute* alignment relative to  $z_{tip} = 0$  representing the dielectric-vacuum boundary. Consequently, after fitting it is possible to plot  $A_{2fel}$  data in Fig. 2 with respect to the position of the lower turning point of the tip oscillation,  $z_{tip}$  [36].

Fig. 2 presents exemplary  $A_{2fel}(z_{tip})$  data for three representative amplitudes for one data set acquired at an exemplary gold nano-particle position (see inset (I) in Fig. 2, together with the corresponding  $A_{2fel}(z_{tip})$  fit functions (see appendix Fig. D.2 for the full data set).

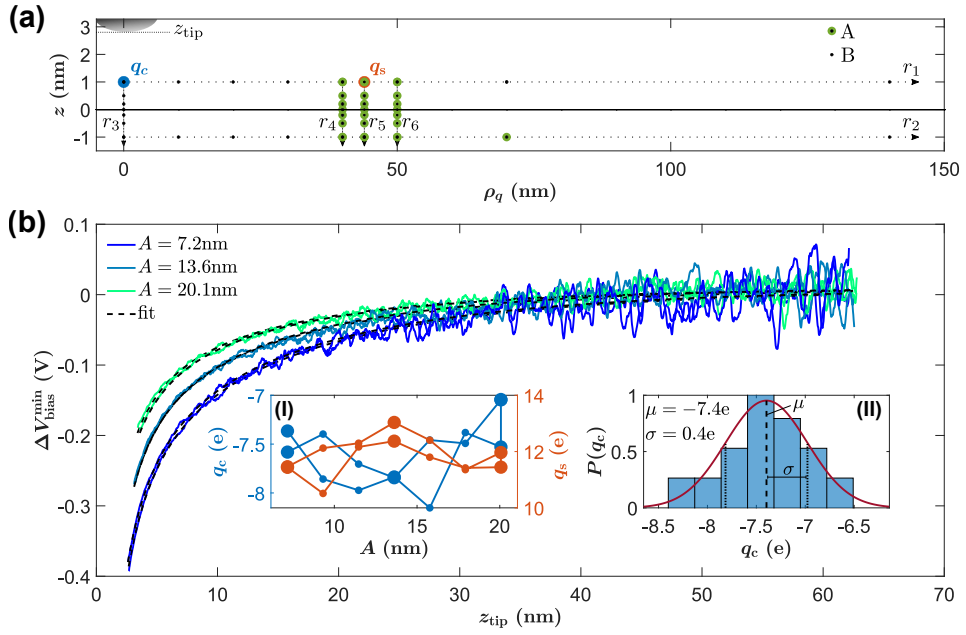


FIG. 3. Charge quantification from  $V_{\text{bias}}^{\text{min}}(z_{\text{tip}})$  data. (a) Model geometry including the positions of the central charge ( $q_c$ ) and the effective surrounding charge ( $q_s$ ). While the central charge is fixed at  $(\rho_c, z_c) = (0, 1 \text{ nm})$ , the analysis is performed for different positions of the surrounding charge  $q_s$  along the six axes  $r_1$  to  $r_6$  (see appendix Tab. D.1 for all results). (b) Distance-dependent  $\Delta V_{\text{bias}}^{\text{min}}(z_{\text{tip}})$  data calculated by subtracting  $V_{\text{bias}}^{\text{min}}(z_{\text{tip}})$  measurement data at the offP position from data acquired at the onP position (see inset (I) in Fig. 2). A total of 14  $A_{2\text{fel}}(z_p)$  curves are acquired using 7 different oscillation amplitudes at each position; data for three exemplary amplitudes are reproduced. Model and fit results (black dashed line) are given for a position of  $(\rho_s, z_s) = (44 \text{ nm}, 1 \text{ nm})$  (marked in (a) by an orange circle). Resulting fit parameters for all amplitudes are shown in inset (I) and the statistical variation of the central charge magnitude  $q_c$  across a total of three measurement sets (42  $V_{\text{bias}}^{\text{min}}(z_{\text{tip}})$  curves in total) is shown in inset (II). As the main result, the central charge magnitude is determined to  $q_c = (-7.4 \pm 0.4) e$ .

Data were acquired at the onP position of a gold nanoparticle, measurements at the offP position are reproduced in the appendix Fig. D.3. The monotonically decreasing  $A_{2\text{fel}}(z_{\text{tip}})$  curves differ depending on the oscillation amplitude. These differences are expected as they are a result of the cap averaging function (Eq. 4). For the electrostatic model [25] used to calculate the fit function, we keep the tip cone opening half-angle fixed at  $23.3^\circ$ , the cone height at  $12.5 \mu\text{m}$ , the cantilever disk radius at  $34.6 \mu\text{m}$ , the cantilever disk thickness at  $4 \mu\text{m}$ , and the substrate dielectric constant at  $\epsilon_s = 24$ . These tip and cantilever parameters are adapted from the values given by the manufacturer, while the dielectric constant for reduced ceria has been determined before [40–42]. In previous simulations [27], we found only a minor effect in  $V_{\text{bias}}^{\text{min}}$  when varying the tip geometry parameters except for  $R_{\text{tip}}$ .

The insets (II)-(IV) in Fig. 2 present results for the fit parameters as a function of the oscillation amplitude for one data set; values for the curves presented in the main figure are marked by large spheres. The tip radius  $R_{\text{tip}}$  expresses a slight dependency on the oscillation amplitude with a systematic increase from about 38 nm

to 44 nm (see inset (II) in Fig. 2). Due to the excellent agreement between the experimental data and the model curves, we assume that this scaling corrects for shortcomings of the oversimplified geometry of the tip model by influencing the cap-averaging in the calculation. The progress of the fit parameter  $z_{\text{offset}}$  (see inset (III) in Fig. 2) has no physical meaning as it is subject to the experimental strategy of keeping the lower turning point at roughly the same tip-sample distance [43] during the data acquisition. However, as the lowest measurement point of each curve will be at larger  $z$  than the nanoparticle top facet, a particle height of less than 2.6 nm can be concluded, in agreement with the typical height of 2 nm retrieved from Fig. 1(c). The fit parameter  $A_{2\text{fel}}^{\text{offset}}$  (inset (IV) in Fig. 2) is rootet in the detection principle and does not deliver insight into the electrostatic model as explained in appendix Sec. C.

With the electrostatic model parameters determined, the weight function for charges  $W_q$  (see Eq. 2) can be evaluated at the charge positions  $\vec{r}_i$ . The central provision within the second step of the charge quantification procedure is the identification of feasible charge positions for surface species contributing to the  $V_{\text{bias}}^{\text{min}}(z_{\text{tip}})$  signal.

Initial fits are performed with a central charge  $q_0$  representing the investigated gold nano-particle, four effective surrounding charges  $q_i^{\text{eff}}$  describing its surroundings, and the contact potential difference  $V_{\text{CPD}}$  between tip and sample as fit parameters [27]. The charges are positioned at  $z_q = 1$  nm above the surface, in centre of the gold nano-particles considering the typical height of 2 nm (see Fig. 1(c)). Charge redistribution at the step edges and other electrostatic inhomogeneities are also covered by the effective charge approach.

The model with five charges yields an excellent match between the experimental  $V_{\text{bias}}^{\text{min}}(z_{\text{tip}})$  data and the model curves (see appendix Fig. D.5(b)) and a magnitude of  $q_0 = (-6.7 \pm 1.8)e$  (with  $e$  representing the positive elementary charge) is found for the charge of the centre gold metal nano-particle under investigation by evaluation of three data sets (see inset of Fig. D.5(b)). Still, the comparably large error for the charge magnitude goes along with a large spread of the effective charges representing the surrounding nano-particles. We find that a decreased signal-to-noise ratio in  $V_{\text{bias}}^{\text{min}}(z_{\text{tip}})$  at tip-sample distances  $z_{\text{tip}} > 30$  nm that is the result of a greatly reduced signal strength causes a large uncertainty of the surrounding charges and, ultimately, leads to instable fits.

Therefore, we reduce the number of fit parameters by taking advantage of the homogeneous distribution and identical character of the gold nano-particles on the surface that allows to adapt the ‘‘on-minus-off’’ approach that is commonly used in site-specific force measurements with NC-AFM [44]. This approach is justified as the  $V_{\text{bias}}^{\text{min}}(z_{\text{tip}})$  signal at large tip-sample distances is dominated by charges located at large radial distances from the lateral tip position as well as by the contact potential difference. The first influence is expected to be on average identical irrespective of the lateral tip position for a homogeneous particle distribution, while the second parameter is fundamentally independent of the lateral tip position. Calculating the difference between  $V_{\text{bias}}^{\text{min}}(z_{\text{tip}})$  data taken onP and offP yields  $\Delta V_{\text{bias}}^{\text{min}}(z_{\text{tip}})$ , which, therefore, is free from the influence of remote species as well as the contact potential difference.

Experimental  $\Delta V_{\text{bias}}^{\text{min}}(z_{\text{tip}})$  data in Fig. 3(b) (green and blue curves) present the difference for three amplitudes between a  $V_{\text{bias}}^{\text{min}}(z_{\text{tip}})$  measurement acquired at the onP and the offP position. A prerequisite for calculating this difference is the correct alignment of the data along the  $z$  axis. Here, this alignment is precisely ensured via the FCA method and the determination of the  $z_{\text{offset}}$  param-

eter by fitting the  $A_{2\text{fel}}$  data. We find that placing a single point charge  $q_c$  at the centre position below the tip (i.e. at  $\rho_{q_c} = 0$ ) does not reproduce the curvature of the experimental  $V_{\text{bias}}^{\text{min}}(z_{\text{tip}})$  curve at intermediate distances around  $z_{\text{tip}} \sim 25$  nm correctly (see Fig. D.7). Although the presence of only one single fit parameter  $q_c$  renders the fitting routine very robust, this model does not correctly represent the physical system. It appears that charge in the vicinity of the investigated gold nano-particle needs to be included in the model.

Therefore, we introduce an additional charge  $q_s$  and test the fit by systematically placing this charge at positions  $(\rho_{q_s}, z_{q_s})$  along five axes  $r_1$  to  $r_5$  as shown in Fig. 3(a). The results can be classified into two groups (see appendix Tab. D.1 for a full overview). In group A, the central charge magnitude  $q_c$  is found to be between  $-7e$  and  $-8e$ , while the surrounding charge is positive with magnitudes between  $10e$  and  $20e$  and is located at lateral positions of  $\rho_{q_s} \sim 40$  nm (positions marked by green dots in Fig. 3(a)). For these cases, the agreement between the experimental data and the model curves is excellent with one example presented in Fig. 3(b). For the second group B, the agreement between the experimental and model data is reduced. In particular, the curvature at intermediate tip-sample distances around  $z_{\text{tip}} = 15$  nm does not match and the  $V_{\text{bias}}^{\text{min}}$  values at small tip-sample distances deviate. Therefore, we understand the models behind these results to not correctly represent the physical system.

It is clear that  $V_{\text{bias}}^{\text{min}}$  data at small  $z_{\text{tip}}$  have a critical influence on the charge magnitude value  $q_c$  of the central gold nano-particle. Thus, to arrive at a reliable measurement for  $q_c$ , the charge measurement is repeated with different values for the lowest position adjusted by the frequency-shift set-point during the experimental data acquisition. The  $A_{2\text{fel}}(z_{\text{tip}})$  and  $V_{\text{bias}}^{\text{min}}(z_{\text{tip}})$  curves are fitted for all data sets as shown in Figures D.2, D.3 and D.8 with the resulting fit parameters presented in the appendix Fig. D.9. The statistical distribution for  $q_c$  across all amplitudes and all measurement sets (total of 42 measurements) is included as inset (II) in Fig. 3 and yields a final value of  $(-7.4 \pm 0.4)e$  for the charge magnitude of the central gold nano-particle. In particular, as there is no apparent bias with respect to amplitude and lowest sampling position, we deem this measurement to be robust. In addition, a positive surrounding charge is found and excellent fits are achieved when positioning a charge of magnitude  $(11.3 \pm 1.0)e$  at position  $(\rho_{q_s}, z_{q_s}) = (44 \text{ nm}, 1 \text{ nm})$ .

[1] E. M. Slavinskaya, A. I. Stadnichenko, J. E. Q. Domínguez, O. A. Stonkus, M. Vorokhta, B. Šmíd, P. Castro-Latorre, A. Bruix, K. M. Neyman, and A. I. Boronin, States of Pt/CeO<sub>2</sub> catalysts for CO oxidation below room temperature, *Journal of Catalysis* **421**, 285 (2023).

[2] M. Sankar, Q. He, R. V. Engel, M. A. Sainna, A. J. Logsdail, A. Roldan, D. J. Willock, N. Agarwal, C. J. Kiely, and G. J. Hutchings, Role of the Support in Gold-Containing Nanoparticles as Heterogeneous Catalysts, *Chemical Reviews* **120**, 3890 (2020).

[3] D. Kim, G. Dimitrakopoulos, and B. Yildiz, Controlling

- the Size of Au Nanoparticles on Reducible Oxides with the Electrochemical Potential, *Journal of the American Chemical Society* **144**, 21926 (2022).
- [4] Y. Lykhach, S. M. Kozlov, T. Skála, A. Tovt, V. Stetsovych, N. Tsud, F. Dvořák, V. Johánek, A. Neitzel, J. Mysliveček, S. Fabris, V. Matolín, K. M. Neyman, and J. Libuda, Counting electrons on supported nanoparticles, *Nature Materials* **15**, 284 (2016).
- [5] K. Chang, H. C. Zhang, M. J. Cheng, and Q. Lu, Application of Ceria in CO<sub>2</sub> Conversion Catalysis, *Acs Catalysis* **10**, 613 (2020).
- [6] Q. Fu, H. Saltsburg, and M. Flytzani-Stephanopoulos, Active nonmetallic au and pt species on ceria-based water-gas shift catalysts, *Science* **301**, 935 (2003).
- [7] A. Trovarelli and J. Llorca, Ceria catalysts at nanoscale: How do crystal shapes shape catalysis?, *ACS Catalysis* **7**, 4716 (2017).
- [8] R. Si and M. Flytzani-Stephanopoulos, Shape and crystal-plane effects of nanoscale ceria on the activity of Au-CeO<sub>2</sub> catalysts for the water-gas shift reaction, *Angewandte Chemie-International Edition* **47**, 2884 (2008).
- [9] J. A. Rodriguez, P. Liu, D. J. Stacchiola, S. D. Senanayake, M. G. White, and J. G. G. Chen, Hydrogenation of CO<sub>2</sub> to methanol: Importance of metal-oxide and metal-carbide interfaces in the activation of CO<sub>2</sub>, *ACS Catalysis* **5**, 6696 (2015).
- [10] R. Olbrich, G. E. Murgida, V. Ferrari, C. Barth, A. M. Llois, M. Reichling, and M. V. Ganduglia-Pirovano, Surface Stabilizes Ceria in Unexpected Stoichiometry, *Journal of Physical Chemistry C* **121**, 6844 (2017).
- [11] T. Duchoň, F. Dvořák, M. Aulická, V. Stetsovych, M. Vorokhta, D. Mazur, K. Veltruská, T. Skála, J. Mysliveček, I. Matolínová, and V. Matolín, Ordered Phases of Reduced Ceria As Epitaxial Films on Cu(111), *Journal of Physical Chemistry C* **118**, 357 (2014).
- [12] G. E. Murgida and M. V. Ganduglia-Pirovano, Evidence for Subsurface Ordering of Oxygen Vacancies on the Reduced CeO<sub>2</sub>(111) Surface Using Density-Functional and Statistical Calculations, *Physical Review Letters* **110**, 246101 (2013).
- [13] J. Engel, E. Schwartz, C. R. A. Catlow, and A. Roldan, The influence of oxygen vacancy and Ce<sub>3+</sub> ion positions on the properties of small gold clusters supported on CeO<sub>2-x</sub>(111), *Journal of Materials Chemistry A* **8**, 15695 (2020).
- [14] M. J. Zachman, V. Fung, F. Polo-Garzon, S. H. Cao, J. Moon, Z. N. Huang, D. E. Jiang, Z. L. Wu, and M. F. Chi, Measuring and directing charge transfer in heterogeneous catalysts, *Nature Communications* **13**, 3253 (2022).
- [15] N. Daelman, M. Capdevila-Cortada, and N. López, Dynamic charge and oxidation state of Pt/CeO<sub>2</sub> single-atom catalysts, *Nature Materials* **18**, 1215 (2019).
- [16] G. Pacchioni and H.-J. Freund, Controlling the charge state of supported nanoparticles in catalysis: lessons from model systems, *Chem. Soc. Rev.* **47**, 8474 (2018).
- [17] O. Bezkrovnyi, A. Bruix, D. Blaumeiser, L. Piliai, S. Schötz, T. Bauer, I. Khalakhan, T. Skála, P. Matvija, P. Kraszkiewicz, M. Pawlyta, M. Vorokhta, I. Matolínová, J. Libuda, K. M. Neyman, and L. Kępiński, Metal-Support Interaction and Charge Distribution in Ceria-Supported Au Particles Exposed to CO, *Chemistry of Materials* **34**, 7916 (2022).
- [18] B. Chatelain, A. El Barraj, C. Laffon, P. Parent, and C. Barth, Characterizing the Water-Forming Reaction on Graphite- and Ceria-Supported Palladium Nanoparticles and Nanoislands by the Work Function, *Journal of Physical Chemistry C* **127**, 5731–5742 (2023).
- [19] Y.-G. Wang, Y. Yoon, V.-A. Glezakou, J. Li, and R. Rousseau, The Role of Reducible Oxide–Metal Cluster Charge Transfer in Catalytic Processes: New Insights on the Catalytic Mechanism of CO Oxidation on Au/TiO<sub>2</sub> from ab Initio Molecular Dynamics, *Journal of the American Chemical Society* **135**, 10673 (2013).
- [20] R. Aso, H. Hojo, Y. Takahashi, T. Akashi, Y. Midoh, F. Ichihashi, H. Nakajima, T. Tamaoka, K. Yubuta, H. Nakanishi, H. Einaga, T. Tanigaki, H. Shinada, and Y. Murakami, Direct identification of the charge state in a single platinum nanoparticle on titanium oxide, *Science* **378**, 202 (2022).
- [21] C. Barth, A. S. Foster, C. R. Henry, and A. L. Shluger, Recent trends in surface characterization and chemistry with high-resolution scanning force methods, *Advanced Materials* **23**, 477 (2011).
- [22] W. Melitz, J. Shen, A. C. Kummel, and S. Lee, Kelvin probe force microscopy and its application, *Surface Science Reports* **66**, 1 (2011).
- [23] Y. Adachi, H. F. Wen, Q. Z. Zhang, M. Miyazaki, Y. Sugawara, and Y. J. Li, Elucidating the charge state of an Au nanocluster on the oxidized/reduced rutile TiO<sub>2</sub>(110) surface using non-contact atomic force microscopy and Kelvin probe force microscopy, *Nanoscale Advances* **2**, 2371 (2020).
- [24] K. J. Satzinger, K. A. Brown, and R. M. Westervelt, The importance of cantilever dynamics in the interpretation of Kelvin probe force microscopy, *Journal of Applied Physics* **112**, 064510 (2012).
- [25] A. Sadeghi, A. Baratoff, S. A. Ghasemi, S. Goedecker, T. Glatzel, S. Kawai, and E. Meyer, Multiscale approach for simulations of kelvin probe force microscopy with atomic resolution, *Physical Review B* **86**, 075407 (2012).
- [26] A. Sadeghi, A. Baratoff, and S. Goedecker, Electrostatic interactions with dielectric samples in scanning probe microscopies, *Physical Review B* **88**, 035436 (2013).
- [27] D. Heile, R. Olbrich, M. Reichling, and P. Rahe, Modelling nanoscale charge measurements, *Physical Review B*, accepted (2023).
- [28] J. F. Gonzalez, A. M. Somoza, and E. Palacios-Lidón, Charge distribution from skpm images, *Physical Chemistry Chemical Physics* **19**, 27299 (2017).
- [29] M. F. Orihuela, A. M. Somoza, J. Colchero, M. Ortuño, and E. Palacios-Lidón, Localized charge imaging with scanning kelvin probe microscopy, *Nanotechnology* **28**, 025703 (2017).
- [30] J. L. Neff and P. Rahe, Insights into Kelvin probe force microscopy data of insulator-supported molecules, *Physical Review B* **91**, 085424 (2015).
- [31] H. Söngen, P. Rahe, J. L. Neff, R. Bechstein, J. Ritala, A. S. Foster, and A. Kühnle, The weight function for charges-A rigorous theoretical concept for Kelvin probe force microscopy, *Journal of Applied Physics* **119**, 025304 (2016).
- [32] M. Nonnenmacher, M. P. O’Boyle, and H. K. Wickramasinghe, Kelvin probe force microscopy, *Applied Physics Letters* **58**, 2921 (1991).
- [33] L. N. Kantorovich, A. I. Livshits, and M. Stoneham, Electrostatic energy calculation for the interpretation of scanning probe microscopy experiments, *Journal of Physics-Condensed Matter* **12**, 795 (2000).

- [34] L. Kelvin, V. contact electricity of metals, *Philosophical Magazine Series 5* **46**, 82 (1898).
- [35] H. Söngen, R. Bechstein, and A. Kühnle, Quantitative atomic force microscopy, *Journal of Physics: Condensed Matter* **29**, 274001 (2017).
- [36] P. Rahe, D. Heile, R. Olbrich, and M. Reichling, Quantitative dynamic force microscopy with inclined tip oscillation, *Beilstein Journal of Nanotechnology* **13**, 610 (2022).
- [37] D. Heile, R. Olbrich, M. Reichling, and P. Rahe, Alignment method for the accurate and precise quantification of tip-surface forces, *Physical Review B* **103**, 075409 (2021).
- [38] P. Rahe and H. Söngen, Imaging Static Charge Distributions: A Comprehensive KPFM Theory, in *Kelvin Probe Force Microscopy: From Single Charge Detection to Device Characterization*, edited by S. Sadewasser and T. Glatzel (Springer International Publishing, Cham, 2018) pp. 147–170.
- [39] H. H. Pieper, C. Barth, and M. Reichling, Characterization of atomic step structures on  $\text{CaF}_2(111)$  by their electric potential, *Applied Physics Letters* **101**, 051601 (2012).
- [40] M. M. El-Nahass, A. M. Hassanien, A. A. Atta, E. M. A. Ahmed, and A. A. Ward, Electrical conductivity and dielectric relaxation of cerium (IV) oxide, *Journal of Materials Science-Materials in Electronics* **28**, 1501 (2017).
- [41] T. Gürel and R. Eryigit, Ab initio pressure-dependent vibrational and dielectric properties of  $\text{CeO}_2$ , *Physical Review B* **74**, 014302 (2006).
- [42] T. Yamamoto, H. Momida, T. Hamada, T. Uda, and T. Ohno, First-principles study of dielectric properties of cerium oxide, *Thin Solid Films* **486**, 136 (2005).
- [43] J. Heggemann and P. Rahe, Accuracy and precision of amplitude calibration in dynamic atomic force microscopy, in preparation (2023).
- [44] A. Sweetman and A. Stannard, Uncertainties in forces extracted from non-contact atomic force microscopy measurements by fitting of long-range background forces, *Beilstein Journal of Nanotechnology* **5**, 386 (2014).
- [45] H. H. Pieper, C. Lammers, L. Tröger, S. Bahr, and M. Reichling, Versatile system for the temperature-controlled preparation of oxide crystal surfaces, *Review of Scientific Instruments* **83**, 055110 (2012).
- [46] H. H. Pieper, C. Derks, M. H. Zoellner, R. Olbrich, L. Tröger, T. Schroeder, M. Neumann, and M. Reichling, Morphology and nanostructure of  $\text{CeO}_2(111)$  surfaces of single crystals and Si(111) supported ceria films, *Physical Chemistry Chemical Physics* **14**, 15361 (2012).
- [47] S. Torbrügge, J. Lübke, L. Tröger, M. Cranney, T. Eguchi, Y. Hasegawa, and M. Reichling, Improvement of a dynamic scanning force microscope for highest resolution imaging in ultrahigh vacuum, *Review of Scientific Instruments* **79**, 083701 (2008).
- [48] P. Rahe, J. Schütte, W. Schniederberend, M. Reichling, M. Abe, Y. Sugimoto, and A. Kühnle, Flexible drift-compensation system for precise 3d force mapping in severe drift environments, *Review of Scientific Instruments* **82**, 063704 (2011).
- [49] J. Lübke, M. Temmen, S. Rode, P. Rahe, A. Kühnle, and M. Reichling, Thermal noise limit for ultra-high vacuum noncontact atomic force microscopy, *Beilstein Journal of Nanotechnology* **4**, 32 (2013).

### Appendix A: The signal amplitude at $2f_{\text{el}}$ : $A_{2f_{\text{el}}}$

The probe displacement  $q$  can generally be described by solving the equation of motion for an externally driven, damped harmonic oscillator with an external force [35]. Commonly, the solution is based on the harmonic approximation, namely on the ansatz  $q(t) = q_0 + A \cos(2\pi f_{\text{exc}}t + \phi)$ . For the case of CFM, additional components are present in  $q(t)$  due to the bias modulation with  $V = V_{\text{bias}} - V_{\text{CPD}} + V_{\text{el}} \cos(2\pi f_{\text{el}}t)$ . While the frequencies of these components are identical to the method of KPFM, the interpretation of the magnitude differ significantly. The Fourier analysis of  $q(t)$  yields:

$$\begin{aligned} \mathcal{F}[q](f) = & G'_{\text{ho}}(f) \times \\ & \mathcal{F}[F_0 \cos(2\pi f_{\text{exc}}t) \\ & + \langle F_{\text{even,a}} \rangle_{\cup} \\ & + \langle F_{\text{el,b}} \rangle_{\cup} \cos(2\pi f_{\text{el}}t) \\ & + \langle F_{\text{el,c}} \rangle_{\cup} \cos(2\pi 2f_{\text{el}}t) \\ & + A/2 \langle k_{\text{el,b}} \rangle_{\cap} \cos(2\pi(f_{\text{exc}} + f_{\text{el}})t + \varphi) \\ & + A/2 \langle k_{\text{el,b}} \rangle_{\cap} \cos(2\pi(f_{\text{exc}} - f_{\text{el}})t + \varphi) \\ & + A/2 \langle k_{\text{el,c}} \rangle_{\cap} \cos(2\pi(f_{\text{exc}} + 2f_{\text{el}})t + \varphi) \\ & + A/2 \langle k_{\text{el,c}} \rangle_{\cap} \cos(2\pi(f_{\text{exc}} - 2f_{\text{el}})t + \varphi)] \quad (\text{A1}) \end{aligned}$$

The signal contains one static as well as four harmonic components, the latter at frequencies  $f_{\text{el}}$ ,  $f_{\text{exc}}$ ,  $f_{\text{exc}} \pm f_{\text{el}}$ , and  $f_{\text{exc}} \pm 2f_{\text{el}}$ . The amplitudes of these components are defined by force contributions given by the excitation force  $F_0$ , the even tip-sample interaction  $F_{\text{even,a}}$ , as well as components of the electrostatic force ( $F_{\text{el,b}}$ ,  $F_{\text{el,c}}$ ) and the electrostatic force gradient ( $k_{\text{el,b}}$ ,  $k_{\text{el,c}}$ ). The full derivation has been given before [38].

The  $V_{\text{bias}}^{\text{min}}$  signal evaluated in closed-loop frequency-modulation CFM follows from the condition [38]

$$0 = \mathcal{F}[q \cos(2\pi f_{\text{exc}}t)](f_{\text{el}}). \quad (\text{A2})$$

From eq. A1, this reduces to the equation

$$0 = \langle k_{\text{el,b}} \rangle_{\cap} \quad (\text{A3})$$

which is a function of  $V_{\text{bias}}^{\text{min}}$ . The quantity  $k_{\text{el,b}}$  depends on both, the electrostatic system parameters as well as the point charge positions and magnitudes. It can explicitly be written as [38]

$$k_{\text{el,b}} = V_{\text{el}} \left( \frac{\partial^2 C_{\text{void}}}{\partial z_{\text{ts}}^2} (V_{\text{bias}} - V_{\text{CPD}}) - \sum_{i=1}^N q_i \frac{\partial^2 \hat{\Phi}_{\text{void}}(\vec{r}_i)}{\partial^2 z_{\text{ts}}} \right). \quad (\text{A4})$$

The signal at  $f_{\text{exc}} \pm 2f_{\text{el}}$  can be measured by lock-in or sideband detection techniques. This signal is of relevance as only the averaged capacitance gradient contributes; this signal is independent of the point charges in the system. In particular,  $k_{\text{el,c}}$  is given by [38]:

$$k_{\text{el,c}} = \frac{1}{4} \frac{\partial^2 C_{\text{void}}}{\partial z_{\text{ts}}^2} V_{\text{el}}^2. \quad (\text{A5})$$

We define  $A_{2f_{\text{el}}}$  as the amplitude of this component at frequency  $f_0 \pm 2f_{\text{el}}$  in the spectrum of  $q$

$$A_{2f_{\text{el}}} = |G'_{\text{ho}}(f_0 + 2f_{\text{el}})| \cdot |A \cdot \langle k_{\text{el,c}} \rangle_{\cap}|. \quad (\text{A6})$$

In this equation, we only consider the positive frequency axis and include a factor of 2 to account for the signal power at  $f_{\text{exc}} - 2f_{\text{el}}$ . This is justified as the input signal is a real signal. The transfer function of the harmonic oscillator,  $G'_{\text{ho}}$ , is defined by [35]

$$G'_{\text{ho}}(f) = \frac{1}{k' - (2\pi f)^2 m + 2\pi i f \gamma'} \quad (\text{A7})$$

and describes the oscillator slightly disturbed by the tip-sample interaction using the effective force gradient and damping coefficients

$$k' = k_0 - \langle k_{\text{ts,a}} \rangle_{\cap} \quad (\text{A8})$$

$$\gamma' = \gamma_0 - \langle \gamma_{\text{ts,a}} \rangle_{\cap} \quad (\text{A9})$$

The averaged tip-sample force gradient is, in the case of CFM and KPFM, usually very small as only long-range forces contribute to the measurement. Therefore, the approximation

$$G'_{\text{ho}}(f_0 + 2f_{\text{el}}) \approx G_{\text{ho}}(f_0 + 2f_{\text{el}}) \quad (\text{A10})$$

can be used. For  $\langle k_{\text{ts,a}} \rangle_{\cap} = 0.02 \text{ Nm}$ , the difference between  $G'_{\text{ho}}(f_0 + 2f_{\text{el}})$  and  $G_{\text{ho}}(f_0 + 2f_{\text{el}})$  is of the order of 0.1 %.

### Appendix B: Experimental Methods

Sample preparation and NC-AFM measurements are performed under ultra-high vacuum (UHV) conditions in the same system at a base pressure in the low  $10^{-11}$  mbar range.

A ceria single crystal (SurfaceNet GmbH, Rheine, Germany) is used as substrate for gold nano-particle deposition and growth. The crystals are prepared with several cycles of Argon ion sputtering ( $U = 1.5 \text{ kV}$ ,  $I = 15 \text{ mA}$ ,  $p_{\text{Ar}} = 5 \times 10^{-5} \text{ mbar}$ ) followed by annealing at high temperatures (1100 K to 1200 K) for 20 min to 30 min. A detailed description of the annealing procedure can be found in refs. [10, 45]. This procedure results in a clean surface rich of small terraces separated predominantly by one triple layer (TL, O-Ce-O) high step edges as also observed for ceria single crystals from a different source [46].

The deposition of gold (purity: 99.95%, Goodfellow, UK) on the ceria sample is carried out with an electron beam sublimator (EFM 3i, Focus GmbH, Hünstetten, Germany) which was carefully degassed prior to the experiments and operated with the settings:  $U = 600 \text{ V}$ ,  $I_{\text{Emission}} = 20 \text{ mA}$ ,  $I_{\text{Fil}} = 2 \text{ A}$ . After a constant flux of

approx. 320 nA is achieved for several minutes, gold is deposited for 60 s on the sample held at room temperature. The deposition time of 60 s results in a surface nearly completely covered by very small Au particles. Larger nano-particles are formed in a post-deposition annealing step at temperatures between 520 K to 620 K and for times between 20 min to 30 min.

NC-AFM and CFM experiments are performed at room temperature using a modified [47] commercial ultra-high vacuum AFM/STM system (Omicron Nano-Technology, Taunusstein, Germany) controlled by a RHK R9 controller (RHK Technology, Inc., Troy, USA) and an atom-tracking system [48] for drift compensation. Standard silicon cantilevers (PPP-NCH from Nanosensors, Switzerland) as well as PtIr-coated silicon cantilevers (NCHPt from Nanosensors, Switzerland) are used for the experiments. Both cantilevers have a resonance frequency in the range of  $f_0 = 230 \text{ kHz} - 350 \text{ kHz}$  and a typical force constant of  $42 \text{ N m}^{-1}$ . The standard Si cantilevers have a lower conductivity but a sharper tip, resulting in higher resolution during imaging.

CFM measurements are performed in the frequency-modulated (FM) closed-loop (CL) mode with  $f_{\text{el}} = 1567 \text{ Hz}$  and  $V_{\text{el}} = 1 \text{ V}$  using PtIr-coated Si probes.  $V_{\text{bias}}^{\text{min}}$  refers to the voltage at the tip with respect to the sample back contact. The sideband detection of the R9 system is used for detection of the components at  $f_{\text{el}}$  and  $2f_{\text{el}}$  and the CFM voltage  $V_{\text{bias}}^{\text{min}}$  is adjusted by a feedback loop such that the spectral component at  $f_{\text{el}}$  is minimised.

CFM data are acquired as both, images in parallel to regular topography mode imaging as well as distance-dependent measurements at well-controlled sample positions. Distance-dependent measurements are performed using the same measurement protocol as introduced as *force curve alignment* [37]. With this protocol, a total of  $2N$  curves (here:  $N = 7$ ) with ascending and descending amplitude values are acquired. Here, amplitude values of  $A_0 = 5.0, 7.14, 9.29, 13.57, 17.86, 20.0 \text{ nm}$  are used. An optimisation algorithm matches the force curves calculated from the frequency-shift  $\Delta f(z)$  data with the sensitivity factor  $S$  and drift parameters as free variables. A reliable force measurement, parameter determination, as well as precise relative alignment of the data are achieved when all curves are identical within the measurement noise.

#### Appendix C: Contributions to the $A_{2f_{\text{el}}}$ signal measurement

The  $A_{2f_{\text{el}}}$  signal is measured at  $f_{\text{exc}} \pm 2f_{\text{el}}$  in the deflection signal  $q$  using the side-band detection method of the R9 control system. This detection method yields the same result as a lock-in based measurement of the  $2f_{\text{el}}$  component in the frequency-shift ( $\Delta f$ ) channel.

The  $A_{2f_{\text{el}}}$  signal in  $q$  is very small compared to the deflection signal  $q$  of the cantilever at  $f_{\text{exc}}$  as well as to the  $V_{\text{bias}}$  signal at  $f_{\text{exc}} + f_{\text{el}}$ . Hence, care has to be taken

that the  $A_{2f_{\text{el}}}$  signal measurement is free from artefacts. In our experiments, we find a decreasing offset  $A_{2f_{\text{el}}}^{\text{offset}}$  with increasing tip oscillation amplitude  $A$ .

When using lock-in based detection, the absence of further components within the lock-in output signal has to be ensured. In particular, for this specific case, the bandwidth has to be chosen small enough such that the components at  $f_{\text{exc}}$  and  $f_{\text{exc}} + f_{\text{el}}$  are not leading to additional contributions. The frequency  $f_{\text{el}}$  is set to  $f_{\text{el}} = 1576 \text{ Hz}$  in the experiments. With time constants smaller than 2.7 ms we found an increase of the  $A_{2f_{\text{el}}}$  signal with the tip oscillation amplitude  $A$ . Note that this effect is opposite to our experimental observations. Instead, when setting the time constant of the lock-in amplifier to 3.2 ms with a filter slope of 18 dB/Oct, we verified that there is neglectable influence by the main signal at  $f_{\text{exc}}$ ;  $A_{2f_{\text{el}}}$  is found to be independent of the tip oscillation amplitude  $A$  with these settings. Still, the detection bandwidth with these settings is still large enough to measure  $A_{2f_{\text{el}}}$  within the experimental sampling times. These settings were used for the experiments.

From a noise analysis it has been found [49] that the total noise amplitude spectral density  $d_{\text{tot}}^{\Delta f}$  in the  $\Delta f$  channel scales with the inverse oscillation amplitude, i.e. with  $1/A$ . Due to the finite bandwidth of the lock-in amplifier low pass filter, the integration over this spectral density within the filter bandwidth contributes to the lock-in output signal and will lead to a scaling of the noise contribution with  $1/A$ . At large tip-sample distances where the  $A_{2f_{\text{el}}}$  signal is predominantly defined by the contributing noise, this contribution appears as an offset. However, this offset is present at all tip-sample distances and, thus, compensated for in the fit procedure of the electrostatic model by introducing a fit parameter  $A_{2f_{\text{el}}}^{\text{offset}}$  that is additive to the model result for  $A_{2f_{\text{el}}}$ .

#### Appendix D: Results

The point charge position map derived from several NC-AFM images acquired in the vicinity of the gold nano-particle of interest is shown in Fig. D.1. Fits of the  $A_{2f_{\text{el}}}$  model (Eq. 3) to all data sets acquired at the gold nano-particle position (onP) are shown in Fig. D.2. Fits to the corresponding data sets taken on an empty terrace (offP position) are shown in Fig. D.3. An overview of the resulting electrostatic model fit parameters for three different data sets are shown in Fig. D.4.

The evaluation of the charge magnitude at onP (Fig. D.5) and offP (Fig. D.6) positions with a model containing one central ( $q_0$ ) and four effective surrounding charges ( $q_i^{\text{eff}}$ ) yields instable values for the surrounding charges and a large error for the magnitude of the central charge.

Fits when using the difference approach with a single central point charge are shown in Fig. D.7. Results when using one surrounding charge in addition to the central charge for three data sets are shown in Fig. D.8 and an

overview of the resulting values are compiled in Fig. D.9. These results are calculated for the surrounding charge located at  $(\rho_{q_s}, z_{q_s}) = (44 \text{ nm}, 1 \text{ nm})$ . Results for further positions are listed in Tab. D.1.

| axis  | $\rho_{q_s}$<br>(nm) | $z_{q_s}$<br>(nm) | $\mu_{q_c}$<br>(e) | $\sigma_{q_c}$<br>(e) | $\mu_{q_s}$<br>(e) | $\sigma_{q_s}$<br>(e) | $\mu_{\epsilon_{\text{RMS}}}$<br>(mV) | group |
|-------|----------------------|-------------------|--------------------|-----------------------|--------------------|-----------------------|---------------------------------------|-------|
| $r_1$ | 10                   | 1                 | -22.4              | 5.0                   | 20.9               | 5.6                   | 15.8                                  | B     |
|       | 20                   | 1                 | -10.8              | 1.2                   | 10.5               | 1.8                   | 14.0                                  | B     |
|       | 30                   | 1                 | -8.5               | 0.6                   | 9.7                | 1.0                   | 12.6                                  | B     |
|       | 40                   | 1                 | -7.6               | 0.4                   | 10.7               | 1.0                   | 11.9                                  | A     |
|       | 44                   | 1                 | -7.4               | 0.4                   | 11.3               | 1.0                   | 11.8                                  | A     |
|       | 50                   | 1                 | -7.2               | 0.4                   | 12.5               | 1.1                   | 11.8                                  | A     |
|       | 70                   | 1                 | -6.9               | 0.4                   | 17.8               | 1.9                   | 12.0                                  | B     |
|       | 140                  | 1                 | -7.1               | 0.5                   | 43.2               | 4.9                   | 12.1                                  | B     |
| $r_2$ | 0                    | -1                | -14.0              | 1.3                   | 20.5               | 2.4                   | 12.6                                  | B     |
|       | 10                   | -1                | -12.2              | 1.1                   | 17.9               | 2.2                   | 12.7                                  | B     |
|       | 20                   | -1                | -9.9               | 0.8                   | 15.3               | 1.7                   | 12.6                                  | B     |
|       | 30                   | -1                | -8.7               | 0.6                   | 14.8               | 1.4                   | 12.1                                  | B     |
|       | 40                   | -1                | -8.0               | 0.5                   | 15.5               | 1.4                   | 11.9                                  | A     |
|       | 44                   | -1                | -7.8               | 0.5                   | 16.1               | 1.4                   | 11.8                                  | A     |
|       | 50                   | -1                | -7.6               | 0.4                   | 17.1               | 1.5                   | 11.8                                  | A     |
|       | 70                   | -1                | -7.3               | 0.4                   | 21.7               | 2.1                   | 11.9                                  | A     |
| 140   | -1                   | -7.2              | 0.5                | 44.6                  | 4.8                | 12.0                  | B                                     |       |
| $r_3$ | 0                    | 0.5               | -35.8              | 3.9                   | 42.3               | 5.0                   | 12.6                                  | B     |
|       | 0                    | 0.2               | -20.1              | 2.0                   | 26.5               | 3.1                   | 12.6                                  | B     |
|       | 0                    | 0                 | -14.8              | 1.4                   | 21.3               | 2.5                   | 12.6                                  | B     |
|       | 0                    | -0.2              | -14.6              | 1.4                   | 21.1               | 2.5                   | 12.6                                  | B     |
|       | 0                    | -0.5              | -14.4              | 1.3                   | 20.9               | 2.4                   | 12.6                                  | B     |
|       | 0                    | -1                | -14.0              | 1.3                   | 20.5               | 2.4                   | 12.6                                  | B     |
|       | 40                   | 1                 | -7.6               | 0.4                   | 10.7               | 0.9                   | 11.9                                  | A     |
| $r_4$ | 40                   | 0.5               | -7.8               | 0.5                   | 12.6               | 1.1                   | 11.9                                  | A     |
|       | 40                   | 0.2               | -7.9               | 0.5                   | 14.1               | 1.2                   | 11.9                                  | A     |
|       | 40                   | 0                 | -8.0               | 0.5                   | 15.3               | 1.3                   | 11.9                                  | A     |
|       | 40                   | -0.2              | -8.0               | 0.5                   | 15.3               | 1.3                   | 11.9                                  | A     |
|       | 40                   | -0.5              | -8.0               | 0.5                   | 15.4               | 1.3                   | 11.9                                  | A     |
|       | 40                   | -1                | -8.0               | 0.5                   | 15.5               | 1.4                   | 11.9                                  | A     |
|       | 44                   | 1                 | -7.4               | 0.4                   | 11.3               | 1.0                   | 11.8                                  | A     |
| $r_5$ | 44                   | 0.5               | -7.6               | 0.4                   | 13.2               | 1.1                   | 11.8                                  | A     |
|       | 44                   | 0.2               | -7.7               | 0.4                   | 14.7               | 1.3                   | 11.8                                  | A     |
|       | 44                   | 0                 | -7.8               | 0.5                   | 15.8               | 1.4                   | 11.8                                  | A     |
|       | 44                   | -0.2              | -7.8               | 0.5                   | 15.9               | 1.4                   | 11.8                                  | A     |
|       | 44                   | -0.5              | -7.8               | 0.5                   | 16.0               | 1.4                   | 11.8                                  | A     |
|       | 44                   | -1                | -7.8               | 0.5                   | 16.1               | 1.4                   | 11.8                                  | A     |
|       | 50                   | 1                 | -7.2               | 0.4                   | 12.5               | 1.1                   | 11.8                                  | A     |
| $r_6$ | 50                   | 0.5               | -7.4               | 0.4                   | 14.4               | 1.3                   | 11.8                                  | A     |
|       | 50                   | 0.2               | -7.5               | 0.4                   | 15.8               | 1.4                   | 11.8                                  | A     |
|       | 50                   | 0                 | -7.6               | 0.4                   | 16.9               | 1.5                   | 11.8                                  | A     |
|       | 50                   | -0.2              | -7.6               | 0.4                   | 16.9               | 1.5                   | 11.8                                  | A     |
|       | 50                   | -0.5              | -7.6               | 0.4                   | 17.0               | 1.5                   | 11.8                                  | A     |
|       | 50                   | -1                | -7.6               | 0.4                   | 17.1               | 1.5                   | 11.8                                  | A     |

TABLE D.1. Results for different positions of the effective surrounding charge  $q_s$  varied along six different axes  $r_i$  (see Fig. 3(a)). The central charge  $q_c$  is located at  $(\rho_{q_c}, z_{q_c}) = (0 \text{ nm}, 1 \text{ nm})$  for all cases. The fit quality is given by  $\mu_{\epsilon_{\text{RMS}}}$ , the mean value over all  $\epsilon_{\text{RMS}}$  values from the three evaluated maps.



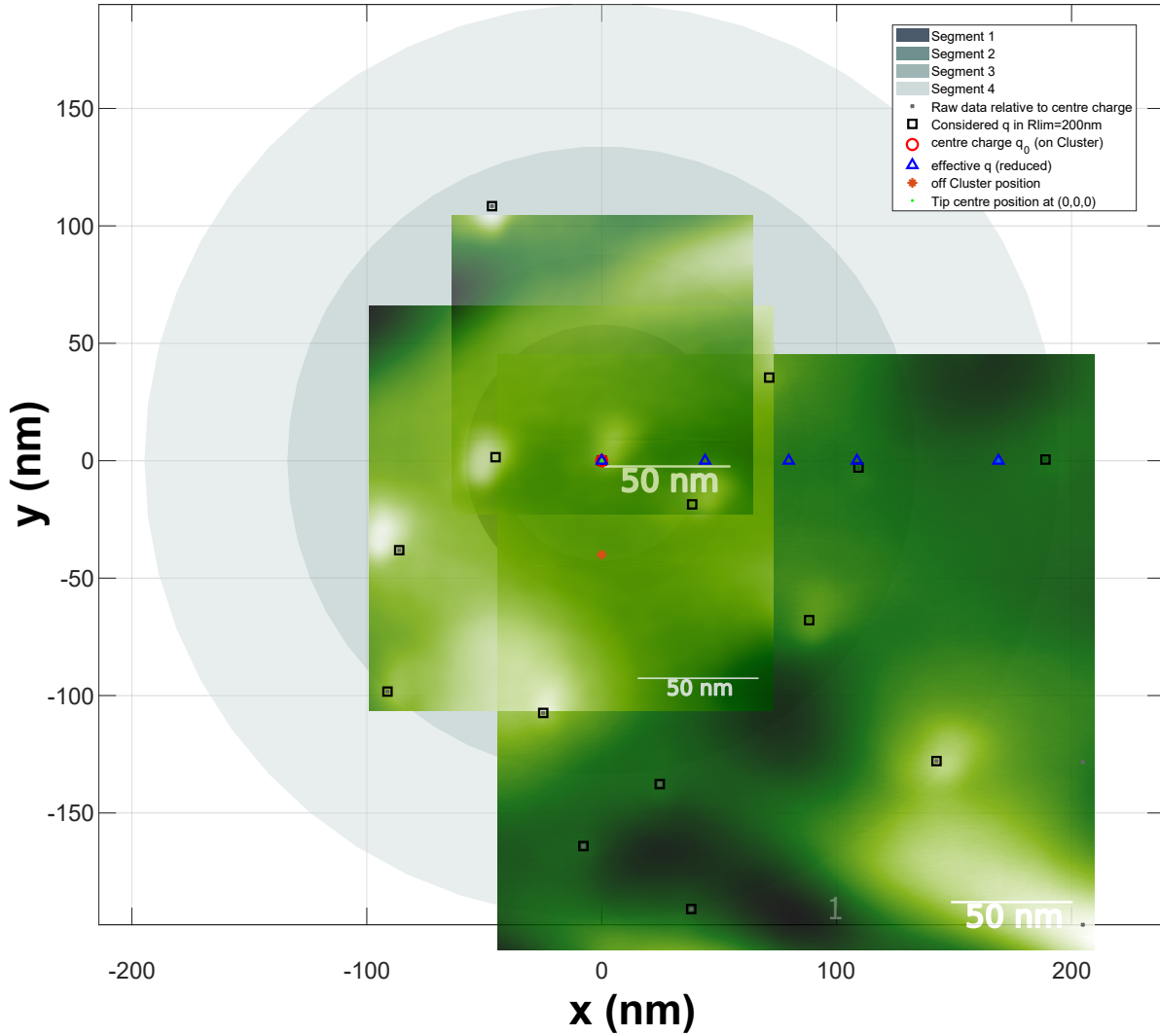


FIG. D.1. Point charge position map (PCPM) describing the position of the central particle (red circle) and position of surrounding particles (black squared) found from evaluating three separate overview images. For finding effective charge positions (blue triangles), four circular segments of increasing width around the investigated central particle are considered (tinted grey circular segments). All particle positions within one segment are averaged giving the position of the effective charge in that segment. The investigated offP position is indicated by a orange star.

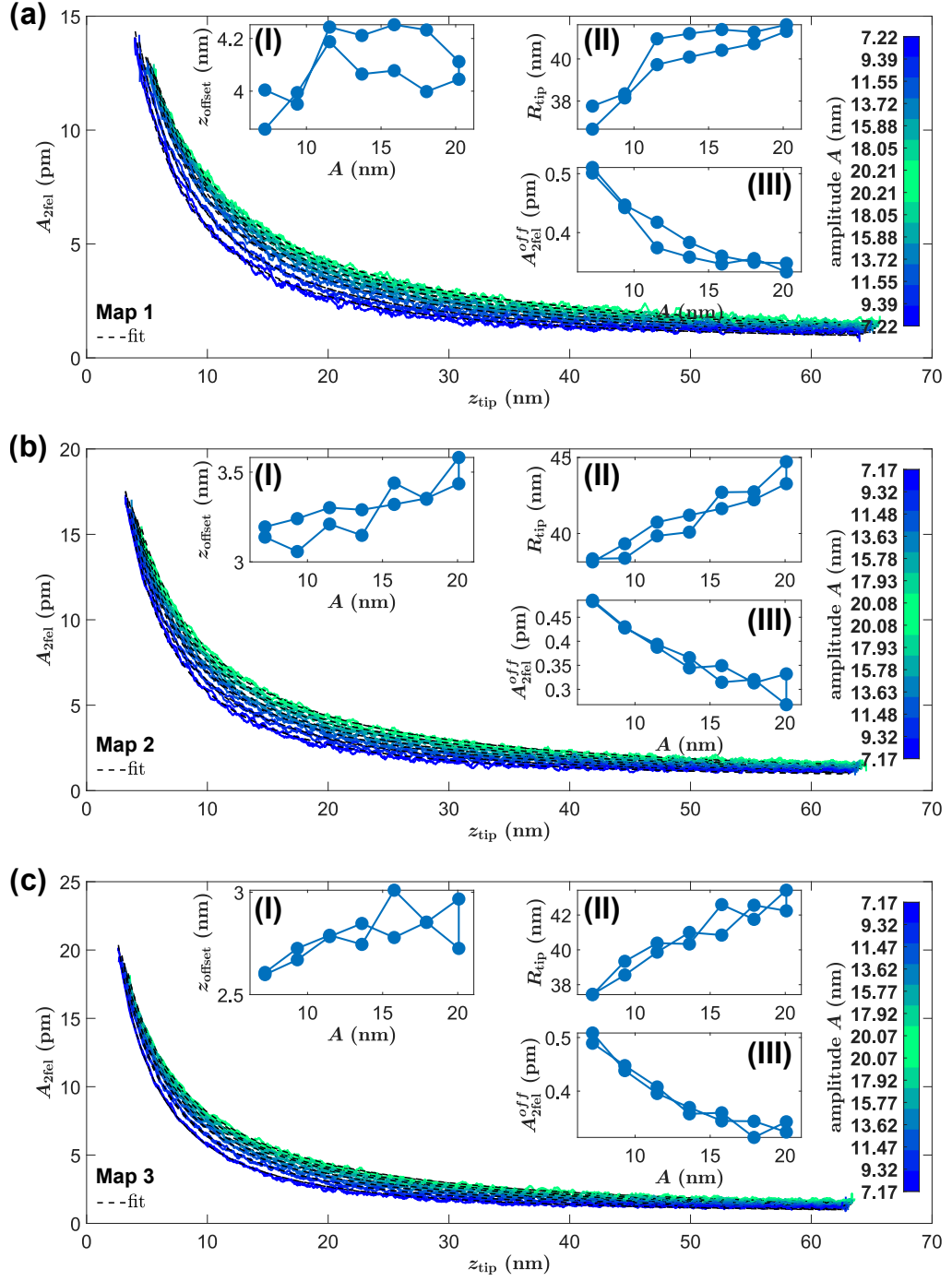


FIG. D.2. Results from fitting the model (Eq. 3) to  $A_{2fel}$  data for all amplitudes and for (a)-(c) maps 1-3 acquired at the **onP** position. The resulting fit parameters are shown as a function of the tip oscillation amplitude in the insets for each data set: (I) offset  $z_{offset}$  between acquisition and model  $z$  axes; (II) tip radius  $R_{tip}$ ; (III)  $A_{2fel}^{offset}$  offset value.

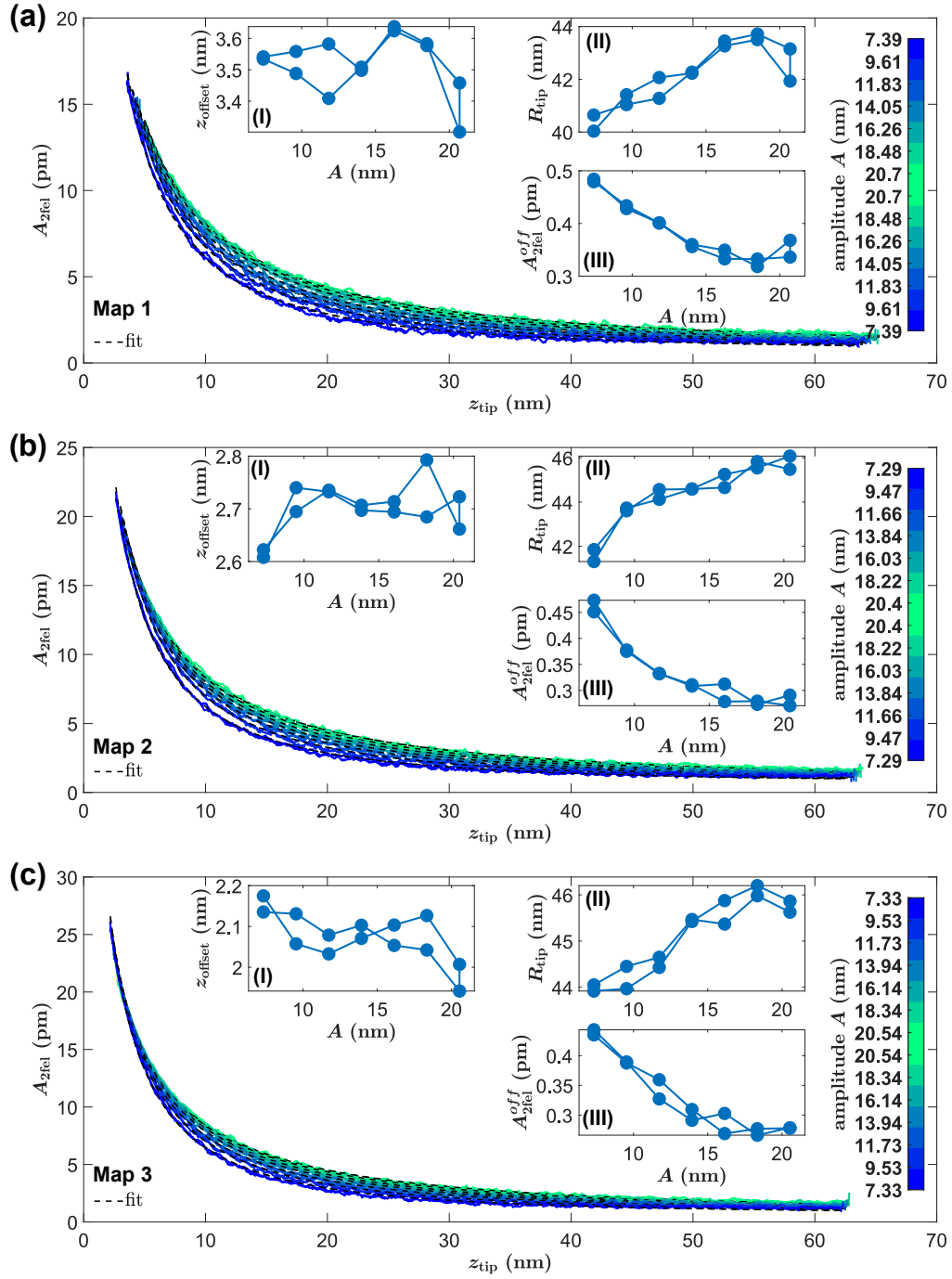


FIG. D.3. Results from fitting the model (Eq. 3) to  $A_{2fel}$  data for all amplitudes and for (a)-(c) maps 1-3 acquired at the **offP** position. The resulting fit parameters are shown as a function of the tip oscillation amplitude in the insets for each data set: (I) offset  $z_{offset}$  between acquisition and model  $z$  axes; (II) tip radius  $R_{tip}$ ; (III)  $A_{2fel}^{offset}$  offset value.

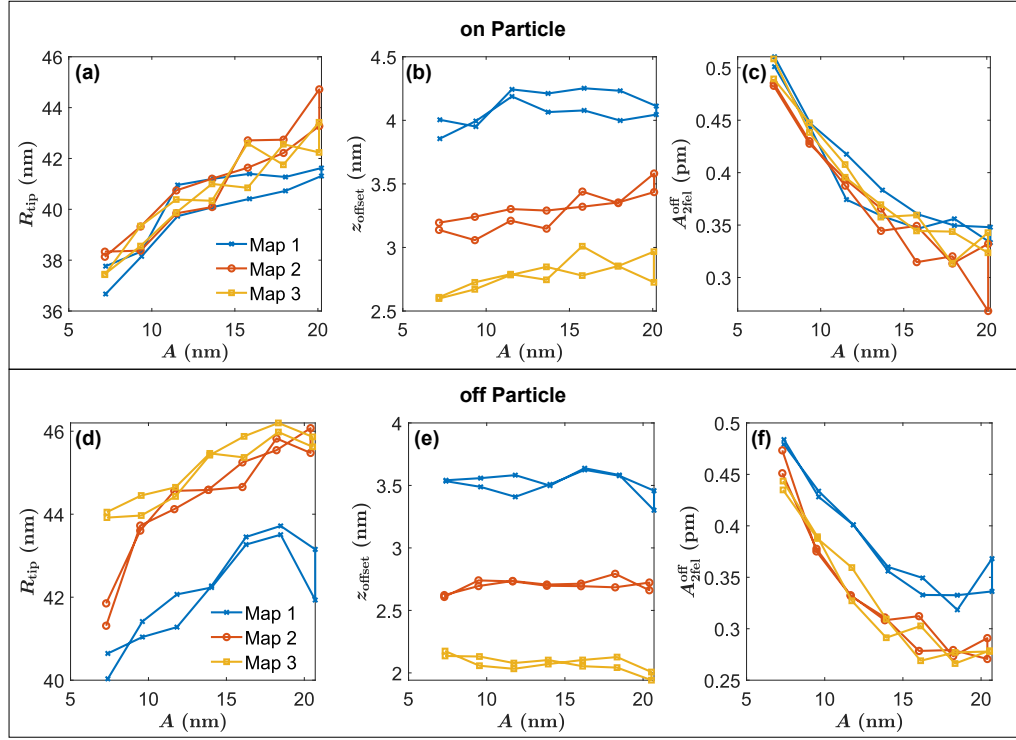


FIG. D.4. Overview for all parameters resulting from fitting  $A_{2fel}$  to the model (Eq. 3) at the onP and offP position. (a)  $R_{tip}$ , (b)  $z_{offset}$ , and (c)  $A_{2fel}^{offset}$  as function of the amplitude  $A$  at the onP position. (d)  $R_{tip}$ , (e)  $z_{offset}$ , and (f)  $A_{2fel}^{offset}$  as function of the amplitude  $A$  at the offP position. Data are acquired with three values for the lower turning point, explaining the systematic shifts in  $z_{offset}$  for the different data sets.

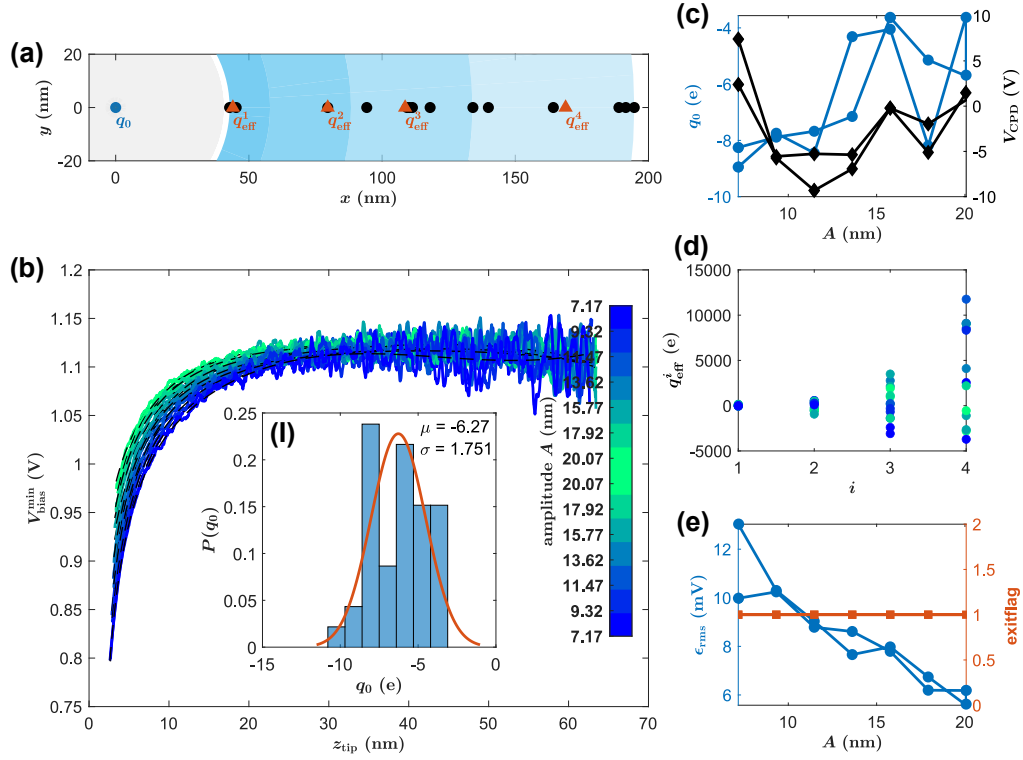


FIG. D.5. Fit to  $V_{\text{bias}}^{\text{min}}$  data taken at the onP position using the model (Eq. 1) with a central charge  $q_0$ , four effective surrounding charges  $q_i^{\text{eff}}$ , and  $V_{\text{CPD}}$  as fit parameters (see also [27]). (a) PCPM with all charge positions projected to the radial axis. (b) Experimental  $V_{\text{bias}}^{\text{min}}(z_{\text{tip}})$  data (blue-green curves) and fit results (black dashed curves) measured at the onP position. Inset (I) shows the result for  $q_0$  when evaluating maps 1-3 with this model. Resulting values for (c)  $q_0$  and  $V_{\text{CPD}}$  as function of amplitude and (d) corresponding results for the effective charges  $q_i^{\text{eff}}$ . (e) Residual error  $\epsilon_{\text{RMS}}$  of each fit. Exitflag=1 denotes a well-converged optimisation.

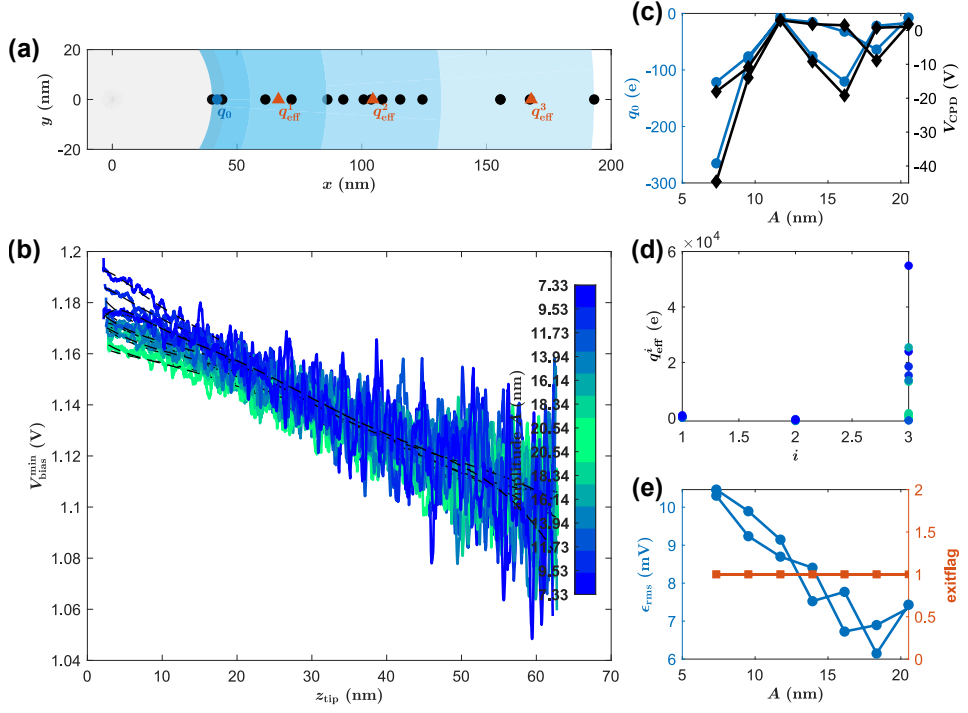


FIG. D.6. Fit to  $V_{\text{bias}}^{\text{min}}$  data taken at the offP position using the model (Eq. 1) with four effective surrounding charges  $q_0$  and  $q_i^{\text{eff}}$ , as well as  $V_{\text{CPD}}$  as fit parameters (see also [27]). (a) PCPM with all charge positions projected to the radial axis. (b) Experimental  $V_{\text{bias}}^{\text{min}}(z_{\text{tip}})$  data (blue-green curves) and fit results (black dashed curves) measured at the offP position. Resulting values for (c) the first effective charge  $q_0$  and  $V_{\text{CPD}}$  as function of amplitude and (d) corresponding results for the effective charges  $q_i^{\text{eff}}$ . (e) Residual error  $\epsilon_{\text{RMS}}$  of each fit. Exitflag=1 denotes a well-converged optimisation.

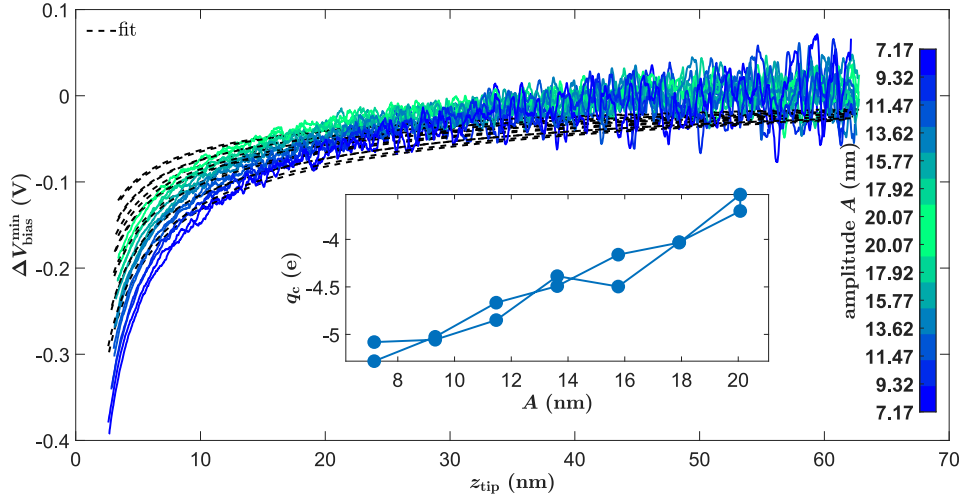


FIG. D.7. Difference approach fits of  $\Delta V_{\text{bias}}^{\text{min}}$  data for all amplitudes of data set 3 including only one central charge  $q_c$  as fit parameter in the model. For the calculations, the charge  $q_c$  is placed at  $(\rho_q, z_q) = (0 \text{ nm}, 1 \text{ nm})$ . The resulting charge value for  $q_c$  for each amplitude is shown in inset (I). A single charge appears to not being sufficient for describing the  $\Delta V_{\text{bias}}^{\text{min}}$  data as no good match between the experimental data and the model could be achieved.

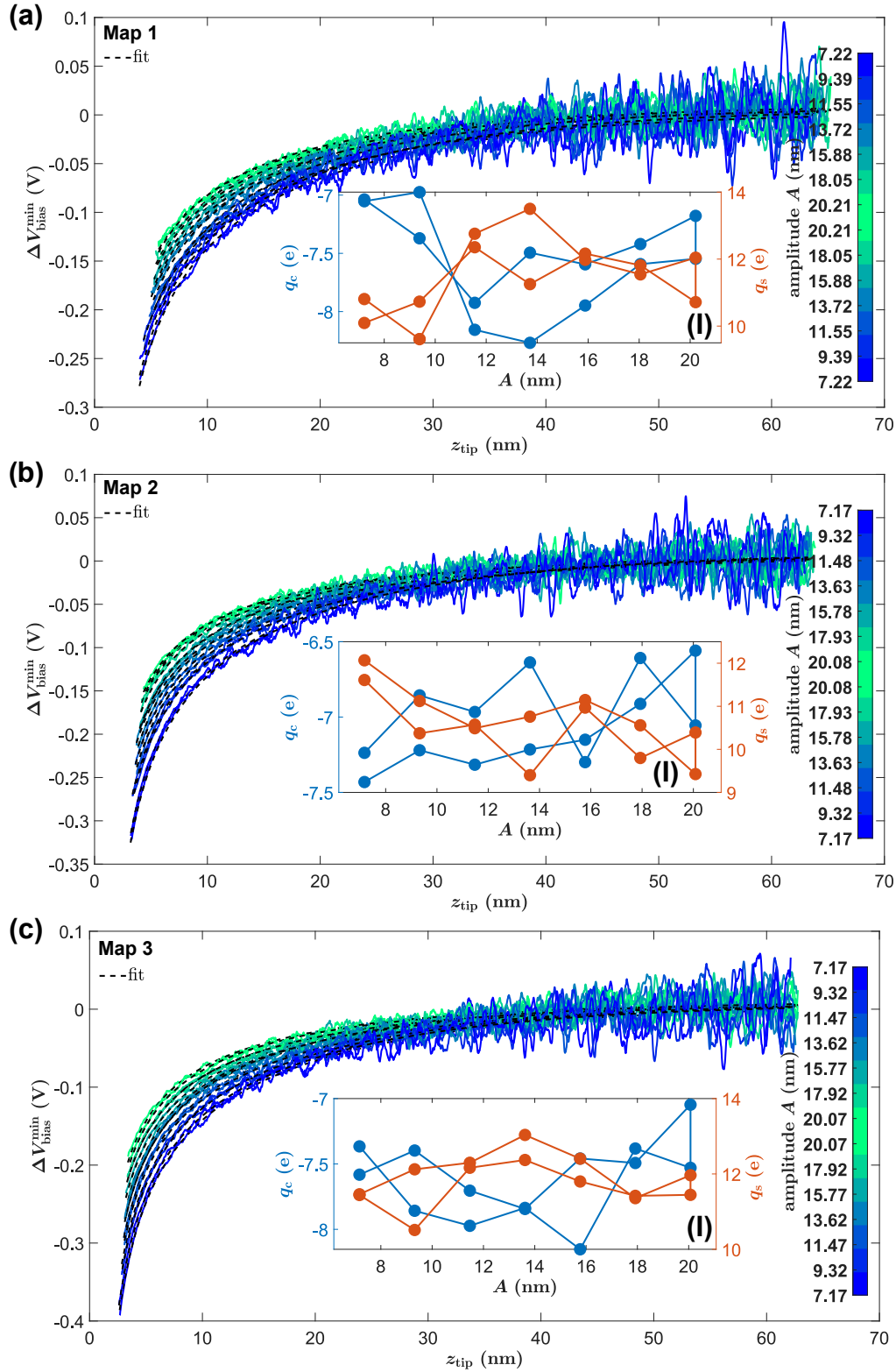


FIG. D.8. Difference approach fits of  $\Delta V_{\text{bias}}^{\text{min}}$  data for all amplitudes and (a)-(c) data sets 1-3 including a central charge  $q_c$  and a surrounding charge  $q_s$  as fit parameters in the model. For the calculations, the charge  $q_c$  is placed at  $(\rho_q, z_q) = (0 \text{ nm}, 1 \text{ nm})$  and the surrounding charge  $q_s$  is placed at  $(\rho_q, z_q) = (44 \text{ nm}, 1 \text{ nm})$ . The resulting charge magnitudes  $q_c$  and  $q_s$  for each amplitude are shown in the inset (I).

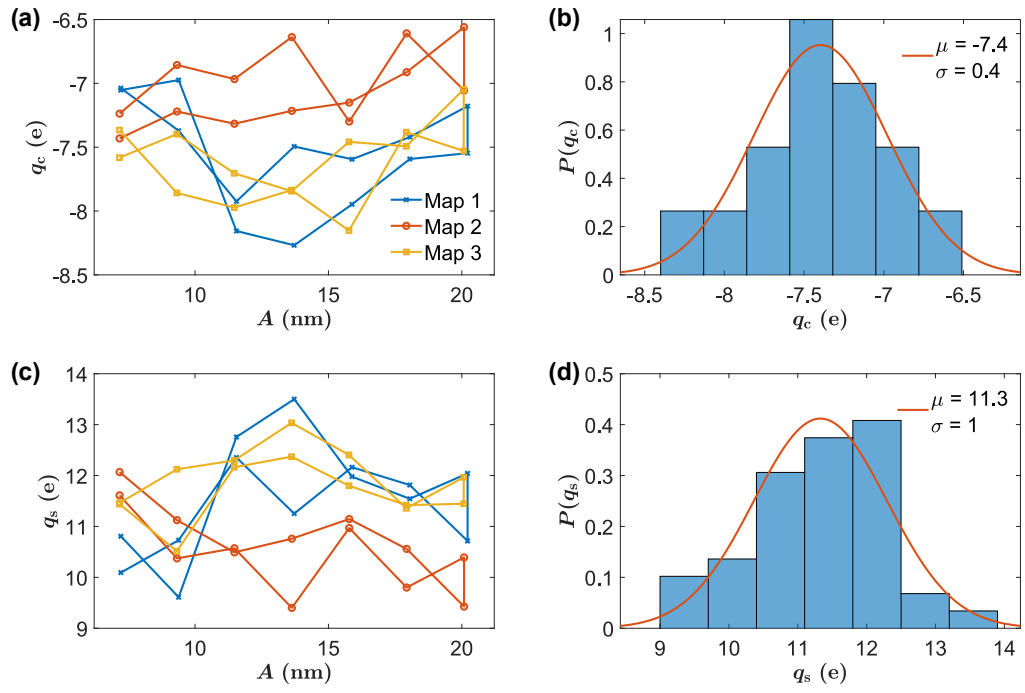


FIG. D.9. Results overview for the centre charge  $q_c$  and surrounding charge  $q_s$  from the difference fit for maps 1-3. (a) The centre charge  $q_c$  as function of amplitude and (b) the normal distribution of resulting values of  $q_c$  over all maps. (c) The centre charge  $q_c$  as function of amplitude and (d) the normal distribution of resulting values of  $q_c$  over all maps. The charge  $q_c$  is placed at  $(\rho_{q_c}, z_{q_c}) = (0 \text{ nm}, 1 \text{ nm})$  and the surrounding charge  $q_s$  is placed at  $(\rho_{q_s}, z_{q_s}) = (44 \text{ nm}, 1 \text{ nm})$  for the calculations.





## 10. Summary

In this thesis, four major results novel to the field of NC-AFM, are introduced. The first development is the FCA method, a procedure facilitating the accurate and precise measurement of force curves, free from experimental artefacts and systematic error. The concept of FCA is the repetitive measurement of the tip-sample interaction with different probe oscillation amplitudes, delivering a data-set, which is robust against disturbing impacts. While a single force curve can be prone to unnoticed systematic error, a match of several individual force curves by an optimisation algorithm enables the self-consistent determination of the error-free tip-sample interaction force. Furthermore, the successful application of the FCA method inherently yields the correct value of the probe oscillation amplitude solving the key challenge of force retrieval from frequency shift data.

Second, the probe tilt with respect to the surface normal, typically given in any NC-AFM setup for technical reasons, is identified as a source of systematic error in the precise measurement of force curves, especially when measuring above nano-objects. Addressing this, the established AFM theory exclusively considering a tip sampling path parallel to the data recording path, is expanded to describe an arbitrary tip oscillation direction with respect to the data recording path. As force inversion algorithms usually assume that tip-sampling path and the data recording path are parallel, it is proposed, to adjust the data recording path to the tip sampling path direction given in experiment for enabling the correct retrieval of the tip-sample interaction.

Third, the formal foundation for CFM is developed based on simulations with different electrostatic models for three tip geometries, namely the S, SC and SCL model. The SCL model evaluated by the CapSol software is found to be best suited for the characterisation of an experimental tip-sample system. Extensive analysis of CFM signal generation for different lateral and vertical charge positions yields distant-dependent CFM data as best suited for charge quantification and show that charges at far distances from the tip contribute to the CFM signal. The radius of the tip sphere, the dielectric permittivity, and the offset of the tip with respect to the surface of the dielectric support are identified as the most crucial parameters for the SCL model. A fit routine based on the CFM theory and SCL model is implemented enabling the precise quantification of the charge centred below the tip

## 10. Summary

and effective surrounding charges as well as the contact potential difference based on distant-dependent CFM data.

Fourth, the FCA method and CFM in combination are employed experimentally on CeO<sub>2</sub> supported Au nano-particles for quantifying their static charge state. Several data sets of distant-dependent  $V_{\text{bias}}^{\text{min}}(z_{\text{tip}})$  data and  $A_{2f_{\text{el}}}(z_{\text{tip}})$  are taken above an Au nano-particle (on particle) and on an empty CeO<sub>2</sub> terrace (off particle). The resulting data sets are evaluated in a two-step procedure for charge quantification. In the first step, the SCL model is fitted to the capacitance signal  $A_{2f_{\text{el}}}(z_{\text{tip}})$  measured at twice the bias modulation frequency  $2f_{\text{el}}$  to experimentally retrieve the actual model parameters characterizing the tip-sample capacitor. In the second step, the CFM fit routine is used to fit the formal description of the CFM signal to the measured  $V_{\text{bias}}^{\text{min}}(z_{\text{ts}})$  data set yielding the charge in the investigated Au-cluster. Noise in the CFM data at large tip-sample distances  $z_{\text{tip}}$  is identified as a source of the significant error in that approach. For an improvement of the precision of the second step, CFM data taken at the off particle position are used to eliminate the contact potential difference and the influence of surrounding charges in the evaluation of the charge of the investigated Au nano-particle. Using the modified CFM fit routine having only two remaining fit parameters, namely the charge in the particle and a effective charge in the near surrounding, yields more precise results.

# 11. Acknowledgements

At this point, I would like to thank all the nice people who supported me on my journey from being a freshman student in physics until finishing my PhD and during the course of this work. Special thanks go to:

- **Prof. Dr. Michael Reichling** for accepting me in his working group for doing my PhD research, his supervision and trust giving me a lot of freedom in my research and for opportunities to present the results on international conferences as well as for all the fruitful discussions.
- **Dr. Philipp Rahe** for answering my many questions, teaching me how to do calculations on the high performance computer (HPC2 and HPC3), creating the CapSol libraries for CFM, and for being a nearly endless source of knowledge and inspiration.
- **Dr. Reinhard Olbrich** for the nice welcome in his lab, teaching me everything I needed to know for working with the NC-AFM, helping me with any technical work and experiment, for tense table football matches, and being an overall great colleague.
- **All above** for helping with the publications and works presented in this thesis.
- **Dr. Clemens Barth** for agreeing to be the second reviewer of this work.
- **Prof. Dr Philipp Maass** and **Dr. Johann Klare** for agreeing to be third and fourth member of the examination committee for this work.

I'm grateful for the nice time at the University Osnabrück, for the things I learned and all the great people I met during that time. Last but not least, I would like to thank my parents for all their support enabling me to study physics in the first place.



# A. Appendix

## A.1. Potential energy within the electric field

In this chapter the derivation steps required to obtain relation (2.3.17) used in [67]. Starting from the fundamental equation [93, 70]

$$U_{\text{el,f}} = \frac{1}{2} \int_V \mathbf{E} \cdot \mathbf{D} \, \text{d}\mathbf{r} \quad (\text{A.1.1})$$

describing the accumulated total energy in the electrostatic field  $\mathbf{E}$  generated by the point charges and metals in the Volume  $V$  in presence of a dielectric medium. For linear and isotropic dielectric media surrounding the conductors, the displacement field is given by  $\mathbf{D} = \epsilon_0 \epsilon_s(\mathbf{r}) \mathbf{E}$ . For simplification it is assumed that the dielectric medium can be described by the macroscopic relative permittivity  $\epsilon_s$ . Hence relation A.1.1 becomes [67]

$$U_{\text{el,f}} = \frac{\epsilon_0 \epsilon_s}{2} \int_V \mathbf{E} \cdot \mathbf{E} \, \text{d}\mathbf{r} \quad (\text{A.1.2})$$

Required for the further derivation is the definition [93]

$$\mathbf{E} = -\nabla \Phi \quad (\text{A.1.3})$$

where  $\Phi$  is the scalar potential in-between the conductors. By inserting this identity into relation (A.1.2) as follows

$$U_{\text{el,f}} = -\frac{\epsilon_0 \epsilon_s}{2} \int_V \mathbf{E} \cdot (\nabla \Phi) \, \text{d}\mathbf{r} \quad (\text{A.1.4})$$

enables the utilisation of the identity [131]

$$\nabla \cdot (\Phi \mathbf{E}) = \Phi \nabla \cdot \mathbf{E} + \mathbf{E} \cdot \nabla \Phi. \quad (\text{A.1.5})$$

By inserting this into (A.1.4) one gains two separate contributions to the electrostatic energy of the field [92]

$$U_{\text{el,f}} = U_{\text{el,f}}^1 + U_{\text{el,f}}^2 \quad (\text{A.1.6})$$

$$= \frac{\epsilon_0 \epsilon_s}{2} \int_V \Phi \nabla \cdot \mathbf{E} \, \text{d}\mathbf{r} - \frac{\epsilon_0 \epsilon_s}{2} \int_V \nabla \cdot (\Phi \mathbf{E}) \, \text{d}\mathbf{r} \quad (\text{A.1.7})$$

## A. Appendix

Where the first term is the energy contribution of the point charges  $U_{\text{el,f}}^1$  and the second term is the energy contribution of the conductors  $U_{\text{el,f}}^2$ . This will become more obvious by further derivations. First, the energy contribution of the point charges  $U_{\text{el,f}}^1$  is brought into a form explicitly containing the charge magnitudes  $q_i$ . In the current equation of the point charge contributions

$$U_{\text{el,f}}^1 = \frac{\epsilon_0 \epsilon_s}{2} \int_V \Phi \nabla \cdot \mathbf{E} \, d\mathbf{r} \quad (\text{A.1.8})$$

the charge magnitudes are only intrinsically given, as the divergence of the electric field is related to the charge distribution  $\rho(\mathbf{r})$  in the volume  $V$  by the differential equation of Gauss's law (first of the Maxwell's equations)

$$\nabla \cdot \mathbf{E} = -\nabla^2 \Phi = \frac{\rho(\mathbf{r})}{\epsilon_0 \epsilon_s} \quad (\text{A.1.9})$$

This relation is also well known as the Poisson equation [93]. Inserting this relation yields

$$U_{\text{el,f}}^1 = \frac{1}{2} \int_V \Phi \rho(\mathbf{r}) \, d\mathbf{r} \quad (\text{A.1.10})$$

According to the considered system, the charge distribution consists of  $N$  point charges  $q_i$  at fixed positions  $\mathbf{r}_i$  in the volume  $V$  in-between the conductors. This discrete distribution can be described by

$$\rho(\mathbf{r}) = \sum_i^N q_i \delta(\mathbf{r} - \mathbf{r}_i) \quad (\text{A.1.11})$$

using the Dirac delta function  $\delta$ . Due to this discrete charge distribution the integral over the volume between the conductors  $V$  containing all  $N$  charges in the system is reduced to

$$U_{\text{el,f}}^1 = \frac{1}{2} \sum_i^N q_i \Phi(\mathbf{r}_i) \quad (\text{A.1.12})$$

After these transformations the contribution of the point charges to the electrostatic energy of the field (first term in equation 2.3.17) explicitly contains the charges  $q_i$ . Now, the second term  $U_{\text{el,f}}^2$  in (A.1.6) describing the contribution of all conductors to the electrostatic energy of the field, given by

$$U_{\text{el,f}}^2 = -\frac{\epsilon_0 \epsilon_s}{2} \int_V \nabla \cdot (\Phi \mathbf{E}) \, d\mathbf{r} \quad (\text{A.1.13})$$

is discussed. In the following, this relation will be brought into a form explicitly containing the potential  $\Phi_m$  and surface charge  $Q_m$  of each conductor. Starting this transformation, Gauss's theorem [131] is applied to the volume integral taken over the divergence of  $\Phi \mathbf{E}$ . As the field inside each conductor is zero, the volume integral can be transformed into a sum of integrals over each conductor surface  $S_m$  [92]

$$U_{\text{el,f}}^2 = \frac{\epsilon_0 \epsilon_s}{2} \sum_m \oint_{S_m} \Phi \mathbf{E} \cdot \mathbf{n} \, ds \quad (\text{A.1.14})$$

where  $\mathbf{n}$  represents the local surface normal vector of the  $m$ -th metal surface. Denoting the potential  $\Phi$  as the constant potential  $\Phi_m$  of the  $m$ -th conductor and inserting the Poisson equation (A.1.3) for the electrostatic field provides

$$U_{\text{el,f}}^2 = -\frac{\epsilon_0\epsilon_s}{2} \sum_m \Phi_m \oint_{S_m} \nabla\Phi \cdot \mathbf{n} \, ds. \quad (\text{A.1.15})$$

The remaining term in the integral can be identified as the normal derivative [94]

$$\nabla\Phi \cdot \mathbf{n} = \frac{\partial\Phi}{\partial n} \quad (\text{A.1.16})$$

leading to

$$U_{\text{el,f}}^2 = -\frac{\epsilon_0\epsilon_s}{2} \sum_m \Phi_m \oint_{S_m} \frac{\partial\Phi}{\partial n} \, ds \quad (\text{A.1.17})$$

The integral taken over the surface of each respective conductor will provide its corresponding surface charge

$$Q_m = -\epsilon_0\epsilon_s \oint_{S_m} \frac{\partial\Phi}{\partial n} \, ds \quad (\text{A.1.18})$$

This finally leads to relation

$$U_{\text{el,f}}^2 = \frac{1}{2} \sum_m Q_m \Phi_m \quad (\text{A.1.19})$$

for the energy contribution of the conductors to the electrostatic field energy explicitly containing the conductor potential  $\Phi_m$  and the conductor surface charge  $Q_m$ . Inserting the transformed terms (A.1.12) and A.1.19 into (A.1.6) provides the relation (2.3.17) for the electrostatic energy of the field used for the further considerations in section 2.3.2.

## A.2. Energy due to the external battery

In order to derive a relation describing the electrostatic force  $F_{\text{el}}$  acting on the tip in the considered system of conductors and point charges with the energy (2.3.17), a movement  $\delta z_{\text{ts}}$  of that tip is considered [92, 67, 70]. For moving the tip in that system the work

$$\delta W = -F_{\text{el}}\delta z_{\text{ts}} \quad (\text{A.2.20})$$

is required. Due to that movement of the tip, the potential  $\Phi(\mathbf{r})$  in the system (2.3.17) will change by  $\delta\Phi(\mathbf{r})$ . Accordingly, the potential of each conductor  $m$



## A. Appendix

would deviate from its fixed value  $\Phi_m$ , which has to be compensated for by a charge flow  $\delta Q_m$  via the external battery. The complete work  $\delta W$  done in the system as consequence of the tip movement consists of the according change of the potential energy of the field (2.3.17)

$$\delta U_{\text{el},f} = \frac{1}{2} \sum_i q_i \delta \phi(\mathbf{r}_i) + \frac{1}{2} (\Phi_1 \delta Q_1 + \Phi_2 \delta Q_2) \quad (\text{A.2.21})$$

and the work  $W_b$  which is done by the battery for the surface charge redistribution ( $\delta Q_1 + \delta Q_2 = 0$ ) between both metals in order to maintain their respective potentials  $\Phi_1$  and  $\Phi_2$ . That work of the battery is given by

$$W_b = \Phi_1 \delta Q_1 + \Phi_2 \delta Q_2 \quad (\text{A.2.22})$$

By understanding the battery as a part of the system, the work carried out by it has to reduce the total potential energy of the system and hence should be taken with a minus sign [67]

$$\delta W = -F_{\text{el}} \delta z_{\text{ts}} = -W_b + \delta U_{\text{el},f} \quad (\text{A.2.23})$$

$$= -(\Phi_1 \delta Q_1 + \Phi_2 \delta Q_2) + \frac{1}{2} \sum_i q_i \delta \phi(\mathbf{r}_i) + \frac{1}{2} (\Phi_1 \delta Q_1 + \Phi_2 \delta Q_2) \quad (\text{A.2.24})$$

$$= \frac{1}{2} \sum_i q_i \delta \phi(\mathbf{r}_i) - \frac{1}{2} (\Phi_1 \delta Q_1 + \Phi_2 \delta Q_2) \quad (\text{A.2.25})$$

$$= \delta U_{\text{el}}^{\text{eff}} \quad (\text{A.2.26})$$

Thus the electrostatic force  $F_{\text{el}}$ , imposed on the tip upon movement, is directly related to the change of the effective energy  $U_{\text{el}}^{\text{eff}}$  as function of the tip position

$$F_{\text{el}} = -\frac{\partial U_{\text{el}}^{\text{eff}}}{\partial z_{\text{ts}}} \quad (\text{A.2.27})$$

Where the effective energy or respectively total potential energy of the system including the batteries is thus given by [67]

$$U_{\text{el}}^{\text{eff}} = \frac{1}{2} \sum_i q_i \phi(\mathbf{r}_i) - \frac{1}{2} (\Phi_1 Q_1 + \Phi_2 Q_2) \quad (\text{A.2.28})$$

In comparison with the potential energy of the field alone (2.3.17), the main difference resulting from the incorporation of the batteries as part of the system, is the minus sign. Kantorovich *et al.* [67] proofs the importance of that difference by showing that relation (2.3.17) does not provide the correct potential energy for a probe point charge far away from the metals, whereas the relation (2.3.19) for the effective energy does. For deriving a valid relation for the electrostatic force imposed on the tip in a system like Figure 2.5 upon movement it thus is crucial to consider the change of the total potential energy including the battery work.

### A.3. S model: Metallic sphere at fixed potential against a dielectric or metallic sample

The electrostatic force (2.3.29) introduced in section (2.3.2) and further used in chapter (7) for deriving the relations describing signals present in CFM requires calculation of the electrostatic potential  $\hat{\Phi}_{\text{void}}$  and capacitance  $C_{\text{void}}$  for the respectively considered tip-sample system. For considering realistic geometries of a metallic tip against a dielectric or conductive sample finite element and finite difference solvers are required [144]. In chapter 8 such realistic tip geometries are considered within the framework of CFM theory using the dedicated CapSol solver [71], where the results are compared to calculations of a metallic sphere at a fixed potential against a dielectric or conductive sample (S model) [145, 96, 70]. Clearly, approximating the tip with a metallic sphere does not hold for accurately calculating the electrostatic forces acting in a realistic tip-sample system. For that solvers as CapSol [71] allowing calculations for more complex tip geometries are much better suited (see chapter 8). However, for exemplifying electrostatic interactions in a tip-sample system the sphere model does hold an practical advantage over the more sophisticated solvers. It is notably less computationally expensive, while still providing exact results and even including dependence on the probe position a comparably simple model considering a parallel-plate capacitor would not hold [70]. For that reason the sphere-sample model, as depicted in Figure A.1, is used in this work for all exemplifications presented in sections 2.3.2. The tip is approximated by an metallic sphere with radius  $r_{\text{sphere}}$ , which surrounded by a medium described by the relative permittivity  $\epsilon_{\text{m}}$  and located at distance  $z_{\text{ts}}$  above a half-space sample characterized by permittivity  $\epsilon_{\text{s}}$ . A single point charge is positioned at  $\mathbf{r} = [0, 0, 0]$  which is located directly below the tip centre on the sample surface  $z_{\text{ts}} = 0$ . Generally, the calculation of  $\hat{\Phi}_{\text{void}}(z_{\text{ts}})$  and  $C_{\text{void}}(z_{\text{ts}})$  is independent of the respectively assumed charge distribution  $q_i$  as they describe the charge-free (void) tip-sample system. Hence, the solution for a metallic sphere against a dielectric or metallic sample suffices to describe the electrostatic force (2.3.29) on the tip for any charge distribution  $q_i$  in the system. For that, the potential  $\hat{\Phi}_{\text{void}}(\mathbf{r}_i)$  from that solution is evaluated at the corresponding charge positions  $\mathbf{r}_i$  as function of  $z_{\text{ts}}$ . The solution for the sphere-dielectric system (or sphere-plate conductor) is based on the infinite charge series model, which will be revisited firmly in the next section following previous works [145, 96, 70].

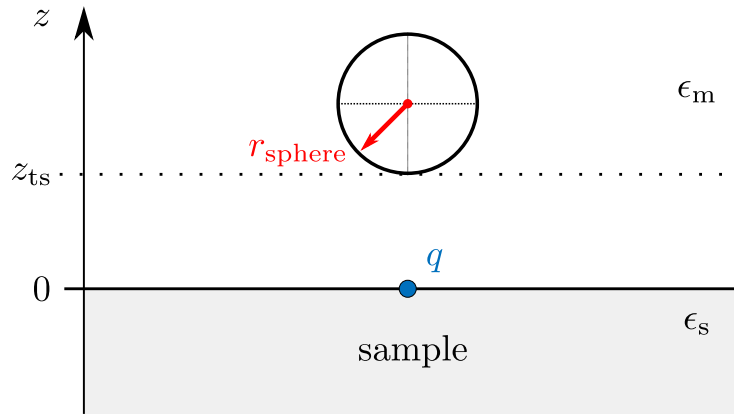


Figure A.1.: Tip-sample capacitor model considering a metallic sphere against a dielectric or metallic half-space sample (sphere-sample system) including a point charge  $q$  at position  $\mathbf{r} = [0, 0, 0]$  located below the spherical tip centre on the sample surface.

### A.3.1. Infinite charge series model

The infinite image charge series method for solving the conductive sphere in front of a metallic or dielectric half-space is based on two well-known textbook concepts, where image charges are used for solving the electrostatic problem: (a) the point charge in front of a dielectric (or metallic) half-space and (b) the point charge in front of a conductive sphere at constant potential. Both concepts are visualised in Figure A.2 and will be introduced first before the full solution is presented.

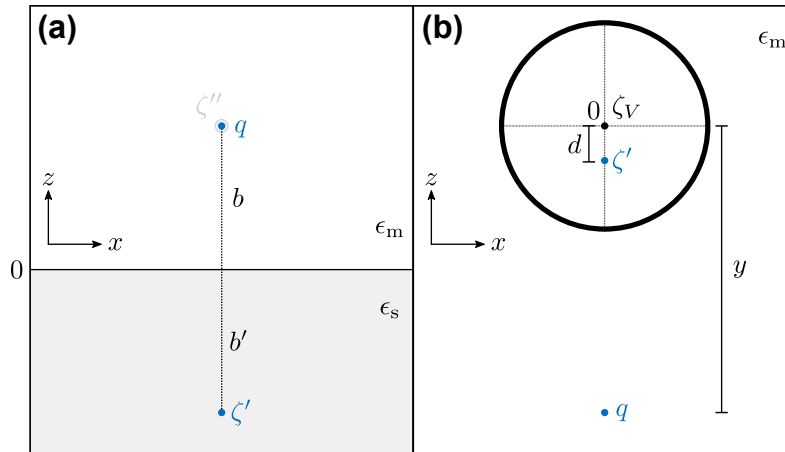


Figure A.2.: Basic concepts for the infinite charge series method. (a) Point charge in front of a dielectric (or metallic) half-space and (b) point charge in front of a conductive sphere at a constant potential  $V$ .

### A.3.1.1. Point charge in front of a dielectric (or metallic) half-space

A point charge  $q$  surrounded by a medium with relative permittivity  $\epsilon_m$  is located at a distance  $b$  above the surface of a half-space medium characterized by the relative permittivity  $\epsilon_s$  as depicted in Figure A.2(a). The interface between both media  $\epsilon_m$  and  $\epsilon_s$  is considered as the zero point  $z = 0$ . For meeting the boundary conditions at the interface, an image charge with magnitude  $\zeta' = \beta q$  is placed at distance  $b' = -b$  from the interface [93, 70]. Thereby the factor  $\beta$  is defined by the dielectric permittivities of both media as

$$\beta = \frac{\epsilon_s - \epsilon_m}{\epsilon_s + \epsilon_m} \quad (\text{A.3.29})$$

Which is  $\beta = 1$  if the point charge is in front of a metal half-space [96]. The potentials of both, point charge  $q$  and its image charge  $\zeta'$ , define the potential in the upper half-space ( $z \geq 0$ ) as

$$\Phi(\mathbf{r}) = \frac{1}{4\pi\epsilon_0\epsilon_m} \left( \frac{q}{\sqrt{x^2 + y^2 + (b - z)^2}} + \frac{-\beta q}{\sqrt{x^2 + y^2 + (b + z)^2}} \right) \quad (\text{A.3.30})$$

To calculate the electrostatic potential in the lower half-space ( $z < 0$ ), it is required to place a different image charge  $\zeta'' = q - \zeta' = q(1 + \beta)$  in the upper half-space at the position of charge  $q$  for accounting for screening due to the induced surface charges at the interface. The potential in the lower half-space ( $z < 0$ ) then reads as

$$\Phi(\mathbf{r}) = \frac{q(1 + \beta)}{\sqrt{x^2 + y^2 + (b - z)^2}} \quad (\text{A.3.31})$$

### A.3.1.2. Point charge in front of a conductive sphere at constant potential

In Figure A.2(b) a point charge  $q$  is placed in front of a conductive sphere at a distance  $y$  from its centre, where both are surrounded by a medium with relative permittivity  $\epsilon_m$ . The sphere of radius  $r_{\text{sphere}}$  is assumed to be at a constant potential  $V$ , which is accounted for by a point charge  $\zeta_V = 4\pi\epsilon_0\epsilon_m r_{\text{sphere}} V$  positioned in the sphere centre. To meet the given boundary conditions at the sphere surface, an image charge  $\zeta'$  of magnitude  $\zeta' = -\frac{r_{\text{sphere}}}{y} q$  has to be placed at distance  $d = \frac{r_{\text{sphere}}^2}{y}$  from the sphere centre in direction of the charge  $q$  [93]. The total electrostatic potential in that system for  $|\mathbf{r}| \geq r_{\text{sphere}}$  then is given by the sum of potentials from each of these three point charges and reads as [70]

$$\Phi(\mathbf{r}) = \frac{1}{4\pi\epsilon_0\epsilon_m} \left( \frac{q}{|\mathbf{r} - \mathbf{y}|} + \frac{-\frac{r_{\text{sphere}}}{y} q}{\left| \mathbf{r} - \frac{r_{\text{sphere}}^2}{y^2} \mathbf{y} \right|} + \frac{4\pi\epsilon_0\epsilon_m r_{\text{sphere}} V}{|\mathbf{r}|} \right) \quad (\text{A.3.32})$$

## A. Appendix

Where the first two terms account for the boundary conditions on the sphere surface due to the there induced charges and the latter term describes the potential  $V$  of the sphere itself. In the case of  $q = 0$  and  $|r| = r_{\text{sphere}}$  the potential  $\Phi(\mathbf{r})$  thus would be equal to  $V$  as assumed above.

### A.3.1.3. Full solution

Both previously presented concepts apply in the method of infinite image charge series for solving the electrostatic problem of a metallic sphere at fixed potential in front of a dielectric or metallic half-space sample as depicted in Figure A.3. The sphere of radius  $r_{\text{sphere}}$  is considered to be at a fixed potential  $V$  and is placed in the upper half-space ( $z \geq 0$ ) where it is surrounded by the medium of relative permittivity  $\epsilon_m$ . Thereby the sphere centre is located at  $z_0 = z_{\text{ts}} + r_{\text{sphere}}$  above the interface  $z = 0$  to the lower half-space ( $z < 0$ ) representing the sample with relative permittivity  $\epsilon_s$ . Hence the metallic back-electrode resides at  $z \rightarrow -\infty$ . As the typical sample thickness is usually much larger compared to the sphere radius  $r_{\text{sphere}}$  and the tip-sample distance, this approximation is in practice usually fulfilled and without loss of generality the potential can be set to ground at that back electrode [70]. For accounting the sphere surface potential  $V$ , a point charge  $\zeta_0 =$

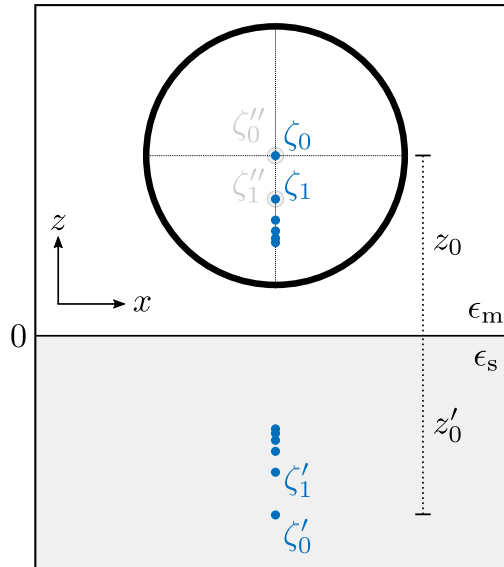


Figure A.3.: Metallic sphere at constant potential in front of a dielectric or conductive sample including positions of the infinite charges series.

$4\pi\epsilon_0\epsilon_m r_{\text{sphere}} V$  is positioned in the sphere centre  $z_0 = z_{\text{ts}} + r_{\text{sphere}}$ . While therewith the boundary conditions at the sphere surface are fulfilled, the boundaries at the

### A.3. S model: Metallic sphere at fixed potential against a dielectric or metallic sample

dielectric interface are not met. This can be corrected by placing an image charge

$$\zeta'_0 = -\beta\zeta_0 \quad \text{at} \quad z'_0 = -z_0 \quad (\text{A.3.33})$$

and the given lateral position  $[x, y]$  of the sphere centre. Thereby, however, the boundary conditions of the sphere are violated by the image charge  $\zeta'_0$  which in return can be corrected by placing another image charge  $\zeta_1$  in the sphere causing the need for another image charge  $\zeta'_1$  in the dielectric half space and so forth. The alternating correction of the two boundary conditions is the general concept of the infinite charge series which fulfils all boundary conditions if proceeded to infinite. The magnitudes  $\zeta_i$  and positions  $z_i$  of the image charges placed inside the sphere are given by the following recursive equations (for  $i > 0$ )

$$z_i = z_0 + \frac{r_{\text{sphere}}^2}{z_0 + z_{i-1}} \quad \text{with} \quad z_0 = R + z_{\text{ts}} \quad (\text{A.3.34})$$

$$\zeta_i = \frac{r_{\text{sphere}}}{z_0 + z_{i-1}} \beta \zeta_{i-1} \quad \text{with} \quad \zeta_0 = 4\pi\epsilon_0\epsilon_m r_{\text{sphere}} V \quad (\text{A.3.35})$$

Which is accompanied by the image charge series  $\{\zeta'_i\}$  in the lower-half space given by

$$z'_i = -z_i \quad (\text{A.3.36})$$

$$\zeta'_i = -\beta\zeta_i \quad (\text{A.3.37})$$

These two image charge series  $\{\zeta_i\}$  and  $\{\zeta'_i\}$  define the electrostatic potential of the upper half-space (above the sample at  $z \geq 0$ ). For describing the electrostatic potential of the lower half-space ( $z < 0$ ) another image charge series  $\{\zeta''_i\}$  is required for correctly considering the screening due to the induced charges at the interface between both half-spaces ( $z = 0$ ) (analogous to consideration in section A.3.1.1). This series is given by

$$z''_i = z_i \quad (\text{A.3.38})$$

$$\zeta''_i = (1 + \beta)\zeta_i \quad (\text{A.3.39})$$

where  $z''_i$  are the  $z$ -positions at which the corresponding image charge  $\zeta''_i$  is placed. Using the three image charge series  $\{\zeta_i\}, \{\zeta'_i\}$  and  $\{\zeta''_i\}$  the electrostatic potential  $\Phi_{\text{void}}(\mathbf{r})$  for both half-spaces can be calculated from the superposition of the respective point charge potentials. The potential in the upper half-space ( $z \geq 0$ ) then is given by

$$\Phi_{\text{void}}(\mathbf{r}) = \frac{1}{4\pi\epsilon_0\epsilon_m} \sum_{i=0}^{\infty} \left[ \frac{\zeta_i}{\sqrt{x^2 + y^2 + (z_i - z)^2}} + \frac{\zeta'_i}{\sqrt{x^2 + y^2 + (z'_i + z)^2}} \right] \quad \text{for } z \geq 0 \quad (\text{A.3.40})$$

and the potential of the lower half-space ( $z < 0$ ) writes as

$$\Phi_{\text{void}}(\mathbf{r}) = \frac{1}{4\pi\epsilon_0\epsilon_s} \sum_{i=0}^{\infty} \frac{\zeta''_i}{\sqrt{x^2 + y^2 + (z''_i - z)^2}} \quad \text{for } z < 0 \quad (\text{A.3.41})$$

## A. Appendix

The corresponding capacitance  $C_{\text{void}}$  of the system is given by the sum over all charges  $\zeta_i$  divided by the tip voltage  $V$  yielding

$$C_{\text{void}} = \frac{1}{V} \sum_{i=0}^{\infty} \zeta_i \quad (\text{A.3.42})$$

The image charge magnitudes in each series converge quickly to zero, which means that in practice a finite number of terms is sufficient for a precise calculation of the electrostatic potential  $\Phi_{\text{void}}$  and capacitance  $C_{\text{void}}$  in the sphere-sample system. Due to the quick convergence of the charge positions it is thus possible, to represent high-index elements by a single charge holding the sum of the remaining image charge series [96, 67, 70].

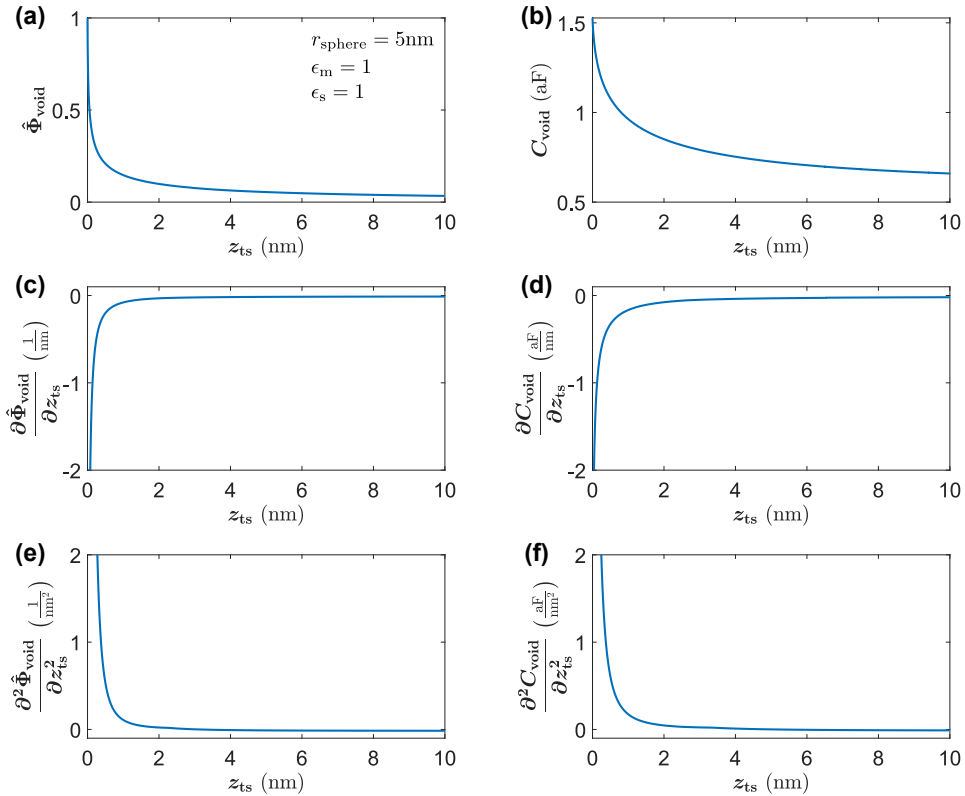


Figure A.4.: Infinite image charge series calculation of the (a) electrostatic potential  $\hat{\Phi}_{\text{void}}$  and (b)  $C_{\text{void}}$ , the first derivatives (c)  $\partial \hat{\Phi}_{\text{void}} / \partial z_{\text{ts}}$  and (d)  $\partial C_{\text{void}} / \partial z_{\text{ts}}$  as well as the second derivatives (e)  $\partial^2 \hat{\Phi}_{\text{void}} / \partial z_{\text{ts}}^2$  and (f)  $\partial^2 C_{\text{void}} / \partial z_{\text{ts}}^2$  as function of  $z_{\text{ts}}$  for the S model as shown in Figure A.1. Parameters used for the calculation are a sphere radius  $r_{\text{sphere}} = 5 \text{ nm}$ , the dielectric permittivities  $\epsilon_{\text{m}} = 1$  (for vacuum) and  $\epsilon_{\text{s}} = 24$  as well as the sphere potential  $V = 1 \text{ V}$ . The potential  $\Phi_{\text{void}}$  is evaluated at the charge position  $\mathbf{r} = [0, 0, 0]$  and the infinite charge series is developed for 300 iterations.

In this work, all infinite charge series calculations of  $\Phi_{\text{void}}$  and  $C_{\text{void}}$  for the sphere-sample system as depicted in Figure A.1 are truncated after 300 image charges and one additional point charge considers the remaining charges of the series. By further forming the normalized potential  $\hat{\Phi}_{\text{void}}$  from  $\Phi_{\text{void}}$  and numerically calculating first and second derivatives of both  $\hat{\Phi}_{\text{void}}$  and  $C_{\text{void}}$  allows the description of the electrostatic force (2.3.29) and its modulated form (7.1.2) for the sphere-sample capacitor. In Figure A.4 the calculated normalized electrostatic potential  $\hat{\Phi}_{\text{void}}$ , the capacitance  $C_{\text{void}}$  and their first as well as second derivatives in respect to  $z_{\text{ts}}$  for a sphere-sample system as shown in Figure A.1 are depicted. Therefore the sphere radius  $r_{\text{sphere}} = 5 \text{ nm}$ , the relative permittivities  $\epsilon_{\text{m}} = 1$  and  $\epsilon_{\text{s}} = 24$  and a sphere potential  $V = 1 \text{ V}$  are assumed. The potential  $\hat{\Phi}_{\text{void}}$  is evaluated at the position  $\mathbf{r} = [0, 0, 0]$  of the point charge  $q$  as depicted in Figure A.1. All exemplifications regarding the electrostatic force (2.3.29) are based on these calculations.

## A.4. Properties of the Fourier transformation

Here the validity of identities (4.2.7) and (4.2.8) are briefly shown. Starting with the derivation of identity (4.2.7) by forming the time dependent derivative of the Fourier transformation (4.2.5) which provides

$$\frac{d}{dt} \mathcal{F}[q(t)](f) = 0 = \frac{1}{\sqrt{2\pi}} \int_{-\infty}^{\infty} \frac{d}{dt} (q(t)e^{-2\pi ift}) dt \quad (\text{A.4.43})$$

$$= \frac{1}{\sqrt{2\pi}} \int_{-\infty}^{\infty} (\dot{q}(t)e^{-2\pi ift} - (2\pi if)q(t)e^{-2\pi ift}) dt \quad (\text{A.4.44})$$

$$= \frac{1}{\sqrt{2\pi}} \int_{-\infty}^{\infty} \dot{q}(t)e^{-2\pi ift} dt - \frac{(2\pi if)}{\sqrt{2\pi}} \int_{-\infty}^{\infty} q(t)e^{-2\pi ift} dt \quad (\text{A.4.45})$$

$$= \mathcal{F}[\dot{q}(t)](f) - (2\pi if)\mathcal{F}[q(t)](f) \quad (\text{A.4.46})$$

As the time derivative of the frequency-dependent Fourier transformation of  $q(t)$  is zero, the identity

$$\mathcal{F}[\dot{q}(t)](f) = (2\pi if)\mathcal{F}[q(t)](f) \quad (\text{A.4.47})$$

as shown in 4.2.7 results. In an analogous manner the second identity (4.2.8) can be derived as follows

$$\frac{d}{dt} \mathcal{F}[\dot{q}(t)](f) = 0 = \frac{1}{\sqrt{2\pi}} \int_{-\infty}^{\infty} \frac{d}{dt} (\dot{q}(t)e^{-2\pi ift}) dt \quad (\text{A.4.48})$$

$$= \frac{1}{\sqrt{2\pi}} \int_{-\infty}^{\infty} (\ddot{q}(t)e^{-2\pi ift} - (2\pi if)\dot{q}(t)e^{-2\pi ift}) dt \quad (\text{A.4.49})$$

$$= \frac{1}{\sqrt{2\pi}} \int_{-\infty}^{\infty} \ddot{q}(t)e^{-2\pi ift} dt - \frac{(2\pi if)}{\sqrt{2\pi}} \int_{-\infty}^{\infty} \dot{q}(t)e^{-2\pi ift} dt \quad (\text{A.4.50})$$

$$= \mathcal{F}[\ddot{q}(t)](f) - (2\pi if)\mathcal{F}[\dot{q}(t)](f) \quad (\text{A.4.51})$$



## A. Appendix

This provides the identity

$$\mathcal{F}[\ddot{q}(t)](f) = (2\pi if)\mathcal{F}[\dot{q}(t)](f) \quad (\text{A.4.52})$$

Via previously derived identity (4.2.7) the Fourier transformation of the second time derivative thus can be linked to the Fourier transformation of  $q(t)$  providing the second identity

$$\mathcal{F}[\ddot{q}(t)](f) = (2\pi if)^2\mathcal{F}[q(t)](f) \quad (\text{A.4.53})$$

as shown in 4.2.8).

## A.5. Decomposition of the tip-sample force in even and odd Fourier coefficients

For the derivation of three fundamental AFM equations (see next section), the properties of  $F_{\text{even}}$  and  $F_{\text{odd}}$  in the Fourier coefficients (4.3.33) and (4.3.34) are utilised. The following identities apply

$$\left\langle F_{\text{even}}(\tilde{z}_{\text{ts}}(t), \dot{\tilde{z}}_{\text{ts}}(t)) \cdot \cos(2\pi n f_{\text{exc}} t + \varphi) \right\rangle_t \neq 0 \quad (\text{A.5.54})$$

$$\left\langle F_{\text{even}}(\tilde{z}_{\text{ts}}(t), \dot{\tilde{z}}_{\text{ts}}(t)) \cdot \sin(2\pi n f_{\text{exc}} t + \varphi) \right\rangle_t = 0 \quad (\text{A.5.55})$$

$$\left\langle F_{\text{odd}}(\tilde{z}_{\text{ts}}(t), \dot{\tilde{z}}_{\text{ts}}(t)) \cdot \cos(2\pi n f_{\text{exc}} t + \varphi) \right\rangle_t = 0 \quad (\text{A.5.56})$$

$$\left\langle F_{\text{odd}}(\tilde{z}_{\text{ts}}(t), \dot{\tilde{z}}_{\text{ts}}(t)) \cdot \sin(2\pi n f_{\text{exc}} t + \varphi) \right\rangle_t \neq 0 \quad (\text{A.5.57})$$

In the scope of the harmonic approximation, the relations for  $\tilde{z}_{\text{ts}}(t)$  and  $\dot{\tilde{z}}_{\text{ts}}(t)$  are given by (4.3.20) and (4.3.21). Thus  $\tilde{z}_{\text{ts}}(t)$  is an even function with respect to  $t$ , while  $\dot{\tilde{z}}_{\text{ts}}(t)$  is an odd function instead. In contrast, as explained in the main script, the even and odd decomposition of the tip-sample force (4.3.24) into  $F_{\text{even}}(\tilde{z}_{\text{ts}}(t), \dot{\tilde{z}}_{\text{ts}}(t))$  and  $F_{\text{odd}}(\tilde{z}_{\text{ts}}(t), \dot{\tilde{z}}_{\text{ts}}(t))$  is with respect to the tip velocity  $\dot{\tilde{z}}_{\text{ts}}(t)$ . Both relations have to be considered to show the validity of these identities. As  $F_{\text{even}}(\tilde{z}_{\text{ts}}(t), \dot{\tilde{z}}_{\text{ts}}(t))$  and  $F_{\text{odd}}(\tilde{z}_{\text{ts}}(t), \dot{\tilde{z}}_{\text{ts}}(t))$  share the same phase with the cosine and sine function, it will be sufficient, to show the validity of these relations for a single case. To simplify the calculation, the phase is chosen to be zero ( $\varphi = 0$ ). The general approach in this proof of validity is splitting of time-dependent average over one cycle into two and calculate via the parities, of those two integrals cancel each other out.

### A.5.1. $F_{\text{even}}(\tilde{z}_{\text{ts}}(t), \dot{\tilde{z}}_{\text{ts}}(t))$ and cosine function

Starting with the first relation (A.5.54), the time-average (4.3.32) in integral form is

$$\left\langle F_{\text{even}}(\tilde{z}_{\text{ts}}(t), \dot{\tilde{z}}_{\text{ts}}(t)) \cdot \cos(2\pi n f_{\text{exc}} t) \right\rangle_t = \int_0^{1/f_{\text{exc}}} F_{\text{even}}(\dot{z}_{\text{ts}}(t)) \cdot \cos(2\pi n f_{\text{exc}} t) dt \quad (\text{A.5.58})$$

where the  $z_{\text{ts}}(t)$  dependency is omitted here for a shorter notation. That integral can be split into two as follows

$$\int_0^{1/f_{\text{exc}}} F_{\text{even}}(\dot{\tilde{z}}_{\text{ts}}(t)) \cdot \cos(2\pi n f_{\text{exc}} t) dt = I_1 + I_2 \quad (\text{A.5.59})$$

where

$$I_1 = \int_0^{1/(2f_{\text{exc}})} F_{\text{even}}(\dot{\tilde{z}}_{\text{ts}}(t)) \cdot \cos(2\pi n f_{\text{exc}} t) dt \quad (\text{A.5.60})$$

$$I_2 = \int_{-1/(2f_{\text{exc}})}^0 F_{\text{even}}(\dot{\tilde{z}}_{\text{ts}}(t)) \cdot \cos(2\pi n f_{\text{exc}} t) dt \quad (\text{A.5.61})$$

As  $F_{\text{even}}(\tilde{z}_{\text{ts}}(t), \dot{\tilde{z}}_{\text{ts}}(t))$  and the cosine function both are periodic with the cycle duration  $T = 1/f_{\text{exc}}$  the limit shift does not change the result, if the difference between upper and lower limit remains equal to the cycle duration. Changing the integration direction of the second integral  $I_2$  by inserting  $-t$  as well as  $-dt$  and accordingly changing the limits yields

$$\begin{aligned} I_2 &= - \int_{1/(2f_{\text{exc}})}^0 F_{\text{even}}(\dot{\tilde{z}}_{\text{ts}}(-t)) \cdot \cos(-2\pi n f_{\text{exc}} t) dt \\ &= - \int_{1/(2f_{\text{exc}})}^0 F_{\text{even}}(-\dot{\tilde{z}}_{\text{ts}}(t)) \cdot \cos(-2\pi n f_{\text{exc}} t) dt \\ &= - \int_{1/(2f_{\text{exc}})}^0 F_{\text{even}}(\dot{\tilde{z}}_{\text{ts}}(t)) \cdot \cos(2\pi n f_{\text{exc}} t) dt \\ &= \int_0^{1/(2f_{\text{exc}})} F_{\text{even}}(\dot{\tilde{z}}_{\text{ts}}(t)) \cdot \cos(2\pi n f_{\text{exc}} t) dt \end{aligned} \quad (\text{A.5.62})$$

Hence  $I_2$  does not cancel out  $I_1$  meaning that the time-average (4.3.32) of the product between  $F_{\text{even}}(\tilde{z}_{\text{ts}}(t), \dot{\tilde{z}}_{\text{ts}}(t))$  and  $\cos(2\pi n f_{\text{exc}} t)$  is unequal to zero.

### A.5.2. $F_{\text{even}}(\tilde{z}_{\text{ts}}(t), \dot{\tilde{z}}_{\text{ts}}(t))$ and sine function

The time-average (A.5.55) can be split into two integrals

$$\int_0^{1/f_{\text{exc}}} F_{\text{even}}(\dot{\tilde{z}}_{\text{ts}}(t)) \cdot \sin(2\pi n f_{\text{exc}} t) dt = I_1 + I_2 \quad (\text{A.5.63})$$

with

$$I_1 = \int_0^{1/(2f_{\text{exc}})} F_{\text{even}}(\dot{\tilde{z}}_{\text{ts}}(t)) \cdot \sin(2\pi n f_{\text{exc}} t) dt \quad (\text{A.5.64})$$

$$I_2 = \int_{-1/(2f_{\text{exc}})}^0 F_{\text{even}}(\dot{\tilde{z}}_{\text{ts}}(t)) \cdot \sin(2\pi n f_{\text{exc}} t) dt \quad (\text{A.5.65})$$

## A. Appendix

As before, changing the integration direction of the second integral  $I_2$  by inserting  $-t$  as well as  $-dt$  and accordingly changing the limits yields

$$\begin{aligned}
I_2 &= - \int_{1/(2f_{\text{exc}})}^0 F_{\text{even}}(\dot{\tilde{z}}_{\text{ts}}(-t)) \cdot \sin(-2\pi n f_{\text{exc}} t) dt \\
&= - \int_{1/(2f_{\text{exc}})}^0 F_{\text{even}}(-\dot{\tilde{z}}_{\text{ts}}(t)) \cdot \sin(-2\pi n f_{\text{exc}} t) dt \\
&= \int_{1/(2f_{\text{exc}})}^0 F_{\text{even}}(\dot{\tilde{z}}_{\text{ts}}(t)) \cdot \sin(2\pi n f_{\text{exc}} t) dt \\
&= - \int_0^{1/(2f_{\text{exc}})} F_{\text{even}}(\dot{\tilde{z}}_{\text{ts}}(t)) \cdot \sin(2\pi n f_{\text{exc}} t) dt \tag{A.5.66}
\end{aligned}$$

Both integrals  $I_1$  and  $I_2$  will equal out, hence the second identity is proven.

### A.5.3. $F_{\text{odd}}(\tilde{z}_{\text{ts}}(t), \dot{\tilde{z}}_{\text{ts}}(t))$ and cosine function

Splitting the time-average (A.5.56) into two integrals yields

$$\int_0^{1/f_{\text{exc}}} F_{\text{odd}}(\dot{\tilde{z}}_{\text{ts}}(t)) \cdot \cos(2\pi n f_{\text{exc}} t) dt = I_1 + I_2 \tag{A.5.67}$$

with

$$I_1 = \int_0^{1/(2f_{\text{exc}})} F_{\text{odd}}(\dot{\tilde{z}}_{\text{ts}}(t)) \cdot \cos(2\pi n f_{\text{exc}} t) dt \tag{A.5.68}$$

$$I_2 = \int_{-1/(2f_{\text{exc}})}^0 F_{\text{odd}}(\dot{\tilde{z}}_{\text{ts}}(t)) \cdot \cos(2\pi n f_{\text{exc}} t) dt \tag{A.5.69}$$

By changing the integrations direction of the second integral  $-dt$ , inserting  $-t$  with changed limits and using the parities of  $F_{\text{odd}}(\tilde{z}_{\text{ts}}(t), \dot{\tilde{z}}_{\text{ts}}(t))$  and  $\cos(2\pi n f_{\text{exc}} t)$  yields

$$\begin{aligned}
I_2 &= - \int_{1/(2f_{\text{exc}})}^0 F_{\text{odd}}(\dot{\tilde{z}}_{\text{ts}}(-t)) \cdot \cos(-2\pi n f_{\text{exc}} t) dt \\
&= - \int_{1/(2f_{\text{exc}})}^0 F_{\text{odd}}(-\dot{\tilde{z}}_{\text{ts}}(t)) \cdot \cos(-2\pi n f_{\text{exc}} t) dt \\
&= \int_{1/(2f_{\text{exc}})}^0 F_{\text{odd}}(\dot{\tilde{z}}_{\text{ts}}(t)) \cdot \cos(2\pi n f_{\text{exc}} t) dt \\
&= - \int_0^{1/(2f_{\text{exc}})} F_{\text{odd}}(\dot{\tilde{z}}_{\text{ts}}(t)) \cdot \cos(2\pi n f_{\text{exc}} t) dt \tag{A.5.70}
\end{aligned}$$

The integrals  $I_1$  and  $I_2$  equal out each other, hence the relation (A.5.56) is valid.

### A.5.4. $F_{\text{odd}}(\tilde{z}_{\text{ts}}(t), \dot{\tilde{z}}_{\text{ts}}(t))$ and sine function

The time-average (A.5.57) split into two integrals is

$$\int_0^{1/f_{\text{exc}}} F_{\text{odd}}(\tilde{z}_{\text{ts}}(t)) \cdot \sin(2\pi n f_{\text{exc}} t) dt = I_1 + I_2 \quad (\text{A.5.71})$$

with

$$I_1 = \int_0^{1/(2f_{\text{exc}})} F_{\text{odd}}(\tilde{z}_{\text{ts}}(t)) \cdot \sin(2\pi n f_{\text{exc}} t) dt \quad (\text{A.5.72})$$

$$I_2 = \int_{-1/(2f_{\text{exc}})}^0 F_{\text{odd}}(\tilde{z}_{\text{ts}}(t)) \cdot \sin(2\pi n f_{\text{exc}} t) dt \quad (\text{A.5.73})$$

Taking  $I_2$  into consideration as before yields

$$\begin{aligned} I_2 &= - \int_{1/(2f_{\text{exc}})}^0 F_{\text{odd}}(\tilde{z}_{\text{ts}}(-t)) \cdot \sin(-2\pi n f_{\text{exc}} t) dt \\ &= - \int_{1/(2f_{\text{exc}})}^0 F_{\text{odd}}(-\tilde{z}_{\text{ts}}(t)) \cdot \sin(-2\pi n f_{\text{exc}} t) dt \\ &= - \int_{1/(2f_{\text{exc}})}^0 F_{\text{odd}}(\tilde{z}_{\text{ts}}(t)) \cdot \sin(2\pi n f_{\text{exc}} t) dt \\ &= \int_0^{1/(2f_{\text{exc}})} F_{\text{odd}}(\tilde{z}_{\text{ts}}(t)) \cdot \sin(2\pi n f_{\text{exc}} t) dt \end{aligned} \quad (\text{A.5.74})$$

Consequently the integrals  $I_1$  and  $I_2$  do not cancel each other out in this case proving relation (A.5.57).

## A.6. Derivation of the three AFM equations

Here the calculations steps for deriving the three AFM equations [44] will be shown and explained step by step.

### A.6.1. Time-averaged form

The three AFM equations in their time-averaged form are derived within the harmonic approximation (see Sec. 4.3.1), where the tip displacement (4.3.19) and excitation (4.3.18) are well known. In the defined time-average (4.3.32) the following

## A. Appendix

identities apply

$$\langle \tilde{q} \rangle_t = q_s \quad (\text{A.6.75})$$

$$\langle \dot{\tilde{q}} \rangle_t = \langle \ddot{\tilde{q}} \rangle_t = \langle \dot{\tilde{q}} \cdot \tilde{q} \rangle_t = \langle \ddot{\tilde{q}} \cdot \dot{\tilde{q}} \rangle_t = \langle \tilde{F}_{\text{exc}} \rangle_t = 0 \quad (\text{A.6.76})$$

$$\langle \tilde{q} \cdot \tilde{q} \rangle_t = q_s^2 + \frac{1}{2}A^2 \quad (\text{A.6.77})$$

$$\langle \tilde{q} \cdot \tilde{F}_{\text{exc}} \rangle_t = \frac{1}{2}AF_0 \cos(\varphi) \quad (\text{A.6.78})$$

$$\langle \dot{\tilde{q}} \cdot \tilde{F}_{\text{exc}} \rangle_t = -\pi f_{\text{exc}}AF_0 \sin(\varphi) \quad (\text{A.6.79})$$

$$\langle \dot{\tilde{q}} \cdot \dot{\tilde{q}} \rangle_t = \frac{1}{2}(2\pi f_{\text{exc}}A)^2 \quad (\text{A.6.80})$$

$$\langle \ddot{\tilde{q}} \cdot \tilde{q} \rangle_t = -\frac{1}{2}(2\pi f_{\text{exc}}A)^2 \quad (\text{A.6.81})$$

where all time-dependencies are omitted for a shorter notation what will be carried on with for the further process of this section. The relations (A.6.75)-(A.6.81) will be used in the now following derivation of the AFM equations in the time-averaged form. Note that these derivations are only valid considering the interaction  $F_{\text{ts}}^z(\tilde{z}_{\text{ts}}(t), \dot{\tilde{z}}_{\text{ts}}(t))$  on the tip path defined by  $\tilde{z}_{\text{ts}}(t)$  and  $\dot{\tilde{z}}_{\text{ts}}(t)$ . For a shorter notation here will be written  $F_{\text{ts}}^z = F_{\text{ts}}^z(\tilde{z}_{\text{ts}}(t), \dot{\tilde{z}}_{\text{ts}}(t))$ ,  $F_{\text{even}} = F_{\text{even}}(\tilde{z}_{\text{ts}}(t), \dot{\tilde{z}}_{\text{ts}}(t))$  and  $F_{\text{odd}} = F_{\text{odd}}(\tilde{z}_{\text{ts}}(t), \dot{\tilde{z}}_{\text{ts}}(t))$  still considering the time-dependent periodic tip-sample interaction on the tip path.

### A.6.1.1. AFM equation 1

The first AFM equation results from the evaluation of  $F_{\text{even}}^{(0)}$  which equals a time-independent constant force offset of the tip-sample interaction  $F_{\text{ts}}^z$ . In the time-average (4.3.32) the tip-sample force is equal to that constant. Note for a clearer notation

$$F_{\text{even}}^{(0)} = \langle F_{\text{even}} \rangle_t = \langle F_{\text{ts}}^z \rangle_t \quad (\text{A.6.82})$$

As a constant function is defined as even, the time-average of the interaction force on the tip path will be equal to the time-average of its even contribution. Inserting the equation of motion (4.3.22) for  $F_{\text{ts}}^z$  yields

$$F_{\text{even}}^{(0)} = \frac{k_0}{(2\pi f_0)^2} \underbrace{\langle \ddot{\tilde{q}} \rangle_t}_{=0} + k_0 \underbrace{\langle \tilde{q} \rangle_t}_{=q_s} + \frac{k_0}{2\pi f_0 Q_0} \underbrace{\langle \dot{\tilde{q}} \rangle_t}_{=0} - \underbrace{\langle \tilde{F}_{\text{exc}} \rangle_t}_{=0} \quad (\text{A.6.83})$$

Due to the harmonic approximation, the displacement  $\tilde{q}$  is equal to relation (4.3.19) and the excitation force is considered as 4.3.18. Consequently, the terms  $\dot{\tilde{q}}$ ,  $\ddot{\tilde{q}}$  and  $\tilde{F}_{\text{exc}}$  become zero in the time-average, as they are simple cosine and sine functions in respect to the time  $t$ . The remaining non-zero term can be found in the time average of  $\tilde{q}$ , because it contains the time-independent static deflection  $q_s$ . Thus relation (A.6.83) simplifies to

$$F_{\text{even}}^{(0)} = k_0 q_s \quad (\text{A.6.84})$$

Considering relations (A.6.82) and (A.6.84) the first AFM equation can be summarized to

$$\boxed{F_{\text{even}}^{(0)} = \langle F_{\text{even}} \rangle_t = \langle F_{\text{ts}}^z \rangle_t = k_0 q_s} \quad (\text{A.6.85})$$

Where the static deflection of the sensor  $q_s$  is the experimental observable of the time-averaged even force  $\langle F_{\text{even}} \rangle_t$  acting upon the tip during movement related via the sensor stiffness  $k_0$ .

### A.6.1.2. AFM equation 2

The second AFM equation is derived by evaluating relation (4.3.33) for  $F_{\text{even}}^{(1)}$  yielding

$$F_{\text{even}}^{(1)} = 2 \langle F_{\text{ts}}^z \cos(2\pi n f_{\text{exc}} t + \varphi) \rangle_t \quad (\text{A.6.86})$$

The cosine function can also expressed as  $1/A(\tilde{q} - q_s)$  providing the relation

$$F_{\text{even}}^{(1)} = \frac{2}{A} \langle F_{\text{ts}}^z \cdot (\tilde{q} - q_s) \rangle_t \quad (\text{A.6.87})$$

Inserting the tip-sample force 4.3.24 leads to

$$F_{\text{even}}^{(1)} = \frac{2}{A} \langle F_{\text{even}} \cdot (\tilde{q} - q_s) \rangle_t + \underbrace{\frac{2}{A} \langle F_{\text{odd}} \cdot (\tilde{q} - q_s) \rangle_t}_{=0} \quad (\text{A.6.88})$$

As the second term is a product of an uneven and even function, its time-average becomes zero. Hence, the  $F_{\text{even}}$  contribution to the tip-sample interaction  $F_{\text{ts}}$  on the tip path remains in the time-average. Inserting the equation of motion 4.3.22 in  $F_{\text{ts}}$  of relation (A.6.87) yields

$$\begin{aligned} \frac{2}{A} \langle F_{\text{ts}}^z \cdot (\tilde{q} - q_s) \rangle_t &= \frac{2k_0}{A(2\pi f_0)^2} \left[ \underbrace{\langle \ddot{\tilde{q}} \cdot \tilde{q} \rangle_t}_{(\text{A.6.81})} - q_s \underbrace{\langle \ddot{\tilde{q}} \rangle_t}_{=0} \right] + \frac{2k_0}{A} \left[ \underbrace{\langle \tilde{q} \cdot \tilde{q} \rangle_t}_{(\text{A.6.77})} - q_s \underbrace{\langle \tilde{q} \rangle_t}_{=q_s} \right] \\ &+ \frac{2k_0}{A2\pi f_0 Q_0} \left[ \underbrace{\langle \dot{\tilde{q}} \cdot \tilde{q} \rangle_t}_{=0} - q_s \underbrace{\langle \dot{\tilde{q}} \rangle_t}_{=0} \right] - \frac{2}{A} \left[ \underbrace{\langle \tilde{F}_{\text{exc}} \cdot \tilde{q} \rangle_t}_{(\text{A.6.78})} - q_s \underbrace{\langle \tilde{F}_{\text{exc}} \rangle_t}_{=0} \right] \end{aligned} \quad (\text{A.6.89})$$

## A. Appendix

where the remaining terms can be collated to the second AFM equation

$$\boxed{F_{\text{even}}^{(1)} = \frac{2}{A} \langle F_{\text{even}} \cdot (\tilde{q} - q_s) \rangle_t = \frac{2}{A} \langle F_{\text{ts}}^z \cdot (\tilde{q} - q_s) \rangle_t = k_0 A \left[ 1 - \frac{f_{\text{exc}}^2}{f_0^2} \right] - F_0 \cos(\varphi)}$$
(A.6.90)

### A.6.1.3. AFM equation 3

The third AFM equation is derived from relation (4.3.34) for  $F_{\text{odd}}^{(1)}$ . Based on the (4.2.16) the Fourier coefficient also can be expressed as

$$F_{\text{odd}}^{(1)} = -\frac{1}{\pi f_{\text{exc}} A} \langle F_{\text{ts}}^z \cdot \dot{\tilde{q}} \rangle_t \quad (\text{A.6.91})$$

inserting the separation (4.3.24) provides

$$F_{\text{odd}}^{(1)} = -\frac{1}{\pi f_{\text{exc}} A} \left[ \underbrace{\langle F_{\text{even}} \cdot \dot{\tilde{q}} \rangle_t}_{=0} + \langle F_{\text{odd}} \cdot \dot{\tilde{q}} \rangle_t \right] \quad (\text{A.6.92})$$

$$(\text{A.6.93})$$

Where the  $F_{\text{even}}$  contribution vanishes in the time-average due to the product with the odd function  $\dot{\tilde{q}}$ . Further, inserting the equation of motion (4.3.22) into (A.6.91) leads to

$$\begin{aligned} -\frac{1}{\pi f_{\text{exc}} A} \langle F_{\text{odd}} \cdot \dot{\tilde{q}} \rangle_t &= -\frac{1}{\pi f_{\text{exc}} A} \left[ \frac{k_0}{(2\pi f_0)^2} \underbrace{\langle \ddot{\tilde{q}} \cdot \dot{\tilde{q}} \rangle_t}_{=0} + k_0 \underbrace{\langle \tilde{q} \cdot \dot{\tilde{q}} \rangle_t}_{=0} \right. \\ &\quad \left. + \frac{k_0}{2\pi f_0 Q_0} \underbrace{\langle \dot{\tilde{q}} \cdot \dot{\tilde{q}} \rangle_t}_{(\text{A.6.80})} - \underbrace{\langle \tilde{F}_{\text{exc}} \cdot \dot{\tilde{q}} \rangle_t}_{(\text{A.6.79})} \right] \end{aligned} \quad (\text{A.6.94})$$

The non-zero time-averages combined with relations (A.6.91) and (A.6.92) provide the third AFM equation as

$$\boxed{F_{\text{odd}}^{(1)} = -\frac{1}{\pi f_{\text{exc}} A} \langle F_{\text{odd}} \cdot \dot{\tilde{q}} \rangle_t = -\frac{1}{\pi f_{\text{exc}} A} \langle F_{\text{ts}}^z \cdot \dot{\tilde{q}} \rangle_t = -\frac{k_0 A}{Q_0} \frac{f_{\text{exc}}}{f_0} - F_0 \sin(\varphi)}$$
(A.6.95)

## A.6.2. Spatial form and derivation of the averaging functions

The projection of the time-averaged form of the three AFM equations to the  $z_{ts}$ -axis yields the cup- and cap-averaging functions as defined in the main script. Here the calculation steps will be carried out for obtaining these averaging functions and with that the final AFM equations.

### A.6.2.1. AFM equation 1

The time-average of the first AFM equation (4.4.35) can be re-parametrised using  $F_{\text{even}}^{\circ}$  as defined in relation (4.5.38), for this the time-average has to be written out again

$$\langle F_{\text{even}}(\tilde{z}_{ts}(t), \dot{\tilde{z}}_{ts}(t)) \rangle_t = f_{\text{exc}} \int_0^{1/f_{\text{exc}}} F_{\text{even}}(\tilde{z}_{ts}(t), \dot{\tilde{z}}_{ts}(t)) dt = k_0 q_s \quad (\text{A.6.96})$$

Considering relation (4.5.38) the function  $F_{\text{even}}^{\circ}(\tilde{z}_{ts}(t))$  can be inserted without changing the result, providing

$$\langle F_{\text{even}}^{\circ}(\tilde{z}_{ts}(t)) \rangle_t = f_{\text{exc}} \int_0^{1/f_{\text{exc}}} F_{\text{even}}^{\circ}(\tilde{z}_{ts}(t)) dt = k_0 q_s \quad (\text{A.6.97})$$

Now the surrounding integral has to be re-parametrised to an integral regarding the  $z$ -direction. Therefore  $\tilde{z}_{ts}(t)$ , which is given within the harmonic approximation by relation (4.3.20), is inserted as the first step into the integral leading to

$$f_{\text{exc}} \int_0^{1/f_{\text{exc}}} F_{\text{even}}^{\circ}(\tilde{z}_{ts}(t)) dt = f_{\text{exc}} \int_0^{1/f_{\text{exc}}} F_{\text{even}}^{\circ}(z_c + A \cos(2\pi f_{\text{exc}} t + \varphi)) dt$$

Substitution with  $\Theta = 2\pi f_{\text{exc}} t + \varphi$  and  $\frac{d\Theta}{dt} = 2\pi f_{\text{exc}}$  yields

$$= \frac{1}{2\pi} \int_{\varphi}^{2\pi+\varphi} F_{\text{even}}^{\circ}(z_c + A \cos(\Theta)) d\Theta$$

As the cosine function  $\cos(\Theta)$  is even and periodic from 0 to  $2\pi$ , the integration limits can be shifted by  $-\varphi$ . Further, the cosine function around  $\Theta = \pi$  is symmetrical, allowing to integrate two times over half the period without changing the result

$$= \frac{1}{\pi} \int_0^{\pi} F_{\text{even}}^{\circ}(z_c + A \cos(\Theta)) d\Theta$$

Substitution with  $z = A \cos(\Theta)$  and  $\frac{d\Theta}{dz} = -\frac{1}{\sqrt{A^2 - z^2}}$  yields

$$= -\frac{1}{\pi} \int_{+A}^{-A} F_{\text{even}}^{\circ}(z_c + z) \frac{1}{\sqrt{A^2 - z^2}} dz$$



## A. Appendix

Exchanging the integration limits and shifting  $1/\pi$  finally yields

$$= \int_{-A}^{+A} F_{\text{even}}^{\circ}(z_c + z) \underbrace{\frac{1}{\pi\sqrt{A^2 - z^2}}}_{=w_{\cup}(z)} dz$$

Using the definition of the cup average (4.5.41) allows thus to write

$$= \langle F_{\text{even}}^{\circ} \rangle_{\cup}(z_c) \quad (\text{A.6.98})$$

Hence from the projection of the time-average from the first AFM equation (4.4.35) to an average along the tip-sampling path parallel to  $z_{\text{ts}}$ , the cup-average definition (4.5.41) intrinsically results. Considering relations (A.6.97) and (A.6.98) the first AFM equation thus becomes

$$\boxed{\langle F_{\text{even}}^{\circ} \rangle_{\cup}(z_c) = k_0 q_s}. \quad (\text{A.6.99})$$

as it is shown in the main manuscript at (4.5.45). Due to the dependency of  $z_c$  on  $z_p$  which directly can be controlled in experiment now the cup-average of the tip-sample force  $\langle F_{\text{even}}^{\circ} \rangle_{\cup}$  directly can be adjusted.

### A.6.2.2. AFM equation 2

The second AFM equation (4.4.36) with written out time-average reads as

$$f_{\text{exc}} \int_0^{1/f_{\text{exc}}} F_{\text{even}}(\tilde{z}_{\text{ts}}(t), \dot{\tilde{z}}_{\text{ts}}(t)) \cdot (\tilde{q}(t) - q_s) dt = \frac{k_0 A^2}{2} \left[ 1 - \frac{f_{\text{exc}}^2}{f_0^2} \right] - \frac{F_0 A}{2} \cos(\varphi) \quad (\text{A.6.100})$$

Inserting the even force along the tip-sampling path (4.5.38) this relation becomes

$$f_{\text{exc}} \int_0^{1/f_{\text{exc}}} F_{\text{even}}^{\circ}(\tilde{z}_{\text{ts}}(t)) \cdot (\tilde{q}(t) - q_s) dt = \frac{k_0 A^2}{2} \left[ 1 - \frac{f_{\text{exc}}^2}{f_0^2} \right] - \frac{F_0 A}{2} \cos(\varphi) \quad (\text{A.6.101})$$

In the harmonic approximation,  $\tilde{z}_{\text{ts}}(t)$  and  $\tilde{q}(t)$  are given by relations (4.3.20) and (4.3.19). Inserting these into the integral and substituting with  $\Theta = 2\pi f_{\text{exc}} t + \varphi$  and  $\frac{d\Theta}{dt} = 2\pi f_{\text{exc}}$  yields

$$f_{\text{exc}} \int_0^{1/f_{\text{exc}}} F_{\text{even}}^{\circ}(\tilde{z}_{\text{ts}}(t)) \cdot (\tilde{q}(t) - q_s) dt = \frac{1}{2\pi} \int_{\varphi}^{2\pi+\varphi} F_{\text{even}}^{\circ}(z_c + A \cos(\Theta)) A \cos(\Theta) d\Theta$$

As in the derivation of the first AFM equation, the integration limits can be shifted by  $-\varphi$ . By using the symmetry of the cosine function around  $\Theta = \pi$ , the integration can be carried out two times from  $[0, \pi]$  without changing the result

$$= \frac{1}{\pi} \int_0^{\pi} F_{\text{even}}^{\circ}(z_c + A \cos(\Theta)) A \cos(\Theta) d\Theta$$

### A.6. Derivation of the three AFM equations

Substitution with  $z = A \cos(\Theta)$  and  $\frac{d\Theta}{dz} = -\frac{1}{\sqrt{A^2 - z^2}}$  leads to

$$= \frac{1}{\pi} \int_{+A}^{-A} F_{\text{even}}^{\circ}(z_c + z) \frac{-z}{\sqrt{A^2 - z^2}} dz$$

Further exchanging the integration limits provides

$$= -\frac{1}{\pi} \int_{-A}^{+A} \underbrace{F_{\text{even}}^{\circ}(z_c + z)}_f \underbrace{\frac{-z}{\sqrt{A^2 - z^2}}}_{g'} dz$$

Using the partial integration  $\int_a^b f \cdot g' = [f \cdot g]_a^b - \int_a^b f' \cdot g$  considering  $f' = \frac{dF_{\text{even}}^{\circ}(z_c + z)}{dz}$  and  $g = \sqrt{A^2 - z^2}$  it can be derived

$$= \frac{1}{\pi} \int_{-A}^{+A} \frac{dF_{\text{even}}^{\circ}(z_c + z)}{dz} \sqrt{A^2 - z^2} dz$$

By defining the force gradient along the tip sampling path as the derivation of the even force along the sampling direction  $k_{\text{ts}}^{\circ}(z_c + z) = \frac{dF_{\text{even}}^{\circ}(z_c + z)}{dz}$  it can be written

$$= \frac{1}{\pi} \int_{-A}^{+A} k_{\text{ts}}^{\circ}(z_c + z) \sqrt{(A^2 - z^2)} dz$$

The final step is moving  $\frac{1}{\pi}$  and expanding the equation by  $\frac{2A^2}{2A^2}$  for norming the weighting function to 1, which yields

$$= \frac{A^2}{2} \int_{-A}^{+A} k_{\text{ts}}^{\circ}(z_c + z) \underbrace{\frac{2}{\pi A^2} \sqrt{(A^2 - z^2)}}_{=w_{\cap}(z)} dz$$

Here, the definition of the cap average (4.5.43) can be applied providing

$$= \frac{A^2}{2} \langle k_{\text{ts}}^{\circ} \rangle_{\cap}(z_c) \quad (\text{A.6.102})$$

The projection of the time-averaged AFM equation (4.4.36) to the tip sampling path along parallel to  $z_{\text{ts}}$  yields intrinsically the definition of the cap-average (4.5.43). Considering (A.6.101) and (A.6.101) the second AFM equation in spatial form can finally be written as

$$\boxed{\langle k_{\text{ts}}^{\circ} \rangle_{\cap}(z_c) = k_0 \left[ 1 - \frac{f_{\text{exc}}^2}{f_0^2} \right] - \frac{F_0}{A} \cos(\varphi)} \quad (\text{A.6.103})$$

### A.6.2.3. AFM equation 3

The third AFM equation (4.4.37) with written out time-average reads as

$$f_{\text{exc}} \int_0^{1/f_{\text{exc}}} F_{\text{odd}}(\tilde{z}_{\text{ts}}(t), \dot{\tilde{z}}_{\text{ts}}(t)) \cdot \dot{q}(t) dt = \frac{\pi k_0 A^2 f_{\text{exc}}^2}{Q_0 f_0} + \pi f_{\text{exc}} A F_0 \sin(\varphi) \quad (\text{A.6.104})$$

Here the odd parity of  $F_{\text{odd}}$  in respect to  $\dot{\tilde{z}}_{\text{ts}}$  provides a challenge, since the direct parametrisation as in relation (4.5.38) is here not possible. This challenge can be addressed by the definitions (4.5.39) containing the even damping function  $\gamma_{\text{ts}}^\circ$  further defined as (4.5.40) along the tip sampling path parallel to  $z_{\text{ts}}$ . Inserting relation (4.5.39) with (4.5.40) allows the expression of the third time-averaged AFM equation (A.6.104) as

$$-f_{\text{exc}} \int_0^{1/f_{\text{exc}}} \gamma_{\text{ts}}^\circ(\tilde{z}_{\text{ts}}(t)) \cdot \dot{q}(t)^2 dt = \frac{\pi k_0 A^2 f_{\text{exc}}^2}{Q_0 f_0} + \pi f_{\text{exc}} A F_0 \sin(\varphi) \quad (\text{A.6.105})$$

Within the harmonic approximation  $\tilde{z}_{\text{ts}}(t)$  and  $\dot{q}(t)$  are well known by relations (4.3.20) and (4.3.19). Inserting both into the integral of the previous equation yields

$$= -f_{\text{exc}} \int_0^{1/f_{\text{exc}}} \gamma_{\text{ts}}^\circ(z_c + A \cos(2\pi f_{\text{exc}} t + \varphi)) \cdot (-2\pi f_{\text{exc}} A \sin(2\pi f_{\text{exc}} t + \varphi))^2 dt$$

Substitution with  $\Theta = 2\pi f_{\text{exc}} t + \varphi$  and  $\frac{d\Theta}{dt} = 2\pi f_{\text{exc}}$  yields

$$= -2\pi f_{\text{exc}}^2 \int_\varphi^{2\pi+\varphi} \gamma_{\text{ts}}^\circ(z_c + A \cos(\Theta)) \cdot (A \sin(\Theta))^2 d\Theta$$

As all contained functions are periodic in the interval  $[0, 2\pi]$  and have the same phase  $\varphi$ , the integration limit can be shifted by  $-\varphi$ .

$$= -2\pi f_{\text{exc}}^2 \int_0^{2\pi} \gamma_{\text{ts}}^\circ(z_c + A \cos(\Theta)) \cdot (A \sin(\Theta))^2 d\Theta$$

Both functions  $\cos(\Theta)$  and  $\sin(\Theta)^2$  are even and symmetric around  $\Theta = \pi$ . Hence twice the integral over half the period  $[0, \pi]$  is equal to the integral over the full period  $[0, 2\pi]$ . Thus, it can be written

$$= -4\pi f_{\text{exc}}^2 \int_0^\pi \gamma_{\text{ts}}^\circ(z_c + A \cos(\Theta)) \cdot (A \sin(\Theta))^2 d\Theta$$

Substitution with  $z = A \cos(\Theta)$  and  $\frac{d\Theta}{dz} = -\frac{1}{\sqrt{A^2 - z^2}}$  and using the identity  $\sin(\Theta)^2 = 1 - \cos(\Theta)^2$  leads to

$$= 4\pi f_{\text{exc}}^2 \int_{+A}^{-A} \gamma_{\text{ts}}^\circ(z_c + z) \cdot \frac{A^2 - z^2}{\sqrt{A^2 - z^2}} dz$$

Exchanging the integration limits and transformation of the fraction further yields

$$= -4\pi f_{\text{exc}}^2 \int_{-A}^{+A} \gamma_{\text{ts}}^{\circ}(z_c + z) \cdot \sqrt{A^2 - z^2} dz$$

By expanding with  $\frac{\pi A^2}{\pi A^2}$  the cap averaging function  $w_{\cap}$  is obtained

$$= -2\pi^2 f_{\text{exc}}^2 A^2 \int_{-A}^{+A} \gamma_{\text{ts}}^{\circ}(z_c + z) \cdot \underbrace{\frac{2}{\pi A^2} \sqrt{A^2 - z^2}}_{=w_{\cap}} dz$$

Applying the definition of the cap average (4.5.43) finally yields the relation

$$= -\frac{1}{2}(2\pi f_{\text{exc}} A)^2 \langle \gamma_{\text{ts}}^{\circ} \rangle_{\cap}(z_c) \quad (\text{A.6.106})$$

The equality of relations (A.6.105) and (A.6.106) leads to the third AFM equation as

$$\boxed{\langle \gamma_{\text{ts}}^{\circ} \rangle_{\cap}(z_c) = -\frac{k_0}{2\pi f_0 Q_0} - \frac{F_0}{2\pi f_{\text{exc}} A} \sin(\varphi)} \quad (\text{A.6.107})$$

## A.7. AFM equations as solution for the equation of motion

In this section the validity of the AFM equations as solution for the equation of motion (4.3.22) describing the tip oscillation in interaction with the sample is demonstrated. Based on the AFM equations (4.5.45)-(4.5.47) the Fourier series describing the tip-sample force (4.3.27) approximated up to  $n = 1$ . The corresponding Fourier coefficients then are given by (consider derivations and boxed relations in Appendix A.6)

$$F_{\text{even}}^{(0)} = \langle F_{\text{even}}^{\circ} \rangle_{\cup}(z_c) \quad (\text{A.7.108})$$

$$F_{\text{even}}^{(1)} = A \langle k_{\text{ts}}^{\circ} \rangle_{\cap}(z_c) \quad (\text{A.7.109})$$

$$F_{\text{odd}}^{(1)} = 2\pi f_{\text{exc}} A \langle \gamma_{\text{ts}}^{\circ} \rangle_{\cap}(z_c) \quad (\text{A.7.110})$$

By further expressing the cosine and sine functions via  $\tilde{q}(t)$  given by (4.3.19) the tip-sample force (4.3.27) in first order can be written as

$$F_{\text{ts}}^z(z_c) \approx \langle F_{\text{even}}^{\circ} \rangle_{\cup}(z_c) + \langle k_{\text{ts}}^{\circ} \rangle_{\cap}(z_c) \cdot (\tilde{q}(t) - q_s) - \langle \gamma_{\text{ts}}^{\circ} \rangle_{\cap}(z_c) \dot{\tilde{q}}(t) \quad (\text{A.7.111})$$

Inserting that approximate relation into the equation of motion (4.3.22) and redistribution of the terms yields

$$\begin{aligned} \frac{k_0}{(2\pi f_0)^2} \ddot{\tilde{q}}(t) + [k_0 - \langle k_{\text{ts}}^{\circ} \rangle_{\cap}(z_c)] \tilde{q}(t) + \left[ \frac{k_0}{2\pi f_0 Q_0} + \langle \gamma_{\text{ts}}^{\circ} \rangle_{\cap}(z_c) \right] \dot{\tilde{q}}(t) \\ = [\langle F_{\text{even}}^{\circ} \rangle_{\cup}(z_c) - \langle k_{\text{ts}}^{\circ} \rangle_{\cap}(z_c) q_s] + \tilde{F}_{\text{exc}}(t) \end{aligned} \quad (\text{A.7.112})$$

## A. Appendix

Considering the terms

$$k' = k_0 - \langle k_{ts}^{\circ} \rangle_{\cap}(z_c) \quad (\text{A.7.113})$$

$$\gamma' = \frac{k_0}{2\pi f_0 Q_0} + \langle \gamma_{ts}^{\circ} \rangle_{\cap}(z_c) \quad (\text{A.7.114})$$

$$F'_s = \langle F_{\text{even}}^{\circ} \rangle_{\cup}(z_c) - \langle k_{ts}^{\circ} \rangle_{\cap}(z_c) q_s \quad (\text{A.7.115})$$

as effective spring constant  $k'$ , effective damping  $\gamma'$  and effective constant force  $F'_s$  the relation (A.7.112) thus can be abbreviated to

$$\frac{k_0}{(2\pi f_0)^2} \ddot{q}(t) + k' \tilde{q}(t) + \gamma' \dot{\tilde{q}}(t) = F'_s + \tilde{F}_{\text{exc}}(t) \quad (\text{A.7.116})$$

Hence it has an analogous form as the relation of a driven, damped harmonic oscillator as equation (4.2.4) treated in Sec 4.2. Accordingly, it is possible to apply the Fourier transformation ansatz (4.2.5) with the identities (4.2.7) and (4.2.8) yielding

$$\mathcal{F}[\tilde{q}(t)] = G'_{\text{ho}}(f_{\text{exc}}) \mathcal{F}[F'_s + \tilde{F}_{\text{exc}}(t)] \quad (\text{A.7.117})$$

with

$$G'_{\text{ho}}(f_{\text{exc}}) = \frac{1}{\left(k' - k_0 \frac{f_{\text{exc}}^2}{f_0^2}\right) + 2\pi i f_{\text{exc}} \gamma'} \quad (\text{A.7.118})$$

Here the  $G'_{\text{ho}}$  is the amplitude transfer function of the harmonic oscillator in interaction where the prime indicates its dependency  $k'$ , and  $\gamma'$  which are given at the current distance  $z_c$  between tip and sample during interaction. Correspondingly the phase of the driven tip oscillation in the sample force field is described by

$$\varphi'_{\text{ho}}(f_{\text{exc}}) = \begin{cases} \arctan\left(\frac{-2\pi f_{\text{exc}} \gamma'}{k' - k_0 \left(\frac{f_{\text{exc}}}{f_0}\right)^2}\right) & \text{for } k_0 \left(\frac{f_{\text{exc}}}{f_0}\right)^2 < k' \\ -\frac{\pi}{2} & \text{for } k_0 \left(\frac{f_{\text{exc}}}{f_0}\right)^2 = k' \\ \arctan\left(\frac{-2\pi f_{\text{exc}} \gamma'}{k' - k_0 \left(\frac{f_{\text{exc}}}{f_0}\right)^2}\right) - \pi & \text{for } k_0 \left(\frac{f_{\text{exc}}}{f_0}\right)^2 > k' \end{cases} \quad (\text{A.7.119})$$

which is in analogy to the arctan2 definition (4.2.12) provided in section (4.2) for the unperturbed harmonic oscillator but now dependent on the effective parameters

$k'$  and  $\gamma'$  due to the interaction with the sample force field. In conclusion, the AFM equations (4.5.45)-(4.5.47) solve the equation of motion (4.3.22). Within the harmonic approximations the tip oscillation in the sample force field is lead back by the AFM equations to a free oscillation of the tip with an effective stiffness  $k'$ , damping  $\gamma'$  and force constant  $F'_s$ . This exactly equals the assumption, that the tip-sample force is a small perturbation on the free harmonic tip motion, which was made at the start of all shown derivations (see Sec. 4.3.1).

## A.8. Common assumptions for the AFM equations in FM NC-AFM

Commonly used assumptions and approximations in FM NC-AFM data evaluation are a stiff force sensor  $q_s = 0$ , an ideal PLL with  $\varphi = -\frac{\pi}{2}$  and small frequency shifts in respect to the sensor eigenfrequency  $\Delta f = f_{\text{exc}} - f_0 \ll f_0$ .

The first approximation addresses the fact, that the static deflection of the sensor  $q_s$  generally lies below the detectability limits and thus is difficult to obtain experimentally. Hence, the first AFM equation (4.5.45) rarely can be evaluated for obtaining the tip-sample force  $F_{\text{even}}^\circ$ .

The second assumption is an ideal PLL optimally maintaining the phase resonance at  $\varphi = -\frac{\pi}{2}$  for any  $z_c$ . This allows to simplify the second (4.5.46) and third AFM equation (4.5.47) to

$$\langle k_{\text{ts}}^\circ \rangle_{\cap}(z_c) = k_0 \left[ 1 - \frac{f_{\text{exc}}^2}{f_0^2} \right] \quad (\text{A.8.120})$$

$$\langle \gamma_{\text{ts}}^\circ \rangle_{\cap}(z_c) = \frac{k_0}{2\pi f_0 Q_0} \left[ \frac{F_0 f_0 Q_0}{k_0 f_{\text{exc}} A} - 1 \right] \quad (\text{A.8.121})$$

When evaluating experimental data, the simplified equations can be used, if there is no significant changes in phase signal  $\varphi$  output by the PLL are given in the data. If changes care observed, the full AFM equations (4.5.46) and (4.5.47) have to be used instead for a correct evaluation.

By further assuming small frequency shifts in respect to the eigenfrequency  $\Delta f = f_{\text{exc}} - f_0 \ll f_0$  additional to an ideal PLL, the right side of the simplified second AFM equation (A.8.120) ia developed in a first order Taylor series around  $f_0$

## A. Appendix

yielding

$$\begin{aligned}
 f'(x) &\approx f'(f_0) + f'(x_0)(f_{\text{exc}} - f_0) + \mathcal{O}(2) \\
 &= 1 - \frac{f_0^2}{f_0^2} - \frac{2f_0}{f_0^2}(f_{\text{exc}} - f_0) + \mathcal{O}(2) \\
 &= -\frac{2}{f_0} \underbrace{(f_{\text{exc}} - f_0)}_{=\Delta f} + \mathcal{O}(2)
 \end{aligned} \tag{A.8.122}$$

Considering the Taylor series as the new right side of the simplified AFM equation (A.8.120) provides the common approximation [80]

$$\langle k_{\text{ts}}^{\circ} \rangle_{\cap}(z_c) \approx -\frac{2k_0}{f_0} \Delta f + \mathcal{O}(2) \tag{A.8.123}$$

Within this approximation, the frequency shift  $\Delta f$  is a direct measure for the averaged tip-sample force gradient  $\langle k_{\text{ts}}^{\circ} \rangle_{\cap}(z_c)$  at the current distance  $z_c$ . However, for obtaining the tip-sample force curve from  $\Delta f(z_c)$  data the inversion algorithms still have to be applied on  $\langle k_{\text{ts}}^{\circ} \rangle_{\cap}(z_c)$  (see section 4.6).

# Bibliography

- [1] L. Kantorovich. *Quantum Theory of the Solid State: An Introduction*. Springer Netherlands, 2004. ISBN: 978-1-4020-2153-4. DOI: 10.1007/978-1-4020-2154-1.
- [2] J. N. Israelachvili. *Intermolecular and Surface Forces (Third Edition)*. Elsevier, 2011, p. iii. DOI: 10.1016/B978-0-12-375182-9.10025-9.
- [3] L. Liu et al. “Subfemtonewton Force Spectroscopy at the Thermal Limit in Liquids”. In: *Physical Review Letters* 116.22 (June 2016), p. 228001. DOI: 10.1103/PhysRevLett.116.228001.
- [4] V. Blūms et al. “A single-atom 3D sub-attonewton force sensor”. In: *Science Advances* 4.3 (Mar. 2018). DOI: 10.1126/sciadv.aao4453.
- [5] H. J. Mamin and D. Rugar. “Sub-attonewton force detection at millikelvin temperatures”. In: *Applied Physics Letters* 79.20 (Nov. 2001), pp. 3358–3360. DOI: 10.1063/1.1418256.
- [6] Y. Sugimoto et al. “Chemical identification of individual surface atoms by atomic force microscopy”. In: *Nature* 446.7131 (Mar. 2007), pp. 64–67. DOI: 10.1038/nature05530.
- [7] H. F. Wen et al. “Contrast inversion of O adatom on rutile TiO<sub>2</sub>(110)-(1×1) surface by atomic force microscopy imaging”. In: *Applied Surface Science* 505 (Mar. 2020), p. 144623. DOI: 10.1016/j.apsusc.2019.144623.
- [8] A. M. Sweetman et al. “Mapping the force field of a hydrogen-bonded assembly”. In: *Nature Communications* 5.1 (May 2014). DOI: 10.1038/Ncomms4931.
- [9] P. Jelínek. “High resolution SPM imaging of organic molecules with functionalized tips”. In: *Journal of Physics: Condensed Matter* 29.34 (July 2017), p. 343002. DOI: 10.1088/1361-648X/aa76c7.
- [10] H. Mönig et al. “Quantitative assessment of intermolecular interactions by atomic force microscopy imaging using copper oxide tips”. In: *Nature Nanotechnology* 13.5 (Apr. 2018), pp. 371–375. DOI: 10.1038/s41565-018-0104-4.



## Bibliography

- [11] L. Costa et al. “Imaging material properties of biological samples with a force feedback microscope”. In: *Journal of Molecular Recognition* 26.12 (Nov. 2013), pp. 689–693. DOI: 10.1002/jmr.2328.
- [12] S. Senapati et al. “Differentiating between Inactive and Active States of Rhodopsin by Atomic Force Microscopy in Native Membranes”. In: *Anal. Chem.* 91.11 (May 2019), pp. 7226–7235. DOI: 10.1021/acs.analchem.9b00546.
- [13] F. S. Ruggeri et al. “Atomic force microscopy for single molecule characterization of protein aggregation”. In: *Archives of Biochemistry and Biophysics* 664 (Mar. 2019), pp. 134–148. DOI: 10.1016/j.abb.2019.02.001.
- [14] E. T. Herruzo et al. “Three-dimensional quantitative force maps in liquid with 10 piconewton, angstrom and sub-minute resolutions”. In: *Nanoscale* 5.7 (Nov. 2013), pp. 2678–2685. DOI: 10.1039/c2nr33051b.
- [15] E. I. Altman, M. Z. Baykara, and U. D. Schwarz. “Noncontact Atomic Force Microscopy: An Emerging Tool for Fundamental Catalysis Research”. In: *Accounts of Chemical Research* 48.9 (Aug. 2015), pp. 2640–2648. DOI: 10.1021/acs.accounts.5b00166.
- [16] A. Sweetman et al. “Visualizing the orientational dependence of an intermolecular potential”. In: *Nature Communications* 7.1 (Feb. 2016), p. 10621. DOI: 10.1038/ncomms10621.
- [17] D. Martin-Jimenez and R. Garcia. “Identification of Single Adsorbed Cations on Mica–Liquid Interfaces by 3D Force Microscopy”. In: *The Journal of Physical Chemistry Letters* 8.23 (Nov. 2017), pp. 5707–5711. DOI: 10.1021/acs.jpcllett.7b02671.
- [18] J. Laurent et al. “Casimir force measurements in Au–Au and Au–Si cavities at low temperature”. In: *Physical Review B* 85.3 (Jan. 2012), p. 035426. DOI: 10.1103/PhysRevB.85.035426.
- [19] E. Voloshina and Y. Dedkov. “Atomic force spectroscopy and density-functional study of graphene corrugation on Ru(0001)”. In: *Physical Review B* 93.23 (June 2016), p. 235418. DOI: 10.1103/PhysRevB.93.235418.
- [20] L. Andres Jurado et al. “Effect of the environmental humidity on the bulk, interfacial and nanoconfined properties of an ionic liquid”. In: *Physical Chemistry Chemical Physics* 18.32 (July 2016), pp. 22719–22730. DOI: 10.1039/c6cp03777a.
- [21] L. Rickard Dickinson et al. “Atomic Force Spectroscopy Using Colloidal Tips Functionalized with Dried Crude Oil: A Versatile Tool to Investigate Oil–Mineral Interactions”. In: *Energy & Fuels* 30.11 (Oct. 2016), pp. 9193–9202. DOI: 10.1021/acs.energyfuels.6b01862.

- [22] P. M. Claesson et al. “From force curves to surface nanomechanical properties”. In: *Phys. Chem. Chem. Phys.* 19.35 (May 2017), pp. 23642–23657. DOI: 10.1039/C7CP02612A.
- [23] R. Pawlak et al. “Quantitative determination of atomic buckling of silicene by atomic force microscopy”. In: *Proceedings of the National Academy of Sciences* 117.1 (Dec. 2019), pp. 228–237. DOI: 10.1073/pnas.1913489117.
- [24] C. Chiutu et al. “Precise Orientation of a Single C<sub>60</sub> Molecule on the Tip of a Scanning Probe Microscope”. In: *Physical Review Letters* 108.26 (June 2012), p. 268302. DOI: 10.1103/PhysRevLett.108.268302.
- [25] M. S. Rodrigues et al. “Why do atomic force microscopy force curves still exhibit *jump to contact*?” In: *Applied Physics Letters* 101.20 (Nov. 2012), p. 203105. DOI: 10.1063/1.4766172.
- [26] A. Calò et al. “Capillary and van der Waals interactions on CaF<sub>2</sub> crystals from amplitude modulation AFM force reconstruction profiles under ambient conditions”. In: *Beilstein Journal of Nanotechnology* 6 (Mar. 2015), pp. 809–819. DOI: 10.3762/bjnano.6.84.
- [27] S. Kawai et al. “Van der Waals interactions and the limits of isolated atom models at interfaces”. In: *Nature Communications* 7.1 (May 2016). DOI: 10.1038/ncomms11559.
- [28] M. J. Shon, S.-H. Rah, and T.-Y. Yoon. “Submicrometer elasticity of double-stranded DNA revealed by precision force-extension measurements with magnetic tweezers”. In: *Science Advances* 5.6 (June 2019). DOI: 10.1126/sciadv.aav1697.
- [29] T. Fukuma et al. “Mechanism of atomic force microscopy imaging of three-dimensional hydration structures at a solid-liquid interface”. In: *Physical Review B* 92.15 (Oct. 2015), p. 155412. DOI: 10.1103/PhysRevB.92.155412.
- [30] H. Söngen et al. “Resolving Point Defects in the Hydration Structure of Calcite (10.4) with Three-Dimensional Atomic Force Microscopy”. In: *Physical Review Letters* 120.11 (Mar. 2018), p. 116101. DOI: 10.1103/PhysRevLett.120.116101.
- [31] H. Söngen et al. “Hydration layers at the graphite-water interface: Attraction or confinement”. In: *Physical Review B* 100.20 (Nov. 2019), p. 205410. DOI: 10.1103/PhysRevB.100.205410.
- [32] B. Reischl et al. “Atomistic Simulation of Atomic Force Microscopy Imaging of Hydration Layers on Calcite, Dolomite, and Magnesite Surfaces”. In: *The Journal of Physical Chemistry C* 123.24 (May 2019), pp. 14985–14992. DOI: 10.1021/acs.jpcc.9b00939.
- [33] A. Sweetman et al. “Measuring the reactivity of a silicon-terminated probe”. In: *Physical Review B* 94.11 (Sept. 2016), p. 115440. DOI: 10.1103/PhysRevB.94.115440.

## Bibliography

- [34] J. Onoda et al. “Electronegativity determination of individual surface atoms by atomic force microscopy”. In: *Nature Communications* 8.1 (Apr. 2017), p. 15155. DOI: 10.1038/ncomms15155.
- [35] J. N. Ladenthin et al. “Force-induced tautomerization in a single molecule”. In: *Nature Chemistry* 8.10 (July 2016), pp. 935–940. DOI: 10.1038/NCHEM.2552.
- [36] S. Garcia-Manyes and A. E. M. Beedle. “Steering chemical reactions with force”. In: *Nature Reviews Chemistry* 1.11 (Nov. 2017). DOI: 10.1038/s41570-017-0083.
- [37] A. Sweetman, I. Lekkas, and P. Moriarty. “Mechano-chemical manipulation of Sn chains on Si(100) by NC-AFM”. In: *Journal of Physics: Condensed Matter* 29.7 (Dec. 2016), p. 074003. DOI: 10.1088/1361-648X/29/7/074003.
- [38] C. Wagner et al. “Scanning Quantum Dot Microscopy”. In: *Physical Review Letters* 115.2 (July 2015), p. 026101. DOI: 10.1103/PhysRevLett.115.026101.
- [39] D. Rugar et al. “Single spin detection by magnetic resonance force microscopy”. In: *Nature* 430.6997 (July 2004), pp. 329–332. DOI: 10.1038/nature02658.
- [40] L. Thiel et al. “Probing magnetism in 2D materials at the nanoscale with single-spin microscopy”. In: *Science* 364.6444 (June 2019), pp. 973–976. DOI: 10.1126/science.aav6926.
- [41] B. Voigtländer. *Scanning Probe Microscopy*. Springer Berlin Heidelberg, 2015. ISBN: 978-3-662-45240-0. DOI: 10.1007/978-3-662-45240-0.
- [42] Z. Sun et al. “Quantitative Atomic Force Microscopy with Carbon Monoxide Terminated Tips”. In: *Physical Review Letters* 106.4 (Jan. 2011), p. 046104. DOI: 10.1103/PhysRevLett.106.046104.
- [43] C. Barth et al. “Recent Trends in Surface Characterization and Chemistry with High-Resolution Scanning Force Methods”. In: *Advanced Materials* 23.4 (Nov. 2010), pp. 477–501. DOI: 10.1002/adma.201002270.
- [44] H. Söngen, R. Bechstein, and A. Kühnle. “Quantitative atomic force microscopy”. In: *Journal of Physics: Condensed Matter* 29.27 (June 2017), p. 274001. DOI: 10.1088/1361-648X/aa6f8b.
- [45] M. Guggisberg et al. “Separation of interactions by noncontact force microscopy”. In: *Physical Review B* 61.16 (Apr. 2000), p. 11151.
- [46] F. J. Giessibl. “A direct method to calculate tip–sample forces from frequency shifts in frequency-modulation atomic force microscopy”. In: *Applied Physics Letters* 78.1 (Jan. 2001), pp. 123–125. DOI: 10.1063/1.1335546.

- [47] J. E. Sader and S. P. Jarvis. “Accurate formulas for interaction force and energy in frequency modulation force spectroscopy”. In: *Applied Physics Letters* 84.10 (Mar. 2004), pp. 1801–1803. DOI: 10.1063/1.1667267.
- [48] J. E. Sader et al. “Interatomic force laws that evade dynamic measurement”. In: *Nature Nanotechnology* 13.12 (Dec. 2018), pp. 1088–1091. DOI: 10.1038/s41565-018-0277-x.
- [49] J. Welker, E. Illek, and F. J. Giessibl. “Analysis of force-deconvolution methods in frequency-modulation atomic force microscopy”. In: *Beilstein Journal of Nanotechnology* 3 (Mar. 2012), pp. 238–248. DOI: doi:10.3762/bjnano.3.27.
- [50] J. Lübke et al. “Noise in NC-AFM measurements with significant tip–sample interaction”. In: *Beilstein Journal of Nanotechnology* 7 (Dec. 2016), pp. 1885–1904. DOI: 10.3762/bjnano.7.181.
- [51] M. Abe et al. “Atom tracking for reproducible force spectroscopy at room temperature with non-contact atomic force microscopy”. In: *Nanotechnology* 16.12 (Oct. 2005), pp. 3029–3034. DOI: 10.1088/0957-4484/16/12/050.
- [52] P. Rahe et al. “Flexible drift-compensation system for precise 3D force mapping in severe drift environments”. In: *Review of Scientific Instruments* 82.6 (June 2011), p. 063704. DOI: 10.1063/1.3600453.
- [53] D. Heile et al. “Alignment method for the accurate and precise quantification of tip-surface forces”. In: *Physical Review B* 103.7 (Feb. 2021), p. 075409. DOI: 10.1103/PhysRevB.103.075409.
- [54] L.-O. Heim, M. Kappl, and H.-J. Butt. “Tilt of Atomic Force Microscope Cantilevers: Effect on Spring Constant and Adhesion Measurements”. In: *Langmuir* 20.7 (Feb. 2004), pp. 2760–2764. DOI: 10.1021/la036128m.
- [55] J. L. Hutter. “Comment on Tilt of Atomic Force Microscope Cantilevers: Effect on Spring Constant and Adhesion Measurements”. In: *Langmuir* 21.6 (Feb. 2005), pp. 2630–2632. DOI: 10.1021/la047670t.
- [56] R. S. Gates. “Experimental confirmation of the atomic force microscope cantilever stiffness tilt correction”. In: *Review of Scientific Instruments* 88.12 (Dec. 2017), p. 123710. DOI: 10.1063/1.4986201.
- [57] C. Wang et al. “Cantilever Tilt Causing Amplitude Related Convolution in Dynamic Mode Atomic Force Microscopy”. In: *Analytical Sciences* 27.2 (Feb. 2011), pp. 143–147. DOI: 10.2116/analsci.27.143.
- [58] P. Rahe et al. “Quantitative dynamic force microscopy with inclined tip oscillation”. In: *Beilstein Journal of Nanotechnology* 13 (July 2022), pp. 610–619. DOI: 10.3762/bjnano.13.53.

- [59] P. Rahe, R. P. Steele, and C. C. Williams. “Consecutive Charging of a Molecule-on-Insulator Ensemble Using Single Electron Tunnelling Methods”. In: *Nano Letters* 16.2 (Jan. 2016), pp. 911–916. DOI: 10.1021/acs.nanolett.5b03725.
- [60] S. Fatayer et al. “Reorganization energy upon charging a single molecule on an insulator measured by atomic force microscopy”. In: *Nature Nanotechnology* 13.5 (Apr. 2018), pp. 376–380. DOI: 10.1038/s41565-018-0087-1.
- [61] Y. Adachi et al. “Charge State Tristability of Oxygen Adatom on a Rutile  $\text{TiO}_2(110)-(1\times 1)$  Surface Controlled by Atomic Force Microscopy”. In: *The Journal of Physical Chemistry C* 126.10 (Mar. 2022), pp. 5064–5069. DOI: 10.1021/acs.jpcc.2c00347.
- [62] Lord Kelvin. “Contact Electricity of Metals”. In: *Philosophical Magazine* 46.278 (July 1898), pp. 82–120. DOI: 10.1080/14786449808621172.
- [63] M. Nonnenmacher, M. P. O’Boyle, and H. K. Wickramasinghe. “Kelvin probe force microscopy”. In: *Applied Physics Letters* 58.25 (June 1991), pp. 2921–2923. DOI: 10.1063/1.105227.
- [64] J. M. R. Weaver and D. W. Abraham. “High resolution atomic force microscopy potentiometry”. In: *Journal of Vacuum Science and Technology, B: Microelectronics and Nanometer Structures* 9.3 (1991), pp. 1559–61.
- [65] W. Melitz et al. “Kelvin probe force microscopy and its application”. In: *Surface Science Reports* 66.1 (Jan. 2011), pp. 1–27. DOI: 10.1016/j.surfrep.2010.10.001.
- [66] K. Wandelt. “The local work function: Concept and implications”. In: *Applied Surface Science* 111 (Feb. 1997), pp. 1–10. DOI: 10.1016/S0169-4332(96)00692-7.
- [67] L. N. Kantorovich, A. I. Livshits, and M. Stoneham. “Electrostatic energy calculation for the interpretation of scanning probe microscopy experiments”. In: *Journal of Physics: Condensed Matter* 12.6 (2000), p. 795. ISSN: 0953-8984.
- [68] J. L. Neff and P. Rahe. “Insights into Kelvin probe force microscopy data of insulator-supported molecules”. In: *Physical Review B* 91.8 (Feb. 2015), p. 085424. DOI: 10.1103/Physrevb.91.085424.
- [69] H. Söngen et al. “The weight function for charges—A rigorous theoretical concept for Kelvin probe force microscopy”. In: *Journal of Applied Physics* 119.2 (Jan. 2016), p. 025304. DOI: 10.1063/1.4939619.
- [70] P. Rahe and H. Söngen. “Imaging a static charge distributions: A comprehensive KPFM theory, in *Kelvin Probe Force Microscopy: From Single Charge Detection to Device Characterization*”. In: 65 (2018). Ed. by Sascha Sade-wasser and Thilo Glatzel, pp. 147–170. DOI: 10.1007/978-3-319-75687-5.

- [71] A. Sadeghi et al. “Multiscale approach for simulations of Kelvin probe force microscopy with atomic resolution”. In: *Physical Review B* 86.7 (Aug. 2012), p. 075407. DOI: 10.1103/PhysRevB.86.075407.
- [72] L. Piliai et al. “In Situ Spectroscopy and Microscopy Insights into the CO Oxidation Mechanism on Au/CeO<sub>2</sub>(111)”. In: *ACS Applied Materials & Interfaces* 14.50 (Dec. 2022), pp. 56280–56289. DOI: 10.1021/acsmi.2c15792.
- [73] M. J. Zachman et al. “Measuring and directing charge transfer in heterogeneous catalysts”. In: *Nature Communications* 13.1 (June 2022). DOI: 10.1038/s41467-022-30923-2.
- [74] R. Aso et al. “Direct identification of the charge state in a single platinum nanoparticle on titanium oxide”. In: *Science* 378.6616 (Oct. 2022), pp. 202–206. DOI: 10.1126/science.abq5868.
- [75] C. Gao and O. Terasaki. “Counting charges per metal particle”. In: *Science Advances* 378.6616 (Oct. 2022), p. 133. DOI: 10.1126/science.adeww6051.
- [76] U. Hartmann. “Magnetic Force Microscopy”. In: *Annual Review of Materials Science* 29.1 (Aug. 1999), pp. 53–87. DOI: 10.1146/annurev.matsci.29.1.53.
- [77] S. Kuhn and P. Rahe. “Discriminating short-range from van der Waals forces using total force data in noncontact atomic force microscopy”. In: *Physical Review B* 89.23 (June 2014), p. 235417. DOI: 10.1103/PhysRevB.89.235417.
- [78] F. J. Giessibl et al. “Subatomic Features on the Silicon (111)-(7×7) Surface Observed by Atomic Force Microscopy”. In: *Science* 289.5478 (July 2000), pp. 422–425. DOI: 10.1126/science.289.5478.422.
- [79] M. Huang, M. Čuma, and F. Liu. “Seeing the Atomic Orbital: First-Principles Study of the Effect of Tip Termination on Atomic Force Microscopy”. In: *Physical Review Letters* 90.25 (2003), p. 256101. DOI: 10.1103/PhysRevLett.90.256101.
- [80] F. J. Giessibl. “Advances in atomic force microscopy”. In: *Reviews of Modern Physics* 75.3 (July 2003), p. 949.
- [81] P. M. Morse. “Diatomic Molecules According to the Wave Mechanics. II. Vibrational Levels”. In: *Physical Review* 34.1 (July 1929), p. 57.
- [82] F. London. “The general theory of molecular forces”. In: *Transactions of Faraday Society* 332 (1936), p. 8.
- [83] A. D. McLachlan. “Retarded dispersion forces between molecules”. In: *Proc. Royal. Soc. London A*. 271.Ser. A (1963), pp. 387–401.
- [84] J. E. Lennard-Jones. “Cohesion”. In: *Proceedings of the Physical Society* 43.5 (1931), pp. 461–482. ISSN: 0959-5309.

## Bibliography

- [85] B. R. Holstein. “The van der Waals interaction”. In: *American Journal of Physics* 69.4 (Apr. 2001), pp. 441–449. DOI: 10.1119/1.1341251.
- [86] H. G. B. Casimir and D. Polder. “The Influence of Retardation on the London-van der Waals Forces”. In: *Physical Review* 73.4 (Feb. 1948), pp. 360–372.
- [87] J. N. Israelachvili and D. R. F. S. Tabor. “The measurement of van der Waals dispersion forces in the range 1.5 to 130 nm”. In: *The Royal Society* 331.1584 (1972), pp. 19–38.
- [88] A. Šiber et al. “Dispersion interactions between optically anisotropic cylinders at all separations: Retardation effects for insulating and semiconducting single-wall carbon nanotubes”. In: *Physical Review B* 80.16 (Oct. 2009), p. 165414. DOI: 10.1103/PhysRevB.80.165414.
- [89] H. C. Hamaker. “The London-van der Waals attraction between spherical particles”. In: *Physica (The Hague)* 4 (1937), pp. 1058–72.
- [90] C. Argento and R. H. French. “Parametric tip model and force–distance relation for Hamaker constant determination from atomic force microscopy”. In: *Journal of Applied Physics* 80.11 (Dec. 1996), pp. 6081–6090.
- [91] S. I. Zanette et al. “Theoretical and experimental investigation of the force–distance relation for an atomic force microscope with a pyramidal tip”. In: *Surface Science* 453.1-3 (Oct. 2000), pp. 75–82. DOI: 10.1016/S0039-6028(00)00306-X.
- [92] L. D. Landau and E. M. Lifshitz. *Electrodynamics of continuous media*. Elsevier, 1984, p. iv. DOI: 10.1016/B978-0-08-030275-1.50003-5.
- [93] J. D. Jackson. *Klassische Elektrodynamik*. Ed. by C. Witte. Gruyter, Walter de GmbH, Dec. 18, 2013. ISBN: 978-3-11-033446-3.
- [94] W. Nolting. *Grundkurs Theoretische Physik 3*. Springer Berlin Heidelberg, 2013. ISBN: 978-3-642-37904-8. DOI: 10.1007/978-3-642-37905-5.
- [95] S. Hudlet et al. “Evaluation of the capacitive force between an atomic force microscopy tip and a metallic surface”. In: *European Physical Journal B: Condensed Matter Physics* 2.1 (1998), pp. 5–10.
- [96] A. Sadeghi, A. Baratoff, and S. Goedecker. “Electrostatic interactions with dielectric samples in scanning probe microscopies”. In: *Physical Review B* 88.3 (July 2013), p. 035436. DOI: 10.1103/PhysRevB.88.035436.
- [97] M. A. Lantz et al. “Quantitative Measurement of Short-Range Chemical Bonding Forces”. In: *Science* 291.5513 (Mar. 2001), pp. 2580–2583. DOI: 10.1126/science.1057824.
- [98] A. Sweetman and A. Stannard. “Uncertainties in forces extracted from non-contact atomic force microscopy measurements by fitting of long-range background forces”. In: *Beilstein Journal of Nanotechnology* 5 (Apr. 2014), pp. 386–393. DOI: 10.3762/bjnano.5.45.

- [99] T. R. Albrecht et al. “Frequency modulation detection using high- $Q$  cantilevers for enhanced force microscope sensitivity”. In: *Journal of Applied Physics* 69.2 (Jan. 1991), pp. 668–673. DOI: 10.1063/1.347347.
- [100] T. R. Albrecht et al. “Microfabrication of cantilever styli for the atomic force microscope”. In: *Journal of Vacuum Science & Technology A: Vacuum, Surfaces, and Films* 8.4 (July 1990), pp. 3386–3396. DOI: 10.1116/1.576520.
- [101] O. Wolter, T. Bayer, and J. Greschner. “Micromachined silicon sensors for scanning force microscopy”. In: *Journal of Vacuum Science Technology B: Microelectronics and Nanometer Structures* 9.2 (Mar. 1991), p. 1353. DOI: 10.1116/1.585195.
- [102] F. J. Giessibl et al. “Stability considerations and implementation of cantilevers allowing dynamic force microscopy with optimal resolution: the qPlus sensor”. In: *Nanotechnology* 15.2 (Jan. 2004), S79–S86. DOI: 10.1088/0957-4484/15/2/017.
- [103] F. J. Giessibl and M. Reichling. “Investigating atomic details of the  $\text{CaF}_2(111)$  surface with a qPlus sensor”. In: *Nanotechnology* 16.3 (Jan. 2005), S118–S124. DOI: 10.1088/0957-4484/16/3/022.
- [104] S. Torbrügge, O. Schaff, and J. Rychen. “Application of the KolibriSensor<sup>®</sup> to combined atomic-resolution scanning tunneling microscopy and noncontact atomic-force microscopy imaging”. In: *Journal of Vacuum Science & Technology B, Nanotechnology and Microelectronics: Materials, Processing, Measurement, and Phenomena* 28.3 (May 2010), C4E12–C4E20. DOI: 10.1116/1.3430544.
- [105] S. Heike and T. Hashizume. “Atomic resolution noncontact atomic force/scanning tunneling microscopy using a 1 MHz quartz resonator”. In: *Applied Physics Letters* 83.17 (Oct. 2003), pp. 3620–3622. DOI: 10.1063/1.1623012.
- [106] Y. Sugimoto and J. Onoda. “Force spectroscopy using a quartz length-extension resonator”. In: *Applied Physics Letters* 115.17 (Oct. 2019), p. 173104. DOI: 10.1063/1.5112062.
- [107] F. J. Giessibl et al. “Comparison of force sensors for atomic force microscopy based on quartz tuning forks and length-extensional resonators”. In: *Physical Review B* 84.12 (Sept. 2011), p. 125409. DOI: 10.1103/PhysRevB.84.125409.
- [108] R. B. Marcus et al. “Formation of silicon tips with  $<1$  nm radius”. In: *Applied Physics Letters* 56.3 (Jan. 1990), pp. 236–238. DOI: 10.1063/1.102841.
- [109] C. Julian Chen. *Introduction to Scanning Tunneling Microscopy*. Oxford University Press Oxford, Sept. 2007. DOI: 10.1093/acprof:oso/9780199211500.001.0001.



## Bibliography

- [110] J. Lübbe, L. Doering, and M. Reichling. “Precise determination of force microscopy cantilever stiffness from dimensions and eigenfrequencies”. In: *Measurement Science and Technology* 23.4 (Feb. 2012), p. 045401. DOI: 10.1088/0957-0233/23/4/045401.
- [111] F. R. Blom et al. “Dependence of the quality factor of micromachined silicon beam resonators on pressure and geometry”. In: *Journal of Vacuum Science & Technology B* 10.1 (1992), pp. 19–26. ISSN: 1071-1023.
- [112] J. Lübbe et al. “Achieving high effective Q-factors in ultra-high vacuum dynamic force microscopy”. In: *Measurement Science and Technology* 21.12 (Nov. 2010), p. 125501. DOI: 10.1088/0957-0233/21/12/125501.
- [113] R. Lifshitz and M. L. Roukes. “Thermoelastic damping in micro- and nanomechanical systems”. In: *Physical Review B* 61.8 (Feb. 2000), pp. 5600–5609. ISSN: 0163-1829.
- [114] U. Gysin et al. “Temperature dependence of the force sensitivity of silicon cantilevers”. In: *Physical Review B* 69.4 (Jan. 2004), p. 045403. DOI: 10.1103/Physrevb.69.045403.
- [115] R. N. Candler et al. “Impact of geometry on thermoelastic dissipation in micromechanical resonant beams”. In: *Journal of Microelectromechanical Systems* 15.4 (Aug. 2006), pp. 927–934. ISSN: 1057-7157.
- [116] K. Naeli and O. Brand. “Dimensional considerations in achieving large quality factors for resonant silicon cantilevers in air”. In: *Journal of Applied Physics* 105.1 (Jan. 2009), p. 014908. DOI: 10.1063/1.3062204.
- [117] Z. Hao, A. Erbil, and F. Ayazi. “An analytical model for support loss in micromachined beam resonators with in-plane flexural vibrations”. In: *Sensors and Actuators A: Physical* 109.1-2 (Dec. 2003), pp. 156–164. DOI: 10.1016/j.sna.2003.09.037.
- [118] S. Bianco et al. “Silicon resonant microcantilevers for absolute pressure measurement”. In: *Journal of Vacuum Science & Technology B: Microelectronics and Nanometer Structures* 24.4 (June 2006), p. 1803. DOI: 10.1116/1.2214698.
- [119] J. Lübbe, H. Schnieder, and M. Reichling. “Pressure Dependence of the Q-factor of Cantilevers used for NC-AFM”. In: *e-Journal of Surface Science and Nanotechnology* 9 (2011), pp. 30–33. DOI: 10.1380/ejssnt.2011.30.
- [120] J. Lübbe et al. “Measurement and modelling of non-contact atomic force microscope cantilever properties from ultra-high vacuum to normal pressure conditions”. In: *Measurement Science and Technology* 22.5 (Mar. 2011), p. 055501. DOI: 10.1088/0957-0233/22/5/055501.
- [121] G. Meyer and N. M. Amer. “Optical-beam-deflection atomic force microscopy: The NaCl (001) surface”. In: *Applied Physics Letters* 56.21 (1990), pp. 2100–2101.

- [122] S. Torbrügge et al. “Improvement of a dynamic scanning force microscope for highest resolution imaging in ultrahigh vacuum”. In: *Review of Scientific Instruments* 79.8 (Aug. 2008), p. 083701. DOI: 10.1063/1.2964119.
- [123] J. Polesel-Maris et al. “Noise in frequency-modulation dynamic force microscopy”. In: *Physical Review B* 79.23 (June 2009), p. 235401. DOI: 10.1103/PhysRevB.79.235401.
- [124] H. Diesinger, D. Deresmes, and T. Mélin. “Noise performance of frequency modulation Kelvin force microscopy”. In: *Beilstein Journal of Nanotechnology* 5 (Jan. 2014), pp. 1–18. DOI: 10.3762/bjnano.5.1.
- [125] G. H. Simon, M. Heyde, and H.-P. Rust. “Recipes for cantilever parameter determination in dynamic force spectroscopy: spring constant and amplitude”. In: *Nanotechnology* 18.25 (June 2007), p. 255503. DOI: 10.1088/0957-4484/18/25/255503.
- [126] Y. Sugimoto et al. “Simultaneous AFM and STM measurements on the Si(111)-(7×7) surface”. In: *Physical Review B* 81.24 (June 2010), p. 245322. DOI: 10.1103/PhysRevB.81.245322.
- [127] S. S. Borysov, D. Forchheimer, and D. B. Haviland. “Dynamic calibration of higher eigenmode parameters of a cantilever in atomic force microscopy by using tip-surface interactions”. In: *Beilstein Journal of Nanotechnology* 5 (Oct. 2014), pp. 1899–1904. DOI: 10.3762/bjnano.5.200.
- [128] J. F. Portolés et al. “Accurate velocity measurements of AFM-cantilever vibrations by Doppler interferometry”. In: *Journal of Experimental Nanoscience* 1.1 (Mar. 2006), pp. 51–62. DOI: 10.1080/17458080500411999.
- [129] F. J. Azcona et al. “Microcantilever Displacement Measurement Using a Mechanically Modulated Optical Feedback Interferometer”. In: *Sensors* 16.7 (June 2016), p. 997. DOI: 10.3390/s16070997.
- [130] F. J. Giessibl. “Forces and frequency shifts in atomic-resolution dynamic-force microscopy”. In: *Physical Review B* 56.24 (Dec. 1997), p. 16010.
- [131] I. N. Bronstein et al. *Taschenbuch der Mathematik (Bronstein)*. Europa Lehrmittel Verlag, July 15, 2020. ISBN: 978-3-8085-5792-1.
- [132] U. Dürig. “Relations between interaction force and frequency shift in large-amplitude dynamic force microscopy”. In: *Applied Physics Letters* 75.3 (July 1999), pp. 433–435. DOI: 10.1063/1.124399.
- [133] U. Dürig. “Conservative and dissipative interactions in dynamic force microscopy”. In: *Surface and Interface Analysis* 27.5-6 (May 1999), pp. 467–473. DOI: 10.1002/(SICI)1096-9918(199905/06)27:5/6<467::AID-SIA519>3.0.CO;2-7.
- [134] N. Sasaki et al. “Dynamics of the cantilever in noncontact atomic force microscopy”. In: *Applied Physics A: Materials Science & Processing* 66.7 (Mar. 1998), S287–S291. DOI: 10.1007/s003390051147.

## Bibliography

- [135] H. Hölscher. “Quantitative measurement of tip-sample interactions in amplitude modulation atomic force microscopy”. In: *Applied Physics Letters* 89.12 (Sept. 2006), p. 123109. DOI: 10.1063/1.2355437.
- [136] A. F. Payam, D. Martin-Jimenez, and R. Garcia. “Force reconstruction from tapping mode force microscopy experiments”. In: *Nanotechnology* 26.18 (Apr. 2015), p. 185706. DOI: 10.1088/0957-4484/26/18/185706.
- [137] U. Dürig. “Interaction sensing in dynamic force microscopy”. In: *New Journal of Physics* 2 (Mar. 2000), pp. 5–5. DOI: 10.1088/1367-2630/2/1/005.
- [138] H. Hölscher. “Theory of phase-modulation atomic force microscopy with constant-oscillation amplitude”. In: *Journal of Applied Physics* 103.6 (Mar. 2008), p. 064317. DOI: 10.1063/1.2896450.
- [139] J. E. Sader et al. “Quantitative force measurements using frequency modulation atomic force microscopy?theoretical foundations”. In: *Nanotechnology* 16.3 (Jan. 2005), S94–S101. DOI: 10.1088/0957-4484/16/3/018.
- [140] U. Dürig. “Extracting interaction forces and complementary observables in dynamic probe microscopy”. In: *Applied Physics Letters* 76.9 (Feb. 2000), pp. 1203–1205. DOI: 10.1063/1.125983.
- [141] F. J. Giessibl. “A direct method to calculate tip-sample forces from frequency shifts in frequency-modulation atomic force microscopy”. In: *Applied Physics Letters* 78.1 (Jan. 2001), pp. 123–125. DOI: 10.1063/1.1335546.
- [142] J. E. Sader and Y. Sugimoto. “Accurate formula for conversion of tunneling current in dynamic atomic force spectroscopy”. In: *Applied Physics Letters* 97.4 (July 2010), p. 043502. DOI: 10.1063/1.3464165.
- [143] Daniel Heile et al. “Modeling nanoscale charge measurements”. In: *Physical Review B* 108.8 (Aug. 2023), p. 085420. DOI: 10.1103/PhysRevB.108.085420.
- [144] G. Gramse, G. Gomila, and L. Fumagalli. “Quantifying the dielectric constant of thick insulators by electrostatic force microscopy: effects of the microscopic parts of the probe”. In: *Nanotechnology* 23.20 (Apr. 2012), p. 205703. DOI: 10.1088/0957-4484/23/20/205703.
- [145] W. R. Smythe. *Static And Dynamic Electricity*. Taylor and Francis, 1989. ISBN: 978-0891169178.

## **B. Erklärung über die Eigenständigkeit der erbrachten wissenschaftlichen Leistung**

Ich erkläre hiermit, dass ich die vorliegende Arbeit ohne unzulässige Hilfe Dritter und ohne Benutzung anderer als der angegebenen Hilfsmittel angefertigt habe. Die aus anderen Quellen direkt oder indirekt übernommenen Daten und Konzepte sind unter Angabe der Quelle gekennzeichnet.

Bei meiner wissenschaftlichen Arbeit und der Entstehung dieser Dissertation haben mir die nachstehend aufgeführten Personen in der jeweils beschriebenen Weise unentgeltlich geholfen.

1. Prof. Dr. Michael Reichling hat bei der physikalischen Deutung von Mess- und Simulationsergebnissen, sowie beim Anfertigen und Veröffentlichen der Publikationen mitgewirkt.
2. Dr. Philipp Rahe hat die Constant-Gamma Simulation in der Publikation "Alignment method for the accurate and precise quantification of tip surface-forces" erstellt, Rechnungen für in die Publikation "Quantitative dynamic force microscopy with inclined tip oscillation" durchgeführt und den CapSol-Code für die Anwendung in CFM vorbereitet, sowie beim Anfertigen und Veröffentlichen der Publikationen mitgewirkt.
3. Dr. Reinhard Olbrich hat als Laborbetreuer bei der Entwicklung und Implementierung von FCA, beim durchführen der Experimente für FCA und CFM, sowie beim Anfertigen und Veröffentlichen der Publikationen mitgewirkt.

Weitere Personen oder maschinelle Systeme waren an der inhaltlichen und materiellen Erstellung der vorliegenden Arbeit nicht beteiligt. Insbesondere habe ich hierfür nicht die entgeltliche Hilfe von Vermittlungs- bzw. Beratungsdiensten (Promotionsberater oder andere Personen) in Anspruch genommen. Niemand hat von mir unmittelbar oder mittelbar geldwerte Leistungen für Arbeiten erhalten, die im

*B. Erklärung über die Eigenständigkeit der erbrachten wissenschaftlichen Leistung*

Zusammenhang mit dem Inhalt der vorgelegten Dissertation stehen.

Die Arbeit wurde bisher weder im In- noch im Ausland in gleicher oder ähnlicher Form einer anderen Prüfungsbehörde vorgelegt.

.....  
(Ort, Datum)

.....  
(Unterschrift)